



National Library
of Canada

Bibliothèque nationale
du Canada

Canadian Theses Service Service des thèses canadiennes

Ottawa, Canada
K1A 0N4

NOTICE

The quality of this microform is heavily dependent upon the quality of the original thesis submitted for microfilming. Every effort has been made to ensure the highest quality of reproduction possible.

If pages are missing, contact the university which granted the degree.

Some pages may have indistinct print especially if the original pages were typed with a poor typewriter ribbon or if the university sent us an inferior photocopy.

Reproduction in full or in part of this microform is governed by the Canadian Copyright Act, R.S.C. 1970, c. C-30, and subsequent amendments.

AVIS

La qualité de cette microforme dépend grandement de la qualité de la thèse soumise au microfilmage. Nous avons tout fait pour assurer une qualité supérieure de reproduction.

S'il manque des pages, veuillez communiquer avec l'université qui a conféré le grade.

La qualité d'impression de certaines pages peut laisser à désirer, surtout si les pages originales ont été dactylographiées à l'aide d'un ruban usé ou si l'université nous a fait parvenir une photocopie de qualité inférieure.

La reproduction, même partielle, de cette microforme est soumise à la Loi canadienne sur le droit d'auteur, SRC 1970, c. C-30, et ses amendements subséquents.

UNIVERSITY OF ALBERTA

INTERFEROMETRIC MEASUREMENT OF ELECTRON DENSITY IN
KRYPTON FLUORIDE LASER-PRODUCED PLASMA

BY

ROBERT GEORGE NEWTON



A THESIS

SUBMITTED TO THE FACULTY OF GRADUATE STUDIES AND RESEARCH
IN PARTIAL FULFILLMENT OF THE REQUIREMENTS FOR THE
DEGREE OF MASTER OF SCIENCE

DEPARTMENT OF ELECTRICAL ENGINEERING

EDMONTON ALBERTA

SPRING 1991



National Library
of Canada

Bibliothèque nationale
du Canada

Canadian Theses Service Service des thèses canadiennes

Ottawa, Canada
K1A 0N2

The author has granted an irrevocable non-exclusive licence allowing the National Library of Canada to reproduce, loan, distribute or sell copies of his/her thesis by any means and in any form or format, making this thesis available to interested persons.

The author retains ownership of the copyright in his/her thesis. Neither the thesis nor substantial extracts from it may be printed or otherwise reproduced without his/her permission.

L'auteur a accordé une licence irrévocable et non exclusive permettant à la Bibliothèque nationale du Canada de reproduire, prêter, distribuer ou vendre des copies de sa thèse de quelque manière et sous quelque forme que ce soit pour mettre des exemplaires de cette thèse à la disposition des personnes intéressées.

L'auteur conserve la propriété du droit d'auteur qui protège sa thèse. Ni la thèse ni des extraits substantiels de celle-ci ne doivent être imprimés ou autrement reproduits sans son autorisation.

ISBN 0-215-66570-X

Canada

UNIVERSITY OF ALBERTA

RELEASE FORM

NAME OF AUTHOR: ROBERT GEORGE NEWTON

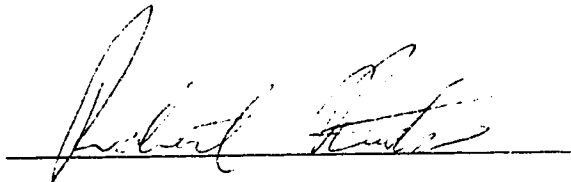
TITLE OF THESIS: INTERFEROMETRIC MEASUREMENT OF
ELECTRON DENSITY IN KRYPTON FLUORIDE LASER-PRODUCED
PLASMA

DEGREE: MASTER OF SCIENCE

YEAR THIS DEGREE GRANTED: SPRING 1991

PERMISSION IS HEREBY GRANTED TO THE UNIVERSITY OF
ALBERTA LIBRARY TO REPRODUCE SINGLE COPIES OF THIS THESIS
AND TO LEND OR SELL SUCH COPIES FOR PRIVATE, SCHOLARLY OR
SCIENTIFIC RESEARCH PURPOSES ONLY.

THE AUTHOR RESERVES OTHER PUBLICATION RIGHTS, AND
NEITHER THE THESIS NOR EXTENSIVE EXTRACTS FROM IT MAY BE
PRINTED OR OTHERWISE REPRODUCED WITHOUT THE AUTHOR'S
WRITTEN PERMISSION.



855 Mayne Rd.

Kamloops BC

V2B 6H4

Date: 28 December 28, 1990

UNIVERSITY OF ALBERTA

FACULTY OF GRADUATE STUDIES AND RESEARCH

THE UNDERSIGNED CERTIFY THAT THEY HAVE READ, AND RECOMMEND TO THE FACULTY OF GRADUATE STUDIES AND RESEARCH FOR ACCEPTANCE, A THESIS ENTITLED INTERFEROMETRIC MEASUREMENT OF ELECTRON DENSITY IN KRYPTON FLUORIDE LASER-PRODUCED PLASMA

SUBMITTED BY ROBERT GEORGE NEWTON IN PARTIAL FULFILLMENT OF THE REQUIREMENTS FOR THE DEGREE OF MASTER OF SCIENCE.

Robert Fedosejevs

DR. R. FEDOSEJEVS

Donald R. Lawson

DR. R. LAWSON

Peter Smy

DR. P. SMY

E. J. Pinnington

DR. E. PINNINGTON

DATE: December 27, 1990

ABSTRACT

Interferometric measurements using a traveling wave excited N_2 laser have been made of 1.5 ns Brillouin compressed 0.248 μm KrF laser-produced aluminum plasma. The main laser is focused onto a slab target using $f/2$ optics producing a 35 μm diameter focal spot and giving intensities up to $1 \times 10^{14} \text{ W cm}^{-2}$. The N_2 laser was used at a filling pressure of 1 atm producing a pulse having a FWHM of 600 ps. The interferometry was done using a Jamin interferometer and the interferogram was recorded as a digitized video image.

The results of the experiment are compared to results obtained from 1D Medusa and 2D Castor numerical simulation. In addition, The data is analyzed using analytic techniques which include planar and spherical self-similar expansion, self-regulating model of planar expansion and a spherical stationary flow model developed in this thesis. The early self-similar planar expansion may be modeled using the self-regulating model by taking into account the lateral expansion of the plasma. This is followed by a predominantly $1/r^2$ density profile indicating spherical stationary flow. The presence of axial jets and late-time conical structures observed are also discussed.

TABLE OF CONTENTS

CHAPTER 1	INTRODUCTION.....	1
	1.1 KrF Laser Facility.....	2
	1.2 Description of the Experiment.....	2
	1.3 Previous Research.....	4
	1.4 Goals of the Present Study.....	4
CHAPTER 2	BACKGROUND AND THEORY.....	6
	2.1 Plasma Equations of Motion.....	6
	(a) Plasma kinetic equation of motion.....	6
	(b) Plasma fluid equations of motion.....	9
	2.2 Analytic Model of Laser Plasma Expansion.....	13
	(a) Planar self-similar rarefaction into vacuum.....	13
	(b) Self-similar solutions with non planar 1D geometry.....	16
	(c) Self-regulating flow model.....	17
	(d) Stationary flow.....	25
	2.3 Computer Simulation of Laser Plasma Expansion..	27
	2.4 Magnetic Field Production in Laser Plasma.....	28
	2.5 Refractive Index of a Plasma.....	31
	2.6 Interferometry of Plasma.....	33
	(a) Interferometry of 2D plasma.....	33
	(b) Routines for calculating Abel's integral...	36
CHAPTER 3	EXPERIMENTAL SETUP.....	42
	3.1 KrF Laser System.....	44
	3.2 Target System.....	45
	3.3 Nitrogen Laser.....	46

3.4 Jamin Interferometer.....	53
3.5 Imaging and Digitization.....	57
3.6 Timing and Calibration.....	58
CHAPTER 4 EXPERIMENTAL RESULTS.....	61
4.1 Experimental Data.....	61
4.2 Interferogram Deconvolution.....	66
4.3 Determination of Scale-Lengths.....	69
4.4 Quick Axial Inversion.....	72
4.5 Deconvolution Example.....	74
4.6 Deconvolution Accuracy.....	77
(a) Random contributions to deconvolution error.....	77
(b) Systematic limitations to deconvolution accuracy.....	82
4.7 Lateral Expansion.....	90
CHAPTER 5 DISCUSSION.....	94
5.1 Spherical Smoothing of Data Points.....	96
5.2 Main Laser Pulse Shape.....	98
5.3 Castor 2D Simulations.....	101
5.4 Initial Plasma Expansion.....	106
(a) Self-similar expansion of the plasma.....	109
(b) Plasma temperature.....	110
(c) Medusa 1D simulation.....	112
(d) Self-regulating model with lateral expansion.....	114
(e) Transition from planar to spherical flow...	119
5.5 Stationary Spherical Flow.....	119

(a) Transition to stationary flow.....	120
(b) Comparison of data to stationary flow model.....	122
5.6 Plasma Collapse Following Laser Turn-Off.....	129
5.7 Self-Generated Magnetic Fields.....	131
CHAPTER 6 CONCLUSION.....	134
REFERENCES.	137
APPENDIX A NUMERICAL TESTS OF DECONVOLUTION ROUTINES..	145
A.1 Testing of Deconvolution Routines.....	145
A.2 Abel Integrated Test Functions.....	155
APPENDIX B CONTOURS OF KRF LASER-PLASMA.....	156

LIST OF TABLES

Chapter 4	
Table 4.1.	Interferogram shot statistics..... 62
Table 4.2.	
(a).	Scale-lengths (early time). Electron densities from Bockastem inversion..... 71
(b).	Electron densities obtained from Bockastem inversion. Scale-lengths measured between 6×10^{18} and 6×10^{19} 71
Table 4.3.	Scale-lengths obtained from quick inversion..... 74
Table 4.4.	Random error in electron density..... 82
Appendix A	
Table A.1.	Inversion accuracy for test function #1.... 149
Table A.2.	Inversion accuracy for test function #2.... 149
Table A.3.	Inversion accuracy for test function #3 with different cutoff points..... 151
Table A.4.	Inversion accuracy of test function #4 with and without 30 degree expansion angle. 153

LIST OF FIGURES

Chapter 2	
Fig. 2.1.	Planar isothermal self-similar expansion of plasma into vacuum..... 15
Fig. 2.2.	Self-regulating plasma flow model..... 18
Fig. 2.3.	Transverse probing of an axially symmetric plasma..... 34
Chapter 3	
Fig. 3.1.	Schematic of the experimental setup..... 43
Fig. 3.2.	N_2 laser levels..... 47
Fig. 3.3.	Electrical schematic for N_2 laser..... 49
Fig. 3.4.	Schematic of N_2 laser physical setup..... 50
Fig. 3.5.	Comparison of the front pulse with the back pulse for different electrode wedge angles..... 52
Fig. 3.6.	Typical streak of N_2 laser pulse..... 52
Fig. 3.7.	Jamin interferometer..... 54
Fig. 3.8.	Interferometer focusing wire..... 59
Chapter 4	
Fig. 4.1.	Interferograms obtained at various times... 65
Fig. 4.2.	Main laser pulse shape for shot 22078821... 75
Fig. 4.3.	Interferogram and corresponding digitized fringes for shot 22078821..... 76
Fig. 4.4.	Axial electron density plot for shot 22078821..... 78
Fig. 4.5.	Electron density contour plot for shot 22078821. Contours represent the \log_{10}

	of the electron density (cm^{-3}).....	79
Fig. 4.6.	Effect of curved ray path through plasma...	86
Fig. 4.7.	Effect of interferometer misfocus.....	83
Fig. 4.8.	Method of determining diameter of expansion cone.....	91
Fig. 4.9.	Measured diameter of the expansion cone at the target surface as a function of time...	92
Chapter 5		
Fig. 5.1.	Experimentally measured scale-lengths for Krf laser produced plasma.....	95
Fig. 5.2.	Contour plot of axial jet for shot 14108808. The plot shows radial cuts used to obtain the averaged scale-lengths.....	97
Fig. 5.3.	Comparison of axial scale-lengths to averaged scale-lengths.....	99
Fig. 5.4.	Typical main laser pulse.....	100
Fig. 5.5.	Contour plots from data and Castor simulation: R and Z represent radial and axial dimensions, contours are \log_{10} of electron density (cm^{-3}).....	103
Fig. 5.6.	Comparison of axial scale-length from the experimental data and Castor simulations...	104
Fig. 5.7.	Instability in the collapse of the density profile for the Castor 1 J simulation.....	105
Fig. 5.8.	Measured lateral growth in radius of early-time laser plasma for medium and high energy shots.....	108

Fig. 5.9		
	(a).	Axial temperature distribution for Castor 1 J simulation..... 111
	(b).	Radial temperature profile at $t = 0.276$ ns and $z = 45$ microns from the target surface. 111
Fig. 5.10.		Scale-length from Medusa 1 J simulation and comparable self-regulating model calculation..... 113
Fig. 5.11.		Self-regulating model using an effective intensity based on the actual plasma diameter..... 115
Fig. 5.12.		Self-regulating model using effective intensity, Castor 1J simulation, medium and high energy data points..... 117
Fig. 5.13.		Experimentally measured axial electron density profiles showing the transition from self-similar to stationary flow..... 121
Fig. 5.14.		Axial electron density profiles showing self-similar type expansion at early times in the Castor 1 J simulation..... 123
Fig. 5.15.		Transition to stationary flow in Castor 1 J simulation..... 124
Fig. 5.16.		Comparison of Castor and experimental axial density profiles illustrating the stationary flow profile..... 125
Fig. 5.17.		Comparison between experimental data and the spherical stationary flow model..... 127

Fig. 5.18.	Comparison of late-time data profiles to stationary flow model showing steepening of the profile.....	130
Appendix A		
Fig. A.1		
(a).	Fringes produced by test function #3.....	147
(b).	Fringes produced by test function #4 with a 30 degree expansion angle.....	147
Fig. A.2		
(a).	Inversion accuracy with smoothing for test function #1.....	150
(b).	Inversion accuracy with smoothing for test function #2.....	150
Fig. A.3		
(a).	Inversion accuracy of test function #3. Inversion is cutoff 500 microns from the inversion axis.....	152
(b).	Inversion accuracy of test function #3 when inversion is cutoff 200 microns from the inversion axis.....	152
Fig. A.4		
(a).	Inversion accuracy of test function #4 with zero expansion angle.....	154
(b).	Inversion accuracy of test function #4 with 30 degree expansion angle.....	154

VARIABLES, CONSTANTS AND SYMBOLS

Following is a list giving the symbols for physical constants used in this thesis:

- c - Speed of light in vacuum.
- e - Elementary electric charge.
- k_b - Boltzmann constant.
- m_e - Electron mass.
- m_p - Proton mass.
- ϵ_0 - Permittivity of vacuum.
- μ_0 - Permeability of vacuum.

The variables used in this thesis are defined as they are introduced. Variable names have in general been chosen to avoid confusion. Following is a list of variable conventions, symbols and abbreviations used consistently throughout the thesis:

- a - Particle acceleration vector.
- A - Plasma absorption coefficient.
- A_{jk} - Inversion matrix coefficients.
- B - Magnetic field vector.
- B - Magnetic field magnitude.
- c_s - Ion acoustic velocity.
- C_p - Heat capacity at constant pressure.
- C_v - Heat capacity at constant volume.
- E - Electric field vector.
- E - Electric field magnitude.
- $f^{(1)}$ - One body distribution function.
- $f^{(2)}$ - Two body distribution function.

$f /$ - Optical f number = focal length / beam diameter.

FWHM - Full width half maximum.

H - Kinetic energy heat flux.

I - Laser intensity.

J - Electric current.

L - Plasma density scale-length.

m - Particle mass.

m_e - Electron rest mass.

m_i - Ion rest mass.

n - Particle density.

n_e - Electron density.

n_i - Ion density.

n_0 - Particle density at the plasma absorption surface.

n_c - Plasma critical density.

n_r - Plasma refractive index.

P - Pressure tensor.

p - Scalar pressure.

p_a - Plasma ablation pressure.

Q - Heat flux.

Q - Magnitude of heat flux.

q - Electric charge.

r - Radial dimension in cylindrical or spherical geometry.

R - Maximum radius of axially symmetric plasma.

t - Time.

T - Temperature.

T_e - Electron temperature.

T_1 - Ion temperature.
 u - Self-similar parameter V/c_s .
 U - Defined as $-\ln(n/n_0)$.
 V - Macroscopic plasma velocity.
 \mathbf{v} - Particle velocity vector.
 \mathbf{x} - Position vector.
 x - Plasma axis perpendicular to probe and main laser.
 z - Axial dimension (laser axis).
 Z - Average ion charge state.
 β - Ratio of kinetic to magnetic field pressure.
 δ - Perturbation to optical path length of probe ray in units of λ .
 γ - Ratio of heat capacities C_p/C_v .
 λ - Wavelength.
 λ_D - Debye length of plasma.
 $\ln\Lambda$ - Coulomb logarithm.
 ν - Frequency.
 ν_c - Electron ion collision frequency.
 θ - Angle.
 ρ - Density.
 ρ_q - Electric charge density.
 ρ_0 - Mass density at the plasma absorption surface.
 σ - Uncertainty (single standard deviation).
 τ - Self-similar parameter $z/c_s t$.
 ω - Angular frequency.
 ω_p - Plasma frequency.

CHAPTER 1

INTRODUCTION

The study of laser plasma interaction at high intensities is important both to obtain a better understanding of the basic processes taking place and to utilize such plasmas in a number of application areas. In the past the motivation for much of this research has been the goal of inertial confinement fusion where fusion is initiated by compression of a fuel pellet by laser ablation of its surface. Inertial confinement fusion has been proposed as one possible inexhaustible energy source for the future.

The results of research in this area are also useful for the production of ion and x-ray sources. The development of x-ray lasers could in the future become extremely important in applications such as biological and surface probes.

In typical laser heated plasma systems short, intense, laser pulses are focused onto various types of targets. The laser beam ionizes the target producing a plasma. The laser then interacts with the plasma, the plasma serving to absorb and couple the laser energy to the target. Studies outlined in this thesis were carried out to determine the evolution of the density profile of the plasma with time and thus elucidate some of the details of its interaction with the laser.

1.1 KrF Laser Facility

Over the past number of years the University of Alberta's laser plasma interaction group has developed a short wavelength KrF laser system and is engaged in laser target interaction experiments. At the Krypton Fluoride Laser Facility experiments are done with 1.5 ns Brillouin compressed $0.248 \mu\text{m}$ KrF laser pulses on planar targets. To date, most studies at short wavelengths have been conducted using harmonically converted Nd lasers but only a few of these have been at the fourth harmonic of $0.26 \mu\text{m}$ and a detailed characterization of the density profile of the ablated plasma for this irradiation wavelength has not yet been reported.

These studies are important because efficient energy coupling of radiation to the target is achievable in the ultraviolet region and are particularly interesting because of the possibility of using high efficiency KrF lasers as inertial confinement fusion drivers.

1.2 Description of the Experiment

This work will deal with an interferometric study of the electron density profile within the plasma. The KrF laser-produced-plasma is probed parallel to the target surface with a short pulse laser. Using a Jamin interferometer the probe beam is split with one half passing through the plasma and the other half missing the plasma. These are then recombined producing an interference

pattern between the two beams and the plasma is imaged onto a vidicon producing an interferogram of the plasma. The image on the vidicon is digitized and stored on computer disk for further analysis.

With the assumption that the plasma is radially symmetric, the interferogram can be deconvolved to obtain the electron density as a function of position within the plasma. By using a short laser pulse probing at various times this technique gives a picture of the time evolution of the plasma density profile.

A nitrogen laser was used to generate the probe pulse for this experiment. The nitrogen laser transition is self quenching meaning that the lasing action is terminated very shortly after it begins. This laser therefore naturally produces a short pulse. The pulse is in the UV with a wavelength of 337 nm which is necessary for probing plasmas up to electron densities of 10^{20} to 10^{21} cm^{-3} . Typical parameters for a transversely excited N_2 laser operating at atmospheric pressure are a pulse of one to several hundred μJ and a pulse length of 0.5 to 1.0 ns [1,2]. By the use of travelling wave excitation and by operation at higher pressures of up to 6 atm, pulses as short as 50 ps have been achieved [3,4]. Plasma interferometry has been done in the past with this type of laser [5,6] and as part of this thesis project a nitrogen laser was built as an optical probe pulse source.

1.3 Previous Research

In the past, because of the availability of high power short pulse CO₂ lasers [7-10] and Nd glass lasers [11-13] many plasma interaction studies have been carried out in the infrared wavelength range of 1.06 - 10.6 μm. Lately, because of increasing interest in the laser plasma interaction at shorter wavelengths a number of studies have been done with Nd lasers operating at their harmonic wavelengths at 0.53 μm, 0.35 μm, and 0.26 μm. These two types of laser systems comprise much of the work that has been done although some work has been done with Krf lasers at Rutherford [14] and the University of Alberta [15-19] and with iodine lasers at the Max-Planck Institute [20-23].

Interferometric studies of the plasma density profile have been much more limited, focusing on steepening of the density profile at high intensities [24-28], and small scale structures [29-33]. Recently, detailed measurements of the plasma density structure have become important in order to understand and optimize x - ray laser systems and some new measurements have been carried out with this aim [34-37].

1.4 Goals of the Present Study

As density profiles for laser produced plasma are generally exponential in nature, a characteristic measurement of laser produced plasma is the e-folding gradient scalelength of the electron density profiles. This

study will concentrate primarily on the axial scalelengths of the plasma and will study its variation with time and dependence on laser energy. The scalelength of the plasma will be compared with the results of simple analytic theory as well as with the results from two different numerical simulations.

A brief examination will also be made of the lateral expansion of the plasma. The question of self-generated magnetic fields will be examined as to their ability to explain certain anomalous features which are observed.

The outline of the thesis is as follows: Chapter 2 presents a discussion on the background theory, Chapter 3 outlines the experimental details, Chapter 4 presents the experimental results and the methods of analysis, Chapter 5 discusses the experimental results in detail and compares them to the theoretical models, and Chapter 6, the conclusion, provides a brief summary.

CHAPTER 2

BACKGROUND AND THEORY

2.1 Plasma Equations of Motion

Due to the large number of degrees of freedom present in a plasma its description requires a statistical approach. A plasma of N particles can be described by the probability distribution function of phase space:

$$F(\mathbf{x}_1, \mathbf{x}_2, \dots, \mathbf{x}_N, \mathbf{v}_1, \mathbf{v}_2, \dots, \mathbf{v}_N, t) \quad (2.1)$$

The coordinates \mathbf{x}_i and \mathbf{v}_i representing the position and velocity of particle i . The distribution function F obeys the Liouville equation given by [38]:

$$\frac{\partial F}{\partial t} + \sum_i \left(\frac{\partial F}{\partial \mathbf{x}_i} \cdot \mathbf{v}_i + \frac{\partial F}{\partial \mathbf{v}_i} \cdot \mathbf{a}_i \right) = 0 \quad (2.2)$$

Where: \mathbf{a}_i = the total acceleration of particle i .

2.1.a Plasma kinetic equation of motion

In practice F cannot be calculated and a reduced description must be obtained. By integrating the distribution function over all the coordinates of phase space except those corresponding to a single particle one obtains the one body distribution function which for a particle of type a is given by [30]:

$$\bar{n}_a f_a^{(1)}(\mathbf{x}_1, \mathbf{v}_1, t) = N_a \int F d\mathbf{x}_2 \cdots d\mathbf{x}_N d\mathbf{v}_2 \cdots d\mathbf{v}_N \quad (2.3)$$

$$\bar{n}_a = \frac{N_a}{V}$$

Where N_a is the total number of particles of type a and V is the volume occupied by the plasma.

The dynamical behavior of the one body distribution is obtained by integrating the Liouville equation. The particle acceleration in the Liouville equation may be separated into that caused by external forces and that caused by forces between the particles. The external forces acting on a particle depend only on the coordinates of that particular particle. While the exact interparticle forces depend on the coordinates of all of the particles it is possible to calculate an average interparticle force which may be separated out and treated the same as an external force. The remaining acceleration caused by interparticle forces will be mostly due to the few nearest neighbors and is referred to as the collision term. If all forces are electromagnetic the integrated Liouville equation becomes:

$$\frac{\partial}{\partial t} f_a^{(1)} + \mathbf{v}_1 \cdot \frac{\partial}{\partial \mathbf{v}_1} f_a^{(1)} + \frac{q_a}{m_a} \langle \mathbf{E} + \mathbf{v}_1 \times \mathbf{B} \rangle \cdot \frac{\partial}{\partial \mathbf{v}_1} f_a^{(1)} \quad (2.4)$$

$$= \left. \frac{\partial f_a^{(1)}}{t} \right|_c$$

This equation is referred to as the kinetic or Boltzmann equation and there is a separate equation for each particle species. Any particle source or sink terms due to ionization or recombination would appear on the right side of the equation with the collision term. The electric and magnetic fields in the equation are the sum of the external fields and the average fields of the particles

and satisfy the average Maxwell equations [38]:

$$\nabla \cdot \langle \mathbf{E} \rangle = \frac{1}{\epsilon_0} \langle \rho_q \rangle \quad (2.5)$$

$$\nabla \times \langle \mathbf{E} \rangle = - \frac{\partial \mathbf{B}}{\partial t}$$

assuming zero polarization. And:

$$\nabla \times \langle \mathbf{B} \rangle = \mu_0 \left(\langle \mathbf{J} \rangle + \epsilon_0 \frac{\partial \langle \mathbf{E} \rangle}{\partial t} \right) \quad (2.6)$$

$$\nabla \cdot \langle \mathbf{B} \rangle = 0$$

assuming zero magnetization.

The collision term on the right side of the equation is given by:

$$\left. \frac{\partial f_a^{(1)}}{\partial t} \right|_c = - \sum_b \bar{n}_b \int (\mathbf{a}_{1b} - \langle \mathbf{a}_{1b} \rangle) \cdot \frac{\partial}{\partial \mathbf{v}_1} f_{ab}^{(2)} d\mathbf{x}_b d\mathbf{v}_b \quad (2.7)$$

where \mathbf{a}_{1b} is the acceleration of particle 1 due to a particle of type b and $\langle \mathbf{a}_{1b} \rangle$ is the acceleration of particle 1 due to particle b averaged over the distribution. The expression $f_{ab}^{(2)}$ is the two body distribution function given by:

$$\begin{aligned} & \bar{n}_a \bar{n}_b f_{ab}^{(2)}(\mathbf{x}_1, \mathbf{x}_2, \mathbf{v}_1, \mathbf{v}_2, t) \\ & = N_a N_b \int F d\mathbf{x}_3 d\mathbf{x}_4 \cdots d\mathbf{x}_N d\mathbf{v}_3 d\mathbf{v}_4 \cdots d\mathbf{v}_N \end{aligned} \quad (2.8)$$

The collision term indicates that the kinetic equation for the one body distribution function is not closed but depends on higher order distribution functions. To close

the kinetic equation some collision model must be used which will necessarily cause some degree of approximation. The simplest model, valid in many cases, is to assume that the plasma is collisionless and that all collision terms are approximately zero. The kinetic equation then becomes the Vlasov equation.

2.1.b Plasma fluid equations of motion

While the one body distribution function generally represents the most complex description of a plasma which can be analyzed it does not represent a macroscopic observable. Macroscopic observables are obtained by taking velocity moments of the one body distribution function.

The density of a particle species at a point in space is given by:

$$n_a(\mathbf{x}, t) = \bar{n}_a \int f_a(\mathbf{x}, \mathbf{v}, t) d\mathbf{v} \quad (2.9)$$

Other quantities related to number density such as charge density are obtained by multiplying by the appropriate factors.

The macroscopic velocity of a species is defined from the particle flux obtained by integrating the first velocity moment of the distribution over \mathbf{v} and is given by:

$$n_a(\mathbf{x}, t) \mathbf{v}_a(\mathbf{x}, t) = \bar{n}_a \int \mathbf{v} f_a(\mathbf{x}, \mathbf{v}, t) d\mathbf{v} \quad (2.10)$$

From this expression current density for a species is obtained by multiplying by the charge of the species:

$$\mathbf{J}_a(\mathbf{x}, t) = q_a n_a(\mathbf{x}, t) \mathbf{V}_a(\mathbf{x}, t) \quad (2.11)$$

The total kinetic energy flux of a species, \mathbf{H}_a , is given by:

$$\mathbf{H}_a(\mathbf{x}, t) = \frac{1}{2} \bar{n}_a m_a \int \mathbf{v} (\mathbf{v} \cdot \mathbf{v}) f_a(\mathbf{x}, \mathbf{v}, t) d\mathbf{v} \quad (2.12)$$

The partial pressure of a particle species is described using the pressure tensor defined by:

$$\mathbf{P}_a(\mathbf{x}, t) = \bar{n}_a m_a \int (\mathbf{v} - \mathbf{V}_a) (\mathbf{v} - \mathbf{V}_a) f_a(\mathbf{x}, \mathbf{v}, t) d\mathbf{v} \quad (2.13)$$

It is also possible to describe a scalar pressure for a particle species given by:

$$p_a(\mathbf{x}, t) = \frac{\bar{n}_a m_a}{3} \int (\mathbf{v} - \mathbf{V}_a) \cdot (\mathbf{v} - \mathbf{V}_a) f_a(\mathbf{x}, \mathbf{v}, t) d\mathbf{v} \quad (2.14)$$

A temperature for a species can be defined from equation 2.14 as:

$$T_a = \frac{p_a}{\bar{n}_a k_b} \quad (2.15)$$

When the distribution function f_a is symmetric in velocity about \mathbf{V}_a The pressure tensor reduces to the diagonal tensor $p_a \mathbf{I}$. In other cases the pressure tensor can be expressed as the sum of $p_a \mathbf{I}$ and a non-diagonal tensor with a zero trace.

The time rate of change of the kinetic energy of a particle species due to the average electromagnetic fields is given by:

$$n_a \mathbf{F}_a \cdot \mathbf{V}_a = \int \bar{n}_a q_a \langle \mathbf{E} + \mathbf{v} \times \mathbf{B} \rangle \cdot \mathbf{v} \, d\mathbf{v} = n_a q_a \langle \mathbf{E} \rangle \cdot \mathbf{V}_a \quad (2.16)$$

From which it is observed that the macroscopic force, \mathbf{F}_a , is given by $\mathbf{F}_a = q_a \langle \mathbf{E} \rangle$.

Equations relating the macroscopic variables are obtained by taking velocity moments of the kinetic equation to obtain what are termed the fluid equations for a particle species [38]. The continuity or particle conservation equation is obtained by integrating the kinetic equation over velocity space. Integrating the product of the kinetic equation with the particle momentum, $m_a \mathbf{v}$, one obtains the equation of momentum conservation. The energy transfer equation is obtained by integrating the product of the particle kinetic energy, $1/2 m_a v^2$, with the kinetic equation.

The equation of continuity is given by:

$$\frac{\partial}{\partial t} n_a(\mathbf{x}, t) + \nabla \cdot (n_a(\mathbf{x}, t) \mathbf{V}_a(\mathbf{x}, t)) = 0 \quad (2.17)$$

The equation of momentum conservation is given by:

$$\begin{aligned} n_a m_a \frac{\partial}{\partial t} \mathbf{V}_a + n_a m_a \mathbf{V}_a \cdot \nabla \mathbf{V}_a - n_a q_a \langle \mathbf{E} + \mathbf{V}_a \times \mathbf{B} \rangle + \nabla \cdot \mathbf{P}_a & \quad (2.18) \\ = m_a \int n_a \mathbf{v} \frac{\partial f_a}{\partial t} \Big|_c \, d\mathbf{v} \approx - \sum_b n_a m_a (\mathbf{V}_a - \mathbf{V}_b) \langle v_{ab} \rangle & \end{aligned}$$

Where the collision term has been approximated using a collision frequency ν_{ab} .

The equation of energy conservation is given by:

$$\frac{\partial}{\partial t} \left(\frac{n_a m_a V_a^2}{2} + \frac{3n_a k_b T_a}{2} \right) - n_a \mathbf{F}_a \cdot \mathbf{V}_a + \nabla \cdot \mathbf{H}_a \quad (2.19)$$

$$= \frac{\partial}{\partial t} \left(\frac{n_a m_a V_a^2}{2} \right) \Big|_c$$

In cases where the pressure tensor may be represented by $p_a \mathbf{I}$ the term $\nabla \cdot \mathbf{P}_a$ in the momentum equation becomes ∇p_a . Due to momentum being conserved in particle collisions the momentum equation is independent of collisions between like particles.

All three of these equations assume that the total number of particles remains constant. Any change in the particle number due to ionization or recombination gives rise to source or sink terms on the right hand side of the equations.

These moments of the kinetic equation represent a reduced form of the kinetic equation implying a necessary loss of information. They do not give a full description of the plasma shown by the fact that there are always more variables than equations. In order to close the equations and obtain solutions one must supply a collision model and a physically relevant equation of state relating, for example, partial pressure to particle number density. In addition, solutions to the fluid equations often involve using further physically appropriate approximations.

2.2 Analytic Model of Laser Plasma Expansion

While a complete treatment requires numerical simulation, it is possible to construct simple analytical models of the interaction of a laser with a slab target. Such models are useful as they help isolate the dominant physical processes giving useful scaling laws and a means for understanding the results of more complicated computer simulations.

2.2.a Planar self-similar rarefaction into vacuum

The simplest plasma flow model is the one dimensional planar expansion of plasma into vacuum, it is possible to obtain analytic solutions once the plasma has expanded sufficiently for the Debye length, λ_D , given by:

$$\lambda_D = \left(\frac{\epsilon_0 k_b T}{n e^2} \right)^{1/2} \quad (2.20)$$

to be considered insignificant compared to the density scale lengths [39,41]. In these cases there are no a priori characteristic lengths or times and the problem falls into a class of self similar problems in fluid mechanics [42], where the quantities of distance and time can only appear in the form z/t .

The solution to this problem has been discussed by many authors using both the kinetic and fluid approach [39-41,43-45]. It is usual to assume that the plasma is collisionless and that the electron temperature is

isothermal. One finds an exponential density profile with scale-length given by $c_s t$, where c_s is the ion acoustic velocity for the plasma. The plasma flow is sonic relative to a surface of constant density. The density and flow velocity are given for $-c_s t < z < \infty$ by:

$$n = n_0 \exp \left(\frac{-z}{c_s t} - 1 \right) \quad (2.21)$$

$$V = c_s + \frac{z}{t} \quad (2.22)$$

Assuming cold ions (due to expansion cooling) the plasma ion acoustic velocity c_s is given by the expression:

$$c_s = \left(\frac{Z k_b T_e}{m_i} \right)^{1/2} \quad (2.23)$$

Where Z = the average charge state of the plasma.

T_e = the electron temperature of the plasma.

m_i = the mass of the ions.

The expansion is modeled as a rarefaction wave into undisturbed hot plasma as shown in Fig. 2.1. The leading edge of the rarefaction wave propagates into the plasma at the sonic velocity.

These equations give a density profile extending to infinity. In reality the self-similar equations are not valid at densities such that the debye length becomes comparable to the plasma scale length and so the plasma will in fact be terminated by a region of charge separation. The characteristics of this region have been

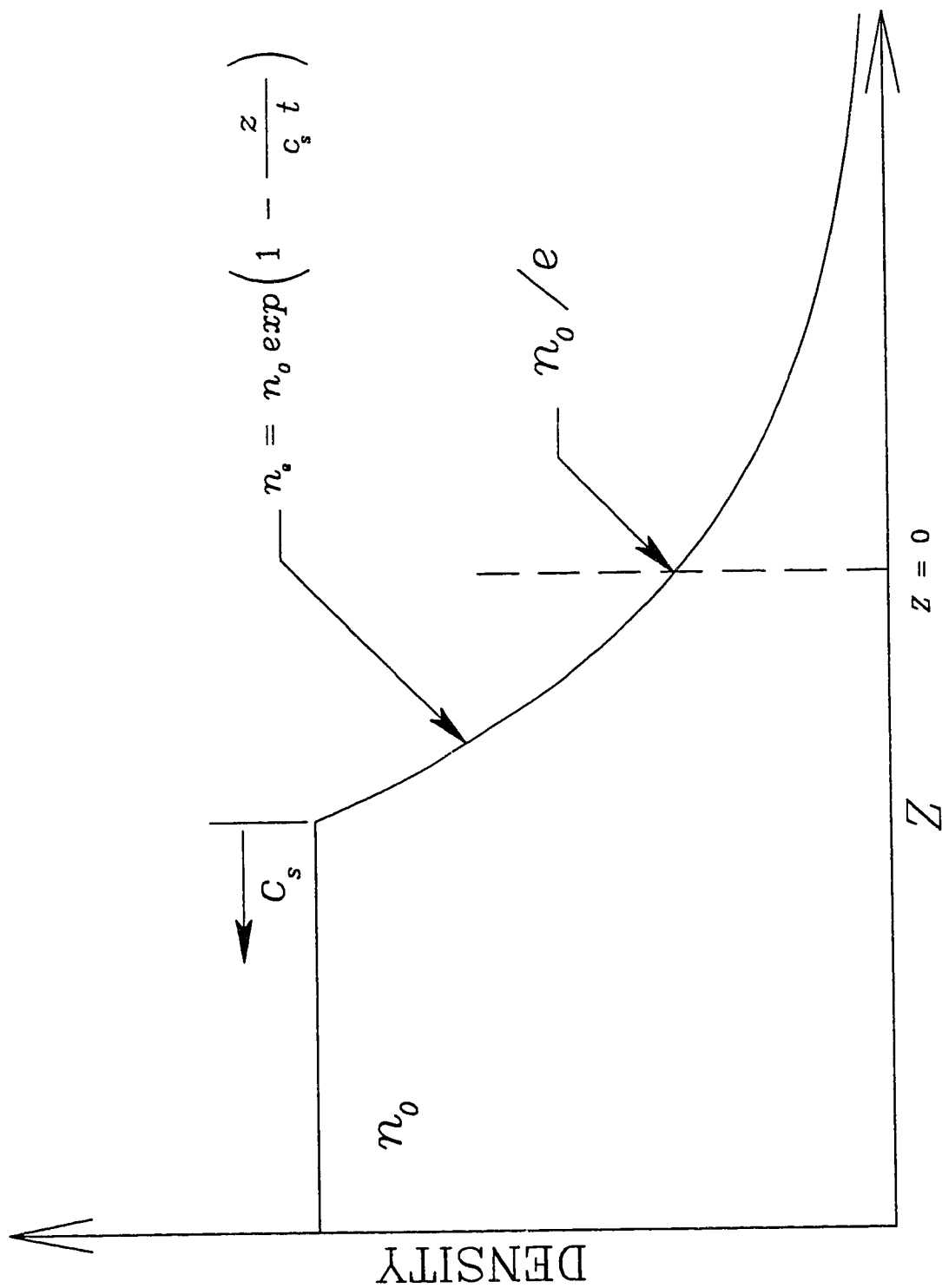


Fig. 2.1. Planar isothermal self-similar expansion of plasma into vacuum.

explored in references [45,46].

2.2.b Self-similar solutions with non-planar 1D geometry

In addition, it has been possible to find partial solutions to the more general case of one-dimensional expansion with either planar, cylindrical, or spherical geometry with various values for the thermodynamic variable $\gamma = C_p/C_v$, the ratio of the heat capacities. The value γ usually ranges from 1 for an isothermal expansion to 5/2 for adiabatic expansion [43].

The one dimensional isothermal self-similar equations of motion may be written in the following form:

$$(u - \tau) \frac{\partial u}{\partial \tau} = - \gamma n_e^{\gamma-1} \frac{\partial}{\partial \tau} (\ln n_e) \quad (2.24)$$

$$(u - \tau) \frac{\partial}{\partial \tau} (\ln n_e) + \frac{\partial u}{\partial \tau} + \frac{(\alpha - 1)}{\tau} u = 0 \quad (2.25)$$

Where: $u =$ the self-similar parameter V/c_s .

$\tau =$ the self similar parameter $z/c_s t$.

The parameter α is determined by the particular type of one dimensional geometry:

$\alpha = 1$: planar geometry.

$\alpha = 2$: cylindrical geometry.

$\alpha = 3$: spherical geometry.

When both $\alpha = 1$ and $\gamma = 1$ the above equations revert to the usual self-similar equations as discussed in section 2.2.

For the case when $\gamma = 1$ (isothermal) these equations of

motion have the following asymptotic solution valid for all values of α :

$$u = \tau + \sqrt{\alpha} \quad (2.26)$$

$$n_e = n_0 \exp(-\sqrt{\alpha} \tau) \quad (2.27)$$

When $\alpha = 1$ the solution reverts to the previous solution as it should where n_0 is now the density of the sonic point. In the case of $\alpha \neq 1$, the solutions are asymptotic solutions valid only when $\tau \gg \sqrt{\alpha}$. When valid, this solution indicates that non planar self-similar expansion would generate plasma scale-lengths which are shorter by a factor $\sqrt{\alpha}$.

2.2.c Self-regulating flow models

The self regulating model provides a more complete treatment of one dimensional laser target ablation [47,48]. This model divides the process into four distinct regions, as shown in Fig. 2.2, and is self regulating in the sense that the four regions, which are each physically simple, satisfy the conservation laws of fluid mechanics while staying in balance with each other and with the absorbed laser energy.

Region I is the plasma corona. Region II is the conduction zone where energy penetrates the plasma solely by heat conduction. Region III is the compressed solid behind the shock propagating into the undisturbed solid of

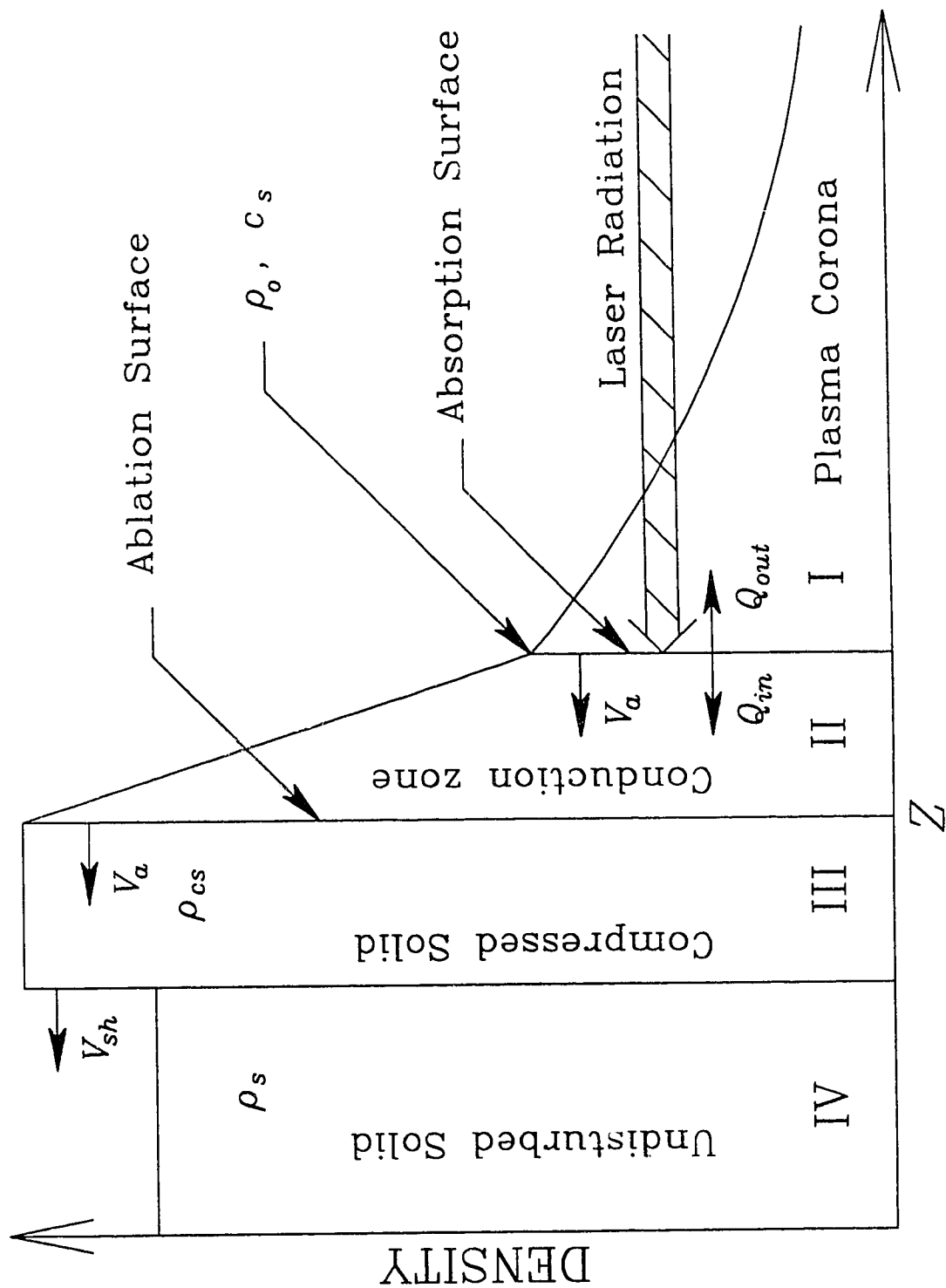


Fig. 2.2. Self-regulating plasma flow model.

region IV. This thesis will make use of the model developed by Patrick Mora (reference [47]) to model the absorption of laser energy and the coronal expansion.

The corona is characterized by a plasma rarefaction into vacuum. Since the electron thermal velocity is much higher than the expansion velocity and the resultant electron thermal conductivity is quite high, the electron temperature is usually assumed isothermal. The ions are taken to be cold due to expansion cooling but as long as the number of electrons greatly exceeds the number of ions, the ion temperature has little importance.

As the laser propagates it is absorbed by the plasma corona. The density surface of maximum laser penetration is termed the absorption surface. If the laser is intense enough it may penetrate to the critical density where the dispersion relations will prevent the light from penetrating further. In this case some portion of the light may be absorbed at the critical density by resonance absorption and the remainder will be reflected. In the latter cases the degree of absorption depends on the amount of resonance absorption which typically is on the order of 50 %. If the laser is not intense enough to penetrate to the critical density it will be completely absorbed by inverse bremsstrahlung. The absorption surface is placed at some density n_0 which is calculated in different manners but is usually taken to be at an optical depth of 2 e-foldings [47]. One should remember that the sharp

dividing line between this region of plasma and the conduction zone is not real.

Because of the high electron thermal conductivity it is not very important where the laser light is absorbed. It is usual to assume that the laser is absorbed totally at the absorption surface but this is purely for convenience. Under these conditions the corona may be modeled using the solution for self-similar isothermal rarefaction. The density n_0 to which the laser penetrates, given an exponential profile, is given by the expression [47]:

$$n_0 = 2 n_c \left(\frac{c}{\nu_c L} \right)^{1/2} \quad (2.28)$$

Where: n_c = the critical density defined by:

$$n_c = \left(\frac{\epsilon_0 m_e \omega^2}{e^2} \right) \quad (2.29)$$

ω = the angular frequency of the radiation under consideration.

ν_c = the electron ion collision frequency at the critical density which is given by [47]:

$$\nu_c = \frac{2}{3} \left(\frac{2}{\pi} \right)^{1/2} \frac{Z n_c e^4 \ln \Lambda}{8\pi m_e^{1/2} \epsilon_0 k_b T_e^{3/2}} \quad (2.30)$$

The length L is the characteristic length of the plasma. For times $t = \tau$ such that $c_s \tau$ is less than the plasma radius which is initially the laser spot size, the flow may be considered planar and one can take $L = c_s \tau$.

When τ is too large for the flow to be considered planar the expansion will become spherical and $L = \alpha R$ where R is the focal spot radius. The factor α is a constant of order unity.

The absorption surface is the boundary between the corona and the conduction zone. As the laser does not penetrate into this region its only source of energy is heat conduction from the corona. Its temperature therefore varies from a few eV (the shock heated temperature) at the boundary with the compressed solid to the temperature of the corona at the opposite boundary. The plasma in this region is accelerated from the ablation surface and ends up with sonic velocity relative to the absorption surface, necessary for a consistent boundary with the corona. This region will tend towards steady state with the energy outflow across the absorption surface equal to the inward conduction of heat from this surface. Once the conduction zone has reached a steady state the ablation and absorption surface will have a constant velocity V_a . There is, therefore, no difficulty connecting the conduction zone to the solution for a self-similar isothermal rarefaction. The only condition being that the plasma has sonic velocity relative to the absorption surface.

The velocity V_a is greater than the fluid flow velocity in region III of shock compressed material but is close enough for them to be considered equal. These velocities are much less than the flow velocity in the coronal region

and thus for the calculation of energy and momentum balance can be approximated as zero. Assuming this, the ablation pressure p_a is determined by integrating the momentum equation over the conduction zone and is given by the common expression [47]:

$$p_a = 2 \rho_o c_s^2 \quad (2.31)$$

Where ρ_o = the material density at the absorption surface.

The only source of energy for this process is from the laser itself. The absorbed laser energy must equal the energy needed to maintain the plasma flow in both the conduction and coronal region. The energy absorbed by the corona is modeled as an outward heat flow from the absorption surface, and equal to the energy necessary to maintain the isothermal expansion. The energy absorbed by the conduction zone is modeled as an inward heat flow. By balancing these heat flows a self consistent model is obtained which in turn gives the corona temperature.

If A represents the fraction of the laser energy absorbed and I the laser intensity then heat flow is given by [47]:

$$A I = Q_{out} + Q_{in} \quad (2.32)$$

Where Q_{out} = the heat flow into the corona.

Q_{in} = the heat flow into the conduction zone.

Assuming a steady state conduction zone and assuming

the energy content of the shock propagating into the target is insignificant the net energy flow into the conduction zone is zero and the deposited laser energy must balance the total energy in the corona. Integrating the energy content of a planar self-similar flow gives:

$$AI = 4 \rho_0 c_s^3 \quad (2.33)$$

As mentioned above, when the laser intensity is intense enough to reach the critical density, the determination of A depends on the degree of resonance absorption present and is handled differently by different authors [47,48]. When the laser intensity is below this point (the case in this study) it is usual to take $A = 1$.

The most inner perturbed region is a shock driven into the target giving a region of compressed solid which is moving into the unperturbed solid with velocity V_{cs} . The energy input to the shock can be calculated using the equation:

$$\frac{\partial E_{cs}}{\partial t} = p_a V_{cs} = 2 \rho_0 c_s^2 V_{cs} \quad (2.34)$$

Estimates of the shock velocity show that V_{cs} is much less than the plasma sonic velocity c_s indicating that the energy content of the shock is negligible in the energy balance as was assumed earlier.

In deriving expressions for laser penetration and electron temperature Mora's model assumes a laser profile with constant intensity (square pulse). In this thesis the

scaling laws of the model will be used primarily to model the plasma expansion during the leading edge of the laser pulse. As the intensity is not constant the calculation at a particular point in time is done using the average laser intensity up to that time. The assumption is thus made that the plasma evolution depends most heavily on the total time since the laser turn-on and the total energy absorbed by the plasma up to that time. The plasma evolution is assumed to depend only secondarily on the detailed intensity profile.

The model described here, while limited by its simplicity has the advantage of offering a simple fully determined picture of the laser plasma interaction. There are many ways in which details of this model could be improved but it is felt that they detract from the simplicity of the model making the model more complex and obscure without greatly improving its accuracy. The scaling laws derived from this model are often still reasonable even in cases where some of the details may not be completely valid. When greater detail is required it is preferable to use numerical simulations for a full treatment. The simple analytic model then gives a simple easily pictured comparison which helps a great deal in interpreting the features of the much more complex numerical solution.

2.2.d Stationary flow

Self-similar models of plasma flow with non planar geometry usually run into difficulty because the plasma usually has some characteristic length such as the radius of the focal spot in the present case. It is, however, possible to look for stationary (time independent) solutions to the one dimensional fluid equations which are useful in describing laser plasma.

The stationary flow model developed for use in this thesis assumes an isothermal plasma in which there is some point r_0 having electron density n_0 such that the plasma flow is sonic, $v = c_s$. This model will prove useful for modeling stationary spherical flow which results after the laser plasma makes the transition from the initial planar self-similar flow to spherical flow.

Setting time derivatives equal to zero and normalizing the velocity to the ion acoustic velocity, c_s , the 1D fluid equations (equations 2.17 and 2.18) become:

$$\frac{(\alpha - 1)}{r} v + v \frac{\partial \ln n}{\partial r} + \frac{\partial v}{\partial r} = 0 \quad (2.35)$$

$$v \frac{\partial v}{\partial r} + \frac{\partial \ln n}{\partial r} = 0 \quad (2.36)$$

Where α is a parameter representing the particular one dimensional geometry present. The value of α equals 1, 2 or 3 respectively for planar, cylindrical, or spherical flow.

By examining the equation for momentum conservation (equation 2.36) at points $r > r_0$ one arrives at the

following condition for the flow velocity:

$$V = (1 + 2U)^{1/2} \quad (2.37)$$

Where: $U \equiv - \ln (n/n_0)$.

Using this result for velocity the continuity equation (equation 2.35) becomes:

$$2U \frac{\partial U}{\partial r} = (1 + 2U) \frac{(\alpha - 1)}{r} \quad (2.38)$$

In the case where $\alpha = 1$ the only stationary solution is the case of constant density as expected. For $\alpha > 1$ solution is obtained by examining two cases.

As r approaches r_0 so that $2U \ll 1$ the solution to the equation is given by:

$$U = \left((\alpha - 1) \ln \frac{r}{r_0} \right)^{1/2} \quad (2.39)$$

This solution gives a derivative for n_e which for $\alpha \neq 1$ becomes infinite at $r = r_0$.

In the other limit as r increases such that $(2U+1)/2U \approx 1$, the case which will be more applicable to the measurements presented in this thesis, the solution becomes:

$$U = (\alpha - 1) \ln \frac{r}{r_0} \quad (2.40)$$

which may be rewritten as:

$$n = n_0 \left(\frac{r_0}{r} \right)^{(\alpha - 1)} \quad (2.41)$$

The effect of the term dropped from the differential equation in making this approximation serves to hasten the increase of U with r and so hasten the point where it becomes insignificant and where this solution becomes valid.

2.3 Computer Simulation of Laser Plasma Expansion

Detailed simulation of laser plasma interactions requires the use of numerical techniques. This work will use the results of two different simulation codes, Medusa and Castor. The simulation codes and 2D simulation results were provided by Dr. Rankin and Dr. Capjack within the Department of Electrical Engineering.

Medusa is a one dimension Lagrangian simulation code and is described in detail in reference [49]. As used for the present studies, this code did not include radiation transport of energy. In addition, laser produced magnetic fields can not be simulated by one dimensional codes. Because of its one dimensional characteristic this code is limited in its ability to reproduce laser target experiments but its results should be useful in those limiting cases where the expansion may be considered one dimensional, either planar or spherical. It is also useful for comparison with the results of simple one dimensional

analytic theory where it gives a measure of the validity of the assumptions used in the simple analytic model.

Castor is a two dimensional hydrodynamics code using Eulerian coordinates [50], which has been modified to run at the University of Alberta. It assumes that the plasma is radially symmetric and so is suitable for many laser plasma simulations. Like Medusa it does not take into account radiation transport of energy. The code as run also ignores any effects caused by magnetic fields within the plasma. Within the limit of radially symmetric plasmas it should be capable of reasonable simulations of laser target experiments.

2.4 Magnetic Field Production in Laser Plasma

The development of a magnetic field is governed by Faraday's law:

$$\frac{\partial \mathbf{B}}{\partial t} = -(\nabla \times \mathbf{E}) \quad (2.42)$$

Assuming that there is no polarization or magnetization in the plasma the fields \mathbf{E} and \mathbf{B} are due to charge and current distributions only. There are two main components to the electric field within an expanding laser plasma. The first component is derived from the charge separation needed to balance the electron pressure in the expanding plasma and may be given approximately by [51]:

$$\mathbf{E} \approx -\frac{1}{e n_e} \nabla (n_e k_b T_e) \quad (2.43)$$

It leads to a generating term for the magnetic field given by:

$$\frac{\partial \mathbf{B}}{\partial t} = -\frac{1}{e n_e} \nabla n_e \times \nabla (k_b T_e) \quad (2.44)$$

This allows for the development of a self generated magnetic field whenever the electron density gradient does not coincide in direction with the temperature gradient.

The second main component of the magnetic field within an expanding plasma is due to the Lorentz force acting on the expanding plasma and is given by [52]:

$$\frac{\partial \mathbf{B}}{\partial t} = \nabla \times (\mathbf{V} \times \mathbf{B}) \quad (2.45)$$

Where: \mathbf{V} = the fluid velocity vector of the plasma.

In this term $\mathbf{V} \times \mathbf{B}$ may be thought of as a radial electric field which develops from the charge separation as the plasma moves through the magnetic field.

In the case of two dimensional radially symmetric plasma expansion, which may only generate toroidal magnetic fields, this term may be broken into the following two terms:

$$\nabla \times (\mathbf{V} \times \mathbf{B}) = -B (\nabla_{2D} \cdot \mathbf{V}) \mathbf{e}_\theta - (\nabla B \cdot \mathbf{V}) \mathbf{e}_\theta \quad (2.46)$$

Where: ∇_{2D} = the two dimensional divergence in the

axial (z) and radial (r) directions.

B = the magnitude of B .

e_θ = unit vector in the $e_z \times e_r$ direction.

The first of these two terms gives rise to a saturation of the magnetic field as it generally gives $\frac{\partial B}{\partial t}$ proportional to but in the opposite direction to B . The effect of the second term is to cause any field present to be dragged with the plasma at the plasma velocity.

Magnetic fields become important to plasma hydrodynamics when the ratio, β , of the ideal gas pressure to the effective magnetic field pressure becomes less than one. β is given by the expression:

$$\beta = \frac{2\mu_0 n_e k_b T_e}{B^2} \quad (2.47)$$

The presence of large self-generated magnetic fields has been shown in the past to be consistent with structural anomalies observed in laser plasmas [53,33]. Direct measurement of these fields using Faraday rotation has been possible in the past but these measurements are usually difficult because the magnetic fields must be extremely strong in order to be observable.

The effects of magnetic fields with $\beta \ll 1$ on laser plasmas has been measured directly by applying an external transverse magnetic field to the expansion of very low density ($1 \times 10^{14} \text{ cm}^{-3}$) laser plasmas [54]. Finally, even in high β plasmas where the magnetic field is not strong

enough to affect the plasma hydrodynamics directly it can still have a significant indirect effect by reducing the heat conduction within the plasma [52].

2.5 Refractive Index of a Plasma

In a highly ionized plasma the primary contribution to the index of refraction arises from the free electron gas. As well there can be contributions to the index of refraction from bound electrons near the frequencies which correspond to transitions within the ions. If the plasma is dilute enough that one may neglect interactions between the ions, a valid approximation for most plasmas, the refractivity from the various sources are additive [55]. That is:

$$(n_r - 1) = \sum_i (n_{ri} - 1) + (n_{re} - 1) \quad (2.48)$$

Where: n_r = the total index of refraction at a point.
 n_{re} = the refractivity of the free electron gas.
 n_{ri} = the individual refractivities from various ion sources.

When there are no external magnetic field present the expression for the index of refraction becomes [56]:

$$n_{re} = \left(1 - \frac{\omega_p^2}{\omega^2 [1 + i(\nu_c / \omega)]} \right)^{1/2} \quad (2.49)$$

Where: ω_p = plasma frequency and is defined as:

$$\omega_p \equiv \left(\frac{n_e e^2}{\epsilon_0 m_e} \right)^{1/2} \quad (2.50)$$

The electron collision frequency, ν_c , may be approximated using equation 2.30.

In hot plasmas at low density the collisional term can generally be neglected in which case a simpler expression for the refractive index is obtained:

$$n_{re} = \left(1 - \frac{\omega_p^2}{\omega^2} \right)^{1/2} \quad (2.51)$$

Due to the much larger mass of the ion and because the number density is usually comparable to or less than the electron density, the contribution of free ions to the refractive index is usually much smaller than the electron contribution and can be ignored.

The background contribution of the different ion transitions is directly proportional to the ion concentration and generally decreases as the state of ionization of the atom increases [56]. In practice ground state ions generally have transitions energies well above visible light. Upper states are usually considered to have no significant population while those transitions which do occur are usually Stark broadened and have small oscillator strengths. Thus, for hot highly ionized plasmas, the free electron contribution dominates.

2.6 Interferometry of 2D Plasmas

In general, interferometry uses the interference properties of light to measure optical path length. In amplitude splitting interferometry a beam of light is split by dividing its amplitude, as with a half silvered mirror, to produce two beams with identical phase information. One beam is used as a reference beam while the other is used as a probe to pass through the sample to be measured. When the probe beam is recombined with the reference beam the interference pattern produced provides a record of the phase difference between the two beams and thus the optical path length through the sample being studied. Optical path length is equal to the integrated index of refraction along the beam path.

Probing hot plasmas with subnanosecond laser radiation whose frequency is well above the plasma frequency encountered provides a useful diagnostic of the refractive index and thus electron density since it is capable of good time resolution and does not perturb the plasma.

2.6.a Interferometry of 2D plasma

To obtain the phase deviation of one position of the probe wavefront from its unperturbed form (ie: in the absence of plasma), $(n_r - 1)$ is integrated along the path of the ray associated with that point. Fig. 2.3 depicts the case of an axially symmetric plasma, $n_r = n_r(r, z)$, probed transversely to the axis of symmetry where the path of a

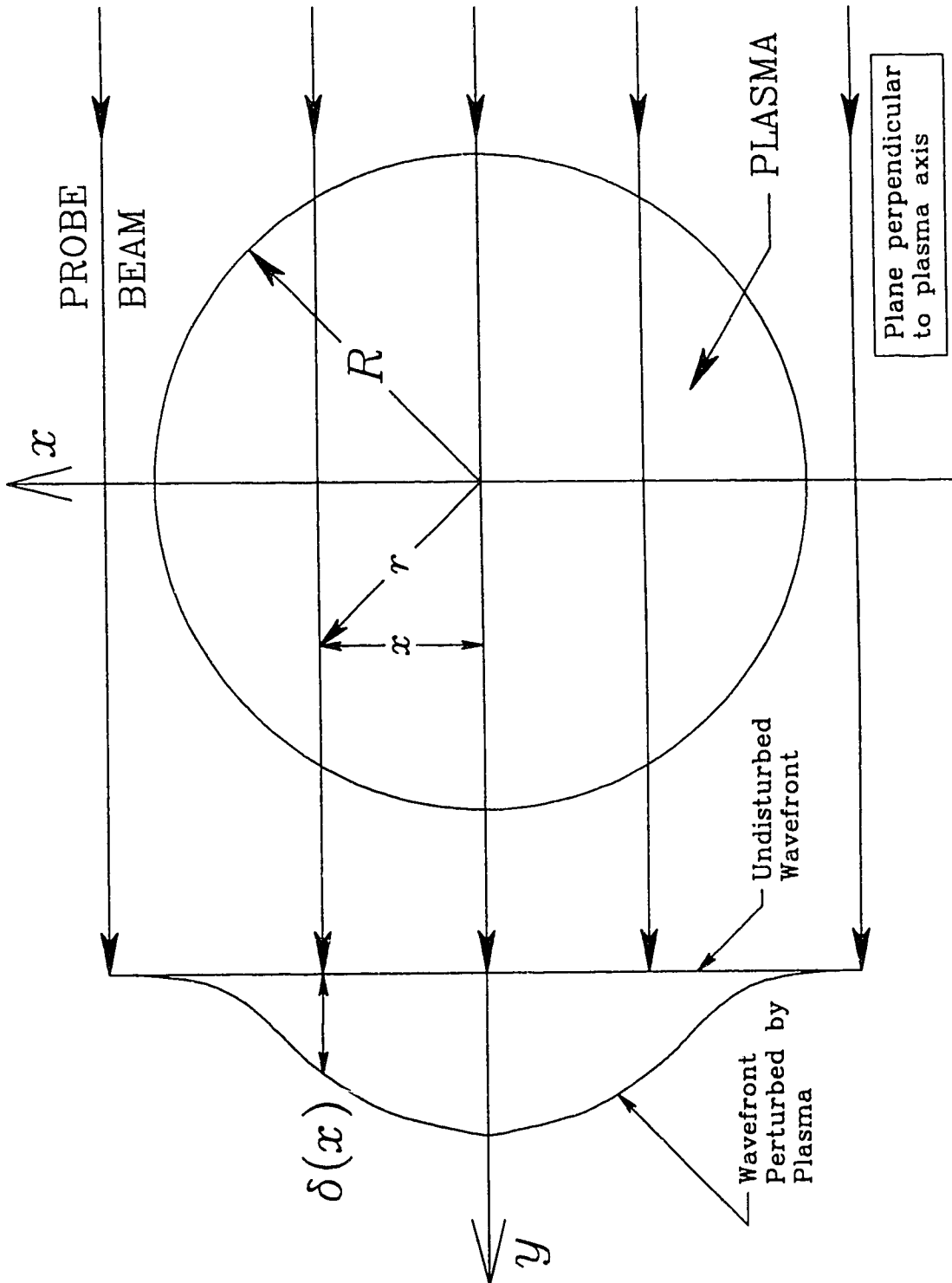


Fig. 2.3. Transverse probing of axially symmetric plasma.

ray is assumed to be undeviated by the plasma. Under these conditions the integral along the path of a ray becomes:

$$\delta(x, z) = \frac{2}{\lambda} \int_x^R [n_r(r, z) - 1] \frac{r}{(r^2 - x^2)^{1/2}} dr \quad (2.52)$$

Where: δ = the deviation of the wave front in wavelengths.

z = the position along the axis of the plasma.

x = the perpendicular distance of the light ray from the symmetry axis of the plasma.

r = the radial distance from the axis of symmetry.

R = the maximum radius of the plasma past which electron density is negligible.

λ = the wavelength of the probe laser.

This is an example of Abel's integral equation and may be inverted to give the following expression for the index of refraction at a point as a function of the distortion of the wavefront:

$$[n_r(r, z) - 1] = - \frac{\lambda}{\pi} \int_r^R \frac{d\delta(x, z)}{dx} \frac{1}{(x^2 - r^2)^{1/2}} dx \quad (2.53)$$

A particular interferogram of a plasma will include both halves of the plasma. This is a practical necessity as it allows for the determination of the plasma axis from the interferogram. It also aids in judging the actual cylindrical symmetry of the plasma. Finally, with both halves of an interferogram present it is possible to take

into account an extra $\cos(\theta)$ term to the refractive index such that:

$$n_r(r, \theta) = n_0(r) + n_1(r) \cos(\theta) \quad (2.54)$$

Where: θ is the angle relative to the x - axis.

The value of $n(r, z, \theta)$ is determined by using an appropriately weighted average of $\delta(x, z)$ and $\delta(-x, z)$ in the deconvolution.

One does not have to be limited to the case of cylindrically symmetric plasmas. Previous authors have used similar methods to investigate plasmas with other two dimensional symmetries. The particular symmetry must of course be known in advance [57-63].

2.6.b Routines for calculating Abel's integral

Many routines have been developed for solving Abel's integral using a given data set [64-69]. Many of these methods have been developed not for interferometry but for analyzing the light emission from optically thin plasmas which give rise to similar equations. All the methods considered here fit some piecewise function form to the data for which the integration can be carried out analytically. Most methods reduce the task to an equation of the form

$$n_j = \sum A_{jk} N_k \quad (2.55)$$

Where: n_j = the refractive index at j.

N_k = the fringe shift data at different points.
 A_{jk} = an inversion coefficient matrix produced
 in the derivation of the method.

There is not just one correct set of A_{jk} but many, the particular A_{jk} depending on the factors and assumptions built into the derivation. The different methods have different properties in terms of accuracy and susceptibility to scatter in the data.

One of the earliest and simplest method is that of O.H. Nestor and H.N. Olsen [66]. This method uses what are perhaps the simplest and most natural assumptions to make. First the change of variables, $r^2=v$ and $x^2=u$ is made and the integral becomes:

$$n_r(v, z) - 1 = - \frac{\lambda}{\pi} \int_v^{R^2} \frac{d\delta}{du} \frac{1}{(u - v)^{1/2}} du \quad (2.56)$$

The assumption is then made that the quantity $d\delta/du$ between two points k and $k+1$ is constant and equal to the slope between the two points. This method is therefore equivalent to fitting a quadratic of the form $ax^2 + b$ between two points. Once the integrals are performed analytically the result may be rearranged into a sum over the different δ_k corresponding to the data.

A more advanced method is the method of Bockasten [67]. Bockasten's method is the method that will be used in this work. It involves the fitting of a cubic to successive sets of four data points and then substituting the fitted

function directly into the integral in place of δ and integrating the resulting integral analytically between the two interior points. Thus the problem breaks up into a sum of integrals. At the point $r = 0$ where there is only 3 data points available for the first integral of the sum, the cubic is fitted by using the condition that $d\delta/dx$ at $r = 0$ is equal to zero. This condition is necessary for the integral to converge and is a necessary condition of any smooth axially symmetric distribution of the quantity $n_r(r,z)-1$. For the integral at the extreme of the data where there is no point past $r = R$ a quadratic is fitted to the three points available. The resulting curves can be found as functions of the data points and the resulting integrals separated into the contributions from the individual data points. The solution can then be rearranged into a sum over the data points with a set of coefficients derived from the above procedure.

There are several sources of error in this method of inversion. The first source of error is caused by inaccuracy in the inversion coefficient values, A_{jk} . This error can be made arbitrarily small by increasing the precision of the A_{jk} values.

The second source of error is due to the finite grid size of the inversion. This source of error is difficult to specify exactly since it depends on the specific function being inverted. The error can however be characterized to some extent. Bockasten examined the error in three test

functions of different shape and noted that the errors were similar and generally were quite small although it can become significant at the extremes where δ goes to zero. This source of error can be kept under control by choosing a small enough grid.

The final source of error in the method is caused by the error in the measured values themselves. This source of error is usually the most significant. It may be given by the expression:

$$\sigma_n = \lambda \sigma_\delta \left(\sum_k (A_{jk})^2 \right)^{1/2} \quad (2.57)$$

Where: σ_n = the estimated absolute error in the values of n_j obtained from the inversion.

σ_δ = the experimental error in the measured values of δ in wavelengths.

λ = the wavelength of the probe laser.

This source of error is worst near the axis of the inversion and becomes worse as the grid size is reduced. For this reason it is important to choose grid size carefully in order to balance the sources of error. This usually comes down to choosing a grid size just small enough to cover the scale size of features in the data which are considered real.

This method has the advantage of producing very accurate results provided there is little scatter in the data. It is however very susceptible to scatter

particularly in the region near the axis and some method of smoothing the raw data is normally considered essential. Bockasten recommends smoothing by least square fitting of a cubic to seven successive points and using this curve to provide a smoothed value for the middle point of the seven. The resulting smoothed value of δ_k , $\bar{\delta}_k$, is given by a weighted average of points around δ_k [67].

Two other methods will be mentioned briefly as they provide interesting alternatives to Bockasten's method. The first is the method of William L. Barr [68]. Barr begins by using an alternate solution of Abel's integral equation which places the derivative outside of the integral. Barr notes that in this way the integral is made much less susceptible to scatter in the data. For the purpose of the integration he makes the same approximation for the data as that made by Nestor and Olsen and arrives at a set of coefficients for the integration. For the purpose of taking the derivative of the resulting integrals which is where the susceptibility to scatter will come into play, Barr fits a least square polynomial to the data which provides the necessary smoothing. Barr points out that by this method smoothing is performed on values which are already fairly accurate with very little scatter. Once again the result is in the form of a sum over a set of data points using a matrix of coefficients. The method is shown to be very accurate. It has the advantage or disadvantage that the smoothing of the data is contained explicitly within

the coefficients.

The last method considered here was developed more recently and published in 1978 by J.Glasser ,J.Chapelle, and J.C.Boettner [69]. This method makes use of third degree spline functions fitted to the data and has the advantage of being able to process unevenly spaced data points (an important consideration in some work). The spline is made up by requiring the individual cubics as well as their first two derivatives to be continuous at their junctions. Smoothing of the spline is achieved by means of a parameter in the fitting expression which is related to the estimated accuracy of the data.

The authors applied the method to plasma spectroscopy and set up the system so that the selected spline could be viewed and the quality of the fit determined interactively. In the authors' tests of their method on analytic test functions they were able to achieve better results than with all other methods tested. Good results combined with smoothing which can be fairly well related to the experimental error make this method seem desirable.

In the present work there was no need to analyze unevenly spaced data points. In addition, as many inversions were required to process one interferogram, it was felt to be beneficial to avoid any active fitting by the operator. Thus the standard Bockasten method was chosen for processing the data.

CHAPTER 3

EXPERIMENTAL SETUP

Fig. 3.1 shows the schematic layout of the experimental setup used to obtain the data for this thesis. The experimental setup consists of 5 basic systems.

1. - Main KrF Laser System
2. - Target System
3. - Probe Laser System
4. - Interferometer System
5. - Timing Monitor

The main laser system produces a nanosecond, 248 nm wavelength laser pulse which is focused onto a target. This system includes calorimeter monitors of the laser energy, streak camera monitoring of the pulse shape and digitized video monitoring of the equivalent plane focal spot. To avoid breakdown in air the target is mounted in a vacuum chamber. Digitized translator systems are used for moving it and controlling its alignment. The main laser also delivers a trigger pulse to the probe laser system at which time this system delivers a subnanosecond pulse for optically probing the plasma. The interferometry system includes an interferometer, a lens for imaging the plasma and a vidicon and a video digitizing system for recording the interferogram. For the interferogram to be useful it is also necessary to have an accurate measure of the relative timing of the probe pulse to the main laser

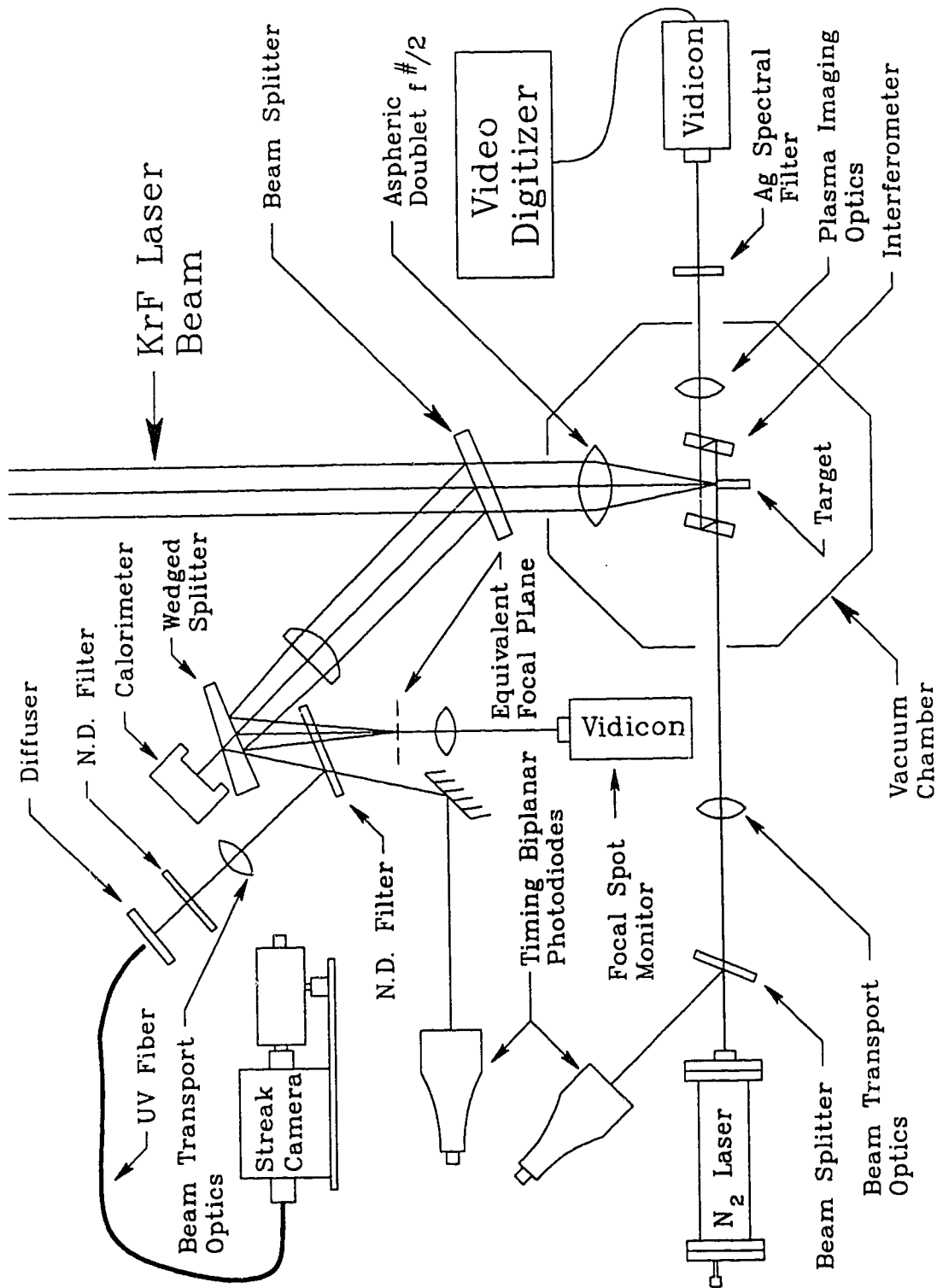


Fig. 3.1. Schematic of the experimental setup.

pulse. These various systems are described in the rest of the chapter.

3.3 KrF Laser System

The experiments were performed using the Krypton Fluoride Laser Facility in the Department of Electrical Engineering. The front end of the KrF laser system produces a pulse which is 20 ns long. This pulse is split into three pulses which are then used to sequentially extract the final stage electron beam amplifier producing three 20 ns pulses. Part of the initial 20 ns pulse is compressed using Brillouin back scattering to produce a short pulse which in turn extracts the energy from the 20 ns pulses in a large aperture Brillouin cell to produce a final pulse with a wavelength of 248 nm, a duration of 1.5 ns and energy up to 2 J

The laser pulse produced by the system is focused on to the target using a 10 cm diameter 18 cm focal length lens. This lens is an aspheric doublet which is necessary to correct for spherical aberration when used at its unstopped aperture of $f / 2$. The focal spot thus produced has been characterized and the focal spot for this system is nominally considered to have 70 % of its energy inside a 35 μm diameter spot.

The contribution of beam divergence to the focal spot is monitored by splitting off a small fraction of the main beam, focusing it with a longer 70 cm focal length lens

and then imaging the focus onto a video digitizing system. The digitized image corresponds to the actual focal spot except for a scale factor of 4 times given by the ratio of the focal lengths used in the monitor and used to focus the beam onto the target. The actual focal spot on target includes the residual aberrations of the 18 cm aspheric lens.

The energy of the main laser pulse was monitored by imaging a small fraction of the beam onto a pyroelectric calorimeter with the trace read directly off of an oscilloscope. The system was calibrated by comparing it to a calorimeter set within the target chamber. The Pulse shape of the main laser was monitored using a Hamamatsu C979 streak camera system.

3.2 Target System

Targets for this experiment were mounted within a vacuum target chamber kept at less than 3×10^{-5} torr during the experiment. The target must be in vacuum as any substantial background gas pressure would interfere with both the laser pulse as it is brought to focus and with the expansion of the plasma.

The target position is controlled by a digital three axis positioning system controlled from outside of the target chamber. The surface of the target is adjusted to the best focus of the main laser, which was determined as the point with the highest keV energy x - ray production.

The position of the target surface is subsequently controlled by means of a He Ne laser alignment system. The He Ne laser beam is parallel to and is cut by the target surface. The cut beam is then reimaged with enough magnification so that the target position may be controlled with an uncertainty less than the depth of focus of the main laser.

For the present experiments plane targets of high purity aluminum were used. The target surface was prepared with a micro surface lath which avoids adding impurities to the surface by polishing. The targets used were one eighth of an inch thick and the data for this thesis was collected by firing on the target edge to minimize shadow effects in the interferometer.

Accurate alignment of the direction of the target normal was required to avoid shadowing effects in the interferometer. The target was aligned by reflecting a He Ne laser, which was set up parallel to the main laser beam, from the target surface. By using this method to control the rotation of the target, the probe laser could be kept parallel to the target surface within 10 mRad.

3.3 Nitrogen Laser

Probe pulses for this experiment were produced with a transversely excited nitrogen laser. The physics of nitrogen lasers is dealt with extensively by Willett in the book Introduction to Gas Lasers [70]. Fig. 3.2 depicts

FIGURE OMITTED DUE TO COPYRIGHT RESTRICTION

Fig. 3.2. N_2 laser levels.

the energy level diagram. The predominant laser line of molecular nitrogen is the transition from the first vibrational level of the $C^3\pi_u$ state to the first vibrational level of the $B^3\pi_g$ state and oscillates with a wavelength of 337 nm. The life time of the upper C state is about 40 ns while the lifetime of the lower B state is about 10 μ s. The laser transition thus is self quenching and inherently provides short pulses, the duration depending on the nitrogen pressure. The medium has high enough gain for the laser to be operated as an amplified spontaneous emission laser without cavity mirrors.

Shown in Fig. 3.3 is the electrical schematic of the laser developed for this thesis. The transient nature of the laser pulse means that inversion can only be obtained by exciting the system within the lifetime of the upper level. Electrical pumping must therefore be done by using a high voltage pulse with current rise time less than about 40 ns [70]. This laser operates by the double discharge process [71] characterized by a relatively slow discharge through the spark gap, the current limited by the inductance of the circuit, (L_1) followed by a discharge between the electrodes which is fast enough (due to inductance L_2 being low) that it is independent of the discharge through the spark gap.

The design for this laser was based on the paper by H. Strohwald and H. Salzmann [4] and is shown schematically in Fig. 3.4. The discharge through the spark

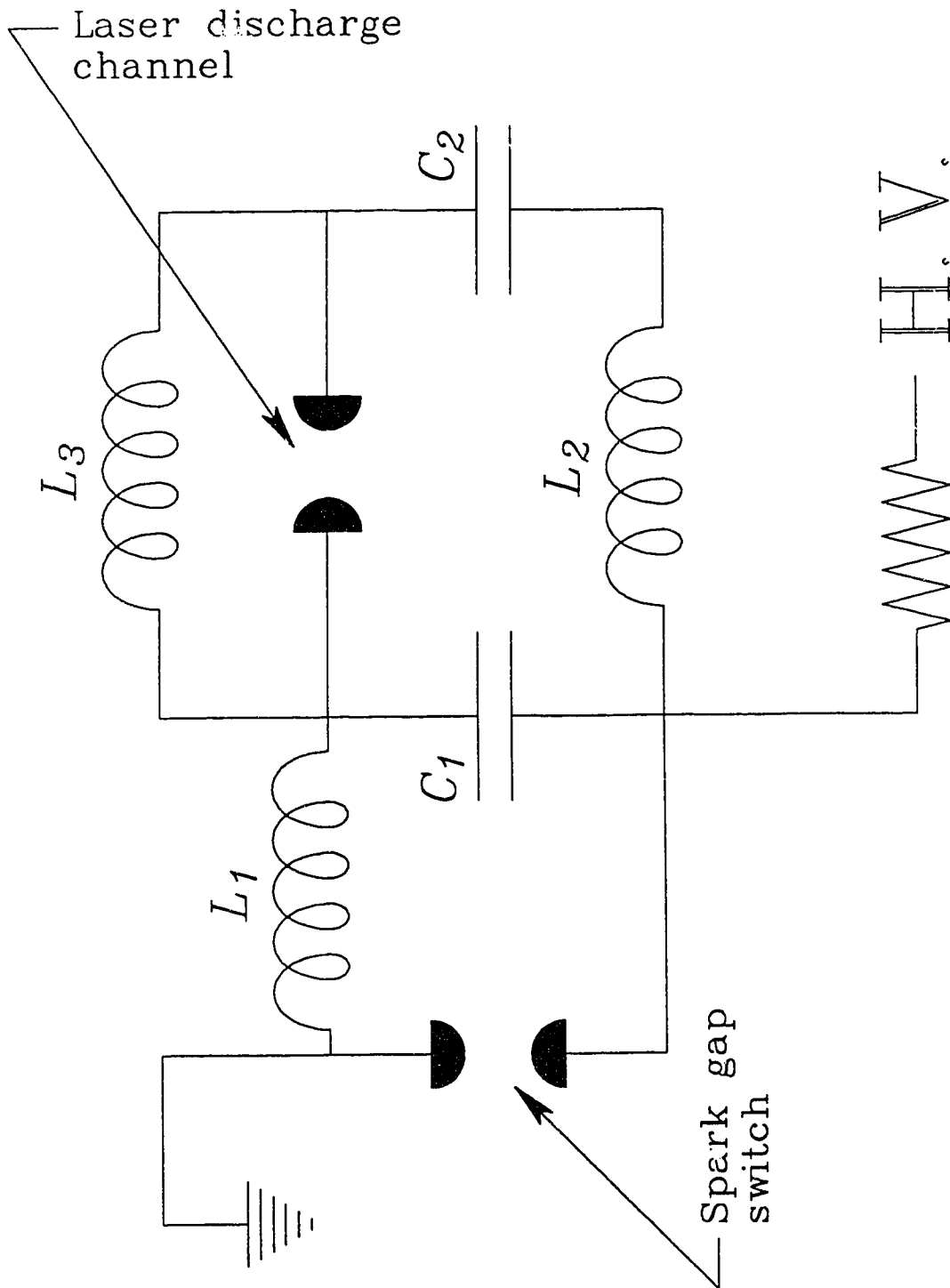


Fig. 3.3. Electrical schematic for N_2 laser.

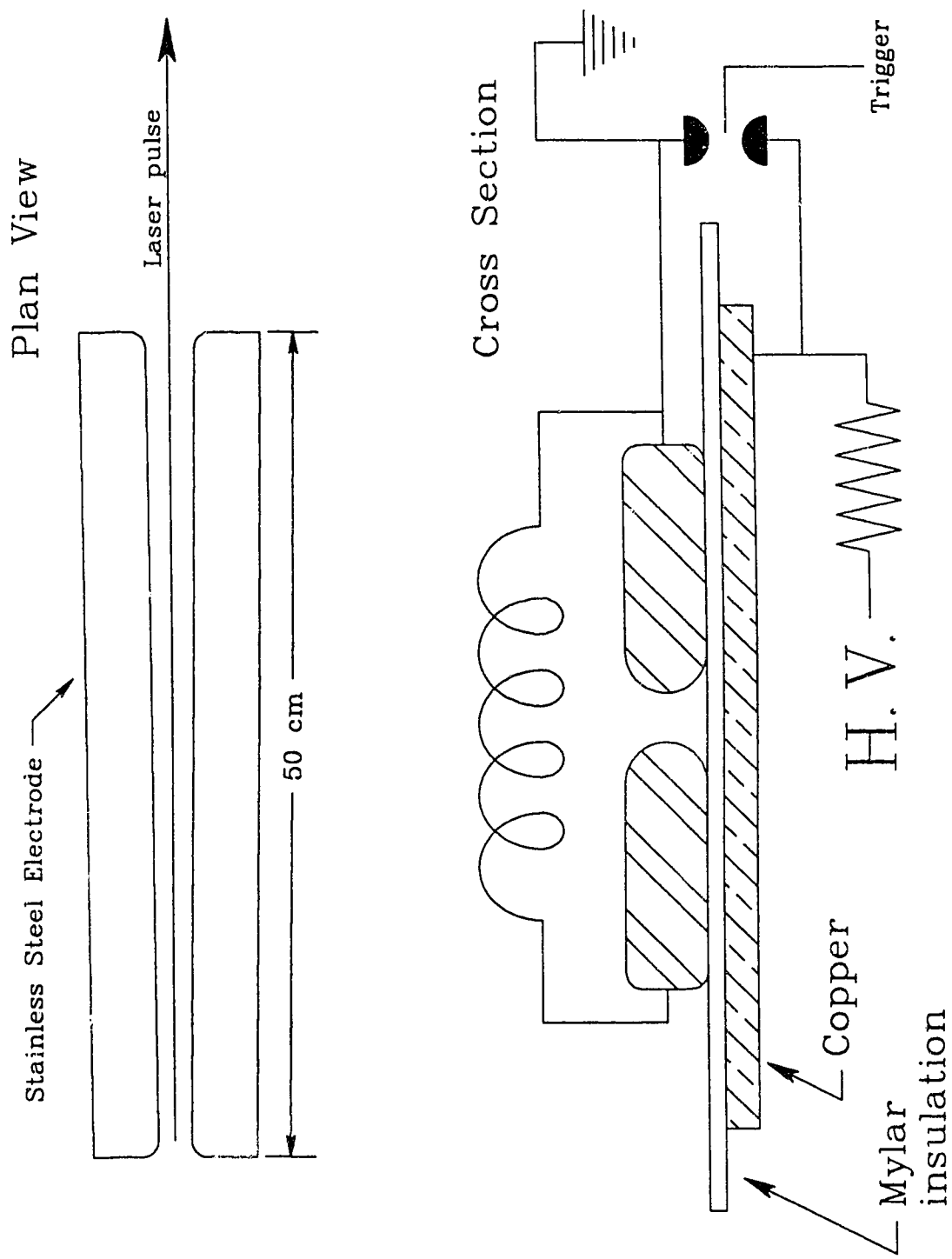


Fig. 3.4. Schematic of N₂ laser physical setup.

gap is slow enough (about 50 ns) that the voltage of the discharging electrode is kept constant along its length. During this time the Blumlein acts as a capacitor. The formation time for the discharge between the electrodes is varied along its length by varying the gap between the electrodes. By setting the electrodes closer at one end of the discharge than the other a travelling wave discharge is produced in the gap, the blumlein now behaving as a transmission line. The discharge can be made to move down the electrodes with about the velocity of light giving preferential amplification to a pulse moving with the discharge. This mode of operation was demonstrated at atmospheric pressure. With the electrodes parallel the pulse from each end of the laser is approximately equal. As the gap is wedged the pulse energy increases from one end of the laser while decreasing from the other. A ratio of about 4 to 1 may be achieved as shown by Fig. 3.5. At higher filling pressures predicting shorter pulse lengths a travelling discharge is necessary as the length of the cavity is much longer than that of the pulse. The ratio between the energy of two pulses is expected to become progressively higher with increasing filling pressure. This dependence on a traveling discharge at higher pressures was in fact observed as a pulse could only be detected from one end at a time.

The pulse length of the laser is varied by altering the nitrogen pressure in the cavity from 1 to 6 atm. Using

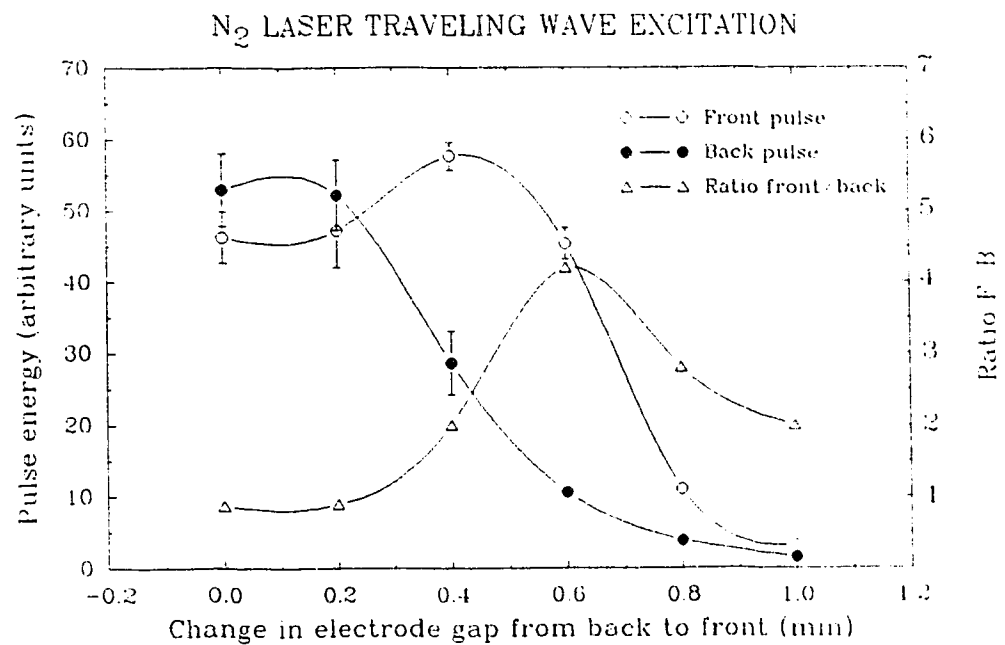


Fig. 3.5. Comparison of the front pulse with the back pulse for different electrode wedge angles.

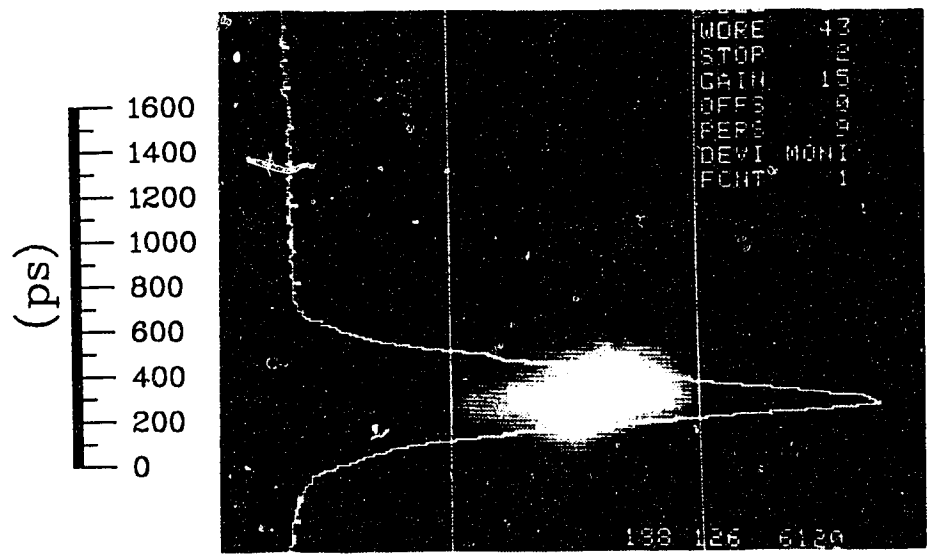


Fig. 3.6. Typical streak of N₂ laser pulse.

a streak camera the pulse width (FWHM) was demonstrated to vary from about 600 ps at a filling pressure of 1 atm to about 300 ps at 3 atm the exact pulse width depending on the alignment of the electrodes. Fig. 3.6 shows an example streak trace of the nitrogen laser pulse.

The energy of the laser was measured using a biplanar photodiode calibrated against a pyroelectric calorimeter. The energy increases with the charging voltage and has a value of about 200 μJ at a charging voltage of 20 kV.

The laser is triggered by means of a 5 kV pulse to a trigatron spark gap. The trigger pulse is produced by another blumlein circuit triggered by a krytron. An avalanche transistor circuit was used to trigger the krytron giving a total jitter in the timing of the laser output of about 2 ns when the system is optimized. This is sufficient for timing the probe laser to the main KrF laser discharge. The avalanche transistor circuit itself was triggered by means of a semiconductor photodiode signal from the main laser. The timing was adjusted by means of changing an electrical delay cable in this line.

3.4 Jamin Interferometer

The plasma interferometry was done with a Jamin interferometer developed for this project. Fig. 3.7 shows the optical setup. The interferometer consists of 2 cm thick quartz plates set parallel at some angle to the probe beam. The splitting and subsequent recombining of

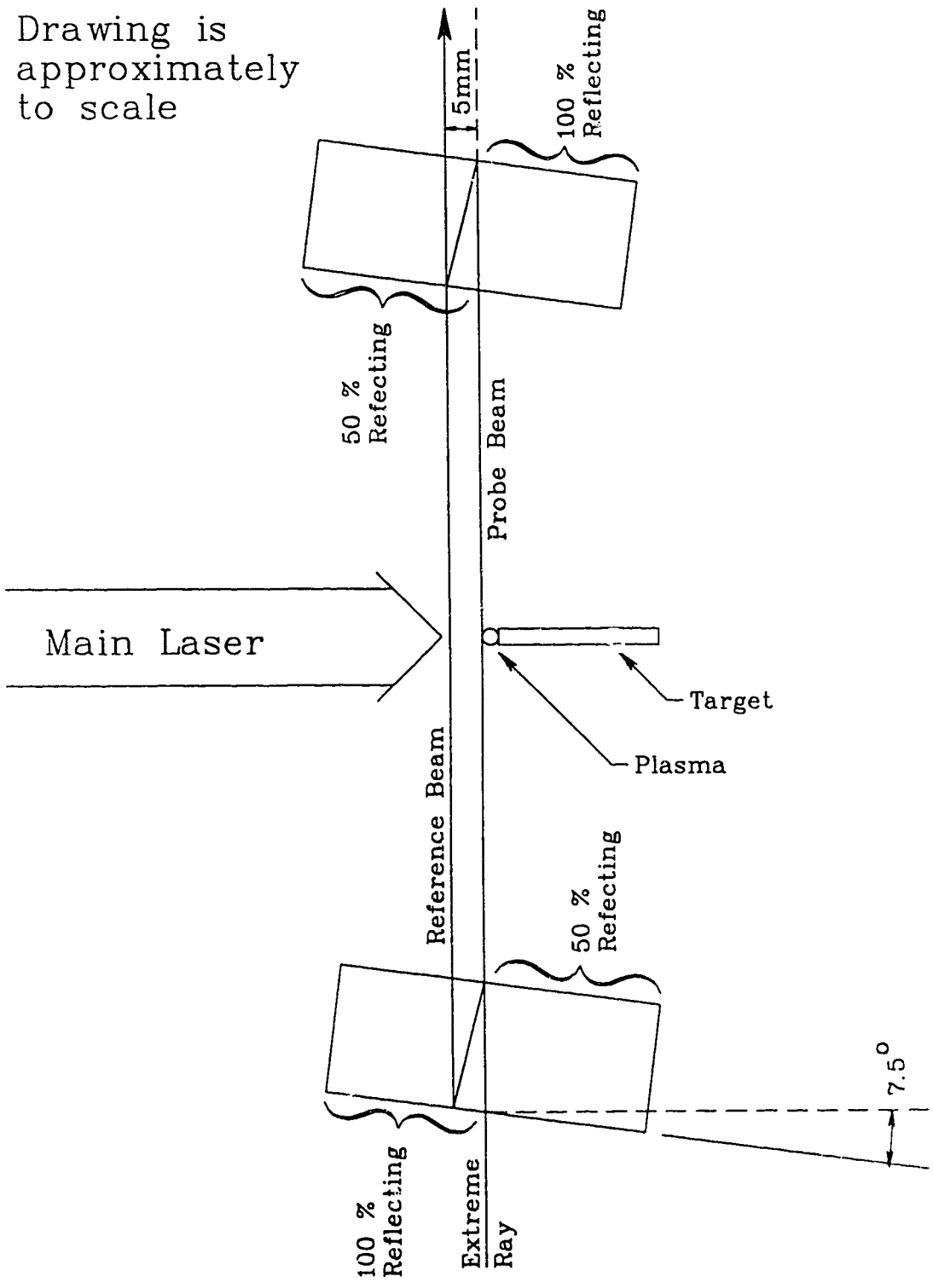


Fig. 3.7. Jamin interferometer.

the probe is accomplished by partially reflecting coatings on the surface of the quartz plates.

The Jamin interferometer is an excellent interferometer for applications where the reference beam can be routed near to the probe beam. The interferometer has the advantage of being very easy to align as the quartz plates only serve to shift the beam pulse in a transverse direction and do not alter the beam direction. The only other limitation to this interferometer is the limitation to its resolution due to the necessity of imaging through a thick plate.

The interferometer developed for this thesis may be used with a plate angle from 7.5 deg to 15 deg giving a separation between the probe and the reference beam of 5 mm to 10 mm. A 5 mm beam separation was considered sufficient to ensure that the plasma density in the region of the reference beam is insignificant. The interferometer was designed to keep the optical elements as far as possible from the plasma consistent with the use of $f / 10$ collecting optics, ensuring that the beam size (as collected by the lens) could be handled by the quartz interferometer plates (diameter less than the beam separation). The probe beam is routed through the target chamber at 15° to the horizontal and the interferometer designed so as not to interfere with the target alignment beam.

The alignment of the interferometer plates is done by

using the probe laser. Alignment consists of adjusting the angle of one of the plates until the spatial position of the probe and the reference beams, upon recombination, coincide exactly. Due to the divergence of the probe laser and the corresponding curvature of its wavefront any misalignment shows itself by producing a series of fringes. the plate is adjusted until the fringe spacing becomes infinite (fringes larger than the field of view).

A back ground fringe pattern is produced by placing a thin wedged plate into the beam path between the first interferometer plate and the target. The wedged plate causes a small deflection to the beam paths introducing a small asymmetry into the interferometer. The overall optical path length of the probe and reference beams remains equal. However, the wavefronts of the beams, which are curved due to the beam transport optics, are distorted so that when recombined they form a series of parallel fringes. This method of producing fringes has the advantage that the fringe spacing is independent of the exact positioning of the wedged plate itself and so is an easy method of producing very stable reproducible fringes.

The wedged plate is placed into the beam path after the interferometer is aligned. Since the probe passes through the wedged plate before passing through the plasma it has a negligible effect on the imaging accuracy of the system.

3.5 Imaging and Digitization

The plasma is imaged onto the vidicon with a 2.5 cm diameter, 25 cm focal length lens. The lens was placed for this experiment to give approximately a ten to one magnification. There are three main sources of aberration in this imaging system, that due to diffraction depending on the f number of the optics and increasing as the diameter of the lens is reduced, spherical aberration which increases as the diameter of the lens increases, and the aberration due to imaging through a thick plate which depends on the angle of the plate and the f number.

The f number of the lens should be chosen in order to minimize the total aberration of the imaging system. The spot sizes due to diffraction and spherical aberration were estimated using standard formulas. The spot size due to imaging through a thick plate was estimated by ray tracing using the extreme rays. The ideal f number was determined to be about $f / 16$ and the lens was stopped down accordingly. The resolution of the total system was estimated as the root of the sum of the squares of the three contributions giving a figure of about $10 \mu\text{m}$.

The resolution and magnification of the system was measured by imaging a resolution test chart placed at the point of main laser focus. The finest line spacing which could be determined was about $12 \mu\text{m}$, which is in reasonable agreement with the estimated resolution as given above.

The system is focused by firing the main laser onto the end of a 56 μm diameter wire, Fig. 3.8, with the end of the wire kept on the focal plane of the main laser. The target position is adjusted laterally until the laser is observed to be hitting the end of the wire. The laser could be observed hitting the wire over a range of movement of 110 - 150 μm . This measurement is in agreement with the outer wings of the 35 μm diameter focal spot.

The interferometer imaging lens is then focused on the wire to produce the sharpest image on the video digitizer. As features on the end of the wire could be focused to within the radius of the wire, the focusing error relative to the main laser is estimated at $\pm 60 \mu\text{m}$.

The plasma light and any stray KrF radiation was filtered from the interferogram by using thin (1.6mm) quartz plates coated with a thin film of silver which acts as a reasonably narrow band pass filter centered close to the nitrogen laser wavelength.

The interferogram was imaged onto an Hamamatsu C1675, type 13, ultraviolet sensitive camera head and the signal was digitized using an Imaging Technology Inc. FG-100-AT video digitizing board inside an AT computer.

3.6 Timing and Calibration

It is essential that the timing between the main laser and the probe laser be known accurately. This was accomplished by imaging a small fraction of both pulses

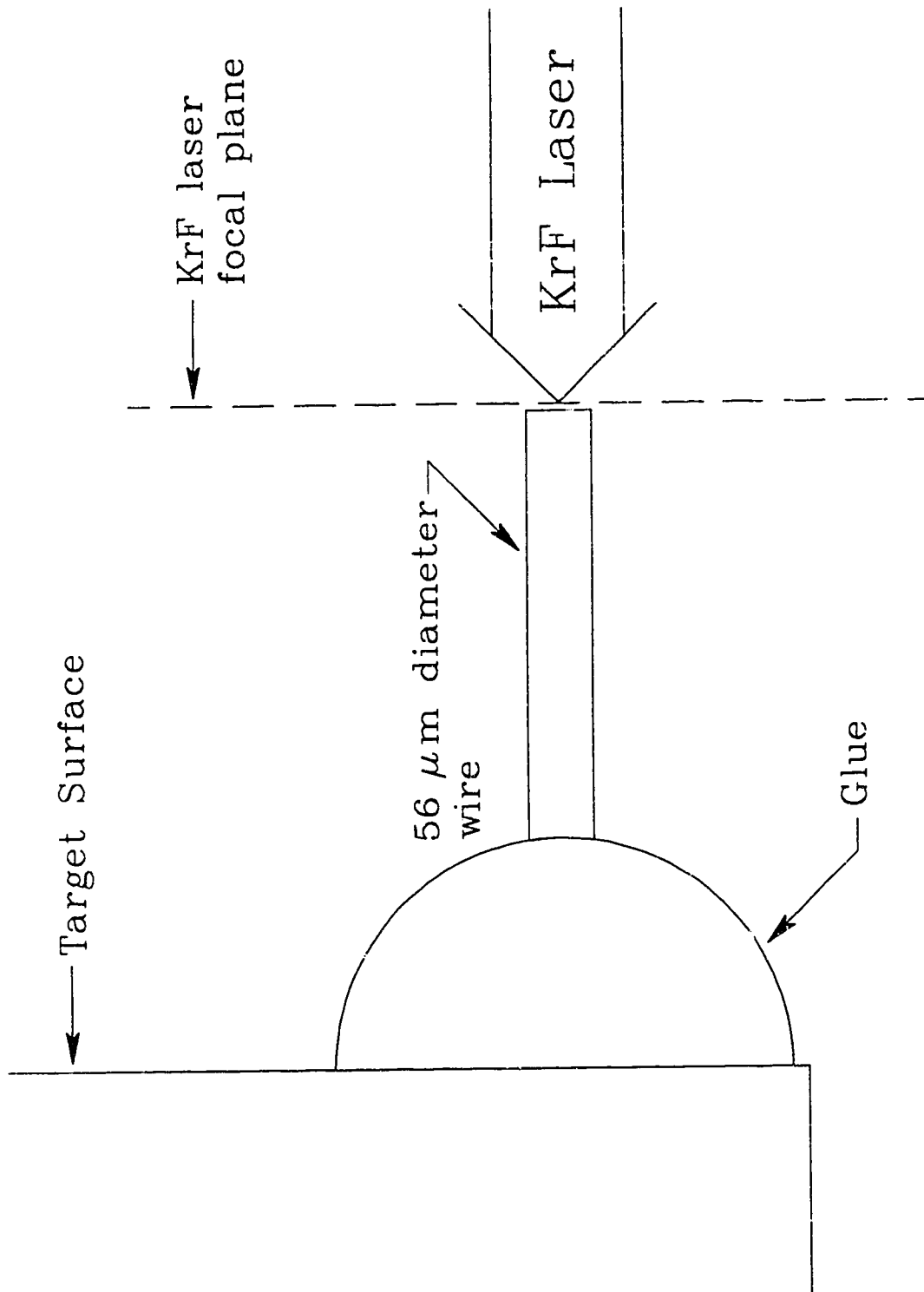


Fig. 3.8. Interferometer focusing wire.

onto Hamamatsu R1193U-02 uv sensitive biplanar photodiodes. The signals were added and observed on a tektronics 7104 oscilloscope. The time base of the scope was calibrated to 1 % accuracy using a 100.0000 MHz signal from a tektronics time mark generator. The relative timing of the two pulses could be measured with this system to within 100 ps.

To calibrate the system a thin quartz plate was placed at the main laser focus at such an angle as to reflect part of the main laser down the same path as the probe laser. The resulting signal was observed on a third photodiode giving an absolute timing which was compared to the relative timing of the monitoring system.

For consistency, as the position of the start and peak of the main laser pulse is usually indeterminate, all reported timings for the probe pulse in this thesis were measured from the half maximum point in the rise of both pulses. Streak traces of the KrF laser pulse show an average rise time of about 1.2 ns for the KrF shots used in this thesis. Thus taking a probe pulse width of 600 ps, a timing given as 0.0 ns nominally corresponds to a probe pulse centered 900 ps after the beginning of the main laser pulse.

CHAPTER 4 EXPERIMENTAL RESULTS

The raw data analyzed in this experiment consists of digitized interferograms which are deconvolved to produce tables of electron density as a function of position. This chapter presents the raw data obtained from the experiment and discusses the methods used to process it. Deconvolution from interferogram to electron density is illustrated using a sample interferogram. Electron density is in turn analyzed to obtain values for the axial scale-length, the time and energy dependence of which forms the primary investigation of this thesis. Sources of error are identified and calculations made of the overall accuracy of the results. This chapter also describes the lateral expansion features of the plasma which will be important in connection with a discussion of the possible presence of strong magnetic fields within the plasma.

4.1 Experimental Data

Interferograms were obtained with probe timings ranging from - 1.3 ns to 12.0 ns and main laser energy ranging from 190 mJ to 1650 mJ. A few interferograms were obtained at lower energies but the pulse timing is not measurable. The following table, Table 4.1, lists the statistics for the interferograms analyzed in this thesis.

Shot number	Probe timing (ns)	Laser energy (mJ)	Pulse duration (ns)	Focal spot digitized
21078822	-1.3	640	1.5	yes
22078811	-1.1	840	1.8	yes
21078827	-1.0	580	2.4	yes
22078810	-0.9	560	1.4	yes
22078812	-0.6	870	1.6	yes
21078823	-0.4	540	2.4	yes
14108807	-0.3	353	—	no
21078813	-0.1	240	1.6	yes
22078818	0.1	670	1.6	yes
22078820	0.1	610	1.5	yes
Shot number	Probe timing (ns)	Laser energy (mJ)	Pulse duration (ns)	Focal spot digitized
14108804	0.1	1140	1.5	no
21078811	0.3	230	—	no
21078830	0.3	190	1.9	yes
22078815	0.3	810	1.6	yes
22078813	0.6	680	1.8	yes
22078824	0.7	270	2.4	no
14108805	0.7	1630	1.7	no
14108803	1.3	1430	1.5	yes
12108807	1.5	190	1.5	no
14108808	1.5	1150	1.7	no
Shot number	Probe timing (ns)	Laser energy (mJ)	Pulse duration (ns)	Focal spot digitized
12108809	1.6	390	1.6	no
12108808	1.8	720	2.5	no
14108802	2.2	1650	—	yes
20078818	2.3-2.6	230	1.7	no
28078801	2.4	280	2.5	yes
20078812	2.5	260	1.4	no
21078815	2.5	480	1.9	yes
21078819	2.5	520	1.5	yes
21078816	2.6	550	1.7	yes
22078804	2.6	230	2.2	yes

Table 4.1. Interferogram shot statistics.

Shot number	Probe timing (ns)	Laser energy (mJ)	Pulse duration (ns)	Focal spot digitized
27078801	2.6	—	3.0	no
20078815	2.8	260	1.6	no
25078803	2.8	960	sat	yes
12108811	3.2	650	2.8	no
21078809	3.3	470	1.5	yes
21078814	3.5	650	—	no
12108810	3.7	1160	3.0	no
20078817	3.9	400	1.6	yes
22078823	4.7	620	1.4	yes
22078826	4.9	—	—	no

Shot number	Probe timing (ns)	Laser energy (mJ)	Pulse duration (ns)	Focal spot digitized
22078808	5.2	940	1.9	yes
22078821	5.2	840	2.0	yes
22078806	5.7	1030	2.1	yes
22078807	6.3	1070	1.9	yes
20078813	7.2-7.9	230	1.5	no
21078807	7.5	750	1.7	yes
21078808	8.3	720	1.6	yes
20078809	8.5	521	1.6	yes
20078808	9.4	400	1.6	yes
21078805	9.7	510	1.8	yes

Shot number	Probe timing (ns)	Laser energy (mJ)	Pulse duration (ns)	Focal spot digitized
20078804	12.0	430	—	no
22078805	—	530	1.5	yes
12108806	—	70	—	no
12108812	—	240	—	no
12108813	—	100	—	no
12108815	—	230	—	no

Table 4.1. Interferogram shot statistics.

As the relative timing between the probe and main laser pulse is measured from the half maximum point in the rise of both laser pulses, plasma is expected to form at about - 0.9 ns with the exact time depending on the energy of the main laser pulse and the shape of its leading edge. The earliest indication of plasma was observed to be at - 1.1 ns with a main laser energy of 840 mJ. In general, initial plasma formation is observed at later times for main laser pulses of lower energy as expected. A pulse of 559 mJ at -0.9 ns shows a slight indication of plasma scattering of the probe pulse but no discernable fringe shift. These observations are consistent with the shape of the leading edge of the main laser pulse which shows some energy on target before -0.9 ns and lends confidence in the calibration of the timing system.

Fig. 4.1 shows a sampling of interferograms obtained at a variety of times in the main laser pulse. At early times the plasma is observed to expand both outwards and laterally. At later times after the peak of the laser pulse an expanding high density cone of plasma surrounding the lower density axial region is observed. (A fringe which curves inwards on axis indicates lower density). The cone exhibits a sharp discontinuity at its outer surface marking the limits of the plasmas lateral expansion. This feature of the plasma will be referenced in this thesis as the expansion cone and is described in section 4.8.

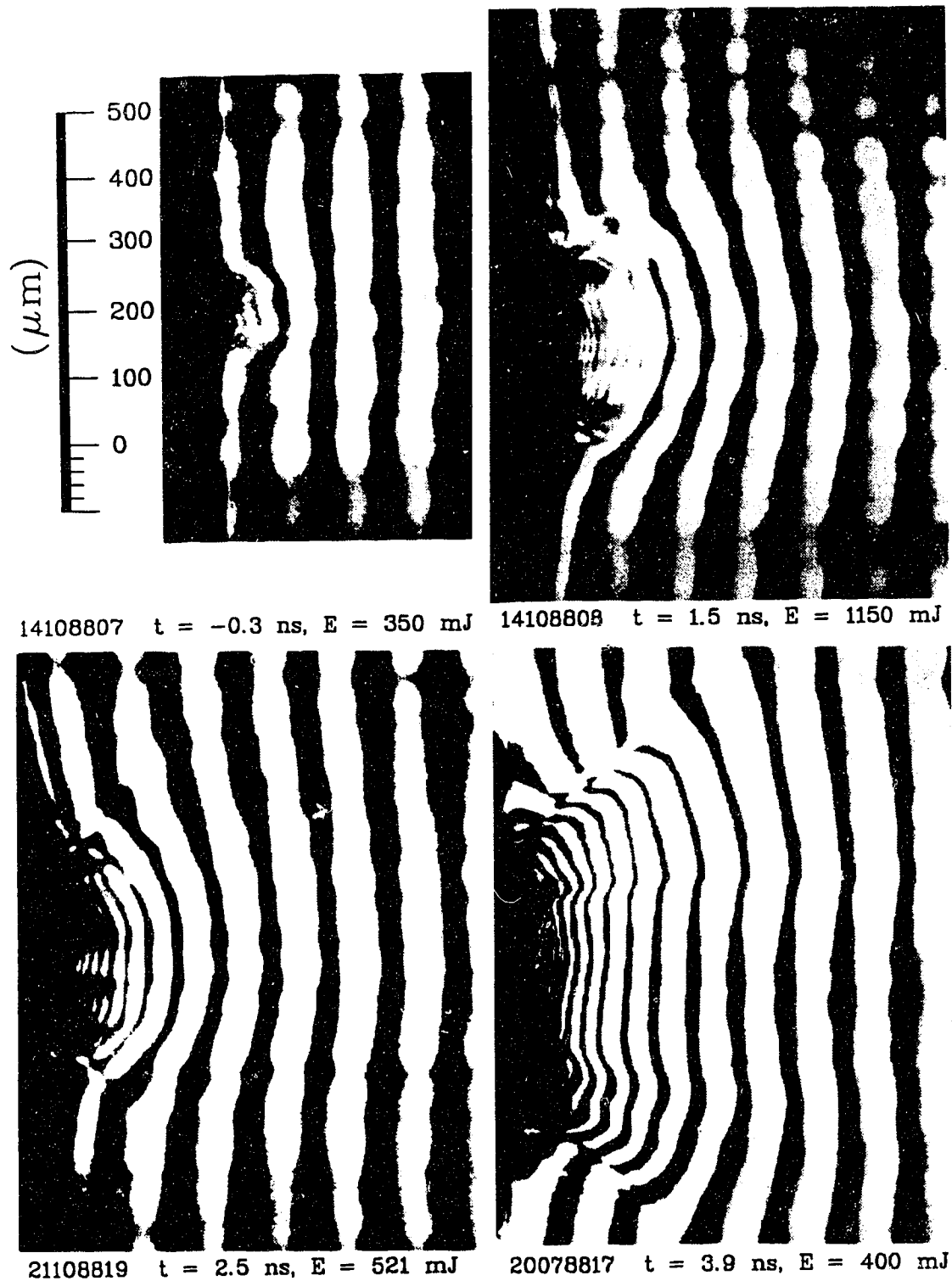


Fig. 4.1. Interferograms obtained at various times.

Vertical video axis shown horizontal in figure.

4.2 Interferogram Deconvolution

The first step in deconvolving the interferogram to obtain electron densities is to determine the position of the fringe maxima and minima. The digitized video image is analyzed in vertical slices which are approximately perpendicular to the undisturbed fringes. In order to be recognized as a fringe maximum the increase in brightness compared to the fringe minimum must exceed a visibility ratio which is set by the programmer. The positions of fringe maxima and minima as determined by the first stage of the program are then edited to correct any incorrectly identified fringes. This editing includes continuing the fringe over any short sections where the computer routine failed to find it, deleting any false fringes caused by noise in the data, and cleaning up the ends of the fringes particularly in interferograms with sharp discontinuities in the fringes or areas where the fringes double back on themselves. The best that may be done on any fringe which doubles back on itself is to indicate a vertical drop. The result is a table giving the position of each fringe along the vertical axis of the video image as a function of the horizontal axis.

Once the fringes have been properly identified along their lengths they may be smoothed. Smoothing is important as the inversion routine is very susceptible to any random scatter in the fringe positions but care must be used as smoothing can cause loss of information.

Numerical inversion requires an axis of symmetry which is defined by a line through the center of the plasma image chosen so as to best divide the interferogram into two similar halves. Determining the best position may involve choosing an initial position, inverting the interferogram and then choosing a new axial position from the inversion. Such an iteration will quickly determine the best axis position.

The fringe shift δ at a point as required for Abel inversion is determined by finding the number of additional fringe shifts at a particular point in the interferogram compared to a reference shot of background fringes with no plasma present.

In order to simplify the calculations the background fringes were fit by an analytic function given by:

$$iy = A + FS n + DELFS n^2 + AX ix + AXX ix^2 + DELAX n ix + GAMMAX n^2 ix \quad (4.1)$$

Where: ix = horizontal position in video pixels units

iy = vertical position in video pixel units

n = background fringe number

The coefficients which determine the function are obtained by fitting the function to a set of undisturbed fringes. The function may be fit to either the undisturbed portion of the interferogram being deconvoluted (if this portion is sufficiently large) or to a separate interferogram showing the undisturbed fringes. The accuracy

of the deconvolution is determined in part by the accuracy with which the analytic function represents the fringes. The actual fringe shift at a point is determined by calculating the fringe shift at the positions of the nearest fringe maximum and minimum and interpolating for the desired point.

Once the fringe shifts are determined at the specified points along one radial cut across the interferogram they are smoothed using the least square cubic fit prescribed by Bockasten and described in section 2.6. The effect of the smoothing was checked for a few test cases where it was observed to produce better results, particularly on axis, without affecting the overall values obtained for the electron density of the plasma. The inversion was carried out by inverting both halves separately and also by using a weighted inversion which allows for the $\cos(\theta)$ asymmetry in the electron density. The Bockasten inversion produces a table of electron densities. In most cases a 20 point inversion was used and was carried out for 24 slices at $25 \mu\text{m}$ intervals along the plasma axis. A few of the very small plasmas were inverted using a 10 point inversion with the slices closer together as dictated by the interferogram. Once the inversion has been carried out the electron densities may be contour plotted to get an overall picture of the plasma structure and line outs through the plasma may be plotted and their scale-lengths measured.

4.3 Determination of Scale-Lengths

This thesis is concerned primarily with the time and energy dependence of the axial scale-length or e-folding distance of the electron density of the plasma. Because a Bockasten inversion gives least accurate values on axis the axial electron density profile used for determining the scale-lengths was obtained by averaging the density on axis with those at the next 2 inversion points on each side of the axis which have much less error. As the plasma density does not vary much over the central 5 inversion points the above average gives a better representation of the plasmas axial profile.

The values for the scale-length are then calculated by least square fitting a straight line to the natural logarithms of the electron densities. The scale-length is the inverse of the slope of this line. In general the axial profile of the logs of the electron density are not straight lines as expected from simple planar expansion theory but are smooth curves which become less steep with increasing z . For consistency it is necessary to measure the scale lengths over the same density range for all the profiles. Most of the scale lengths quoted here were measured over one decade between electron densities of 6×10^{18} and $6 \times 10^{19} \text{ cm}^{-3}$ which was judged from the data to be the most accurate region encompassing most of the interferograms obtained. Scale-lengths measured at higher densities would in general be shorter and those at lower

densities longer.

For interferograms obtained early in the main laser pulse (before 0.3 ns) the scale-lengths were obtained by using all available points above $1 \cdot 10^{18} \text{ cm}^{-3}$ below which the data becomes very inaccurate. This was necessary as the plasma was steep enough that there are generally only 3 or 4 points available. The density range generally included the range from 6×10^{18} to $6 \times 10^{19} \text{ cm}^{-3}$ used at later times.

The accuracy of the least square fit represents a combination of the random error in the electron density values and the accuracy with which the profile in question may be fitted with a straight line. The accuracy of the scale-lengths is obtained by combining the error to the scale-length obtained from the fit with any error expected from systematic effects as described in section 4.7.b.

Table 4.2 gives the scale-lengths obtained from Bockasten inversion of the data. Also presented is σ_f the accuracy of the fit determining the scale-length, σ_m the estimated error in the scale-length due to misfocus of the imaging system, and σ_t the total error resulting from these sources calculated as the root of the sum of the squares. For this experiment the calculation for σ resulting strictly from the curved path of the probe beam through the plasma gives a value of 1.2 % and is not included as it is much smaller than the other sources.

Shot number	Timing (ns)	Energy (mJ)	scale-length	σ_r (μm)	σ_f (μm)	σ_t (μm)
21078823	-0.4	540	38.4	8.0	2.2	8.3
14108807	-0.3	353	42.0	2.9	2.2	3.7
21078813	-0.1	240	43.0	4.4	2.3	4.9
14108804	0.1	1140	65.5	8.6	2.3	8.9

Table 4.2 (a). Scale-lengths (early time). Electron densities from Bockasten inversion.

Shot number	Timing (ns)	Energy (mJ)	scale-length	σ_r (μm)	σ_f (μm)	σ_t (μm)
21078811	0.3	230	51.0	7.4	2.3	7.7
21078830	0.3	190	76.3	9.2	2.3	9.5
22078813	0.6	680	114.0	4.3	2.3	4.9
22078824	0.7	270	60.3	3.9	2.3	4.5
14108805	0.7	1630	191.5	9.5	2.4	9.8
14100803	1.3	1430	149.7	10.3	2.3	10.6
14108808	1.5	1150	211.5	13.3	2.4	13.5
12108809	1.6	390	94.1	5.7	2.3	6.2
12108808	1.8	720	107.2	7.0	2.3	7.4
14108802	2.2	1650	216.5	17.4	2.3	17.6

Shot number	Timing (ns)	Energy (mJ)	scale-length	σ_r (μm)	σ_f (μm)	σ_t (μm)
20078818	2.3-2.6	230	65.0	4.5	2.3	5.1
28078801	2.4	280	96.4	7.1	2.3	7.5
20078812	2.5	260	76.8	5.5	2.3	6.0
21078815	2.5	480	131.5	7.8	2.3	8.1
21078819	2.5	520	107.6	6.6	2.3	7.0
21078816	2.6	550	145.2	5.8	2.3	6.3
22078804	2.6	230	101.0	5.9	2.3	6.3
20078815	2.8	260	86.4	6.1	2.3	6.5
12108811	3.2	650	89.8	4.6	2.3	5.2
21078809	3.3	470	130.3	8.3	2.3	8.6

Table 4.2 (b). Electron densities obtained from Bockasten inversion. Scale-lengths measured between 6×10^{18} and 6×10^{19} .

Shot number	Timing (ns)	Energy (mJ)	scale-length	σ_r (μm)	σ_f (μm)	σ_t (μm)
21078814	3.5	650	87.0	1.2	2.3	2.6
12108810	3.7	1160	141.1	5.9	2.3	6.3
20078817	3.9	400	111.3	8.2	2.3	8.5
22078823	4.7	620	91.8	4.5	2.3	5.1
22078826	4.9	—	108.7	7.8	2.3	8.1
22078808	5.2	940	100.9	6.8	2.3	7.2
22078821	5.2	840	89.8	5.7	2.3	6.2
22078806	5.7	1030	91.5	5.1	2.3	5.6
22078807	6.3	1070	114.0	5.0	2.3	5.5
20078813	7.2-7.9	230	134.4	3.3	2.3	4.0

Shot number	Timing (ns)	Energy (mJ)	scale-length	σ_r (μm)	σ_f (μm)	σ_t (μm)
21078807	7.5	750	108.1	8.3	2.3	8.6
20078809	8.5	521	100.4	2.7	2.3	3.6
20078808	9.4	—	74.5	2.4	2.3	3.3
21078805	9.7	—	79.9	2.7	2.3	3.6
22078805	—	—	80.2	2.4	2.3	3.3

Table 4.2 (b). Electron densities obtained from Bockasten inversion. Scale-lengths measured between 6×10^{18} and 6×10^{19} .

4.4 Quick Axial Inversion

Not all interferograms are suitable for Bockasten inversion particularly those obtained very early in the main laser pulse when the plasma is very small. Also the highest density regions of some interferograms are not invertible using Bockasten inversion as the fringes are not complete. In these cases it is often still possible to obtain some information about the axial density and scale length of the plasma. The following method has the advantage that it works best for small plasmas with well

defined boundaries where the fringe shift is often only determinable on the plasma axis, which is just the sort of interferogram where Bockasten inversion becomes impossible or very inaccurate. Because of its simplicity and directness the method also serves as a very useful check on the results of Bockasten inversion especially at low densities where questions can arise as to the validity of the results obtained.

The index of refraction on the axis of a symmetrical plasma is given by:

$$n_r(0,z) - 1 = \frac{1}{2} F \frac{\lambda}{R} \delta(0,z) \quad (4.2)$$

where F is a factor which depends on the function for the radial dependence of the electron density. A plasma of constant density would have $F = 1$. A plasma with a parabolic radial density profile would have $F = 3/2$ while a linear density variation from 0 at R to a maximum on axis would have $F = 2$. A plasma with a gaussian radial profile would have $F = \pi^{1/2}$ if R is taken as the gaussian e-folding distance. Thus the accuracy of this method depends on the accuracy of the choice of F but for most well behaved plasmas with maximum density on axis (smooth arcs for fringes) F appears to lie between 1 and 2. This method should therefore be able to give densities within a factor of two. If the radial shape is the same at various axial distances the factor F is then a constant. From the interferogram this often appears to be the case since the

fringe shapes have the same characteristic appearance for different axial positions. In this case the scale-length of the plasma is independent of the factor F . This inversion technique is thus most useful for obtaining estimates of axial scale-lengths. Most of the results used in this thesis were obtained by doing a full deconvolution, however, the scale-lengths in table 4.3 were obtained using the quick method. Shot number 12108809 was used as a check on the method.

Shot number	Timing (ns)	Energy (mJ)	scale-length	σ_r (μm)	σ_r (μm)	σ_t (μm)
22078812	-0.6	870	18.8	2.6	2.1	3.3
21078813	-0.1	241	50.0	1.2	2.3	2.6
12108807	1.5	190	85.8	16.6	2.3	16.8
12108809	1.6	390	95.5	11.8	2.3	12.0

Table 4.3. Scale-lengths obtained from quick inversion.

4.5 Deconvolution Example

Fig. 4.2 shows a streak trace of the main laser pulse for shot number 22078821 which had an energy of 840 mJ on target. The timing of the probe was determined to be 5.2 ns and Fig. 4.3 shows a photograph of the interferogram obtained for shot. The interferogram represents a typical interferogram obtained at later times in the main laser pulse featuring a sharp expansion cone.

Fig. 4.3 also shows the digitized fringes obtained from the interferogram along with the focal spot position and

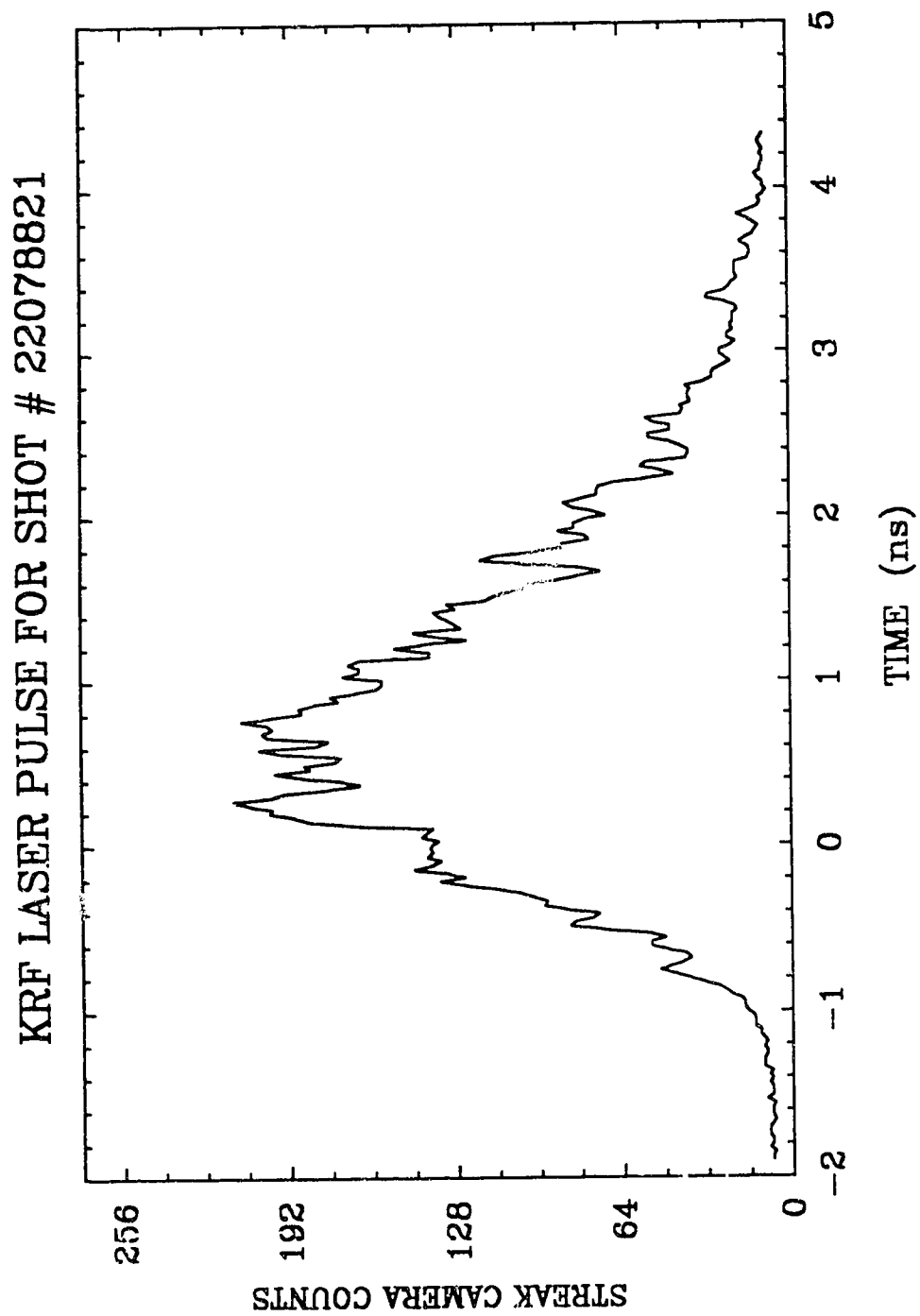
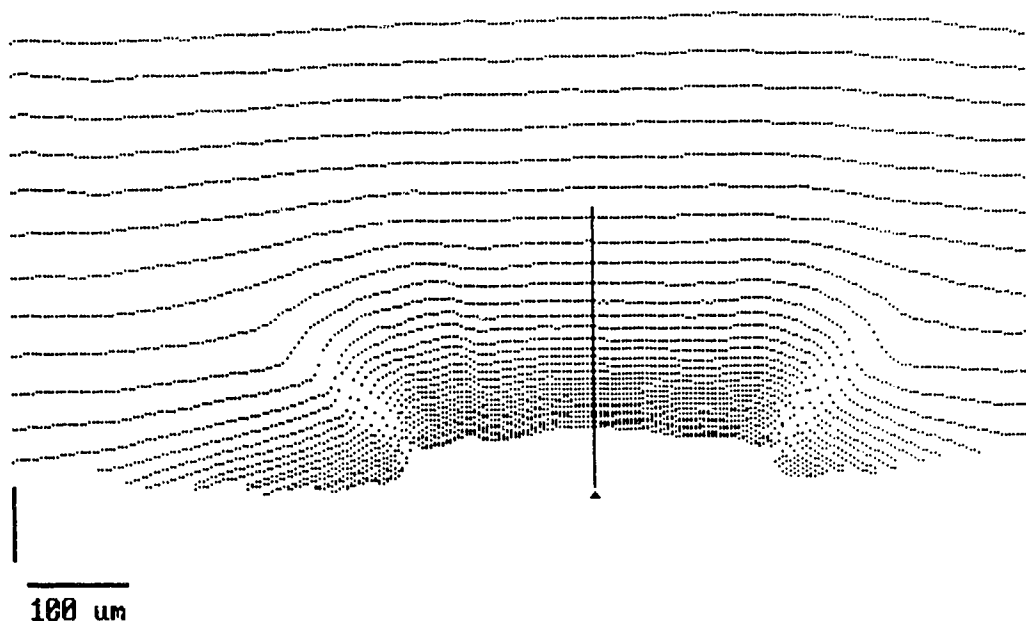
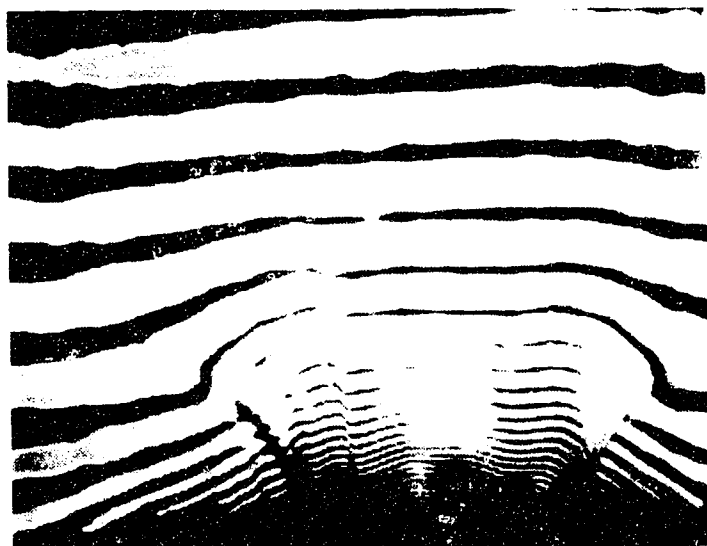


Fig. 4.2. Streak trace of the main laser for shot # 22078821.



SHOT # 22078821 $T = 5.2 \text{ ns}$, $E = 840 \text{ mJ}$

Fig. 4.3. Interferogram and corresponding digitized fringes for shot 22078821.

inversion axis used in the deconvolution. The background fringes used in the deconvolution were determined by fitting to a background interferogram obtained on that day during the same experimental run. The fringes were inverted using both separate inversions for each side and using the weighted inversion. Fig. 4.4 shows the averaged axial profile of the electron density giving a scale-length of $89.8 \mu\text{m}$. Fig. 4.5 shows a contour plot of the resultant electron densities obtained from the inversion process.

4.6 Deconvolution Accuracy

It is important to estimate the accuracy of the results obtained from the deconvolution of an interferogram and in particular the accuracy of the derived scale-lengths. Error in the results arises from a number of sources and includes both random and systematic contributions. In addition the operation of the deconvolution routines themselves must be checked in order to give confidence in the results. An account of the testing of the deconvolution routines is given in appendix A.

4.6.a Random contributions to deconvolution error

Random error in the derived values for electron density is generally due to inaccuracy in determining the values of $\delta(x,z)$ from the interferogram. There are two main contributions. The first is determined by the accuracy of the method of determining fringe position from the

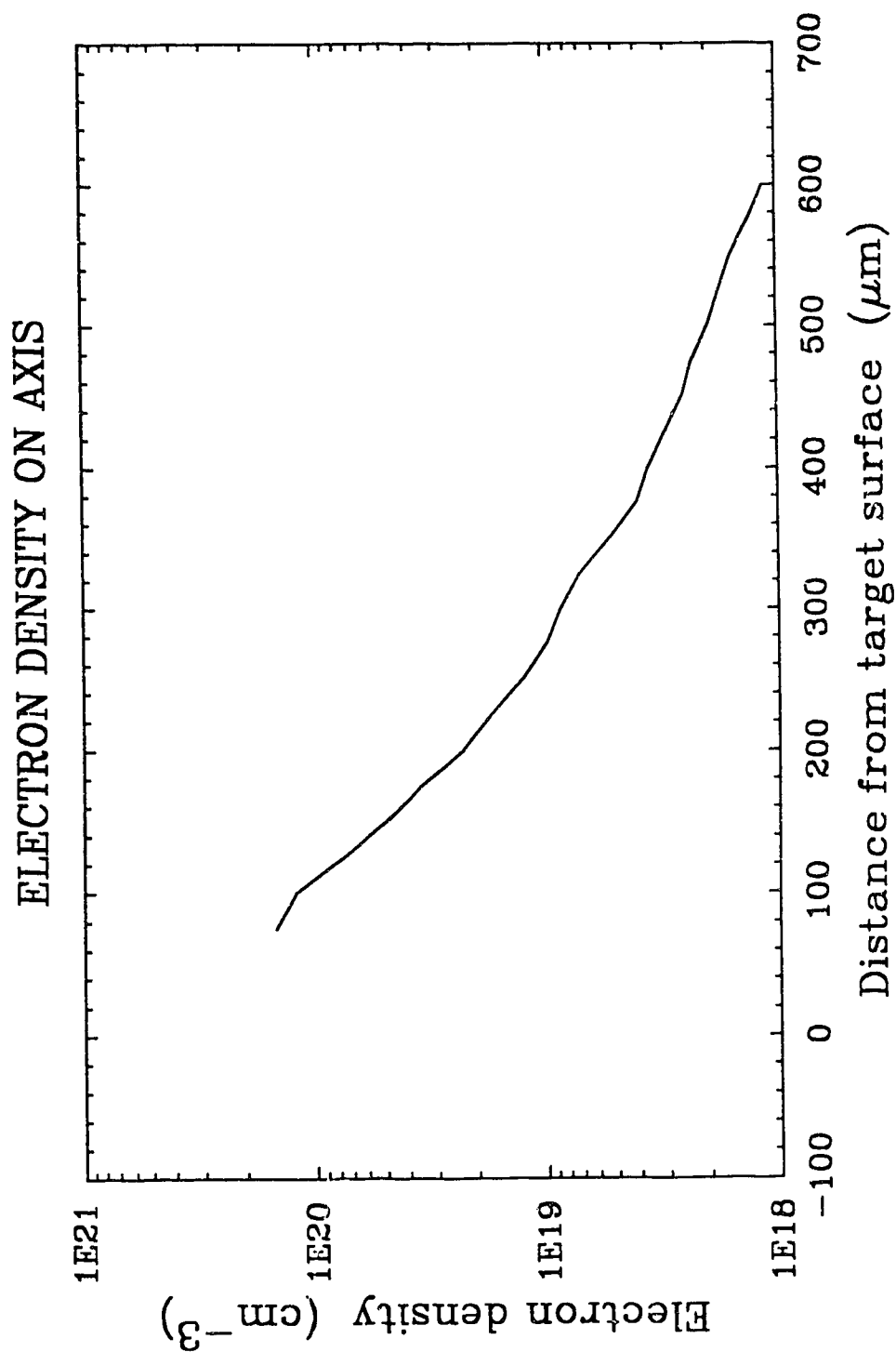


Fig. 4.4. Axial electron density plot for shot 22078821.

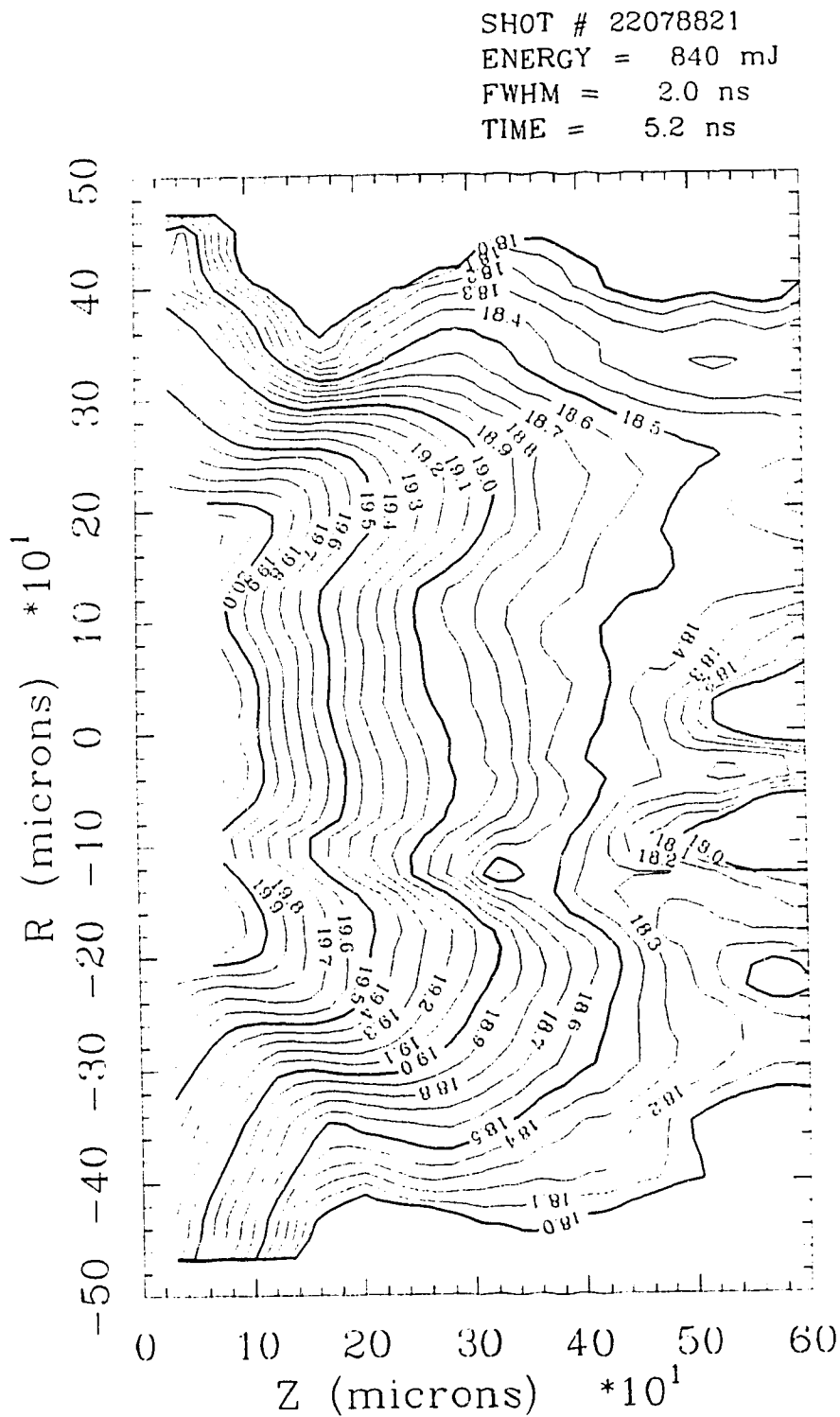


Fig. 4.5. Electron density contour plot for shot 22078821. Contours represent the \log_{10} of the electron density (cm^{-3}).

interferogram and the second is due to the accuracy with which the background fringe positions are represented by the analytic function used in the inversion.

As the inverted Abel integral (equation 2.53) integrates $\partial\delta/\partial x$, random scattering in the values of δ is the most sensitive source of error in n_r . It is minimized by smoothing the fringes as mentioned in section 2.6. While it is important to minimize this source of error to obtain accurate results with low noise, it is not the worst source of error since it generally shows itself as scattering in the final results.

The absolute error in the values of n_r obtained from Bockasten inversion is governed by the equation:

$$\sigma_n = \frac{\lambda \sigma_\delta}{R} s \quad (2.57)$$

$$s = \left(\sum_k (A_{jk})^2 \right)^{1/2}$$

Where σ_δ is the absolute error in the values of δ . The factor s varies greatly with the radial position in the plasma, becoming particularly large near the plasma axis. In this thesis the error associated with axial data was minimized by averaging over the five central inversion points. Except for a few of the very early, very small plasmas a 20 point inversion was used as it seemed to be the most suitable considering the accuracy of the data. The factor s , on axis has a value of 19.219, however the value

arrived at by averaging over the central 5 inversion points, signified here by \bar{s} , is 10.308 thus cutting the error in half.

The random scatter of the data was assumed to be within the space of one digitized video pixel since it is difficult to determine fringe position more accurately than this. This gives a value for the standard deviation of $0.85 \mu\text{m}$ or $1/4$ of a pixel. In order to determine values for σ_δ a fringe spacing of 5 pixels was used for an electron density of 10^{20} cm^{-3} , 10 pixels for 10^{19} cm^{-3} and 25 pixels for 10^{18} cm^{-3} . These values were characteristic of the data for plasmas with a radius of about $400 \mu\text{m}$.

The use of an analytic function to represent the background fringes also introduces a contribution to the random noise level of the inversion. As the inversion equations are linear this noise level is independent of the plasma and so may be estimated by performing an inversion of a set of background fringes. The RMS error was determined to be $5 \times 10^{17} \text{ cm}^{-3}$ for the plasma as a whole and twice this value for the averaged axial data.

Table 4.H gives estimates of the random error associated with the average axial electron densities. For the calculation, R was taken as $400 \mu\text{m}$ which was the usual value used in the inversions and λ was $0.3371 \mu\text{m}$. The variable σ_s is the estimated accuracy of the measured fringe shifts and σ_a is the corresponding error in the electron density. σ_b is the error due to the analytic

function for background fringes and σ_t is the total random error given as a fraction.

electron density	fringe σ_δ	error components (cm^{-3})		error σ_t
		σ_a	σ_b	
10^{20} cm^{-3}	0.05	8.5×10^{18}	1.0×10^{18}	0.086
10^{19} cm^{-3}	0.025	4.25×10^{18}	1.0×10^{18}	0.44
10^{18} cm^{-3}	0.01	1.7×10^{18}	1.0×10^{18}	2.0

Table 4.4. Random error in electron density.

The increase in the error at low densities indicated in the table was observed in the data. The above values are average estimates. The error associated with early time plasmas of small radius will generally be larger than the above numbers particularly at low density. When evaluating a particular shot the quality of the interferogram should also be taken into account.

4.6.b Systematic limitations to deconvolution accuracy

In general the plasma has large density gradients transverse to the path of the probe laser causing the rays of the probe laser to follow a curved path through the plasma. This leads to systematic errors in the deconvolution accuracy of the interferograms. The curved paths of the probe rays cause in essence a systematic shifting of the fringes from their expected position using the assumption that the rays follow straight paths through

the plasma.

The problem of estimating the inversion accuracy in the case of high densities and steep gradients, causing large deviations to the probe path is difficult and has been examined by a number of authors [72-75]. The problem is much less severe in the experiment considered here and simpler calculations are used to deal with the error.

The error is estimated by considering two main components. First is the innate error caused by the ray following a curved path. Second is the error caused by misfocus of the imaging optics of the interferometer combined with the curved path of the probe rays. The estimates will be made for the axial region of the plasma where the effects are most severe.

Both sources of systematic error are estimated by calculating the resulting shift, Δz , in the interferogram's axial fringe positions. On axis where the index of refraction is given by equation 4.2 the fractional error in the derived electron densities is given by:

$$\Delta\sigma = \frac{\Delta\delta}{\delta} \quad (4.3)$$

where δ is the fringe shift on axis and $\Delta\delta$ is the error in the fringe shift due to shifting the fringe pattern by an amount Δz . Assuming an exponential axial profile with scale-length L , one obtains $\Delta\delta = -(\delta/L) \Delta z$ and the fractional error in the measured value for the electron density becomes:

$$\Delta\sigma = \frac{\Delta z}{L} \quad (4.4)$$

The shift for the fringes on axis, Δz , will vary along the profile but is always in the same direction with the maximum values occurring at higher densities. The maximum error induced into the measured values of scale-length is estimated by applying the maximum possible error to the high end of the density range used in determining the scale-length and no error to the low end. The resulting error in the measured scale-lengths is then given by:

$$\sigma_{sl} = \frac{1}{h} \ln \left(1 + \frac{\Delta z}{L} \right) \quad (4.5)$$

Where h is the difference in the natural logarithms of the extremes of the range over which scale-length is measured and for the results quoted here which were measured between $6 \times 10^{18} \text{ cm}^{-3}$ and $6 \times 10^{19} \text{ cm}^{-3}$, $h = 2.3$. Expression 4.11 is fairly general. Using it requires estimating the value of Δz caused by the particular source of error under consideration which for curved rays depends on the degree to which the plasma deflects the probe.

The angle of deflection for the probe rays, θ , is estimated by considering the deflection of a ray probing a plasma of radius R having constant refractive index along the probe path but with an exponential transverse profile characterized by the scale-length L . Assuming small angle deflection the resulting deflection angle is given by the expression:

$$\theta = 2 \frac{R}{L} (n_r - 1) \quad (4.6)$$

The maximum deflection angle recordable by the interferogram is limited by the size of the imaging optics and is given by the inverse of the f number. Assuming that the plasma radius is given by $R = 3L$, a good approximation for the plasmas studied here, equation 4.6 gives densities for the maximum deflection angle which correspond approximately to the density at which the interferograms become dark. Thus the deflection of the probe beam determines the maximum density which could be probed in this experiment.

Fig. 4.6 shows the case for an exactly focused interferogram. The curved path taken by the probe causes a ray to effectively probe less deep than the theoretical ray used to interpret the interferogram. This shift will vary from zero for rays just grazing the plasma to a maximum for the rays of deepest penetration. The error is calculated by estimating the distance, Δz , between the theoretical ray and the position of a straight ray, referred to in the diagram as the equivalent ray, having the same optical path length as the real ray. This distance then gives the shift in the resulting fringe position from where it would be expected if the rays followed straight paths and so gives Δz used in the expressions for systematic error (equations 4.4 and 4.5). Calculating Δz requires detailed knowledge of

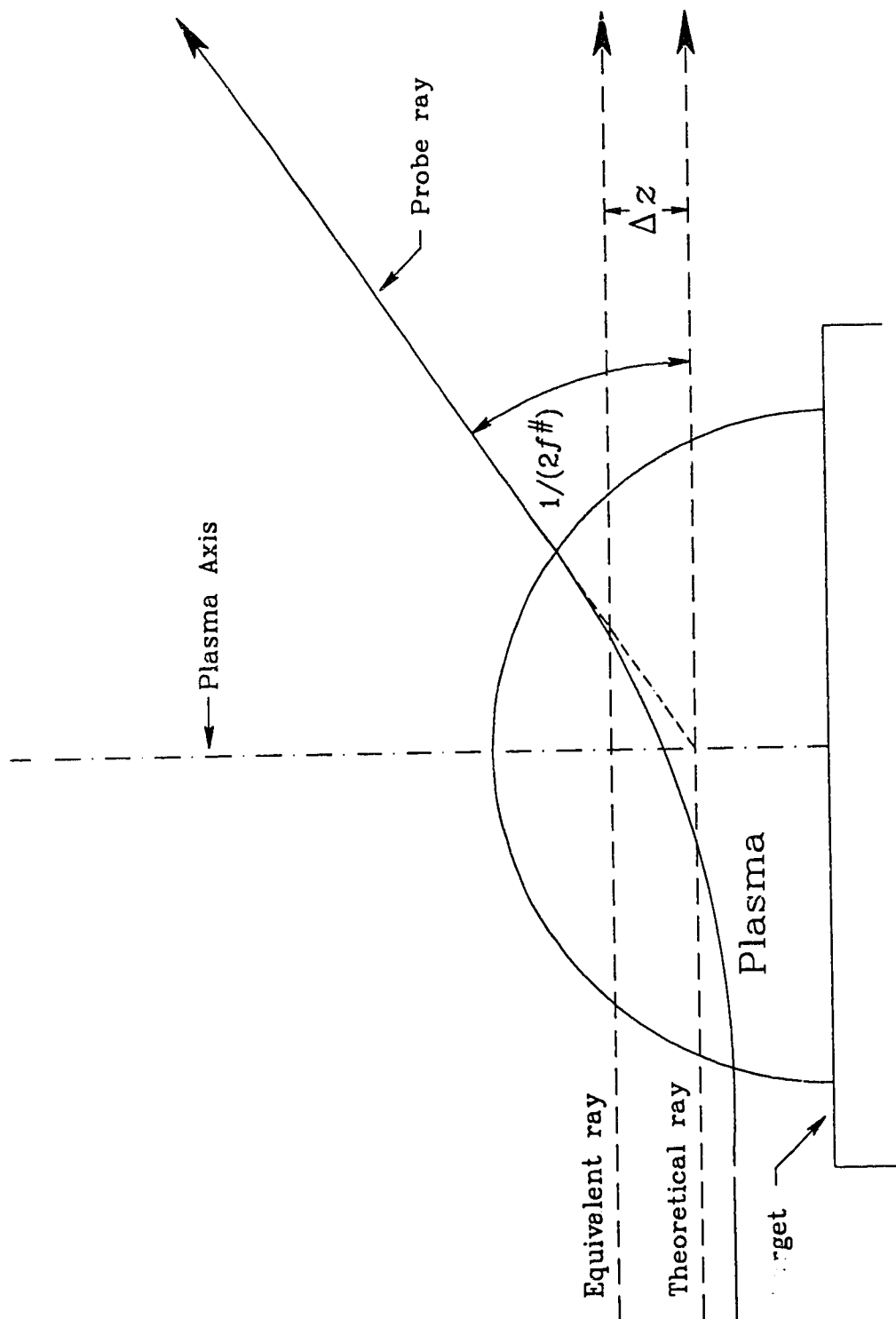


Fig. 4.6. Effect of curved ray path through plasma.

the plasma electron density distribution but an upper bound may be estimated and, assuming small deflection angle, is given by:

$$\Delta z < \frac{R}{2} \theta \quad (4.7)$$

where R is the radius of the plasma and θ is the maximum deflection angle.

Focusing error in the plasma imaging system can greatly increase the amount of error caused by the curved path of the rays. Misfocus of straight rays causes the fringes to lose visibility but does not change their position. As shown in Fig. 4.7 the amount of error caused by misfocus depends on the angle of deflection of the probe ray. The degree to which the imaging system is misfocused causes a shift in the position where the ray is re-imaged in the interferogram and therefore a shift in the position of the fringe corresponding to that ray. For small angle deflection the shift, Δz , is given by:

$$\Delta z = \Delta y \theta \quad (4.3)$$

Where: Δy = the misfocus of the imaging system

Although the interferometer could be initially focused to within $60 \mu\text{m}$, the focal spot of the main laser was observed to drift $200 - 300 \mu\text{m}$ over the course of a day's data collection. In addition the focal spot was observed to shift by up to $300 \mu\text{m}$ on subsequent days owing to realignment of the laser. The imaging system sometimes had

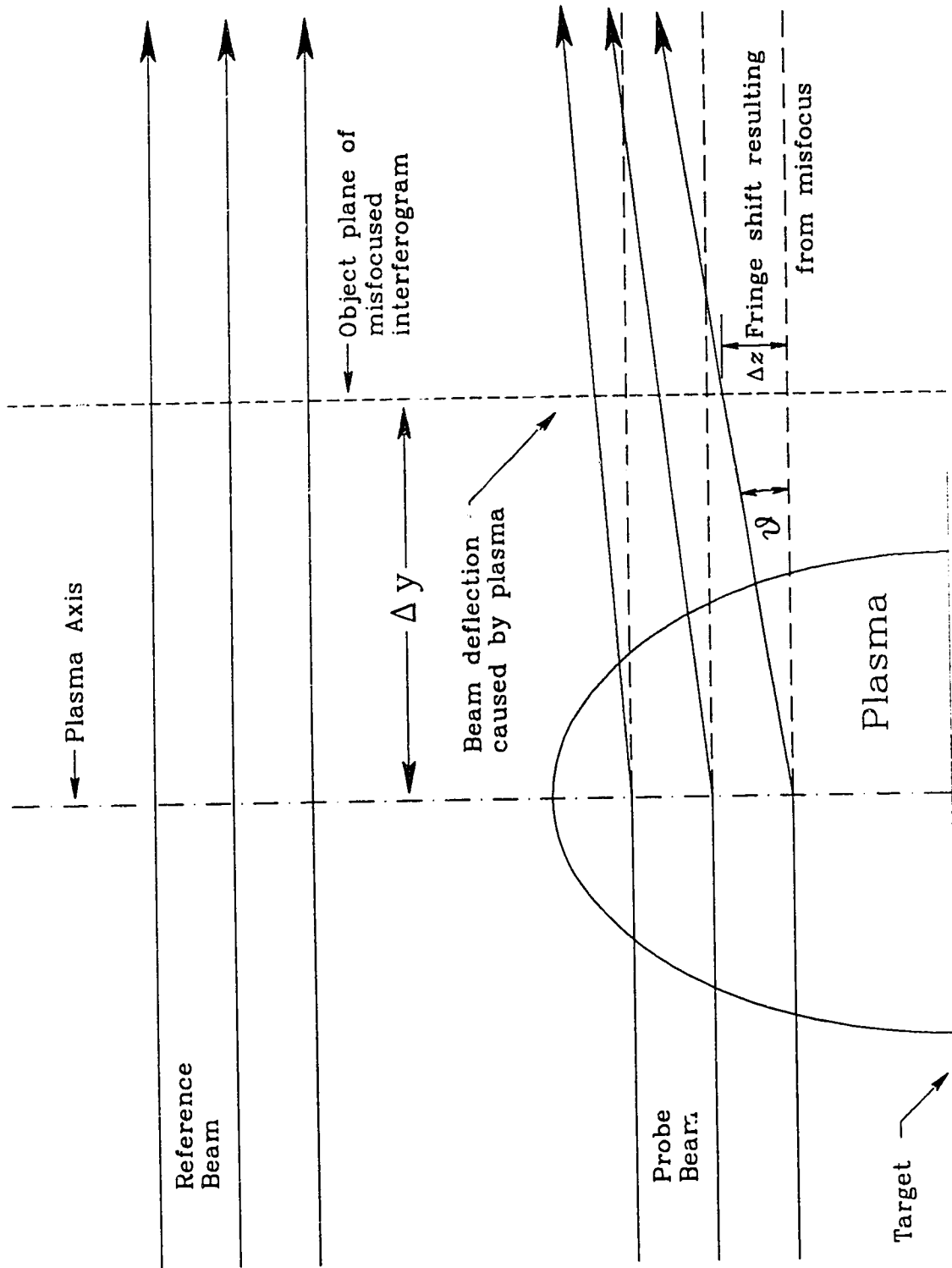


Fig. 4.7. Effect of interferometer misfocus.

to go 2 days without refocusing. With these considerations an average error of $300 \mu\text{m}$ was assumed for this experiment. For this amount of misfocus and an f number of 16 as used in this experiment one arrives at a maximum value for Δz of $19 \mu\text{m}$. This is the maximum amount of error and would only apply to the most dense visible regions of the plasma.

There are a few other sources of error which should be considered. As the plasma is probed with a beam whose path is parallel to the target surface any misalignment of the target will cause shadowing of the probe beam and an error in the determination of the surface of the target in the deconvolution. As the data was obtained by focusing the main laser approximately in the center of an eighth inch thick target which was aligned to within 10 mRad the maximum error in determining the target surface is about $16 \mu\text{m}$. This should be kept in mind when examining the absolute expansion of the profiles but makes no difference to the derived scale-lengths.

Any deviation of the plasma from being axially symmetric will provide another source of error. This error must be evaluated shot by shot. The result of inverting a non symmetric plasma is essentially to find a symmetric average of what is present with the total integrated number of electrons remaining essentially constant.

4.7 Lateral Expansion

The lateral expansion of the plasma at late times appears to be inhibited, forming the expansion cone which is visible in the interferograms and in the contour plots of electron density. The expansion cone appears to originate as a small discontinuity in density very close to the target surface outside of the main focal spot. The feature develops following the end of heating by the laser pulse and is observed to expand out from the target surface and laterally away from the plasma axis forming a cone which includes an angle of about 60 deg. It appears to develop as a surface of discontinuity which acquires thickness as it expands. This feature has been observed in previous laser plasma experiments [53].

Fig. 4.8 shows the method used to measure the diameter of the expansion cone. First lines are drawn tangent to the contours in the manner depicted in the figure (1). Then the angle formed by the tangents is bisected and the bisector is projected back to the target surface (2). The results using this technique are very reproducible and are approximately equivalent to finding the intersection with the target surface of a curve through the center of the thickness of the cone.

Fig. 4.9 shows the diameter of the expansion cone at the target surface as a function of time with error bars representing the accuracy of the measurement technique. Data from the July 20/88 shots is offset from the other

SHOT # 22078821
 ENERGY = 840 mJ
 FWHM = 2.0 ns
 TIME = 5.2 ns

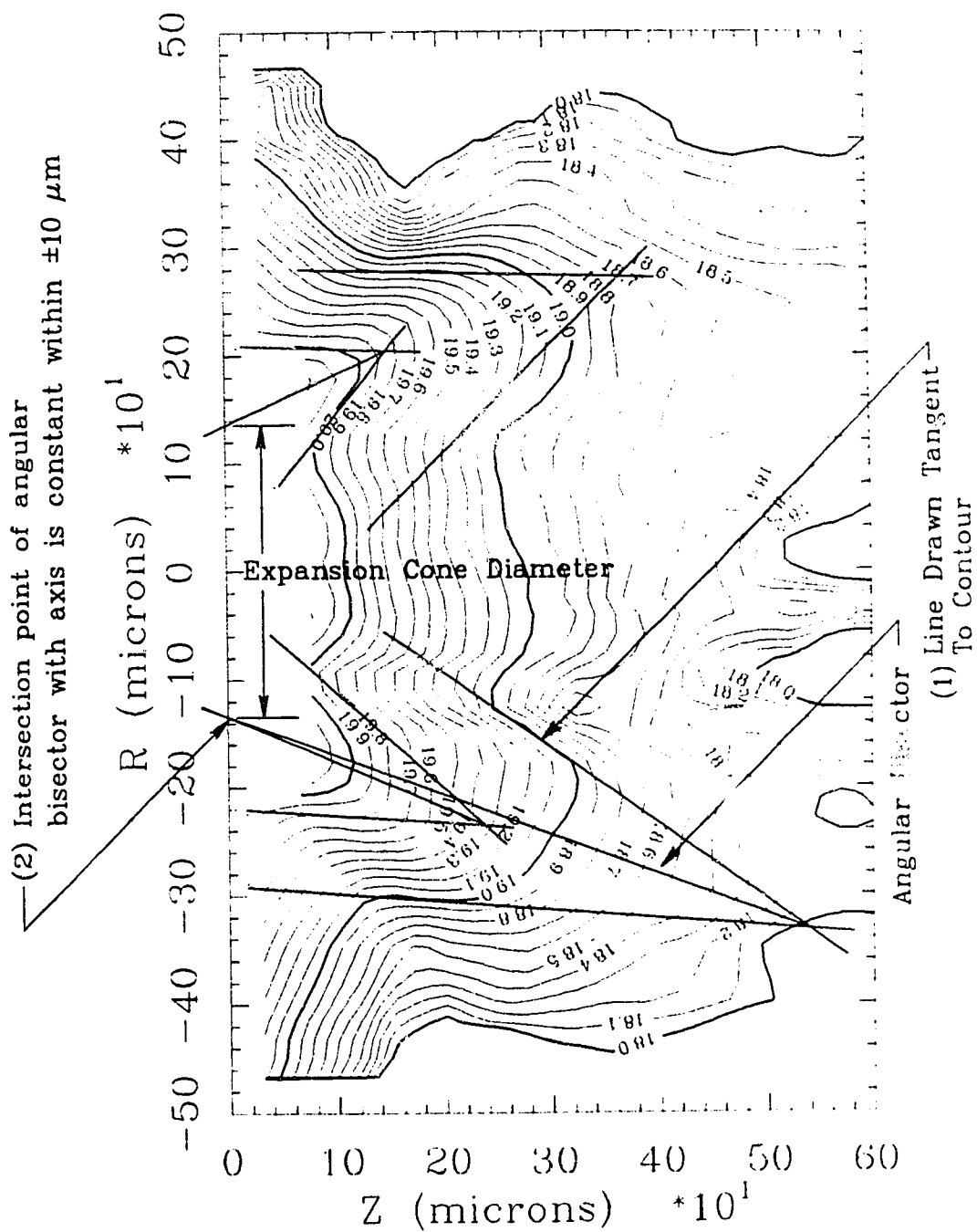


Fig. 4.8. Method of determining diameter of expansion cone.

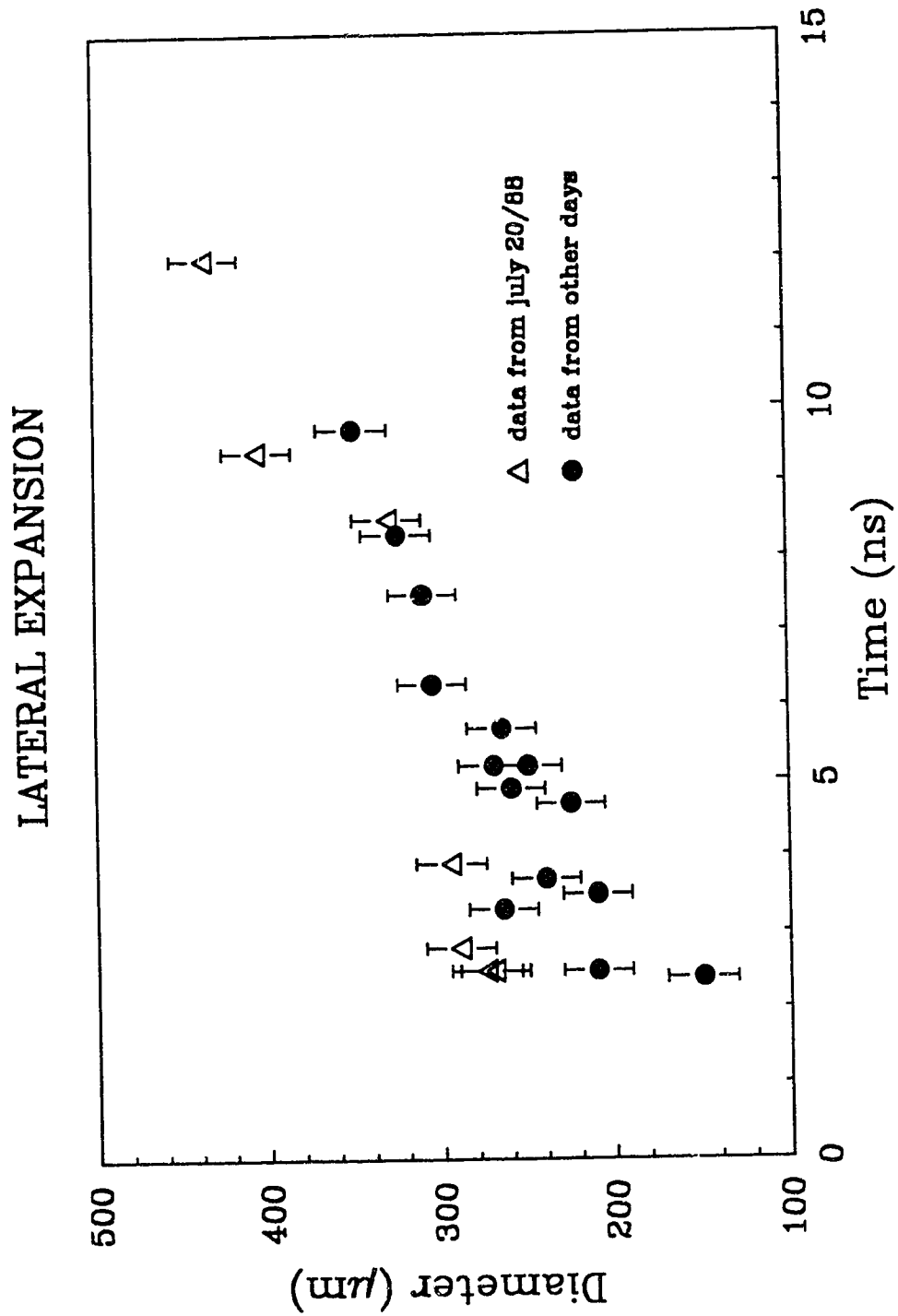


Fig. 4.9. Measured diameter of the expansion cone at the target surface as a function of time.

data although the rate of growth is approximately the same. This may indicate that the focal spot was larger on this day. The rate of change of the diameter of the expansion cone was determined by least square fit and found to be about 2×10^6 cm/s.

The discussion in chapter 5 will examine the possibility that the expansion cone indicates the presence of a large toroidal magnetic field which traps the late time cooling plasma.

CHAPTER 5

DISCUSSION

This chapter will compare the results of the experiment to different analytic and numerical laser plasma models. The goal is to provide a consistent description of the results leading to an understanding of the dominant processes involved in the plasmas evolution. The discussion centers on the time development of the axial scale-length of the plasma but will conclude with a brief discussion of additional axial and conical features also observed within the plasma.

Fig. 5.1 shows the measurements of the axial scale length obtained from the experiment plotted against time and divided into three energy bands which will be referred to as low, medium and high energy. Low energy is from 190 mJ to 300 mJ, medium energy is from 300 mJ to 800 mJ and high energy is from 800 mJ to 1650 mJ. The graph includes a plot of the time dependence of the laser power of a typical laser pulse. The power is shown in arbitrary units and is given here to provide a visual timing reference. The discussion here will show that the plasma's time development is divided into three main regimes.

The first regime is the initial expansion of the plasma and lasts approximately one nanosecond from the onset of the main laser pulse, up to 0.6 ns on the graph. In this regime the plasma on axis is characterized by an approximately planar expansion. This regime of plasma flow

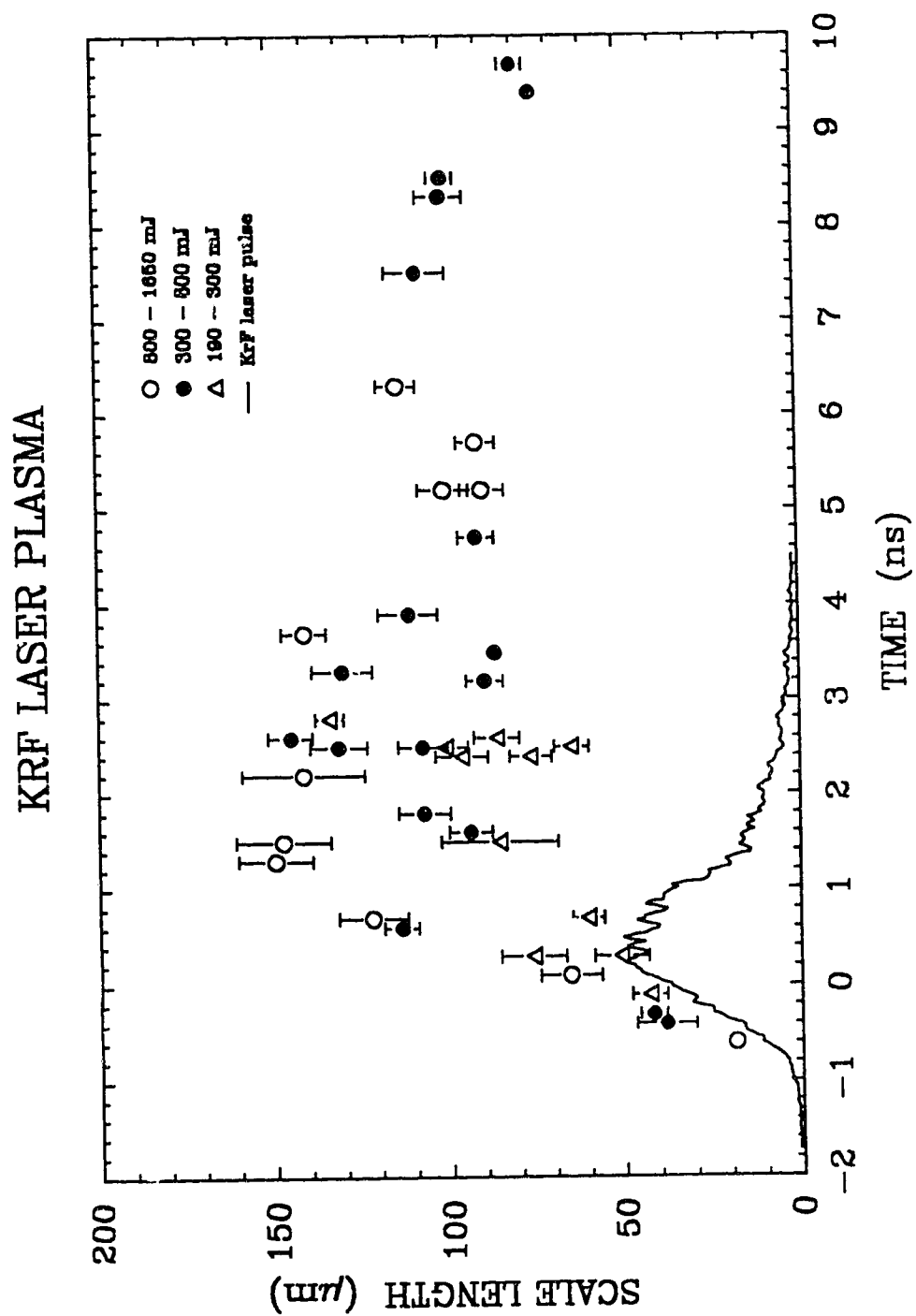


Fig. 5.1. Experimentally measured scale-lengths for KrF laser produced Aluminum plasma.

is examined using the self-regulating model of planar expansion, a Medusa 1D planar expansion simulation and two Castor 2D simulations.

The next region extends from 0.6 ns to around 4.0 ns and is characterized by a stationary spherical plasma flow.

The time 4.0 ns corresponds closely with the absolute turn off of the laser energy and in the final region from 4.0 ns onward the plasma flow begins to collapse as the target cools.

5.1 Spherical Smoothing of Data Points

All of the low and medium energy shots analyzed exhibited smooth plasma profiles for which the scale-length on axis was representative of the average scale-length of the plasma. However, three of the high energy shots over the time period 0.6 ns to 2.2 ns (shots 14108802, 14108805 and 14108808) exhibited a high density jet of plasma on axis. For the purpose of the analysis here, which will compare the scale-length data in this time regime to spherically symmetric models, the scale-lengths for these three points were taken from an average of the axial scale-length with those at an angle of $\pi/8$ on each side of axis. This gives an average scale-length over a cone angle of $\pi/4$ centered on the axis giving values which are more suitable for comparing to spherical expansion theory.

Fig. 5.2 shows a contour plot depicting the axial plasma jet for shot 14108808. Lines are drawn showing the

SHOT # 14108808
ENERGY = 1154 mJ
FWHM = 1.7 ns
TIME = 1.5 ns

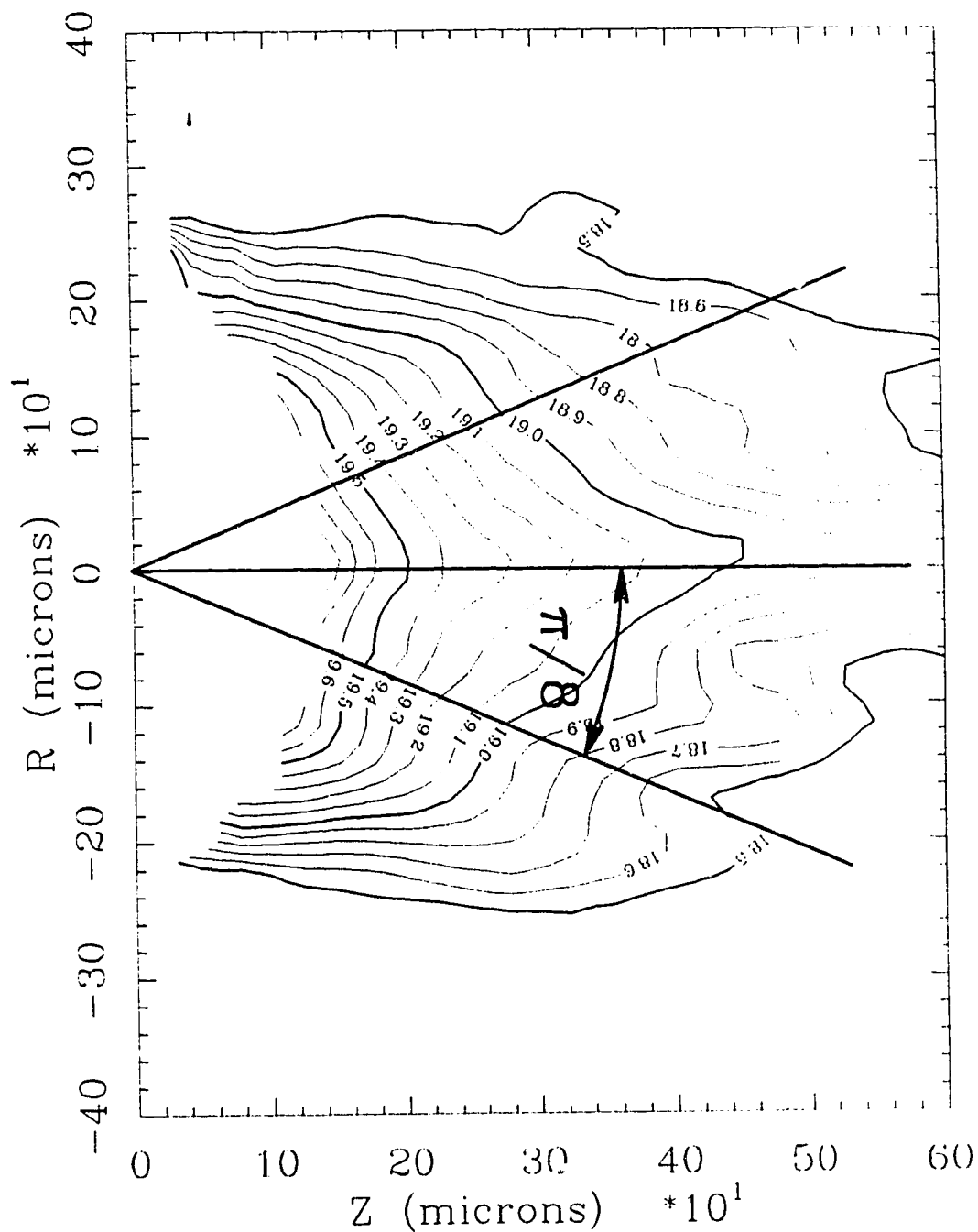


Fig. 5.2. Contour plot of axial jet for shot 14108808.

The plot shows radial cuts used to obtain
the averaged scale-lengths.

position of the three averaged lineouts. Fig. 5.3 compares the averaged scale-lengths which are used in the subsequent discussion in this chapter to the axial scale-length for these three shots.

5.2 Main Laser Pulse Shape

Modeling of laser plasma first requires a model of the spatial and temporal distribution of the laser energy. Fig. 5.4 shows a streak trace giving the temporal distribution of a typical main laser pulse. The pulse features a sharp rise in pulse intensity followed by a curved decay which leads into a long tail. This gives a pulse which in this case has a total pulse length on the base of about 4.6 ns while having a FWHM of 1.6 ns. Most of the pulses adhere to this shape having widths ranging from 1.4 ns to about 2.0 ns, with 1.6 ns being the most representative value. The few pulses analyzed which were longer than 2.0 ns had slightly longer rise and fall times. Spatially the laser pulse is modeled as a Gaussian radial profile with 70 % of the energy within a 35 μm diameter focal spot.

In the interest of simplicity the modeling was done with one of two pulses having a triangular profile which may be defined by their FWHM and the rise-time of their leading edge as shown in Fig. 5.4. Both had a FWHM of 1.5 ns. The first with a rise time of 0.6 ns was used in the numerical simulations and some of the self-regulating model calculations. A second having a rise-time of 1.2 ns,

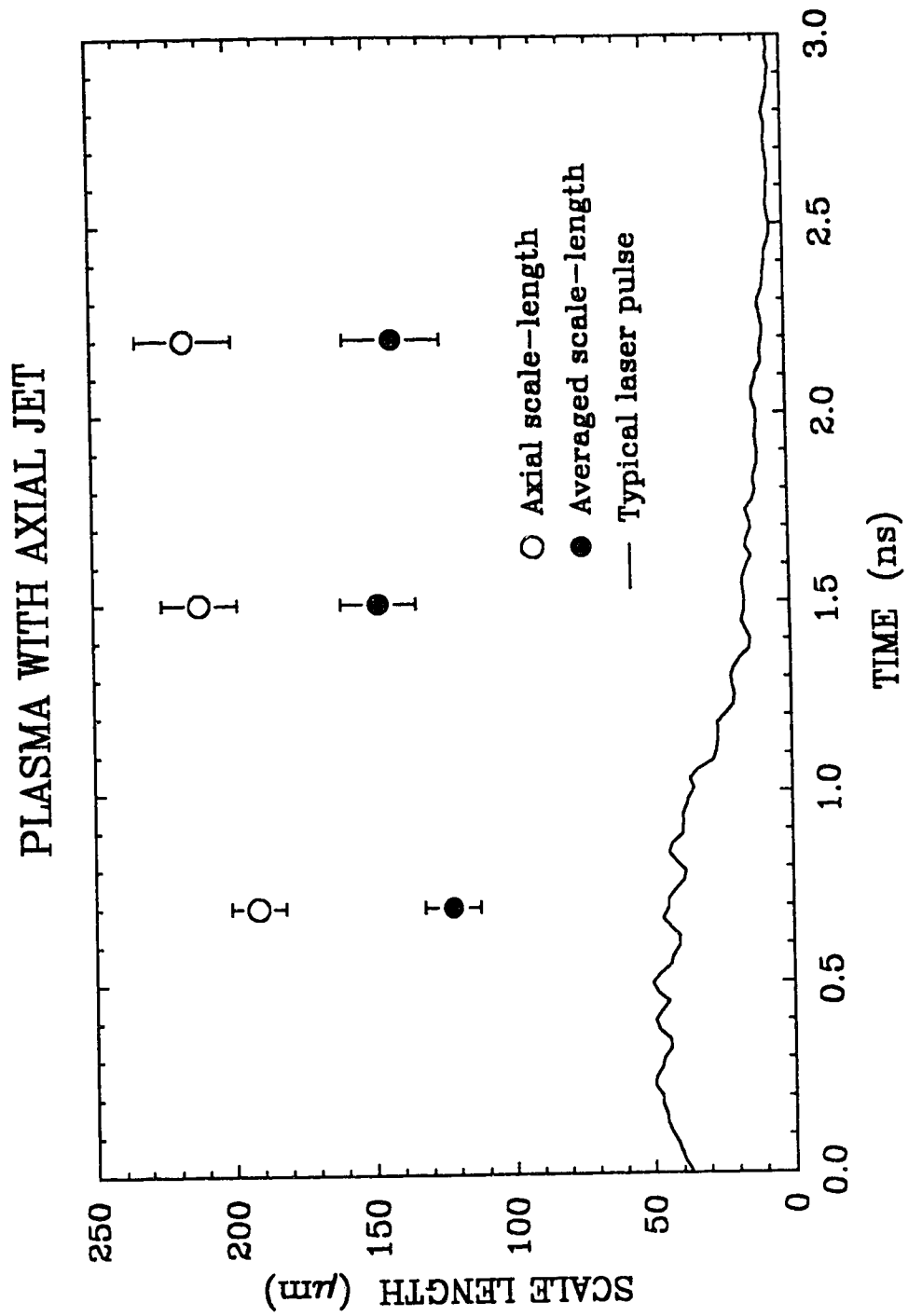


Fig. 5.3. Comparison of axial scale-lengths to averaged scale-lengths.

KRF TEMPORAL PULSE SHAPE

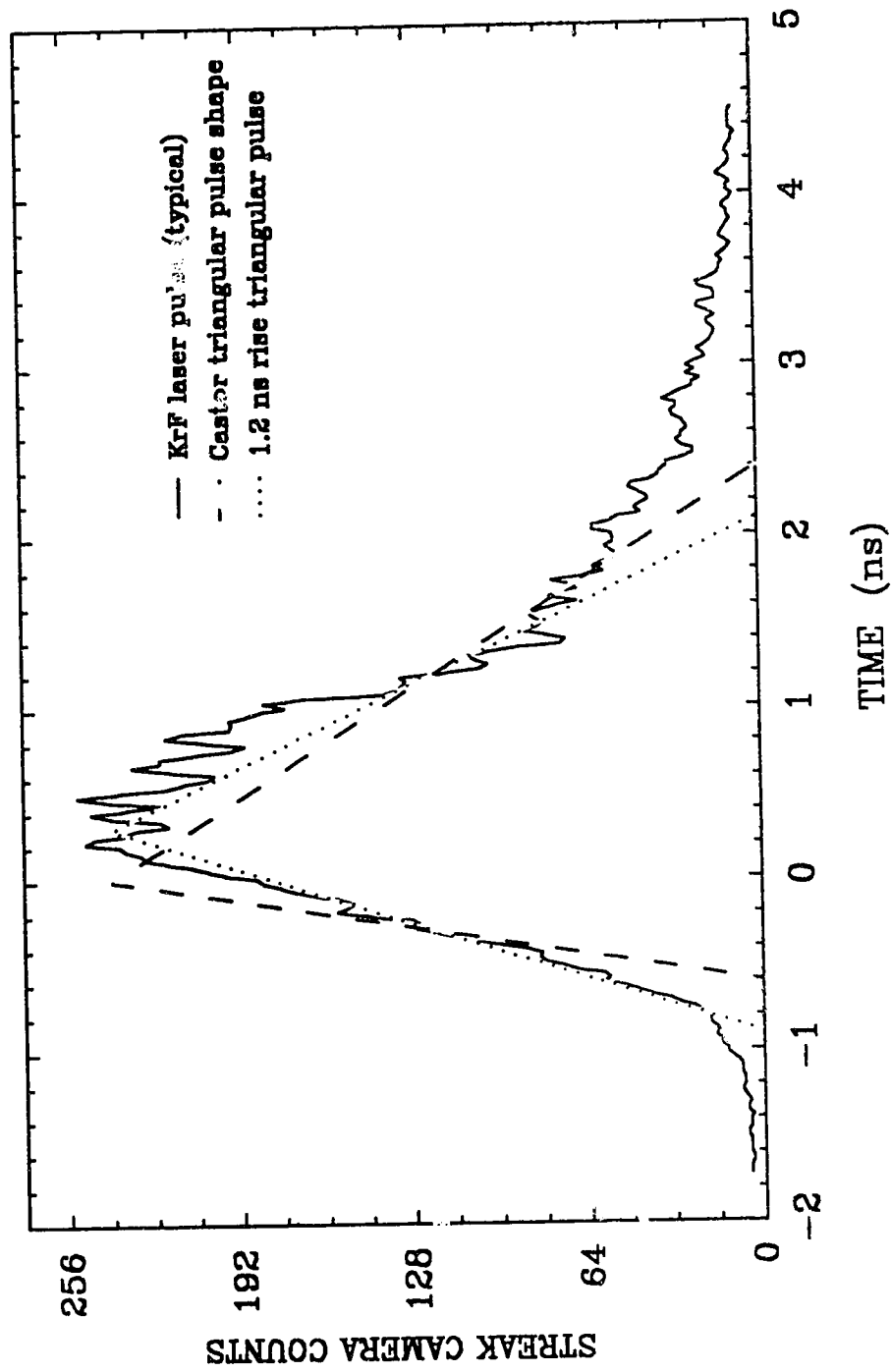


Fig. 5.4. Typical main laser pulse.

considered to be a better representation of the actual pulse, was used for some of the self regulating model calculations. Simple triangular pulses do not do a good job of representing the tail of the real pulse which still contains a significant amount of laser energy and slows down the decay of the plasma after the main part of the pulse.

In order to keep the timing consistent with that of the data all laser pulses used in this discussion have the half maximum point in their rise set at -0.3 ns.

5.3 Castor 2D Simulation

This thesis compares with two available Castor simulations of laser irradiation of a planar aluminum target, Run:A11 which has a total laser energy of 1.0 J and run:A17 with an energy of 0.1 J. These simulation runs were carried out by Drs. Capjack and Rankin and were primarily designed to model features of the ion expansion and recombination of the plasma in support of another experimental investigation. The simulation used a triangular pulse with a rise time of 0.6 ns. The focal spot used in the simulations had 70 % of its energy inside a diameter of 70 μm which is twice that of the focal spot used for this experiment. The front surface of the target in the simulation is not a hard discontinuity but a smooth density profile having an initial scale-length of about 4 μm . The exact position of the front face of the target is

therefore to a small degree arbitrary.

The simulation reproduces many but not all of the features of the experimental plasma. In particular, the simulation does not reproduce the expansion cone observed at late time in the experimental plasma, possibly due to magnetic effects not being included in the simulation. Fig. 5.5 compares electron density contour plots from Castor and the experiment. The plots represent similar stages in the plasma development but as the laser pulse used in the experiment is not identical to that used in the simulation time cannot be compared exactly.

Fig. 5.6 shows the axial scale-lengths obtained from the two simulations. The simulation reproduces the general features of the data in particular the leveling off of the scale-length after approximately 1.0 ns. The simulation also illustrates the correlation between the scale-length and the laser energy, higher energies having generally longer scale-lengths at a given time. However, the simulation lags the observed plasma expansion by ~ 0.4 ns which is related to the overly steep rise time.

The large fluctuation in the scale-length of run:All as the laser turns off at 2.4 ns is caused by the collapse of the plasma and is partially an artifact of the method of measuring scale-length used in this work. Fig. 5.7 shows the sequence of the electron density profiles as the plasma collapses for run:All. Marked on the plot is the range over which scale-length was measured. The collapse starts near

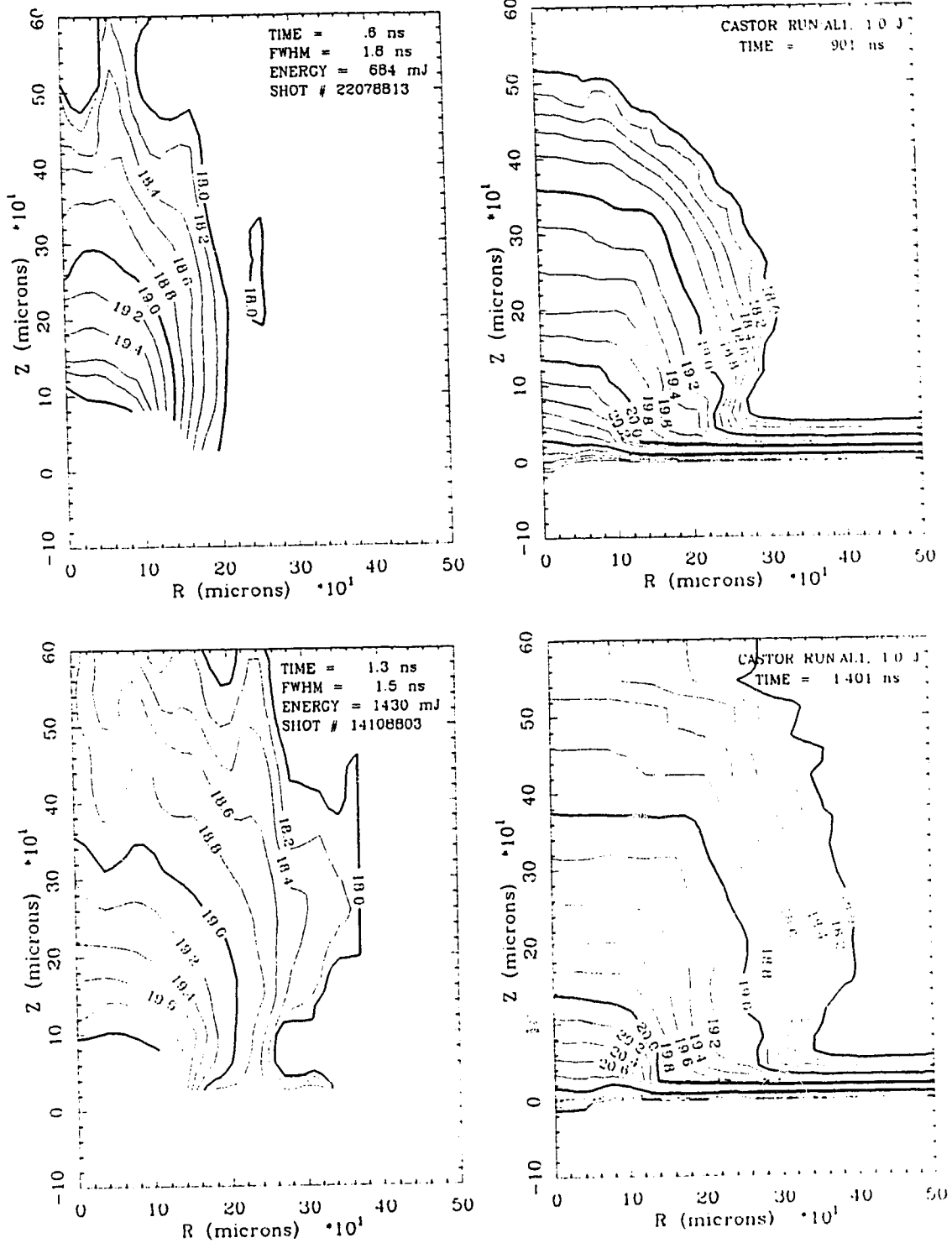


Fig. 5.5. Contour plots from data and Castor simulation:
 R and Z represent radial and axial dimensions,
 contours are \log_{10} of electron density (cm^{-3}).

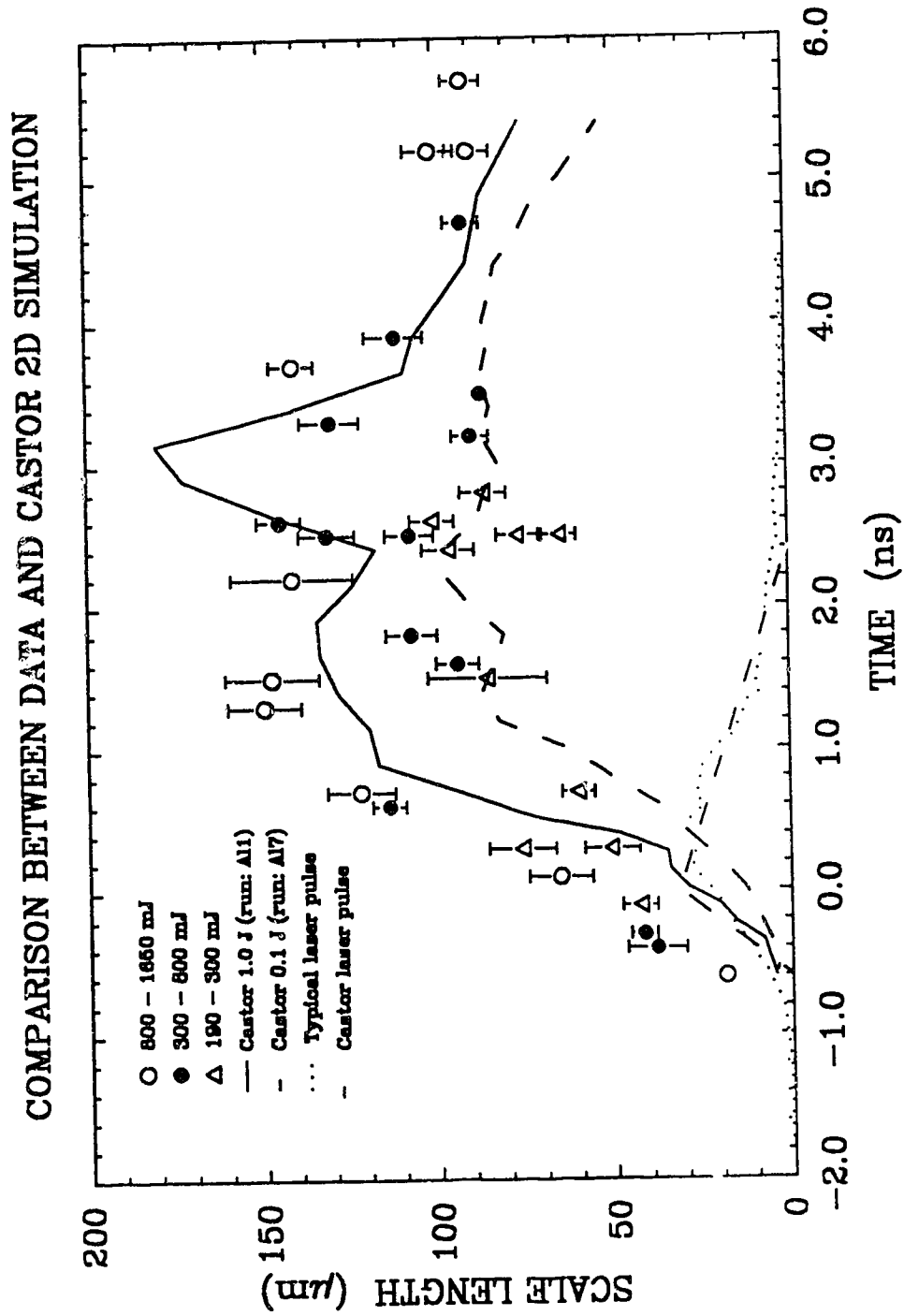


Fig. 5.6. Comparison of axial scale-length from the experimental data and Castor simulations.

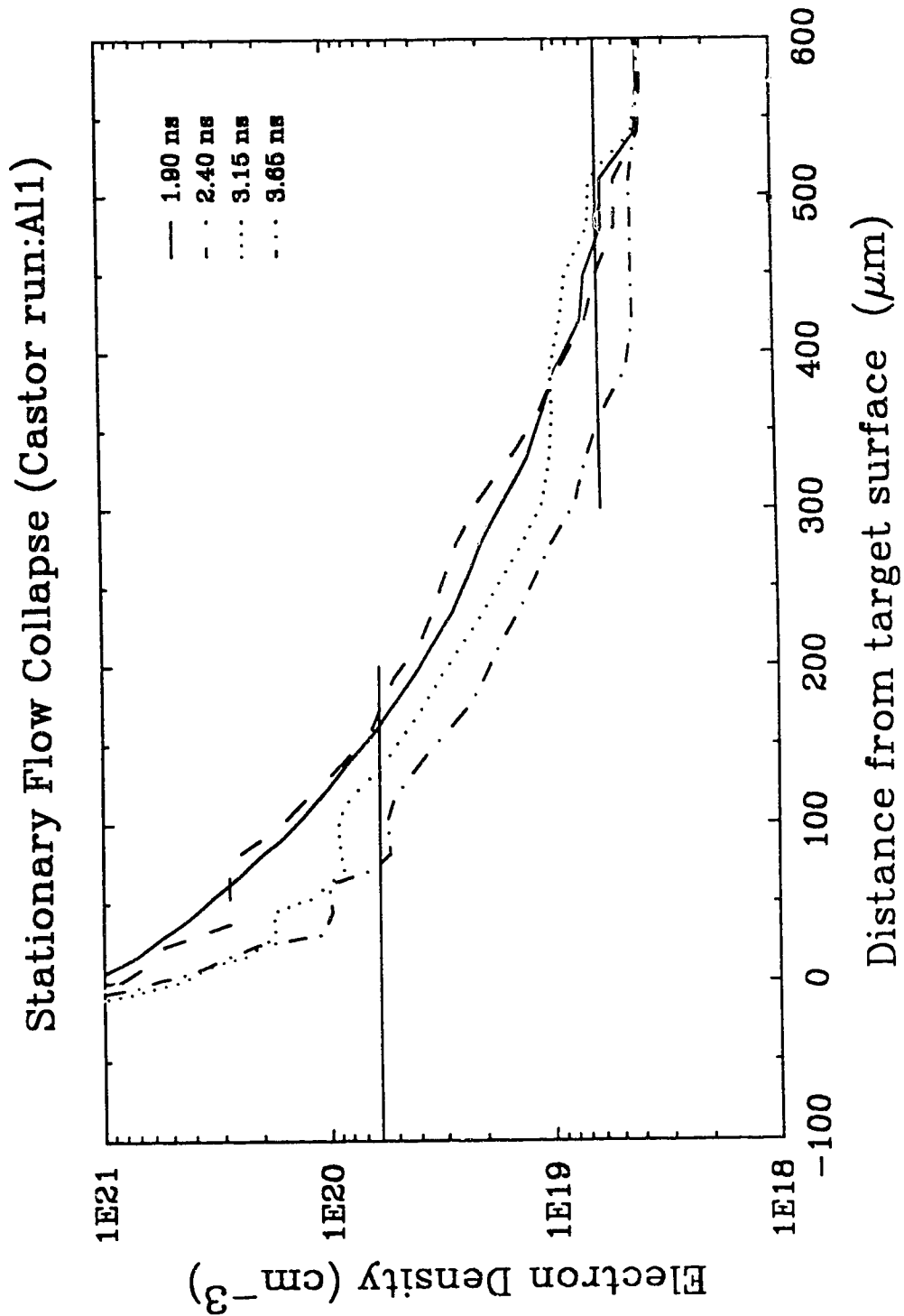


Fig. 5.7. Instability in the collapse of the density profile for the Castor 1 J simulation.

the target surface and progresses outward. The measurement technique manages to just catch a low density foot at 3.15 ns leading to a large scale-length. The low energy run:Al7 (0.1 J) exhibits a much smoother collapse, an interesting point in itself as it relates to the question of plasma instability at higher irradiances.

5.4 Initial Plasma Expansion

As the laser focal spot is not a point, the initial expansion of the plasma is expected to be planar except near its edge. Until the plasma expands outwards perpendicular to the target to a distance equivalent to its lateral radius at the target surface, it should be reasonably described by planar expansion models. This radius will initially be the focal spot of the laser system used in the experiment which is nominally $17.5 \mu\text{m}$. However, the plasma is also expected to expand laterally as well as outwards as time progresses. Because of this lateral expansion the plasma cannot be completely described by one-dimensional model.

The earliest and consequently smallest plasmas able to cause a discernible fringe shift in the interferograms occur at -0.6 ns and have a scale-length of about $20 \mu\text{m}$. The diameter of the earliest observed plasma is $70 \mu\text{m}$ or twice the focal spot diameter. This early expansion diameter is consistent with the result of the Castor simulation which uses a laser focal spot diameter of $70 \mu\text{m}$

and indicates that the initial plasma expansion with comparable electron density to that detectable in this experiment has a diameter of about 140 μm .

The large size of the initial expansion can be understood with the realization that the heat conductivity of a hot plasma is very high and that the low intensity wings of the laser spot are still intense enough to ionize a large surrounding region of the target surface. Because of the high heat conductivity heat is transported to the edge of a plasma quickly even at very low electron densities causing the diameter of the plasma to increase from a very early point in its evolution. Fig. 5.8 plots the radius of the plasma for medium and high energy laser shots during the early stages of its development. The edge of the plasma radius is defined as the point where the fringe shift becomes essentially zero (electron density approximately $1 \times 10^{18} \text{cm}^{-3}$) The error bars represent the accuracy with which the radius could be measured from the interferograms. The plot indicates a linear expansion with a rate of growth of $7.2 \times 10^6 \text{cm s}^{-1}$ which should coincide approximately with the ion acoustic velocity at the plasma edge.

It is important to note that due to the high conductivity, lateral growth of the plasma is not inconsistent with planar flow. The target is ablated everywhere within the radius of the plasma as if the spot size of the laser was increasing with time and the dominant

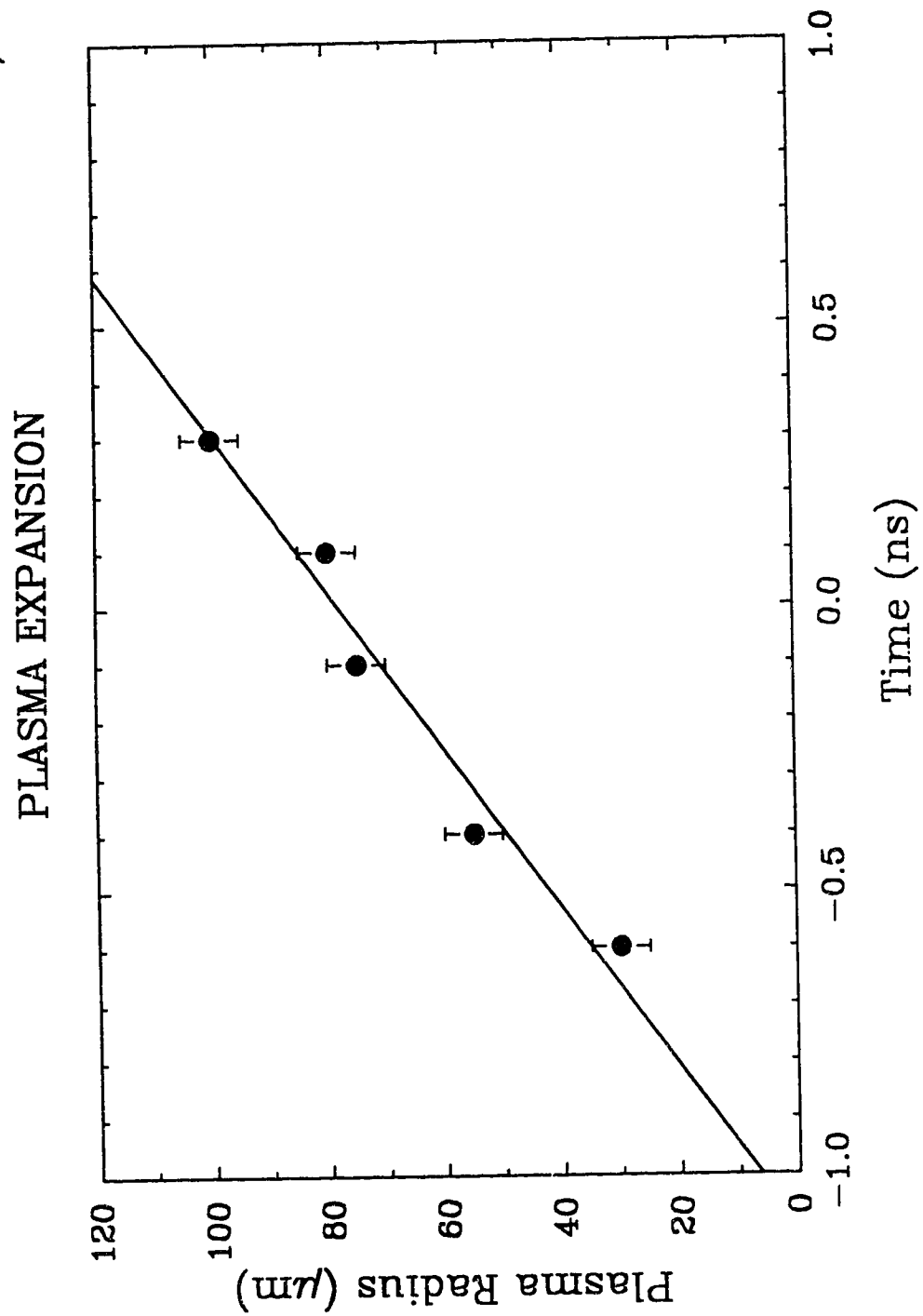


Fig. 5.8. Measured lateral growth in radius of early-time laser plasma for medium and high energy shots.

flow excluding the laterally moving edge may still be planar. The actual flow geometry is controlled by the overall shape of the plasma with lateral growth acting to maintain planar flow longer than would be otherwise expected.

The increasing radius of the plasma may be thought of as giving an effective focal spot. An understanding of the plasma in this time regime depends on both the actual intensity of the laser as determined by the actual focal spot and an effective intensity which is defined using the plasma radius as an effective focal spot radius.

5.4.a Self-similar expansion of the plasma

The initial expansion of the plasma may be analyzed using the simple isothermal self-similar expansion model. According to the model the scale-length of the plasma is given by the expression $L = c_s t$. By measuring the slope of the rise in the plasma scale-length one may determine a value of c_s and hence the average electron temperature of the expanding plasma. A least square fit to the medium and high energy data up to $t = 0.7$ ns, over which time the data exhibits an approximately linear increase in scale-length with time, gives a value for c_s of $7.8 \times 10^6 \pm .4 \times 10^6$ cm s⁻¹.

The average ionization, Z , as a function of electron temperature and density can be obtained using a collisional-radiative model for aluminum [76]. The model

gives an ionization which varies from 9.04 at 100 eV and $n_e = 1 \times 10^{18} \text{ cm}^{-3}$ to 10.98 at 316 eV and $n_e = 1 \times 10^{21} \text{ cm}^{-3}$. As Z varies only slightly over this range it was generally assumed to have a constant value of 10.0 in the calculations carried out in the analysis. Using this value an electron temperature corresponding to self-similar plasma expansion of $171 \pm 17 \text{ eV}$ is obtained from the self-similar expansion velocity above.

5.4.b Plasma temperature

Plasma temperature can be determined by experimentally measuring the ratios of x-rays transmitted through foils of different thickness. Temperatures measured by another student during the course of this experiment ranged from approximately 250 to 430 eV for laser energies of 350 to 750 mJ on target [77]. These temperatures agree well with the intensity scaling measured previously [15]. The temperature measurements indicate a temperature for a 1 J laser pulse of 450 - 500 eV which is much higher than indicated by the expansion profile. This apparent discrepancy is explained by the fact that the foil filter temperature measurement technique measures the maximum temperature which occurs at the laser focus while the plasma hydrodynamics depends more on the average plasma temperature over the effective plasma radius.

Temperature distribution profiles of the Castor 1 J simulation, run:All, are shown in Fig. 5.9 (a) and (b). The

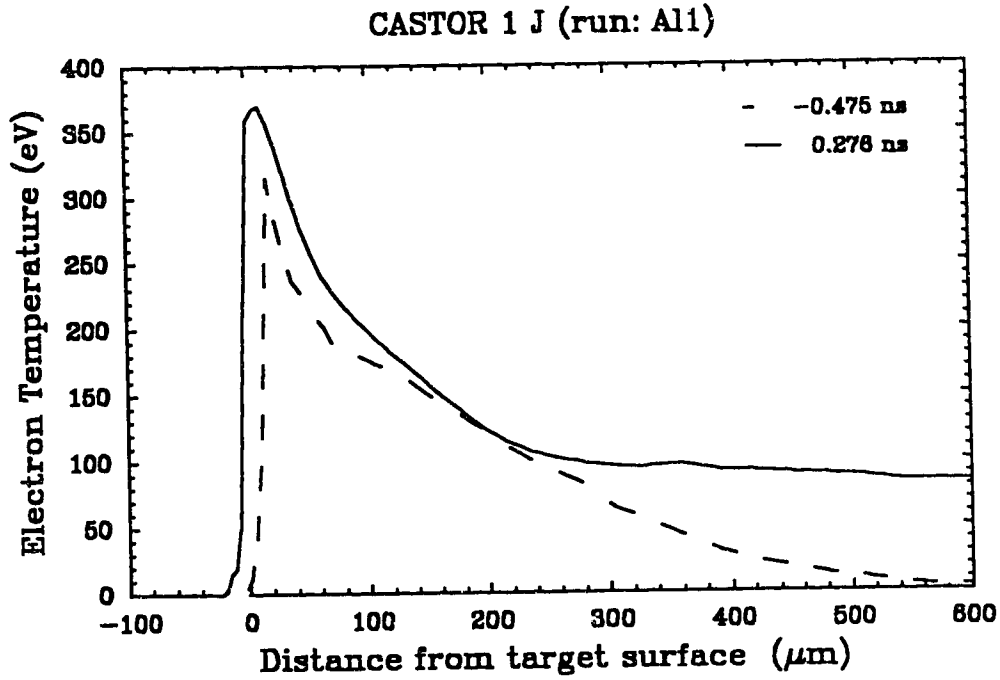


Fig. 5.9 (a). Axial temperature distribution for
Castor 1 J simulation.

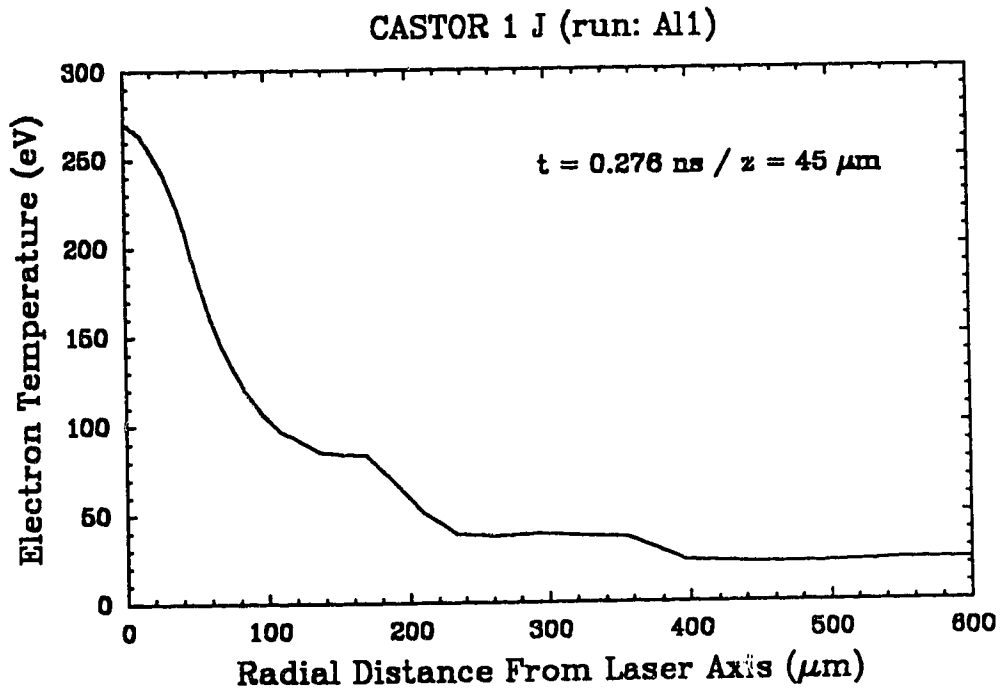


Fig. 5.9 (b). Radial temperature profile at $t = 0.376 \text{ ns}$
and $z = 45 \text{ microns}$ from the target surface.

temperature profile very quickly takes the shape shown for time 0.276 ns which corresponds to the simulation's peak temperature. The maximum temperature at the laser focus is 370 eV which coincides very closely with the temperature given by the published scaling law at the same intensity ($2 \times 10^{13} \text{ W cm}^{-2}$). The figure also shows a radial temperature profile 45 μm in front of the initial target surface. The overall average temperature of plasma over the effective plasma radius would be closer to 200 eV which is more consistent with the measured axial expansion of the plasma.

5.4.c Medusa 1D simulation

Fig. 5.10 shows the results of the medusa simulation carried out with a laser intensity as a function of time equal to the axial intensity used in Castor run:All ($2 \times 10^{13} \text{ W cm}^{-2}$ at the peak of the pulse). It is plotted along with the result from the self-regulating model carried out with the same intensity profile. This plot shows that the coronal scale-lengths obtained from the Medusa simulation are similar to those obtained from the analytic calculation. Although the laser pulse in both cases begins at -0.6 ns the development of the plasma in Medusa falls behind that of the self-regulating model by - 0.15 ns very early in the plasma's development. This may be a result of the self-regulating model not taking into account the initial ionization energy of the plasma.

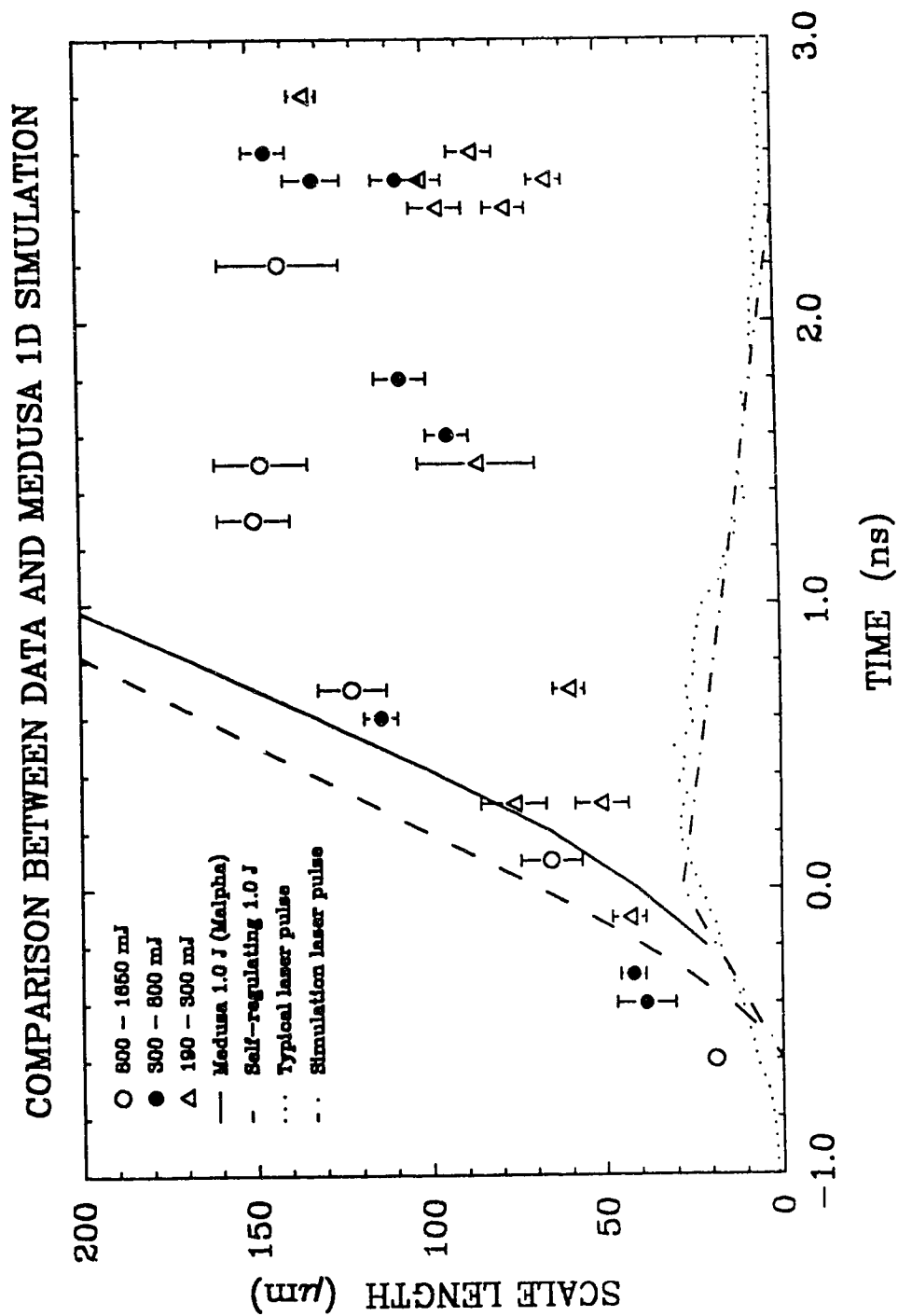


Fig. 5.10. Scale-length from Medusa 1 J simulation and comparable self-regulating model calculation.

The intensity used in the calculations is equivalent to the axial intensity obtained from the main laser when the pulse energy is 250 mJ. While the calculations give an approximately linear rise in the scale-length the slope of the rise is much steeper than in the experiment indicating that the overall temperature of the simulated plasma is too high even compared to the high energy data. This is probably a result of the 1D models not taking into account the increase in the lateral effective size of the plasma which consequently reduces the average plasma temperature.

5.4.d Self-regulating model with lateral expansion

In order to estimate the effect of the lateral expansion the self-regulating model was recalculated by replacing the actual laser intensity with an effective intensity obtained by dividing the laser power by the effective radius of the plasma. While not strictly valid this model allows one to take into account the lateral growth of the plasma and use the energy balancing feature of the self-regulating model.

Fig. 5.11 shows the result of the self-regulating model calculated using the effective laser intensity. The laser power was given by the triangular pulse shape with 1.2 ns rise time. The intensity at a given time was calculated by dividing the power by the area, πR^2 , with R given by $R_0 + \bar{c}_s \tau$, where \bar{c}_s is the expansion velocity measured from the interferograms, R_0 is the first measured radius (35 μm)

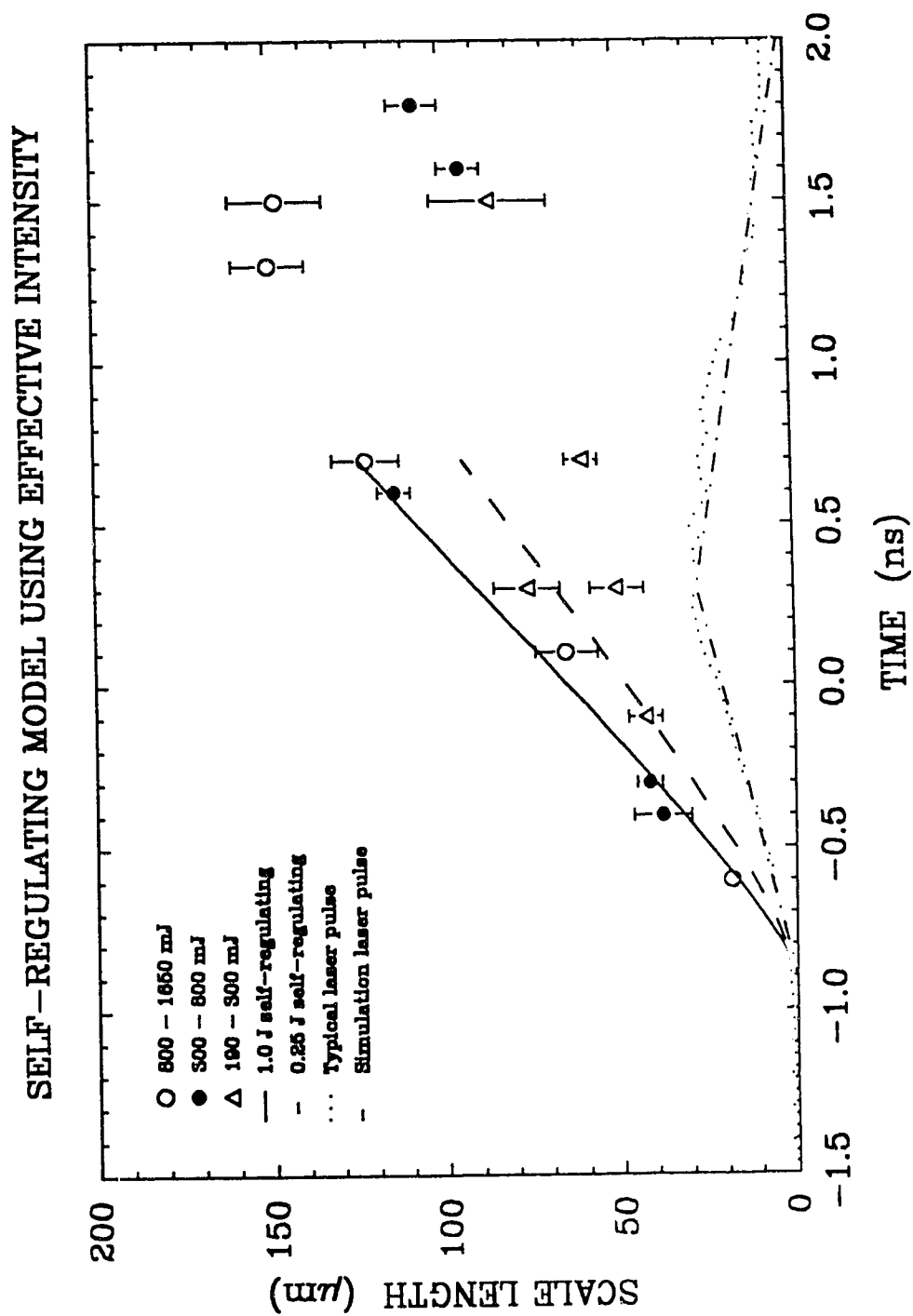


Fig. 5.11. Self-regulating model using an effective intensity based on the actual plasma diameter.

of the plasma and $\tau = t + 0.9$ ns. This model predicts a rise of the scale-length whose slope agrees closely with the medium and high energy data.

The model predicts an electron temperature and hence ion acoustic velocity, c_s , which increases with time reaching a value at the end of the planar expansion phase (0.6 ns) of about 180 eV for a 1.0 J laser pulse. However as c_s depends on the square root of the temperature it quickly reaches a fairly constant value. After the first 0.3 ns of the expansion, corresponding to the range over which the lateral expansion velocity of the plasma was measured c_s varies from 6.14×10^6 cm s⁻¹ to 7.56×10^6 cm s⁻¹. The average value of c_s is 7.0×10^6 cm s⁻¹ which corresponds closely to the measured lateral expansion velocity of the plasma.

It is noted that when making a calculation at any point in time the self-regulating model used here assumes implicitly in its derivation that the intensity has been constant and the calculation is carried out with an average intensity based on the energy absorbed up to that point. This makes the calculation particularly appropriate for modeling the plasma produced in this experiment as the leading edge of the laser intensity profile keeps the effective intensity used in the calculation approximately constant.

Fig. 5.12 shows the previous result along with the Castor 1 J simulation. Only the medium and high energy

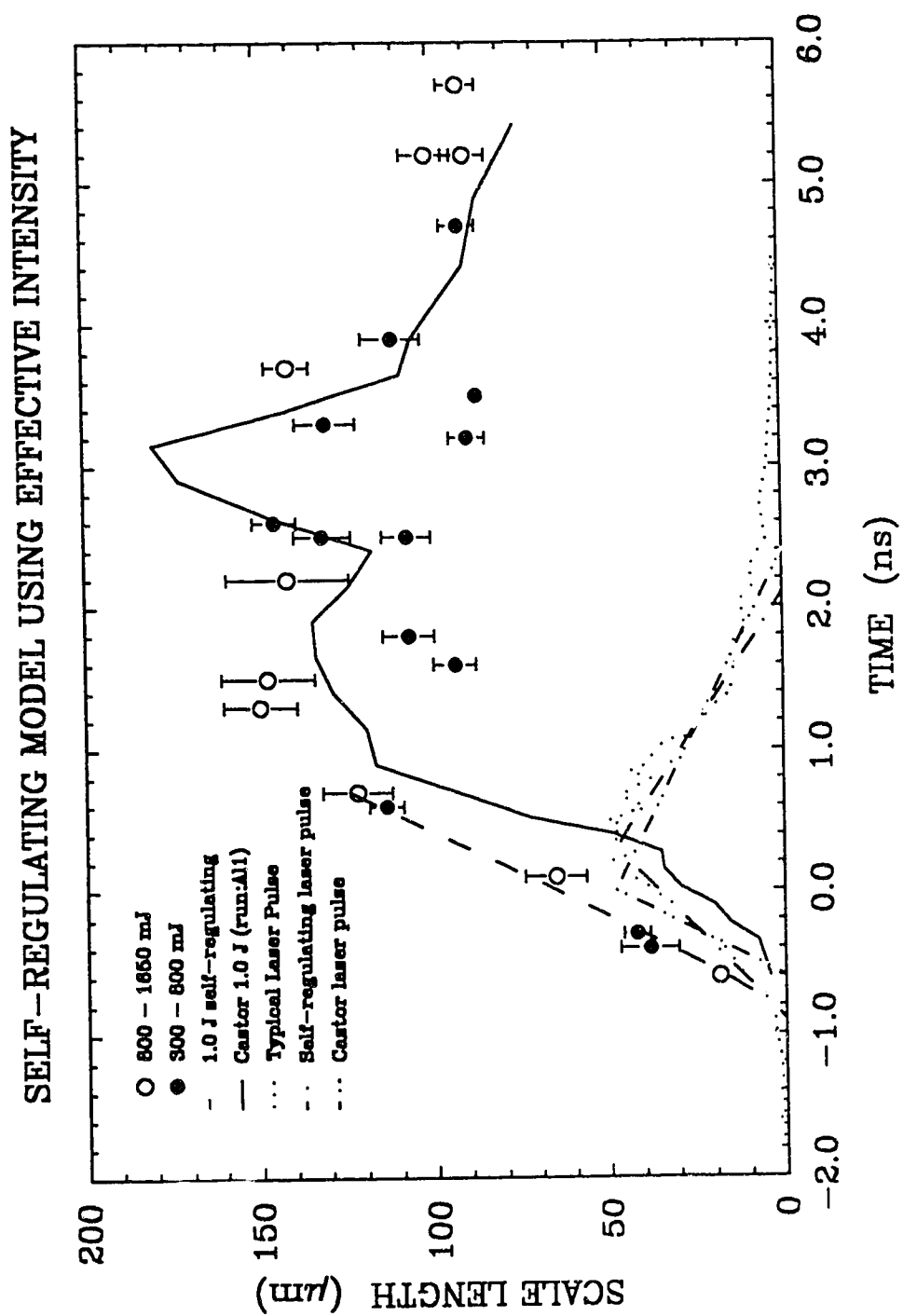


Fig. 5.12. Self-regulating model using effective intensity, Castor 1 J simulation, medium and high energy data points.

shots are shown for clarity. The initial rise of the Castor result may now be seen to be fairly close to the data and to the predictions from the self-regulating model except for its starting point which is translated due to the different shape of the leading edge of the laser pulse. The large focal spot size used in the Castor simulation will only have an effect very early in the plasma development where it will result in lower effective laser intensity. As the plasma develops the faster rise time of the Castor laser pulse will tend to compensate for the initial focal spot size, the effect of which decreases as the plasma expands. As time progresses after the peak of the laser pulse the plasma should become less dependent on the initial laser spot size or the shape of the leading edge and depend more on the total energy deposited.

These comparisons suggest a theoretical model of the early expansion characterized by a planar self-similar expansion. The average temperature of the expansion may be calculated using the effective laser intensity as determined by the radius of the plasma. The radius is given initially by the focal spot size and is increased at a rate equal to the ion acoustic velocity. The actual energy is deposited in the center of the plasma to the laser's penetration depth giving a peak temperature fairly consistent with that calculated using the self-regulating model with the actual laser intensity.

5.4.e Transition from planar to spherical flow

The laser plasma expansion on axis should remain approximately planar in form as long as its forward expansion remains less than the lateral radius of the plasma. As the forward expansion approaches the lateral radius the plasma should make a smooth transition from planar to spherical flow with a corresponding roll over in the scale-length. Assuming that lateral expansion keeps up with forward expansion a limit on planar expansion may be set to where $c_s \tau \cong 2 D_f$, where D_f is the diameter of the laser focal spot. At this point the plasma has become essentially a hemisphere and a transition to spherical flow should have taken place.

5.5 Stationary Spherical Flow

Beginning at about 0.6 ns the experimentally measured axial scale-length levels off indicating that a stationary flow pattern has developed. The overall flow is expected by this time to be dominated by spherical hydrodynamics. The plasma in this region is modeled using the solution for stationary flow developed in section 2.2.d. Provided that $(1+2U)/2U \cong 1$, where U equals $\ln(n_0/n)$, the electron density is given by:

$$n_e = n_0 \left(\frac{r_0}{r} \right)^{(\alpha-1)} \quad (2.39)$$

where $\alpha = 3$ for spherical geometry. As n_0 is the electron

density at the solution boundary where the plasma flow is assumed to be sonic, it is equivalent to the absorption surface in the previous self-regulating model. The self-regulating model gives predictions for the density of the absorption surface of about $2 \times 10^{21} \text{ cm}^{-3}$ which is also in good agreement with Castor. As scale-lengths for this thesis were measured between $6 \times 10^{18} \text{ cm}^{-3}$ and $6 \times 10^{19} \text{ cm}^{-3}$ the approximation is well satisfied with $(2U+1)/2U \approx 1.1$.

As the stationary profile is not exponential it predicts a scale-length which is not constant but with a value depending on the position at which it is measured and is given by:

$$L = \frac{r}{(\alpha - 1)} \quad (5.1)$$

5.5.a Transition to stationary flow

Shown in Fig. 5.13 are three plasma density profiles which are considered to be representative of the transition from self-similar to stationary flow. The early time profile shows the characteristic profile of self-similar expansion. The negative curvature to the profile indicates that the plasma has a finite heat conductivity and thus the plasma is not completely isothermal but is hotter near the target surface. The late time profile shows the very characteristic shape observed in the later time data exhibiting a gentle curve with positive curvature

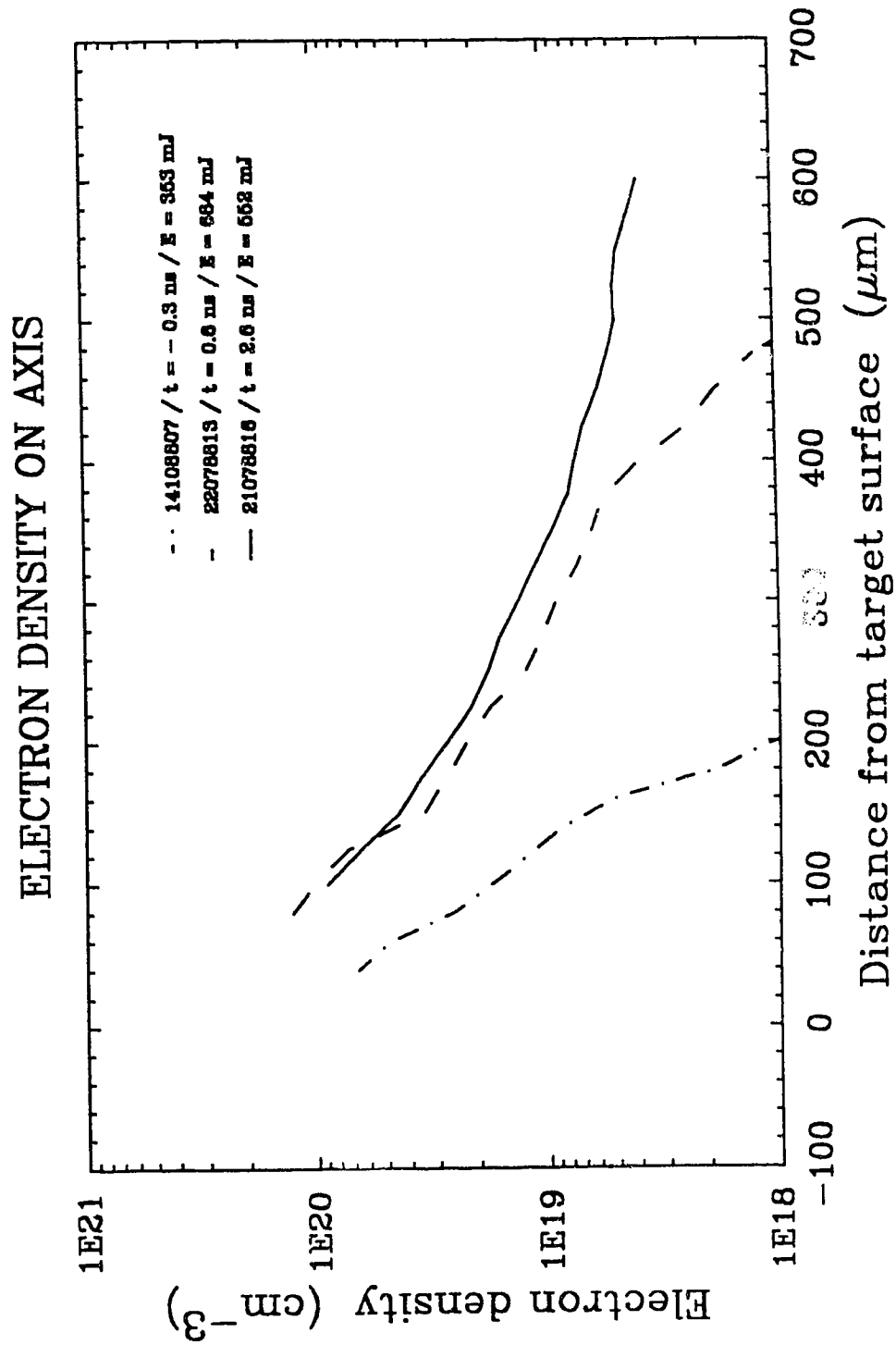


Fig. 5.13. Experimentally measured axial electron density profiles showing the transition from self-similar to stationary flow.

corresponding to the $1/r^2$ profile. At intermediate times a sharp transition from stationary flow near the target to self-similar flow far from the target is observed with a transition shelf like profile as shown in the figure. The transition between flow patterns progresses from the high density region towards lower densities.

This interpretation is supported by Castor which helps clarify the details. Fig. 5.14 shows plots of the axial electron density from Castor run:All before the transition. The corona, with its characteristic negative curvature, can be clearly seen expanding away from the target.

Fig. 5.15 (note different scales on plot axis) shows the transition from self-similar to stationary flow illustrating the progress of the transition point from the target surface outwards. At the absorption surface where the solution connects to the conduction zone of the plasma the stationary flow solution is similar to that of self-regulating expansion. Thus a smooth transition from self-regulating to stationary flow is possible at least for energies up to 1 J. The plasma adapts smoothly to the spherical stationary flow solution with the plasma ahead of the stationary flow undergoing isothermal self-similar expansion modified by finite heat conductivity.

5.5.b Comparison of data to stationary flow model

Fig. 5.16 shows a log-log plot of the axial profile for shot 21078816 obtained at $t = 2.6$ ns and a plot of a

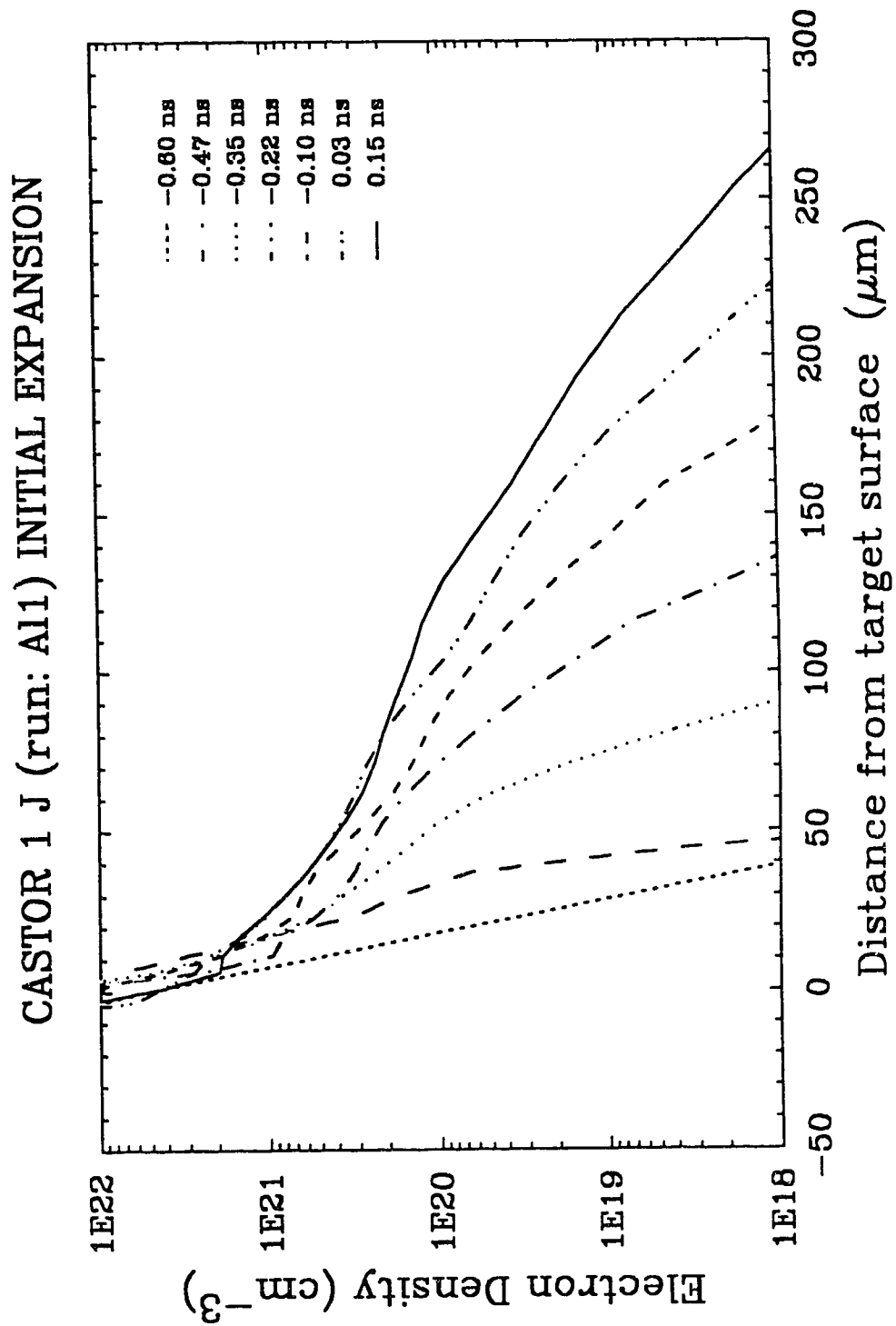


Fig. 5.14. Axial electron density profiles showing self-similar type expansion at early times in the Castor 1 J simulation.

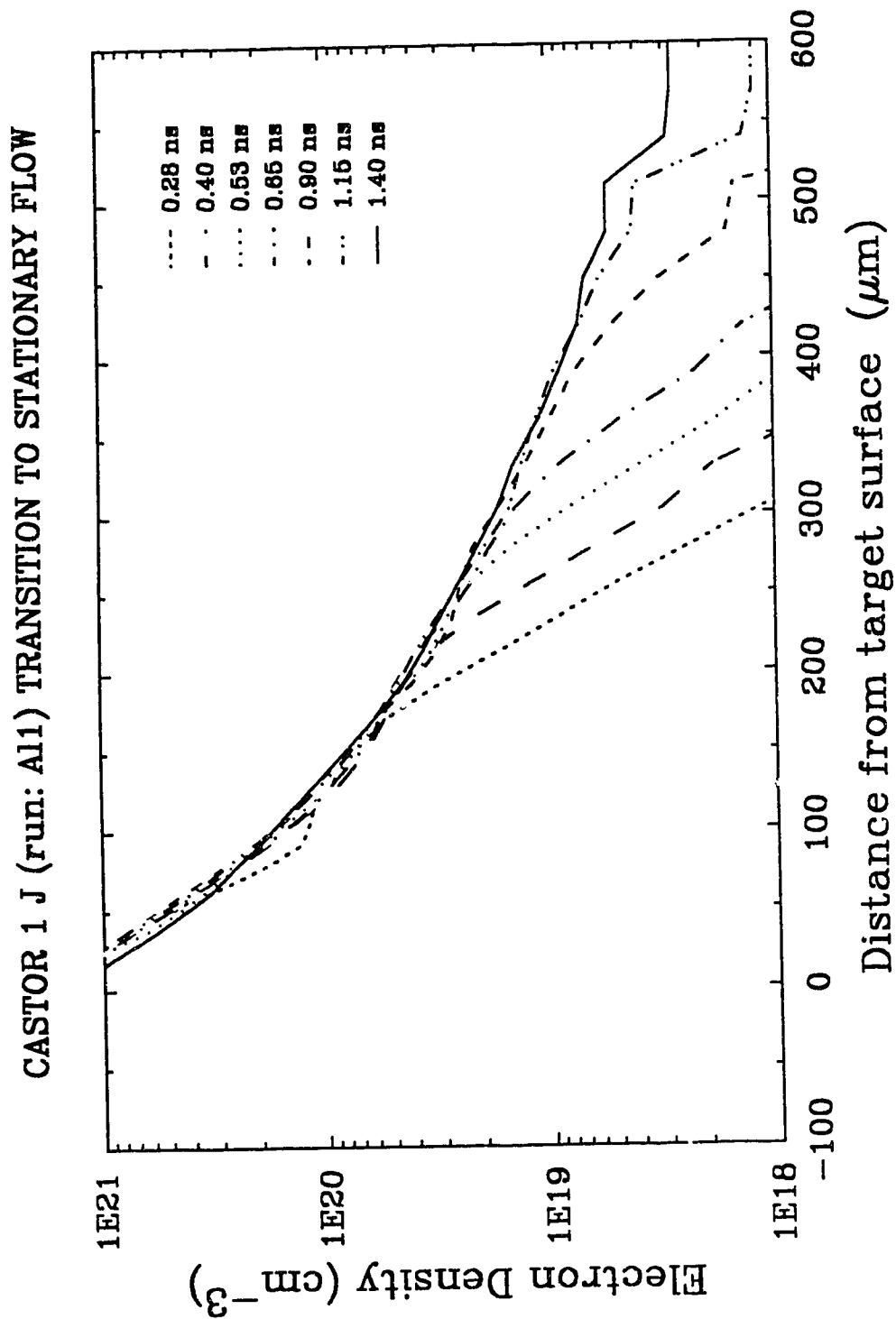


Fig. 5.15. Transition to stationary flow in Castor 1 J simulation.

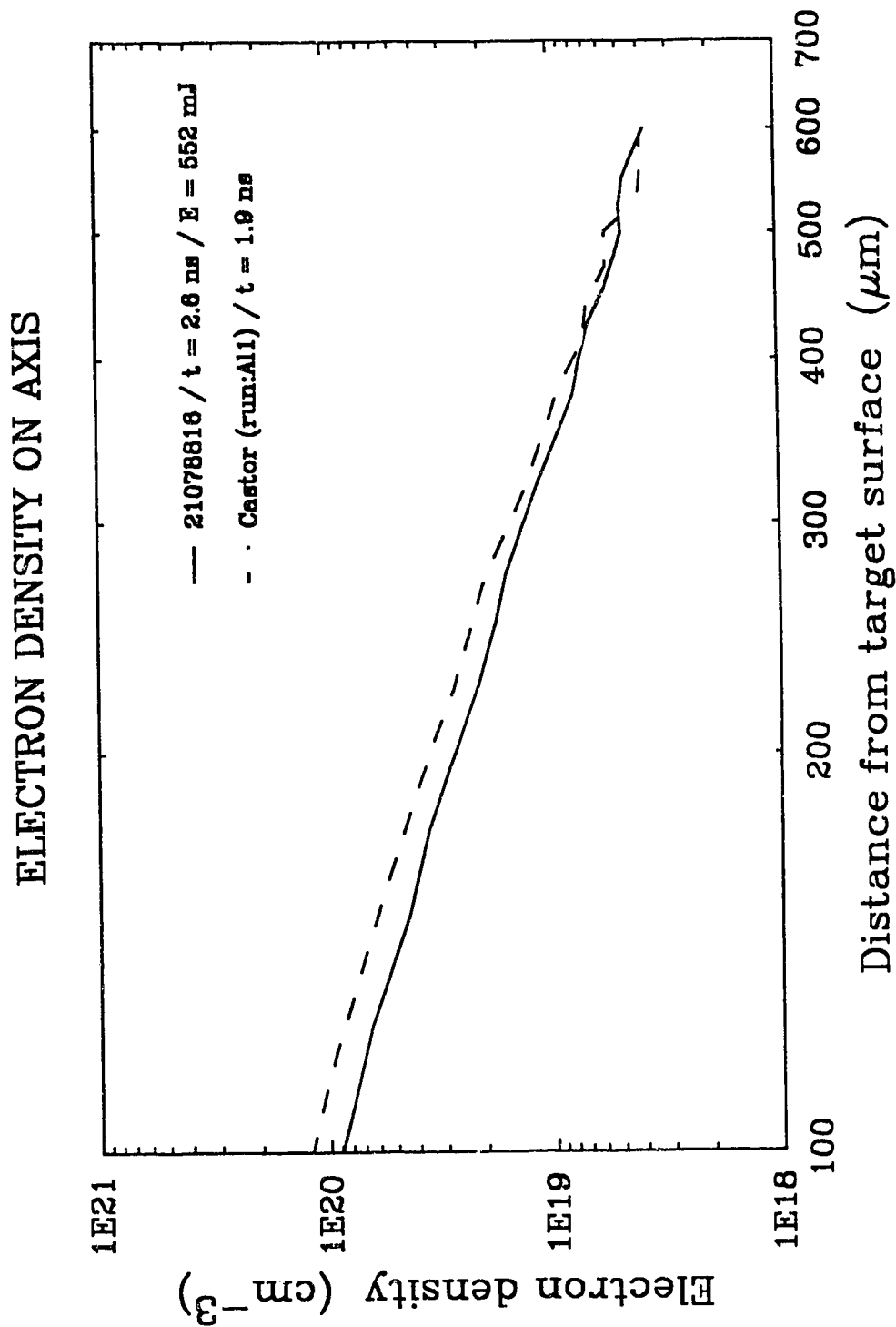


Fig. 5.16. Comparison of Castor and experimental axial density profiles illustrating the stationary flow profile.

stationary profile from Castor run:All. The linear nature of the plots clearly indicates the power nature of the profiles.

The stationary flow model predicts that the measured scale-lengths obtained from the data should equal the value $r/2$. Fig. 5.17 shows the scale-length plotted against $r/2$ (where r is taken as the midpoint of the range of z over which the scale-length was measured) for the data in the time regime from 0.6 ns to 4.0 ns. The graph shows both the line representing the least square fit to the data and the theoretical line having slope = 1 and passing through the origin. The slope of the linear regression fit is 1.03 ± 0.08 with an intercept on the scale-length axis of $-8 \pm 9 \mu\text{m}$. The data agrees with equation 5.1 within the error of the fit.

The standard deviation of the points from the regression line is $10 \mu\text{m}$ which is in reasonable agreement but larger than the average estimated error in the measured scale-length. The scatter of the data indicates that the stationary solution tends to control the plasma profile without necessarily describing the exact flow of a particular plasma which must adjust for variations in laser intensity as a function of time.

While the scale-length of the stationary profile depends only on the position where it is measured, the magnitude of the electron density depends on the magnitude of n_0 and r_0 . The variable n_0 increases with laser

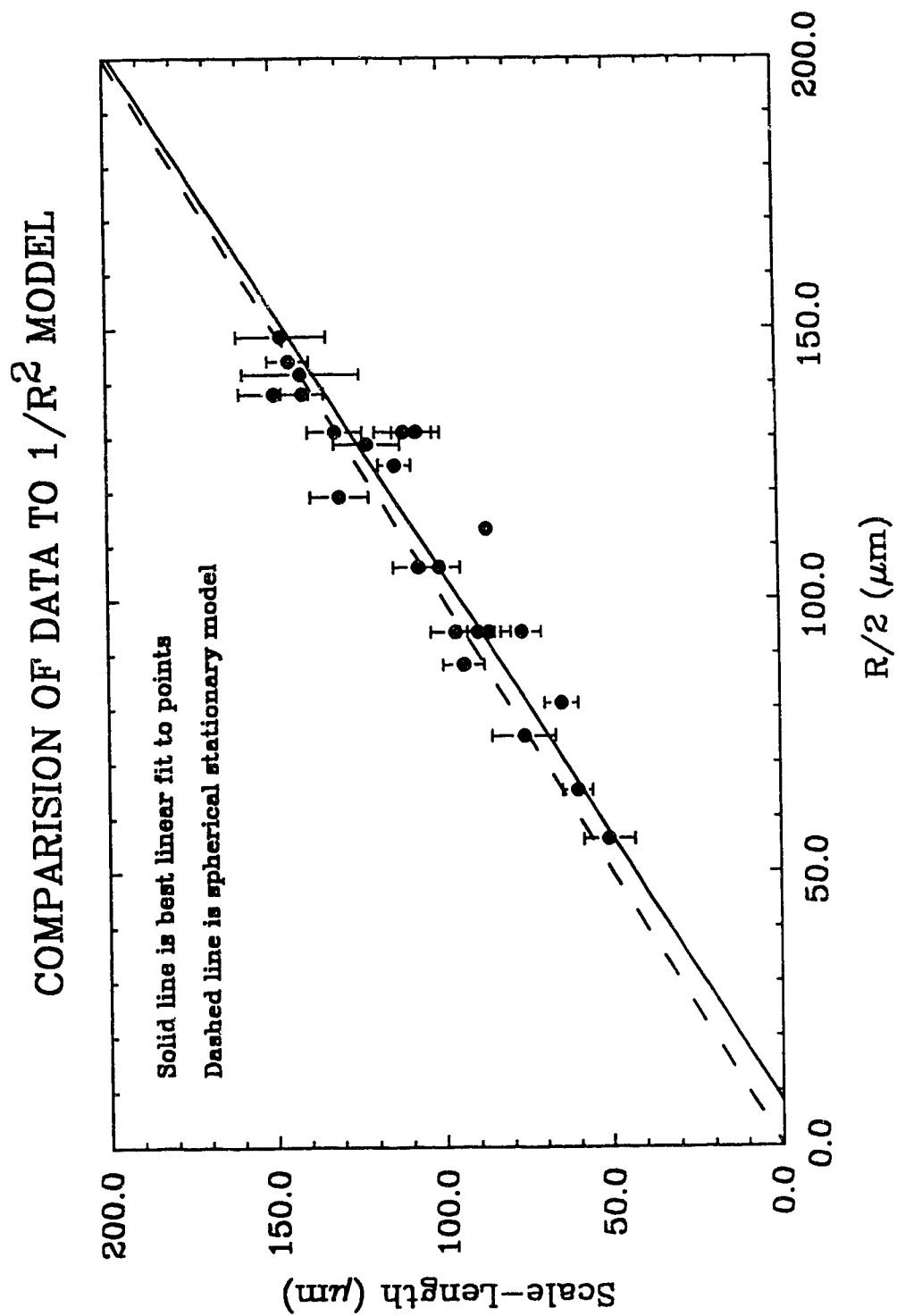


Fig. 5.17. Comparison between experimental data and the spherical stationary flow model.

intensity explaining the correlation between measured scale-length and laser energy. The scale-length is always measured over the same density range which at higher energy is thus further from the target surface.

The degree to which the individual electron density profiles follow an inverse square law is examined with the use of a least square straight line fit to the log-log density profiles from both the data and the Castor simulation. The result of such a fit depends on the absolute position of the zero point for r . For lack of any better value it is assumed that $r = z$ (center of spherical expansion is at target surface). The fit was carried out over the same range of density used to measure scale-length. For the data in the stationary flow region, excluding the three high energy points exhibiting plasma jets, the average power for the best fit power law is -1.99 with a standard error of 0.05 making the result consistent with a power law of -2 . The standard deviation of the individual points from the average is 0.25 . Thus the average power law profile appears to follow the $1/r^2$ dependence of the stationary flow but with shot to shot variations. Individual profiles are not necessarily exactly inverse square curves as mentioned before. The variation could also be explained by small shifts, $\sim 20 \mu\text{m}$, in the plasma's expansion center.

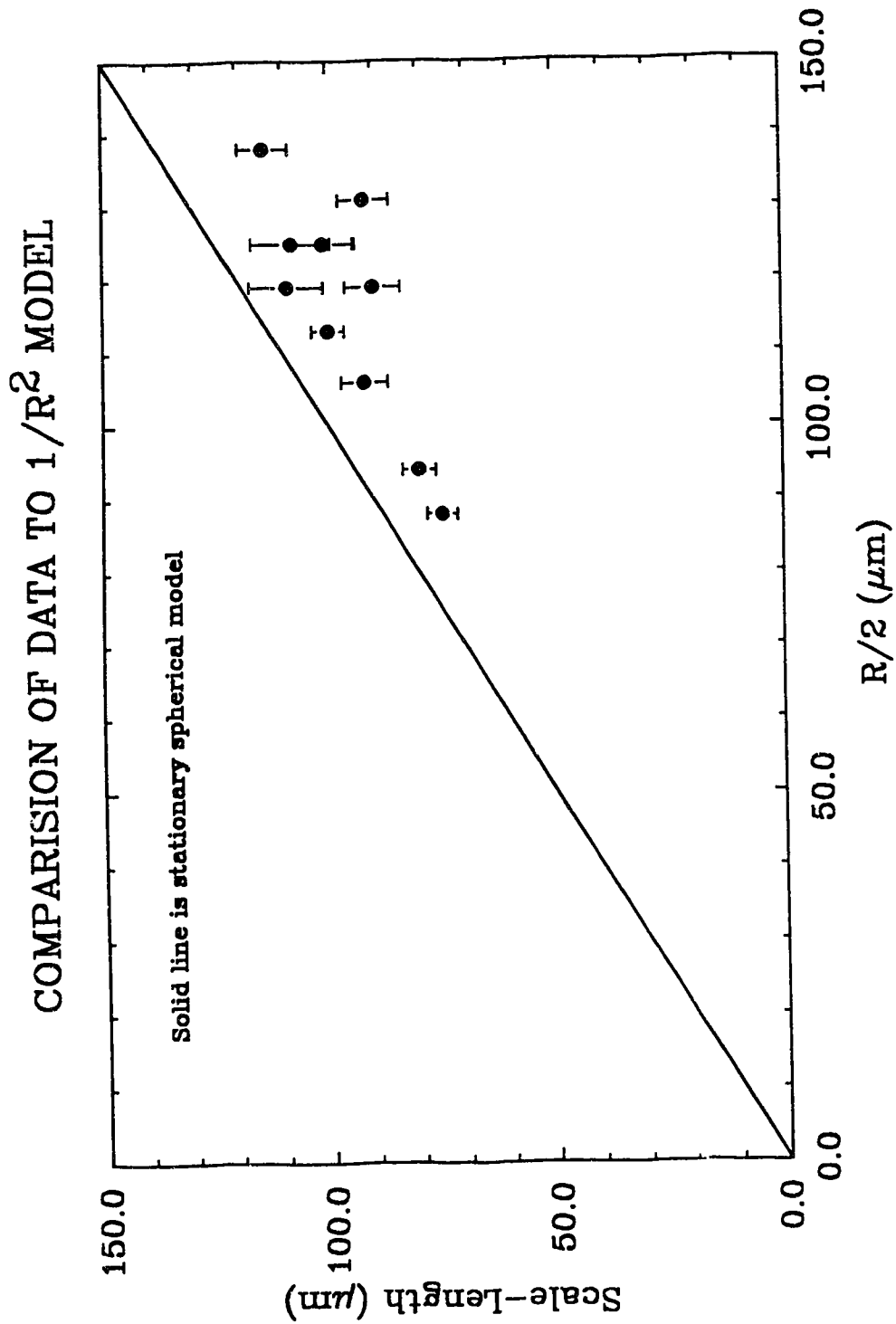
In applying the analysis to the Castor simulations a position for the target surface and hence $r = 0$ is defined

so as to be as consistent as possible with the experiment. As the initial position of the target surface in Castor is not well defined the point $r = 0$ is equated with the earliest ($t = -0.47$ ns) position of the absorption surface, which was defined as the point of maximum temperature in the axial temperature profile, available. The fit is applied to the results from Castor in the time interval where the profile is stationary (after the initial expansion but before the collapse). The average power of the best fit power law is -2.18 with a standard error of 0.04 . The standard deviation of the individual profiles from the average is 0.08 . The result shows reasonable agreement with the experimental data.

5.6 Plasma Collapse Following Laser Turn-Off

The laser pulse has a fairly long tail which turns off completely at about 4 ns. After 4.0 ns the scale-length of the plasma shows a slow decline as would be expected as the target cools. The collapse of the plasma is clearly identified when scale-length is plotted against $r/2$, the scale-length corresponding to stationary flow, as shown in Fig. 5.18. The figure indicates that there is still a correlation between scale-length and the position at which it is measured but the scale-length is consistently shorter than $r/2$.

In the Castor simulation the collapse of the plasma away from its stationary flow profile begins at about



2.75 ns which is consistent with the experimental data considering that the turn-off of the laser in the simulation is at 3.0 ns. Profiles of the collapsing plasma from the Castor simulation were shown in section 5.3 Fig. 5.7.

5.7 Self-Generated Magnetic Fields

At late times conical structures were observed in the lateral wings of the plasma. These structures follow a consistent development and have a distinctive appearance. However, they have not been observed to develop in the 2D Castor hydrodynamic simulations. These features could perhaps be explained by the presence of toroidal magnetic fields.

The main generation term for self-generated magnetic fields is due to electron density gradients which are not aligned with temperature gradients and is given by equation 2.44. This generation term may give large results at the edge of the focal spot where primarily axial density gradients combine with large radial temperature gradients. In order to estimate the rate of development of these fields equation 2.44 may be rewritten using convenient units and is given by:

$$\left(\frac{\Delta B}{1MG} \right) = 10 \left(\frac{\Delta t}{1ns} \right) \left(\frac{T}{1eV} \right) \left(\frac{1\mu m^2}{L_n L_T} \right) \sin \theta \quad (5.2)$$

where L_n and L_T are the electron density and electron

temperature scale-lengths and θ is the angle between the density and temperature gradients and may approach $\pi/2$ just outside the focal spot of the main laser. Values for L_n may be obtained from the data. Here we use the value of $70 \mu\text{m}$ which corresponds to the state of the plasma at about a 1 ns following the first arrival of laser energy on target and makes a good average number for the initial expansion of the plasma. From the data one may infer that 200 eV is a reasonable value for the electron temperature and this value is in good agreement with the Castor simulation. The transverse electron temperature gradient scale-length may be estimated from the Castor simulation which indicates a value of about $60 \mu\text{m}$. The actual temperature gradients should be even steeper as the real focal spot is significantly smaller than used in the simulation. These values indicate a magnetic field formation of about a megagauss per nanosecond.

The magnetic field will tend to reach a saturation value due to the saturation term given in equation 2.46. This saturation value may be estimated by equations 2.44 and 2.46 and gives rise to the following expression:

$$\left(\frac{B_s}{\text{MG}} \right) = 2.04 \left(\frac{T_e}{\text{1eV}} \right)^{1/2} \left(\frac{1\mu\text{m}R}{L_n L_T} \right) \left(\frac{A}{Z+1} \right)^{1/2} F(\theta) \quad (5.3)$$

where $F(\theta)$ is a factor due to all the angular dependencies of the original equation but is expected to be of order unity. For aluminum A is 27 and Z is taken to be about 10

Taking R , the distance from the laser axis, as $100 \mu\text{m}$ and keeping the temperature and various scale-lengths the same as the previous calculation indicates that magnetic field production should saturate at about a megagauss. Thus it is reasonable to expect that magnetic fields of 1 MG could be generated after one or two nanoseconds from the start of the laser pulse.

The ratio of kinetic pressure to magnetic pressure, β , is given by equation 2.47. At an electron temperature of 200 eV and at electron densities of $1 \times 10^{20} \text{cm}^{-3}$, a magnetic field of 1 MG gives a value of 0.8 for β indicating that magnetic fields could be strong enough to affect the plasma hydrodynamics.

Strong off axis toroidal magnetic fields would tend to trap the cooler off axis plasma. In addition they would tend to decrease the transverse heat capacity of the plasma which could further steepen the transverse temperature gradient of the plasma. Any magnetic fields produced near the target surface would be carried out from the target with the plasma as indicated by equation 2.46. As the expansion cone structure observed in the later time plasmas seems to originate from the region where magnetic field production is expected to be strongest it is possible that this structure is a result of potentially strong magnetic fields in the plasma.

CHAPTER 6

CONCLUSION

An interferometric study of the time development of KrF laser-produced-plasma has been carried out focusing primarily on the time development of the axial scale-length of the plasma. Data was collected from the start of the laser pulse through to the collapse of the plasma following laser turn-off.

The N_2 laser has been shown to be suitable for laser-produced-plasma interferometry. The pulse length produce by the N_2 laser used here may be shortened by operating the laser at higher filling pressures which would improve the measurements particularly during the initial expansion period during which the electron density distribution is changing rapidly.

Analysis of the experimental data showed that at early-time the plasma could be modeled as a planar expansion but that, due to the small size of the focal spot used in this experiment, 1D calculations predict unreasonably high plasma temperatures unless some method is employed to take into account the plasma's lateral expansion.

The Castor 2D simulation was shown to do a fair job of simulating the plasma with many of the differences between the simulation and the experimental data attributable to differences in the characteristics of the laser pulses used. The simulation does a particularly good job of

illustrating the transition from self-similar type flow to spherical stationary flow. The simulation does not reproduce the late-time structures observed in the lateral wings of the plasma nor the the axial jets observed in the experimental plasma during a few of the high energy shots.

From the experimental data it was found that the lateral size of the plasma increased at a rate close to the average ion acoustic velocity in the plasma. Taking this into account, the early planar expansion of the plasma could be well modeled using the self-regulating model and a time dependant effective intensity defined as the laser power divided by the area of the plasma as a function of time.

At a time of approximately 0.6 ns the flow undergoes a transition from planar to spherical geometry. The scale-length of the resultant stationary spherical plasma flow was analyzed with the aid of a stationary analytic model for spherical flow. The experimental data was shown to be in reasonable agreement with the predicted $1/r^2$ density profile making scale-length purely a function of the position where it is measured.

The stationary flow model developed and used here can be easily extended to the case of a transition from planar to cylindrical flow such as may be achieved using a line focus on a solid target. Plasma hydrodynamics in cylindrical geometries are of interest to x - ray laser studies particularly when preformed plasma systems are

desired.

In summary, the experimental measurements have helped to clarify the different flow regimes which occur in nanosecond ultraviolet wavelength laser-produced-plasmas. The measurements establish the overall validity of the 2D flow patterns predicted by numerical simulations though some detailed features are not reproduced. The different flow regimes can be modeled in a simple fashion using 1D analytic models.

REFERENCES

- 1 Ernest E. Bergmann, "Compact TEA N₂ laser," *Review of Scientific Instruments*, 48, pp. 545-546.
- 2 R. Cubeddu, and S. De Silvestri, "A simple and reliable atmospheric pressure nitrogen laser," *Optical and Quantum Electronics - Short Communication*, 11, pp. 276-277 (1979).
- 3 H. Salzmann and H. Strohwal, "High power, subnanosecond pulse from a TEA nitrogen laser with a travelling wave excitation," *Optics Communications*, 12, pp. 370-372 (1974).
- 4 H. Strohwal and H. Salzmann, "Picosecond uv laser pulses from gas discharges in pure nitrogen at pressures up to 6 atm," *Applied Physics Letters*, 28, pp. 272-274 (1976).
- 5 H. Schmidt, H. Salzmann, H. Strohwal, "Interferometry using subnanosecond pulses from TEA nitrogen lasers," *Applied Optics*, 14, pp. 2250-2251 (1975).
- 6 I. Baltog, M. Ganciu, L. Mihut, and V. Zâmbreanu, "Four-channel TEA nitrogen laser for interferometric measurements on the plasma focus," *Journal of Physics E: Scientific Instruments*, 19, (1986).
- 7 R. Fedosejevs, I.V. Tomov, N.H. Burnett, and M.C. Richardson, "Application of a synchronized ultrashort Nd:glass laser pulse to the diagnosis of CO₂ laser-produced plasmas," *High Speed Photography*, SPIE, 97, pp. 401-406 (Toronto 1976).
- 8 R.L. Carman, A.G. Engelhardt, and N. Clabo, "Multiwave picosecond interferometry of CO₂-laser produced plasmas," *IEEE International Conference on Plasma Science*, 60, (1977).
- 9 M.D. Burgess, G.D. Enright, R. Fedosejevs, and M.C. Richardson, "Picosecond interferometric studies of CO₂ laser produced plasmas," *Picosecond Phenomena II*, pp. 64-68 (1980).

- 10 A.E. Alimov, V.Yu. Baranov, V.L. Borzenko, S.M. Kozochkin, K.N. Makarov, D.D. Malyuta, Yu.A. Satov, I.Yu. Skobelev, S.S. Sobolev, A.P. Strel'tsov, and A.Ya. Faenov, "Study of the supercritical region in a CO₂-laser plasma in the x-ray spectra of multiply charged ions," *JEPT Letters*, 42, pp. 103-105 (1985).
- 11 O. Willi, and A. Raven, "Holographic microinterferometer to study laser-produced plasma," *Applied Optics*, 19, pp. 192-194 (1980).
- 12 M.D. Burgess, R. Dragila, B. Luther-Davies, K.A. Nugent, A.J. Perry, and G.J. Tallents, "Characterization of plasmas produced by a laser line focus," *Physical Review A*, 32, pp. 2899-2908 (1985).
- 13 L.J. Dhareshwar, P.A. Naik, P.D. Nandwana, and H.C. Pant, "Characteristics of plasma flow from laser irradiated planar thin foil targets," *Journal of Applied Physics*, 61, pp. 4458-4463 (1987).
- 14 Y. Matsumoto, M.J. Shaw, F. O'Neill, J.P. Partanen, M.H. Key, R. Eason, I.N. Ross, and E.M. Hodgson, "X-ray emission from KrF laser-produced Al plasmas," *Applied Physics Letters*, 46, pp. 28-30 (1985).
- 15 P.D. Gupta, R. Popil, R. Fedosejevs, A.A. Offenberger, D. Salzmann, and C.E. Capjack, "Temperature and x-ray intensity scaling in KrF laser plasma interaction," *Applied Physics Letters*, 48, pp. 103-105 (1986).
- 16 A.A. Offenberger, R. Fedosejevs, P.D. Gupta, R. Popil and Y.Y. Tsui, "Experimental results for high intensity KrF laser/plasma interaction," *Lasers and Partical Beams*, 4, pp. 329-347 (1986).
- 17 P.D. Gupta, Y.Y. Tsui, R. Popil, R. Fedosejevs, and A.A. Offenberger, "Energy transport in gold coated plastic targets irradiated by a KrF laser," *Optics Communications*, 63, pp. 165-170 (1987).
- 18 P.D. Gupta, Y.Y. Tsui, R. Popil, R. Fedosejevs, and A.A. Offenberger, "Ablation parameters in KrF laser/plasma interaction: An experimental study," *The Physics of Fluids*, 30, pp. 179-185 (1987).

- 19 R. Fedosejevs, Y.Y. Tsui, R. Popil, P.D. Gupta, J. Baker, and A.A. Offenberger, "Foil calorimeter measurements of soft-x-ray energy emission from KrF-laser-produced plasmas," *Journal of Physics D: Applied Physics*, **20**, pp. 1259-1263 (1987).
- 20 A.G.M. Maaswinkel, R. Sigel, H. Baumhacker, and G. Brederlow, "3-ps synchronized multiframe photographic diagnostic for target experiments with the iodine laser," *Review of Scientific Instruments*, **55**, pp. 48-51 (1983).
- 21 R. Fedosejevs, Yung-lu Teng, R. Sigel, K. Eidmann, and R. Petsch, "Internal breakdown in a dielectric target at high laser irradiance," *Journal of Applied Physics*, **52**, pp. 4186-4188.
- 22 K. Eidmann, F. Amiranoff, R. Fedosejevs, A.G.M. Maaswinkel, R. Petsch, R. Sigel, G. Spindler, Yung-lu Teng, G. Tsakiris, and S. Witkowski, "Interaction of 1.3- μm laser radiation with thin foil targets," *Physical Review A*, **30**, pp. 2568-2589 (1984).
- 23 Yung-lu Teng, R. Fedosejevs, R. Sigel, K. Eidmann, R. Petsch, and G. Spindler, "High-speed photography of laser irradiated thin foils," *14th European Conference on Laser Interaction with Matter*, (Palaiseau 1980).
- 24 R. Fedosejevs, I.V. Tomov, N.H. Burnett, G.D. Enright, and M.C. Richardson, "Self-steepening of the density profile of a CO_2 -laser-produced plasma," *Physical Review Letters*, **39**, pp. 932-935 (1977).
- 25 H. Azechi, S. Oda, K. Tanaka, T. Norimatsu, T. Sasaki, T. Yamanaka, and C. Yamanaka, "Measurement of density modification of laser-fusion plasmas," *Physical Review Letters*, **39**, pp. 1144-1147 (1977).
- 26 D.T. Attwood, D.W. Sweeney, J.M. Auerbach, and P.H.Y. Lee, "Interferometric confirmation of radiation-pressure effects in laser-plasma interactions," *Physical Review Letters*, **40**, pp. 184-187 (1978).

- 27 H.A. Baldis, J.C. Samson, and P.B. Corkum, "Two-plasmon decay and profile modification produced by 10.6- μ m radiation at quarter-critical density," *Physical Review Letters*, 41, 1719 (1978).
- 28 J.C. Kieffer, H. Pépin, F. Martin, P. Church, T.W. Johnston, and H. Decoste, "Electron energy transport into targets irradiated by CO₂-laser light," *Physical Review Letters*, 44, pp. 1128-1131 (1980).
- 29 A. Raven, and O. Willi, "Electron-density structures in laser-produced plasmas at high irradiances," *Physical Review Letters*, 43, pp. 278-282 (1979).
- 30 P.E. Young, H.A. Baldis, T.W. Johnston, W.L. Kruer, and K.G. Estabrook, "Filamentation and second-harmonic emission in laser-plasma interactions," *Physical Review Letters*, 63, pp. 2812-2815 (1989).
- 31 E.F. Gabl, B.H. Failor, C.J. Armentrout, N.D. Delamater, W.B. Fechner, R.A. Bosch, Gar E. Busch, and Z.M. Koenig, "Plasma Jets from laser-irradiated planar targets," *Physical Review Letters*, 63, pp. 2737-2740 (1989).
- 32 B. Grek, F. Martin, T.W. Johnston, H. Pépin, G. Mitchel, and F. Rheault, "Fine-scale structures in plasmas stimulated by a CO₂ laser," *Physical Review Letters*, 41, pp. 1811-1814 (1978).
- 33 A. Raven, and O. Willi, "Megagauss magnetic field profiles in laser-produced plasmas," *Physical Review Letters*, 41, pp. 554-557 (1978).
- 34 E.F. Gabl, B.H. Failor, Gar E. Busch, R.J. Schroeder, D. Ress, and L. Suter, "Plasma evolution from laser-driven gold disks. I. Experiments and results," *Physics of Fluids B*, 2, pp. 2437-2447 (1990).
- 35 D. Ress, L.J. Suter, E.F. Gabl, and B.H. Failor, "Plasma evolution from laser-driven gold disks. II. Computational design and analysis," *Physics of Fluids B*, 2, pp. 2448-2455 (1990).

- 36 M.D. Rosen, P.L. Hagelstein, D.L. Matthews, E.M. Campbell, A.U. Hazi, B.L. Whitten, B. MacGowan, R.E. Turner, and R.W. Lee, "Exploding-foil technique for achieving a soft x-ray laser," *Physical Review Letters*, 54, pp. 106-109 (1985).
- 37 M.D. Rosen, J.E. Trebes, B.J. MacGowan, P.L. Hagelstein, R.A. London, D.L. Matthews, D.G. Nilson, T.M. Phillips, D. Whelan, G. Charatis, G.E. Busch, C.L. Shepard, and V.L. Jacobs, "Dynamics of collisional-excitation X-ray lasers," *Physical Review Letters*, 59, 2283 (1987).
- 38 Nicholas A. Krall, Alvin W. Trivelpiece, *Principles of Plasma Physics*, McGraw-Hill Inc. (1973).
- 39 A.V. Gurevich, L.V. Pariiskaya, and L.P. Pitaevskii, "Self-similar motion of rarefied plasma," *Soviet Physics JEPT*, 22, pp. 449-454 (1966).
- 40 A.V. Gurevich, L.V. Pariiskaya, and L.P. Pitaevskii, "Self-similar motion of a low-density plasma II," *Soviet Physics JEPT*, 27, pp. 476-482 (1968).
- 41 Patrick Mora, R. Pellat, "Self-similar expansion of a plasma into vacuum," *Physics of Fluids*, 22, pp. 2300-2304 (1979).
- 42 L.D. Landau, and E.M. Lifshitz, *Fluid Mechanics*, Pergamon Press (1959).
- 43 R.F. Schmalz, "New self-similar solutions for the unsteady one-dimensional expansion of a gas into vacuum," *Physics of Fluids*, 28, pp. 2923-2925 (1985).
- 44 J.E. Allen, and J.G. Andrews, "A note on ion rarefaction waves," *Journal of Plasma Physics*, 4, pp. 187-194 (1970).
- 45 J.E. Crow, P.L. Auer, and J.E. Allen, "The expansion of plasma into vacuum," *Journal of Plasma Physics*, 14, pp. 65-76 (1975).
- 46 J.G. Andrews, "The sheath criterion for a growing sheath," *Journal of Plasma Physics*, 4, pp. 603-606 (1970).

- 47 Patrick Mora, R. Pellat, "Theoretical model of absorption of laser light by a plasma," *Physics of Fluids*, 25, pp. 1051-1056 (1982).
- 48 W.M. Manheimer and D.G. Colombant, "Steady-state planar ablative flow," *Physics of Fluids*, 25, pp. 1644-1652 (1982).
- 49 J.P. Christiansen, D.E.T.F. Ashby, and K.V. Roberts, "Medusa a one-dimensional laser fusion code," *Computer Physics Communications*, 7, pp. 271-287 (1974).
- 50 J.P. Christiansen, "Castor 2: A two-dimensional laser target code," *Computer Physics Communications*, 17, pp. 397-412 (1979).
- 51 Kieth A. Brueckner, and Siebe Jorna, "Laser-driven fusion," *Reviews of Modern Physics*, 46, pp. 325-326 (1974).
- 52 Claire Ellen Max, Wallace M. Manheimer, J.J. Thomson, "Enhanced transport across laser generated magnetic fields," *Physics of Fluids*, 21, pp. 128-139 (1978).
- 53 N.A. Ebrahim, M.C. Richardson, and R Fedosejevs, "Observations consistent with self-generated magnetic fields in CO₂ laser-produced plasmas," *Applied Physics Letters*, 35, pp. 106-108 (1979).
- 54 A.N. Mostovych, B.H. Ripin, and J.A. Stamper, "Laser-produced plasma jets: collimation and instability in strong transverse magnetic fields," *Physical Review Letters*, 62, pp. 2837-2840 (1989).
- 55 R.A. Alpher, and D.R. White, *Plasma Diagnostic Techniques*, Chap. 10: Optical Interferometry, Academic Press Inc. (1965).
- 56 F.C. Jahoda, and G.A. Sawyer, *Methods of Experimental Physics Vol 9*, Chap. 11: Optical Refractivity of Plasmas, Academic Press Inc. (1971).
- 57 G.J. Tallents, "Interferometry and refraction measurements in plasmas of elliptical cross-section," *Journal of Physics D: Applied Physics*, 17, pp. 721-732 (1984).

- 58 András Kuthy, "An interferometer and an Abel inversion procedure for the measurement of the electron density profile in a cold gas-blanket experiment," *Nuclear Instruments and Methods*, 180, pp. 7-16 (1981).
- 59 N.G. Demas, R.P. Howard, and M.E. Plemmons, "Method of Abel inversion for non-circular tokamak geometries," *IEEE Southeastcon (Conference proceedings)*, pp. 430-433 (1983).
- 60 Yuichi Yasutomo, Katsuyuki Miyata, Shun-Ichi Himeno, Takeaki Enoto, and Yasutomo Ozawa, "A new numerical method for asymmetrical Abel inversion," *IEEE Transactions on Plasma Science*, PS-9, pp. 18-21 (1981).
- 61 E. Silver, and W. Roney, "Distribution of emitters in an elliptical source," *IEEE Transactions on Plasma Science*, PS-8, pp. 231-234 (1980).
- 62 Shun-ichi Himeno, Masaharu Seki, Hitoshi Mochizuki, Takeaki Enoto, and Tadashi Sekiguchi, "Computer method for new elliptical Abel inversion applied to holographic plasma diagnostics," *Journal of the Physical Society of Japan*, 54, pp. 1737-1742 (1984).
- 63 J.M. Wetzer, "Asymmetrical Abel inversion of MHD generator discharges," *IEEE Transactions on Plasma Science*, PS-11, pp. 72-75 (1983).
- 64 Von W. Frie, "Zur auswertung der abelschen integralgleichung," *Annalen der Physik*, 7, pp. 333-339 (1963).
- 65 Clifford J. Cremers and Richard C. Birkebak, "Application of the Abel integral equation to spectrographic data," *Applied Optics*, 5, pp. 1057-1064 (1966).
- 66 O.H. Nestor, and H.N. Olsen, "Numerical methods for reducing line and surface probe data," *SIAM Review*, 2, pp. 200-207 (1960).
- 67 Kjell Bockasten, "Transformation of observed radiances into radial distribution of the emission of a plasma," *Journal of the Optical Society of America*, 51, pp. 943-947 (1961).

- 68 William L. Barr, "Method for computing the radial distribution of emitters in a cylindrical source," *Journal of the Optical Society of America*, 52, pp. 885-888 (1961).
- 69 J. Glasser, J. Chapelle, and J.C. Boettner, "Abel inversion applied to plasma spectroscopy: a new interactive method," *Applied Optics*, 17, pp. 3750-3754 (1978).
- 70 C.S. Willett, *Introduction to Gas Lasers: Population Inversion Mechanisms*, Pergamon Press (1974).
- 71 A.J. Smith, K.H. Kwek, T.Y. Tou, A.V. Gholap, and S. Lee, "Measurement of nitrogen laser channel current, inductance, and resistance," *IEEE Journal of Quantum Electronics*, QE-23, pp. 283-286 (1987).
- 72 D.T. Attwood, "Ultraviolet probing of laser produced plasmas with picosecond pulses," *High Speed Photography*, SPIE, 97, pp. 413-420 (Toronto 1976).
- 73 G. Gillman, "Interferometer focusing accuracy and the effect on interferograms for density measurements of laser produced plasmas," *Optics Communications*, 35, pp. 127-132 (1980).
- 74 M.D.J. Burgess, G.B. Gillman, and B. Luther-Davies, "Limitation to the accuracy of interferometrically measured electron density profiles of laser-produced plasmas," *Journal of Applied Physics*, 54, pp. 1787-1791 (1982).
- 75 C.M. Vest, "Interferometry of strongly refracting phase objects," *Applied Optics*, 14, pp. 1601-1606 (1975).
- 76 D. Salzmann, and A. Krumbein, "Calculation of x-ray production rate and ionization-state density in hot aluminum plasma," *Journal of Applied Physics*, 49, pp. 3229-3238 (1978).
- 77 Douglas Vick, private communication.

APPENDIX A

NUMERICAL TESTS OF DECONVOLUTION ROUTINES

A.1 Testing of Deconvolution Routines

It is important to test the deconvolution routines in order to check their accuracy and to give confidence that the programming is correct (check that the inversion gives correct results). For this purpose analytic test functions for n_r were developed which could be integrated analytically in Abel's integral equation (equation 2.32). These functions were integrated and the results used to produce test fringes which were generated as video images in the video digitizer system and put through the complete deconvolution process. The resulting values for electron density were then compared with the starting function. All of the test functions were given an exponential decay in the z direction, similar to the real plasma.

The first function, which will be referenced as test function #1 was a simple linear profile given by:

$$n_r - 1 = n_{r0} \left(1 - \frac{r}{R} \right) e^{-z/L} \quad (\text{A.1})$$

Where: L = the scale-length of the plasma in the z direction.

The next function called test function #2 was parabolic in nature and given by:

$$n_r - 1 = n_{r0} \left(1 - \frac{r^2}{R^2} \right) e^{-z/L} \quad (\text{A.2})$$

It should be noted that these two test functions, unlike the real plasma, have a sharp boundary at $r = R$. The third test function called test function #3 uses a gaussian profile. The analytic integration is carried out to infinity much as a real probe pulse would do (infinity being a distance much larger than the dimensions of the interferogram). The resulting test fringe patterns are shown in Fig. A.1 (a). The deconvolution is finite and so this test function provides a useful check on the accuracy associated with finite deconvolution. It is given by:

$$n_r - 1 = n_{r0} \left(e^{-r^2/l^2} \right) e^{-z/L} \quad (\text{A.3})$$

The fourth test function called test function #4 is a cubic. It is used to check the deconvolution of a profile which, like some of the data, has an off axis maximum. The function is given by:

$$n_r - 1 = n_{r0} \left(1 + \frac{a}{R^2} r^2 - \frac{b}{R^3} r^3 \right) e^{-z/L} \quad (\text{A.4})$$

$$a = \frac{3 d}{2 - 3 d}$$

$$b = \frac{2}{2 - 3 d}$$

where $r = d \cdot R$ is the radial position of maximum electron density. Positive values for a and b are desired requiring that $d < 2/3$. The ratio of the maximum electron density to

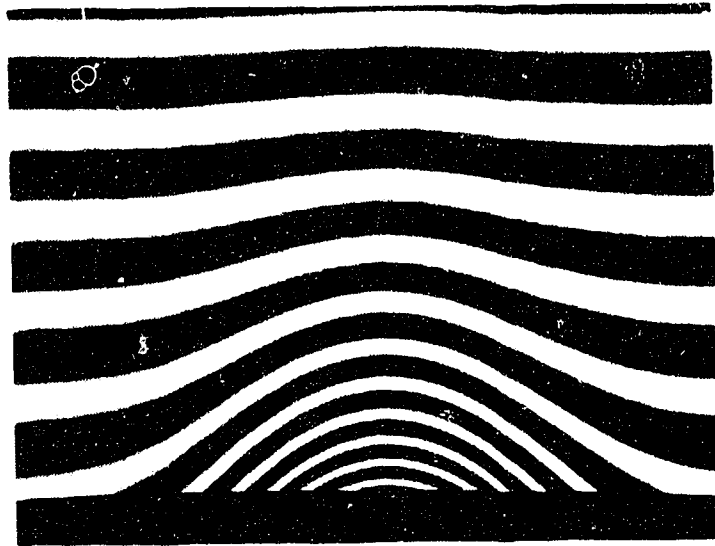


Fig. A.1 (a). Fringes produced by test function #3.

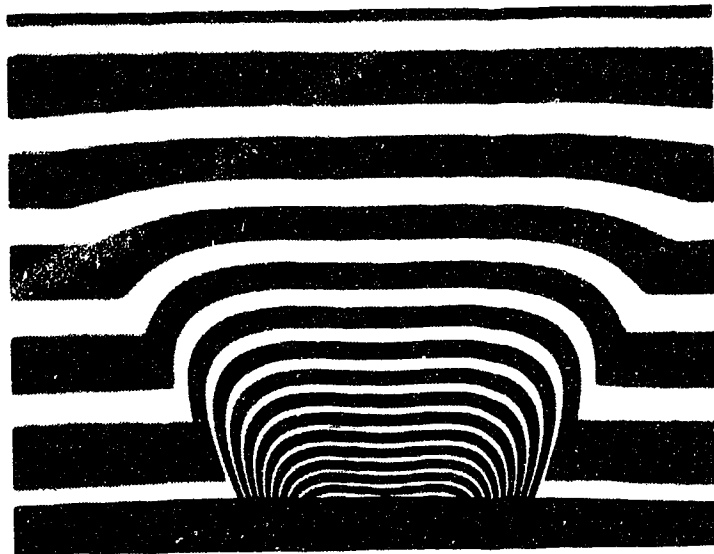


Fig. A.1 (b). Fringes produced by test function #4
with a 30 degree expansion angle.

the axial density is completely determined by the choice of d with the value of n_r at $r = d \cdot R$ given by:

$$n_r - 1 = n_{r0} \left(1 + \frac{d^3}{2 - 3d} \right) \quad (\text{A.5})$$

This function was used as is and with R increasing linearly from R_0 according to the relation $R = R_0 + z \tan(\theta)$ causing a lateral expansion with z in order to test the error introduced by deconvoluting interferograms where the fringes double back on themselves. A value of 30° was used to give an effect much like the real interferograms as may be seen in Fig. A.1 (b). The integrated form of these four test functions is given at the end of this appendix.

Test functions #1 and #2 were tested with a radius $R = 200 \mu\text{m}$ and a scale-length $L = 100 \mu\text{m}$. Test function #3 was implemented with gaussian width parameter $l = 200 \mu\text{m}$ and the axial scale-length $L = 150 \mu\text{m}$. Test function #4 with the off axis maximum was implemented with a radius $R = 200 \mu\text{m}$, an axial scale-length of $100 \mu\text{m}$, and $d = .596$ corresponding to an maximum electron density of twice the value on axis. All of the test functions were given an axial density at $z = 0$ of $1 \times 10^{20} \text{ cm}^{-3}$ and assumed $\lambda = 0.337 \mu\text{m}$. They were processed using 20 point Bockasten inversions and test functions 1 and 2 were inverted with and without smoothing. All test functions were inverted along six slices from $z = 0 \mu\text{m}$ to $z = 500 \mu\text{m}$.

Test functions 1 and 2 inverted very accurately as shown in table A.1 and A.2 and Fig. A.2 (a) and (b). As

z (μm)	density mean (cm^{-3})	no smoothing		smoothing	
		σ (cm^{-3})	σ %	σ (cm^{-3})	σ %
0	5.25 e19	6.61 e18	12.6	3.99 e18	7.6
100	1.94 e19	3.12 e17	1.6	3.11 e17	1.6
200	7.12 e18	3.00 e17	4.2	2.22 e17	3.1
300	2.62 e18	1.60 e17	6.1	1.20 e17	4.6
400	9.64 e17	9.13 e16	9.5	6.09 e16	6.3
500	3.55 e17	6.99 e16	19.7	4.01 e16	11.3

Table A.1. Inversion accuracy for test function #1.

z (μm)	density mean (cm^{-3})	no smoothing		smoothing	
		σ (cm^{-3})	σ %	σ (cm^{-3})	σ %
0	6.92 e19	3.99 e18	5.8	3.24 e18	4.7
100	2.55 e19	5.01 e17	2.0	4.57 e17	1.8
200	9.38 e18	2.74 e17	2.9	1.86 e17	2.0
300	3.45 e18	2.11 e17	6.1	1.63 e17	4.7
400	1.27 e18	9.72 e16	7.7	9.88 e16	7.8
500	4.67 e17	7.60 e16	16.3	6.14 e16	13.2

Table A.2. Inversion accuracy for test function #2.

expected, the accuracy becomes less with falling density due to increasing relative error in determining the fringe shift (the total fringe shift is much smaller). In addition the slice at 0 μm also shows an increase in error. This reflects the fact that the target cuts off the fringes at this point and the inversion routine is forced to do some extra extrapolation. This increase in error is the price of being able to invert to the target face. The accuracy of the inversions improved by an average of 22 % when smoothing was applied to the fringe shifts. This is a

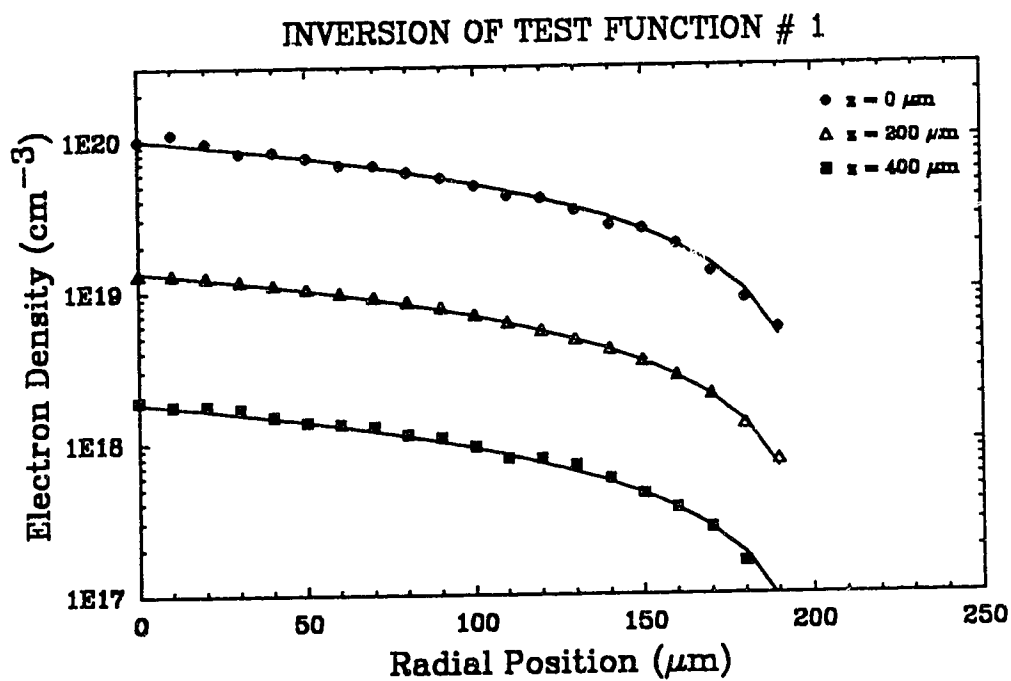


Fig. A.2 (a). Inversion accuracy with smoothing for test function #1.

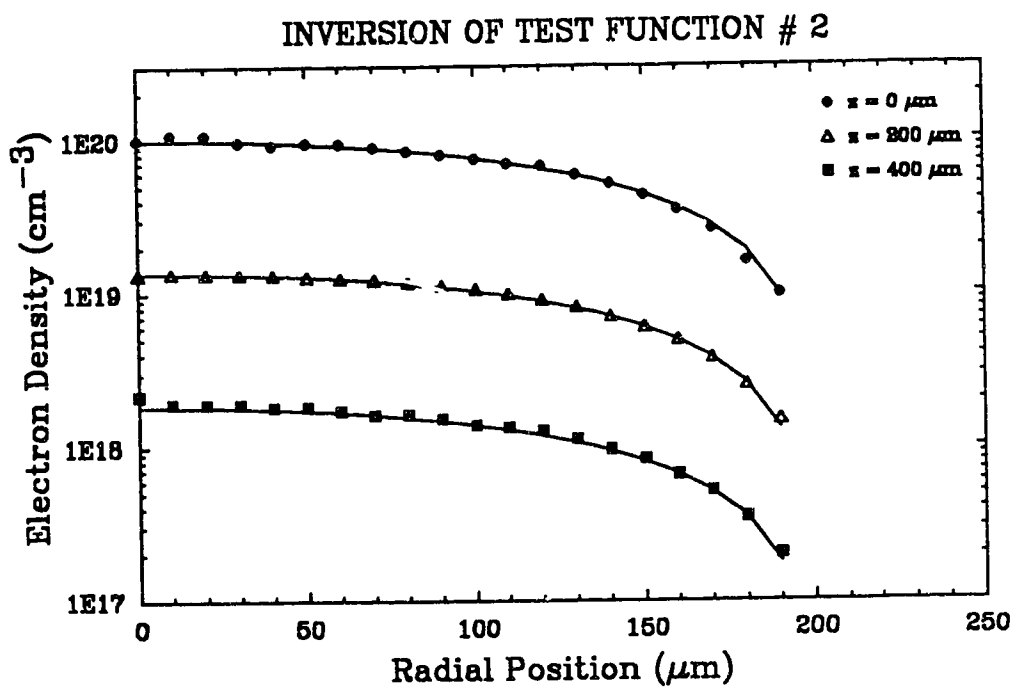


Fig. A.2 (b). Inversion accuracy with smoothing for test function #2.

considerable improvement considering the quality of the fringes being inverted and illustrates the importance of smoothing when doing Bockasten inversion.

Test function #3 was inverted out to 500 μm from the plasma axis where the fringe shift was almost imperceptible similar to the case with a real interferogram. It inverted accurately with slight inaccuracy at the limits of the inversion. The inaccuracy at the extremes of the inversion increased as the maximum radius of the inversion was drastically reduced. Fig. A.3 (a) and (b) shows the effect on the inversion with $R = 200 \mu\text{m}$ which represents an extreme cutting of the fringes. The accuracy of the inversion on axis remains unaffected by the finiteness of the inversion. Table A.3 summarizes the results.

z (μm)	$R = 500$			$R = 400$		
	mean (cm^{-3})	σ (cm^{-3})	σ %	mean (cm^{-3})	σ (cm^{-3})	σ %
0	3.80 e19	1.61 e18	4.2	4.66 e19	1.58 e18	3.4
100	1.95 e19	2.80 e17	1.4	2.39 e19	5.38 e17	2.3
200	1.00 e19	1.15 e17	1.2	1.23 e19	2.27 e17	1.8
300	5.15 e18	9.99 e16	1.9	6.32 e18	1.22 e17	1.9
400	2.64 e18	8.37 e16	3.2	3.24 e18	1.21 e17	3.7
500	1.36 e18	5.01 e16	3.7	1.66 e18	9.92 e16	6.0

z (μm)	$R = 300$			$R = 200$		
	mean (cm^{-3})	σ (cm^{-3})	σ %	mean (cm^{-3})	σ (cm^{-3})	σ %
0	5.93 e19	3.86 e18	6.5	7.63 e19	1.93 e19	25.3
100	3.05 e19	1.82 e18	6.0	3.92 e19	1.02 e19	26.0
200	1.57 e19	8.88 e17	5.7	2.01 e19	5.29 e18	26.3
300	8.04 e18	4.82 e17	6.0	1.03 e19	2.75 e18	26.7
400	4.13 e18	2.67 e17	6.5	5.31 e18	1.40 e18	26.4
500	2.12 e18	1.43 e17	6.7	2.73 e18	7.12 e17	26.1

Table A.3. Inversion accuracy for test function #3 with different cutoff points.

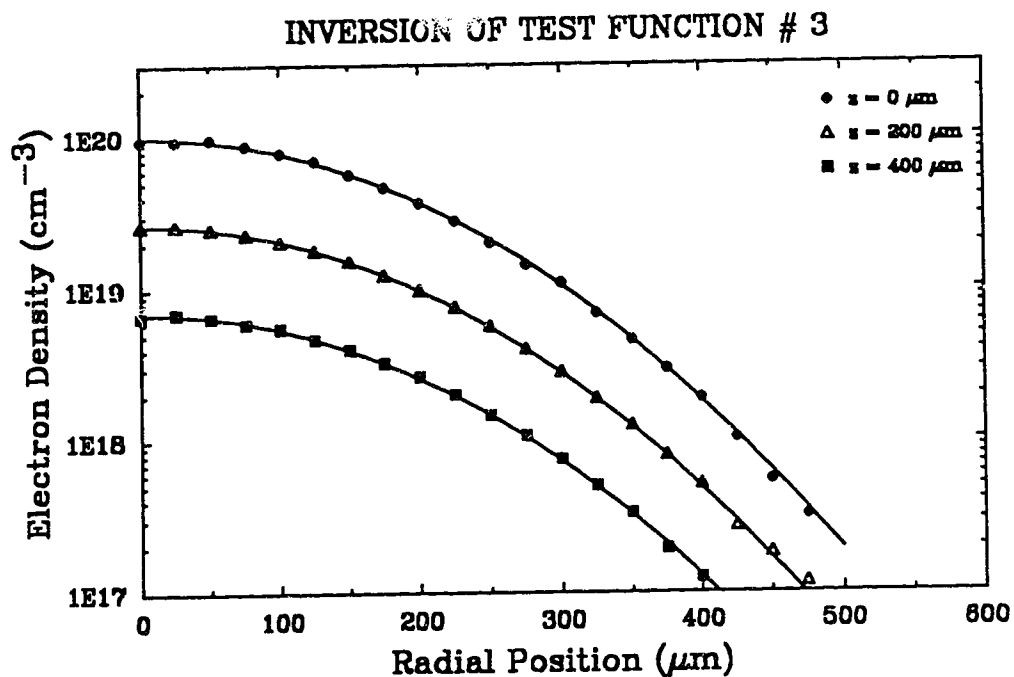


Fig. A.3 (a). Inversion accuracy of test function #3.

Inversion carried out to 500 microns

from the inversion axis.

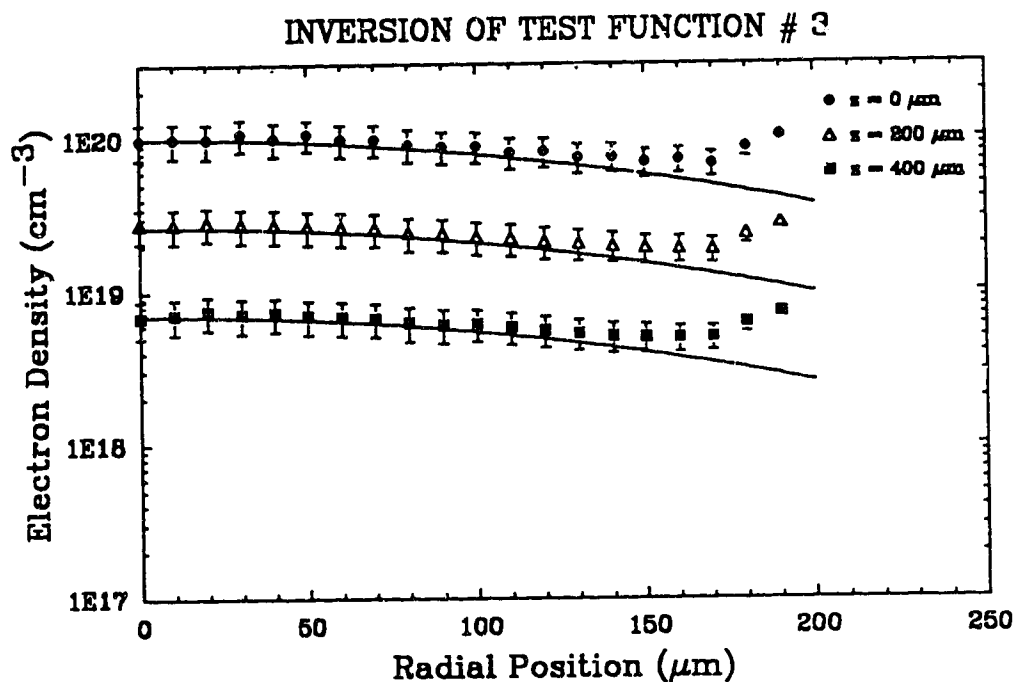


Fig. A.3 (b). Inversion accuracy of test function #3.

Inversion carried out to 200 microns

from the inversion axis.

Test function #4 inverted as well as the others when the expansion angle was set at 0 deg. Fig. A.4 (a) and (b) shows the result when an expansion angle of 30 deg was given to the test function to simulate the effect of inverting fringes which double back on themselves. The only significant error introduced is to smooth out the extreme edge of the plasma where the density drops abruptly to zero. Thus plasmas with well defined expansion cones will have the shock like edge of the cone smoothed somewhat in the deconvolution. Table A.4 gives the accuracy of the results for test function #4 for expansion angles of 0 and 30 deg. No smoothing was applied to either function #3 or function #4.

z (μm)	density mean (cm^{-3})	$\theta = 0$ deg		$\theta = 30$ deg	
		σ (cm^{-3})	σ %	σ (cm^{-3})	σ %
0	1.48 e20	9.47 e18	6.4	1.40 e19	9.5
100	5.45 e19	1.77 e18	3.2	9.82 e17	1.8
200	2.01 e19	4.29 e17	2.1	1.65 e18	8.2
300	7.38 e18	2.01 e17	2.7	3.46 e17	4.7
400	2.72 e18	1.46 e17	5.4	1.13 e17	4.2
500	9.99 e17	8.79 e16	8.8	1.20 e17	12.0

Table A.4. Inversion accuracy of test function #4
with and without 30 degree expansion angle.

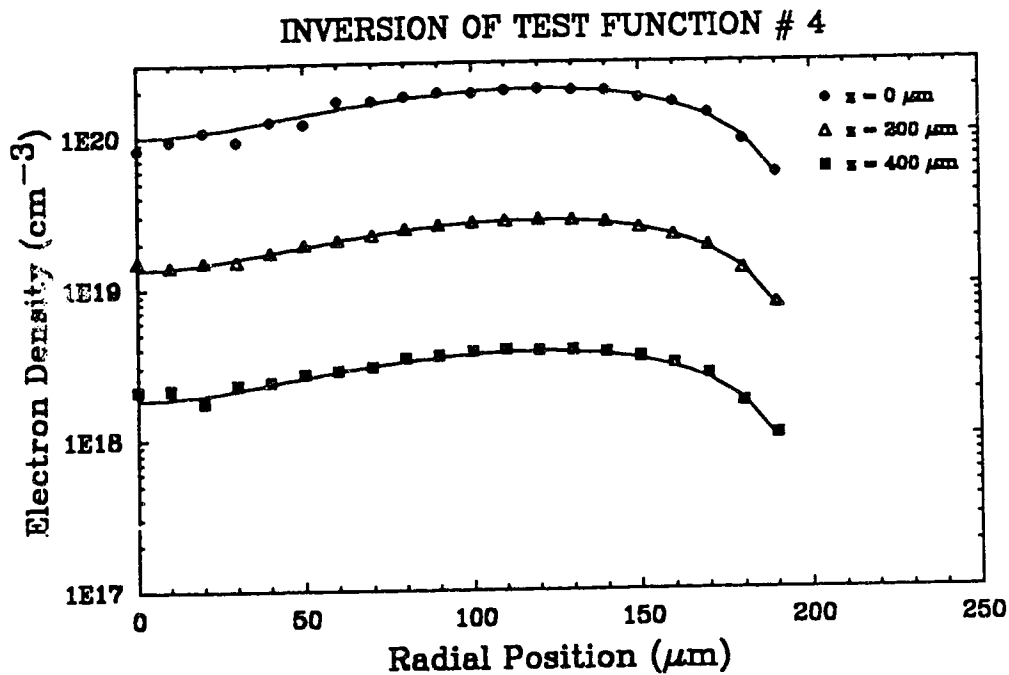


Fig. A.4 (a). Inversion accuracy of test function #4 with zero expansion angle.

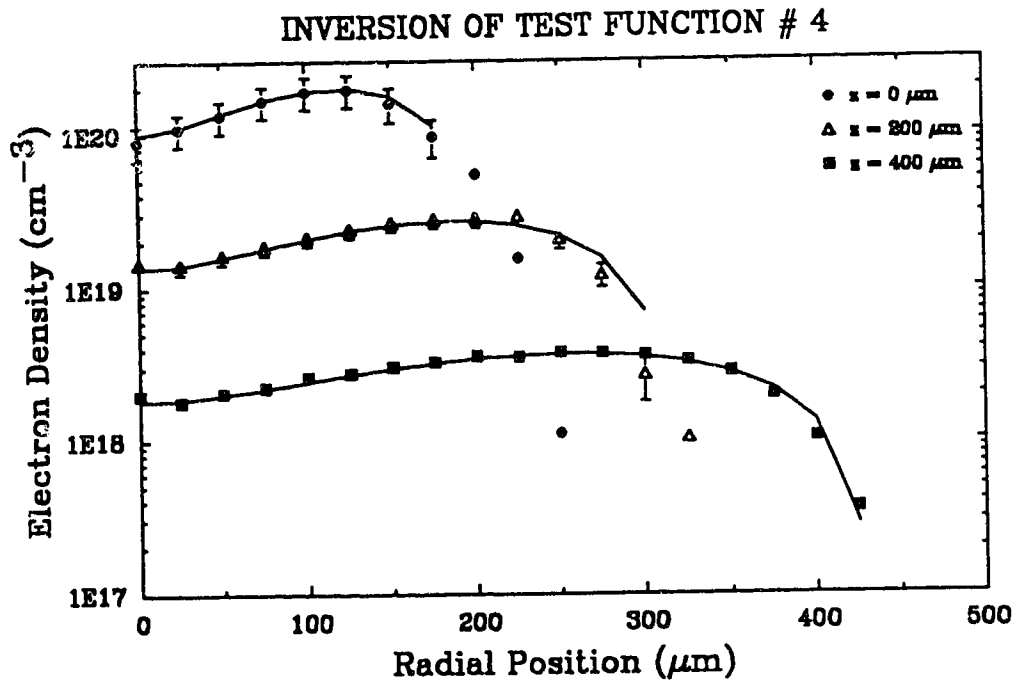


Fig. A.4 (b). Inversion accuracy of test function #4 with 30 degree expansion angle.

A.2 Abel Integrated Test Functions

Following is the integrated form of test function #1:

$$\delta(x, z) = -n_{r_0} \frac{2}{\lambda} e^{-z/L} \quad (A.6)$$

$$\left(\left(\frac{1}{2}(R^2 - x^2)^{1/2} + \frac{x^2}{2R} \ln \left(\frac{R + (R^2 - x^2)^{1/2}}{x} \right) \right) + \right.$$

$$\left. (R^2 - x^2) \right) \quad x < R, x \neq 0$$

$$\delta(0, z) = n_{r_0} \frac{R}{\lambda} e^{-z/L}$$

Following is the integrated form of test function #2:

$$\delta(x, z) = -n_{r_0} \frac{2}{\lambda} e^{-z/L} \quad (A.7)$$

$$\left(\frac{1}{3R^2} (R^2 - x^2)^{3/2} + \frac{x^2}{R^2} (R^2 - x^2)^{1/2} + (R^2 - x^2)^{1/2} \right)$$

Following is the integrated form of test function #3:

$$\delta(x, z) = -n_{r_0} \frac{1}{\lambda} \pi^{1/2} e^{-z/L} \left(e^{-x^2/l^2} \right) \quad (A.8)$$

Following is the integrated form of test function #4:

$$\delta(x, z) = n_{r_0} \frac{2}{\lambda} e^{-z/L} \left((R^2 - x^2)^{1/2} \quad (A.8)$$

$$+ \frac{a}{R^2} \left(\frac{1}{3}(R^2 - x^2)^{3/2} + x^2 (R^2 - x^2)^{1/2} \right)$$

$$- \frac{3b}{8R^3} \left((R^2 - x^2)^{1/2} \left(x^2 R + \frac{2}{3} R^3 \right) + \right.$$

$$\left. x^4 \ln \left(\frac{R + (R^2 - x^2)^{1/2}}{x} \right) \right) \quad x < R, x \neq 0$$

$$\delta(0, z) = n_{r_0} \frac{2}{\lambda} e^{-z/L} R \left(1 + \frac{a}{3} - \frac{b}{4} \right)$$

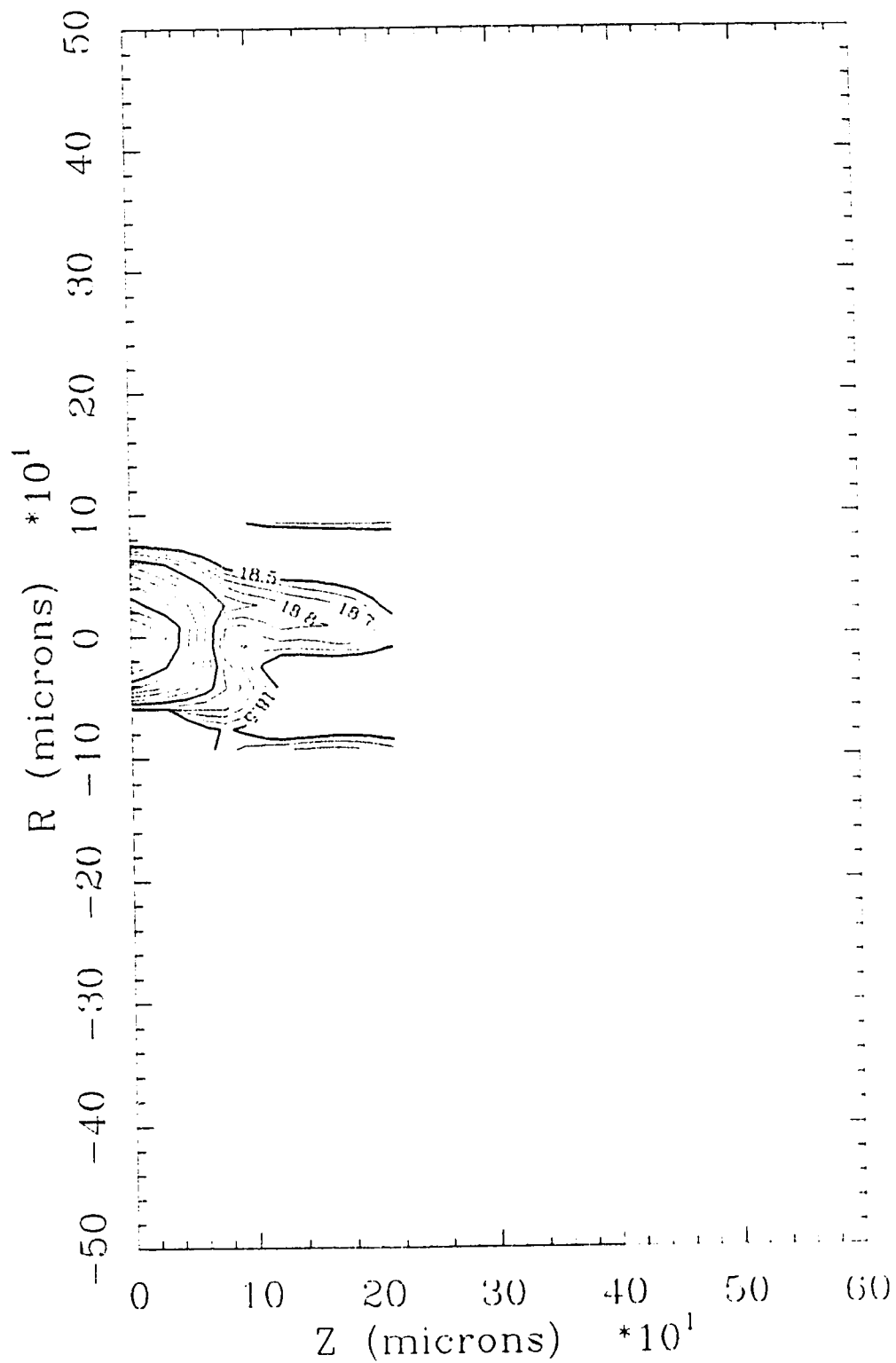
APPENDIX B

CONTOURS OF KrF LASER-PLASMA

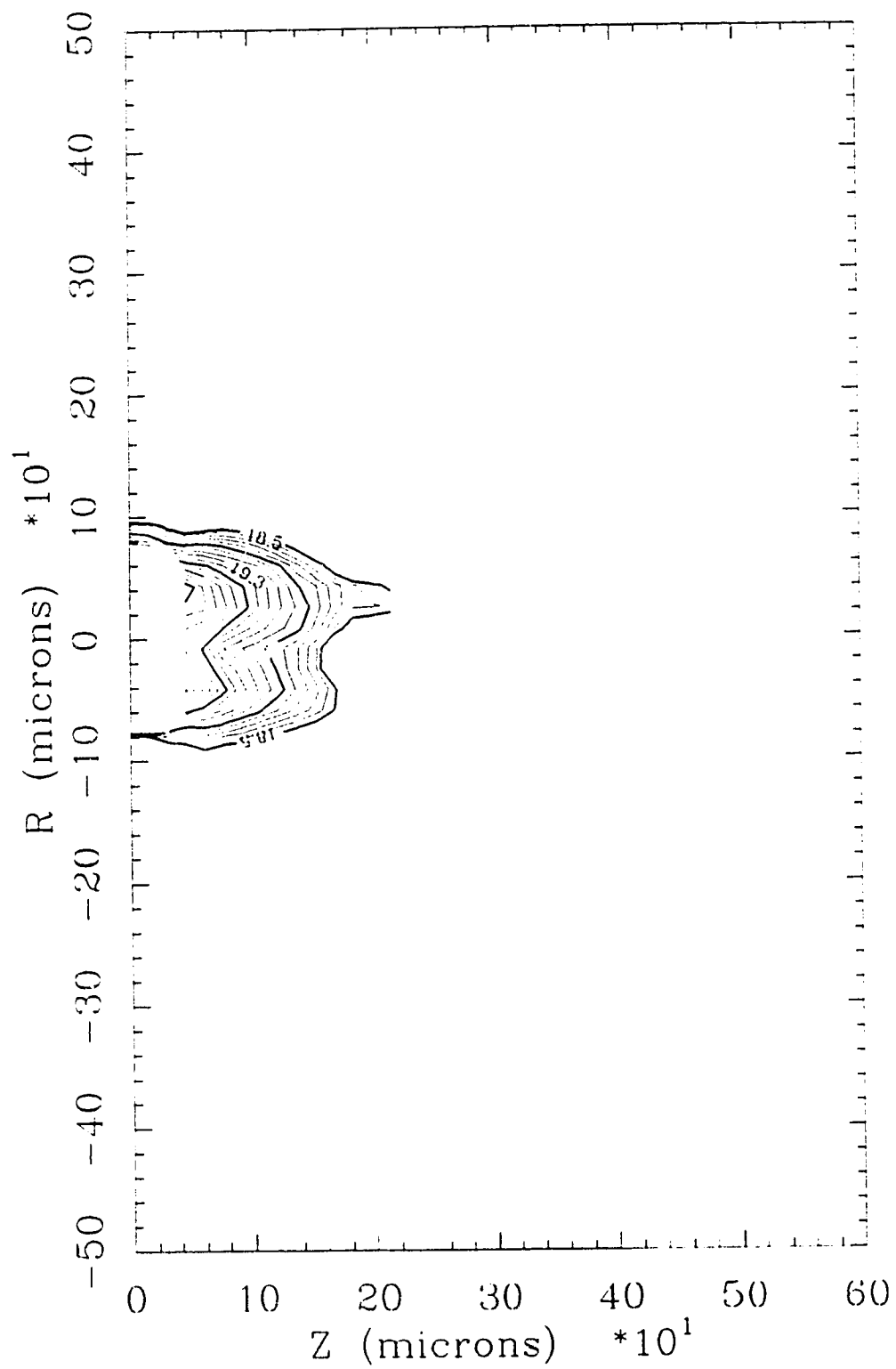
Following are the electron density contour plots for all of the fully analysable interferograms obtained for this thesis. The electron density was determined by 20 point weighted assymetrical Bockasten inversion with smoothing and the contours represent the logarithm, base ten, of the density in units of cm^{-3} .

On the plots "TIME" refers to the probing time as defined in chapter 3, "FWHM" refers to the width of the main laser pulse, and "ENERGY" refers to the energy of the main laser pulse. A value of -99 for any of these indicates that the particular information is unknown.

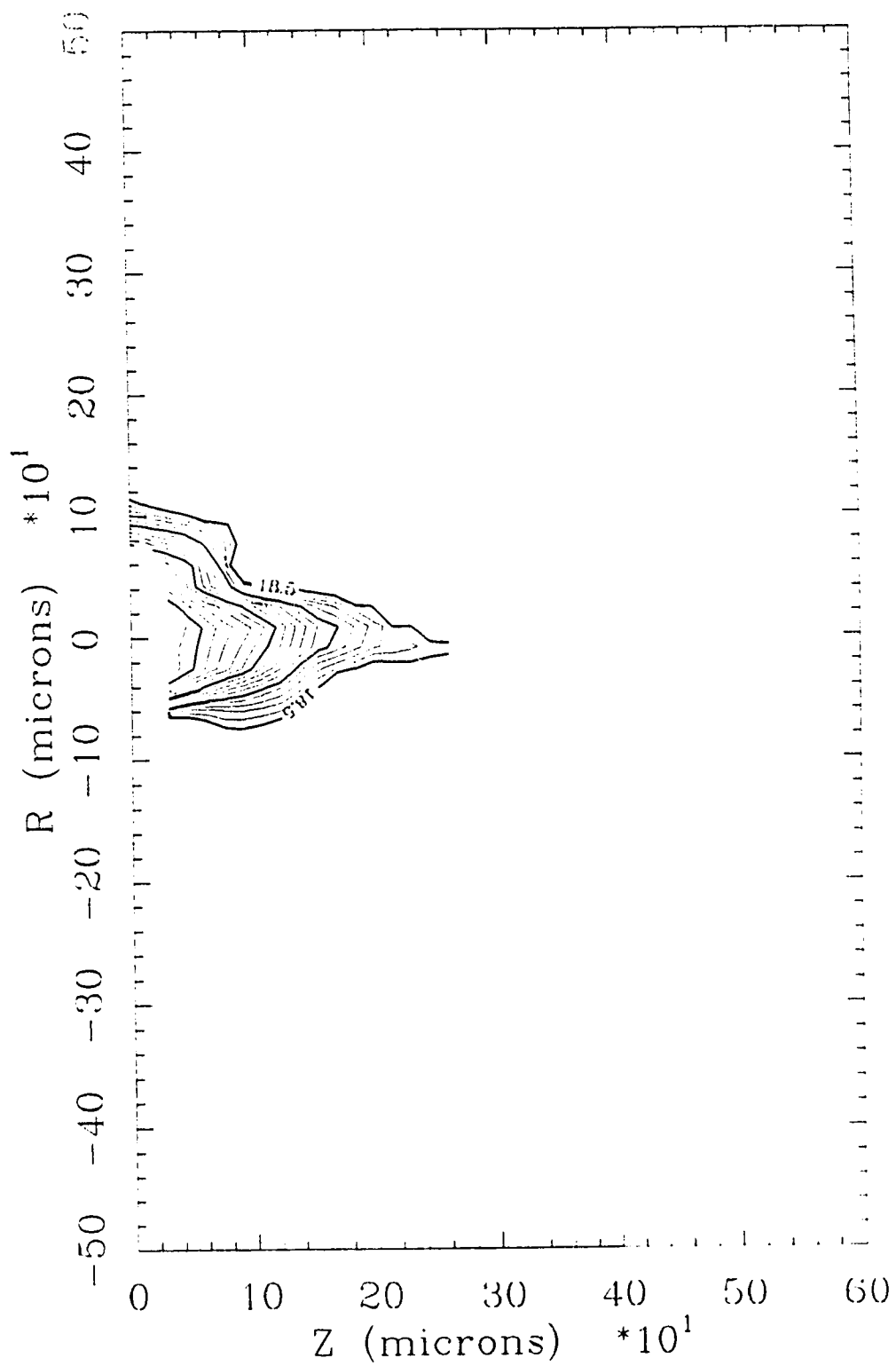
SHOT # 21078823
ENERGY = 536 mJ
FWHM = 2.4 ns
TIME = -4 ns



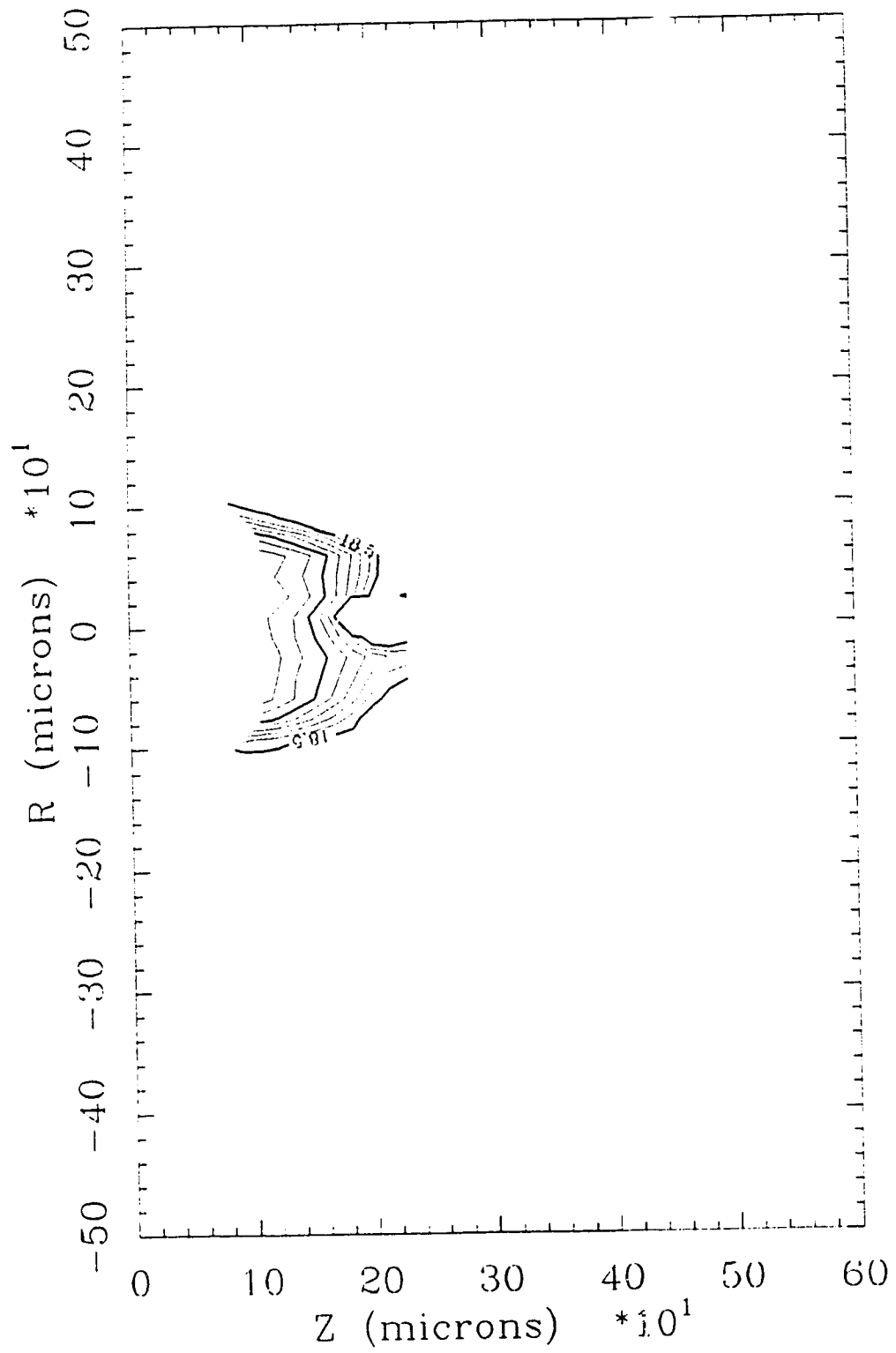
SHOT # 14108807
ENERGY = 353 mJ
FWHM = -99.0 ns
TIME = -3 ns



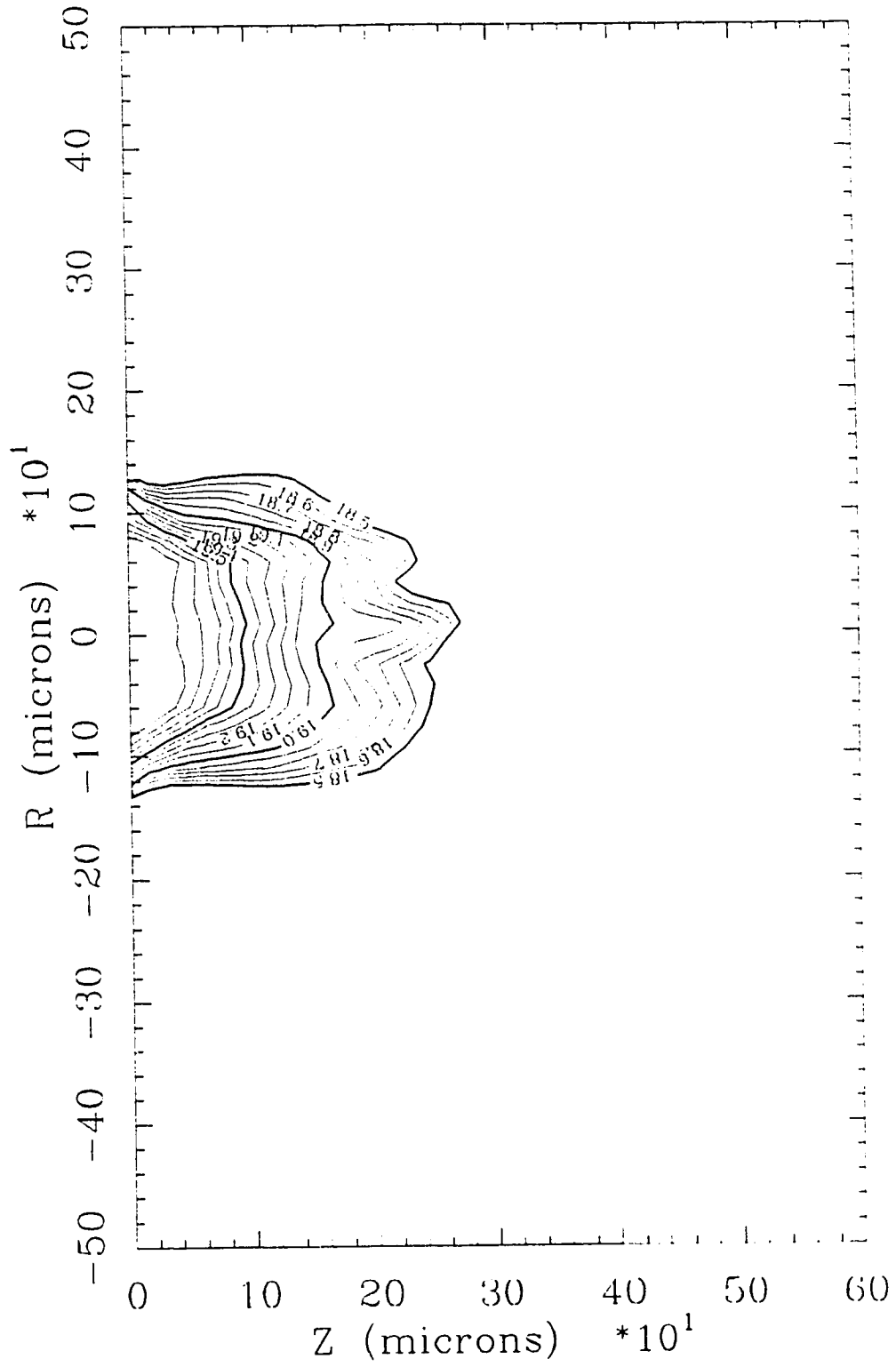
SHOT # 21078813
ENERGY = 241 mJ
FWHM = 1.6 ns
TIME = -1 ns



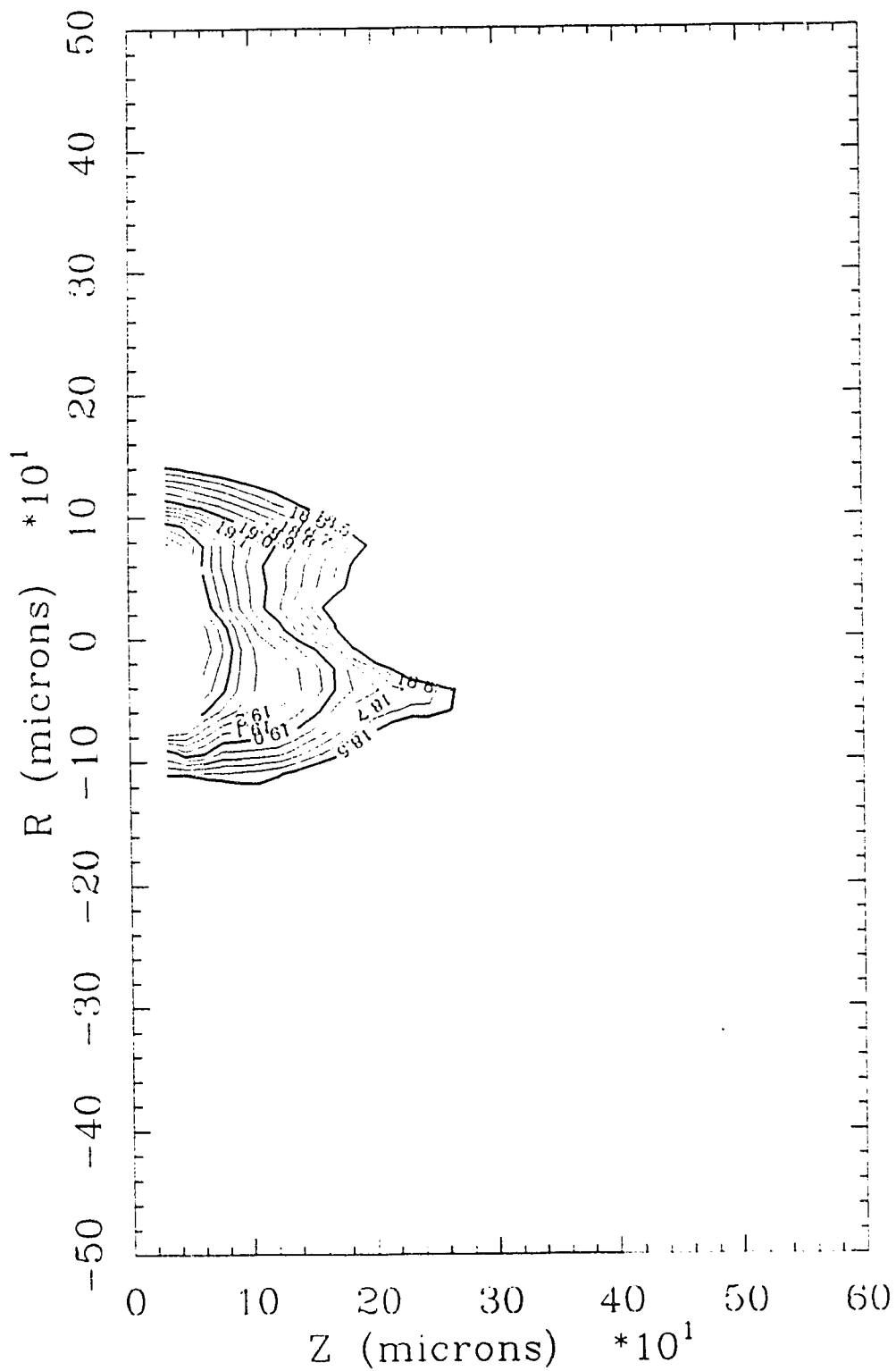
SHOT # 14108804
ENERGY = 1141 mJ
FWHM = 1.5 ns
TIME = .1 ns



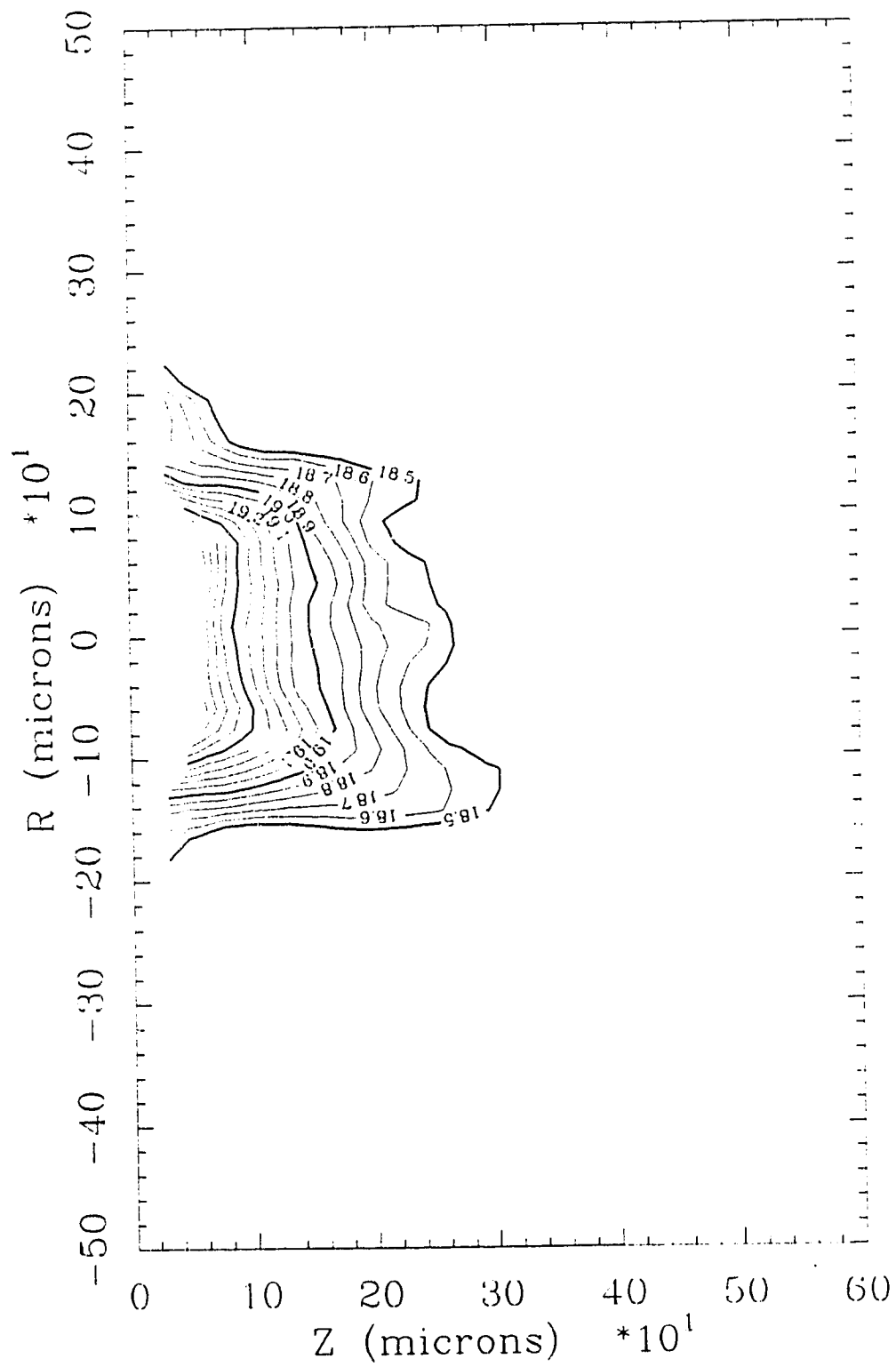
SHOT # 21079830
ENERGY = 186 mJ
FWHM = 1.9 ns
TIME = .3 ns



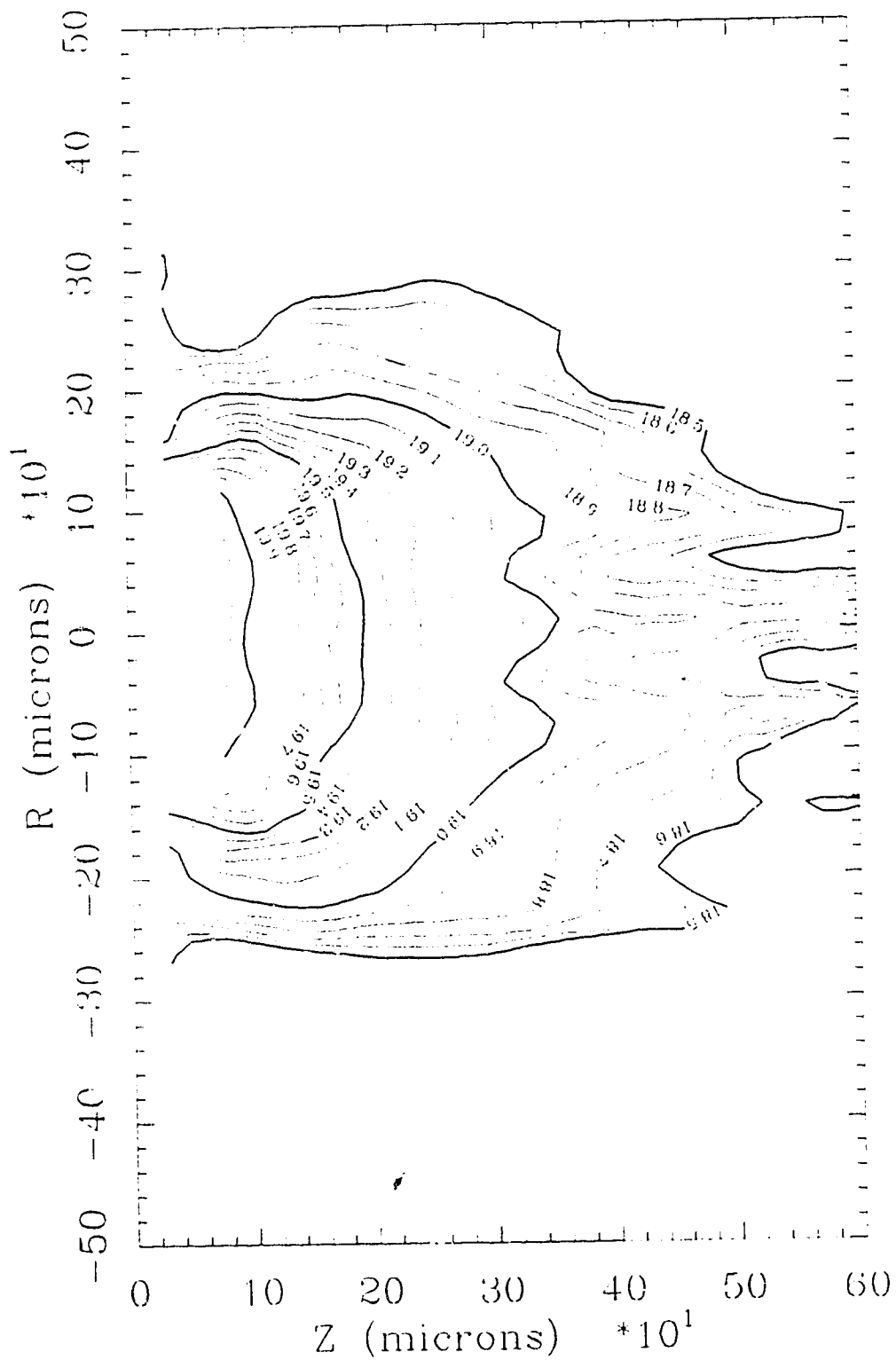
SHOT # 21078811
ENERGY = 233 mJ
FWHM = -99.0 ns
TIME = .3 ns



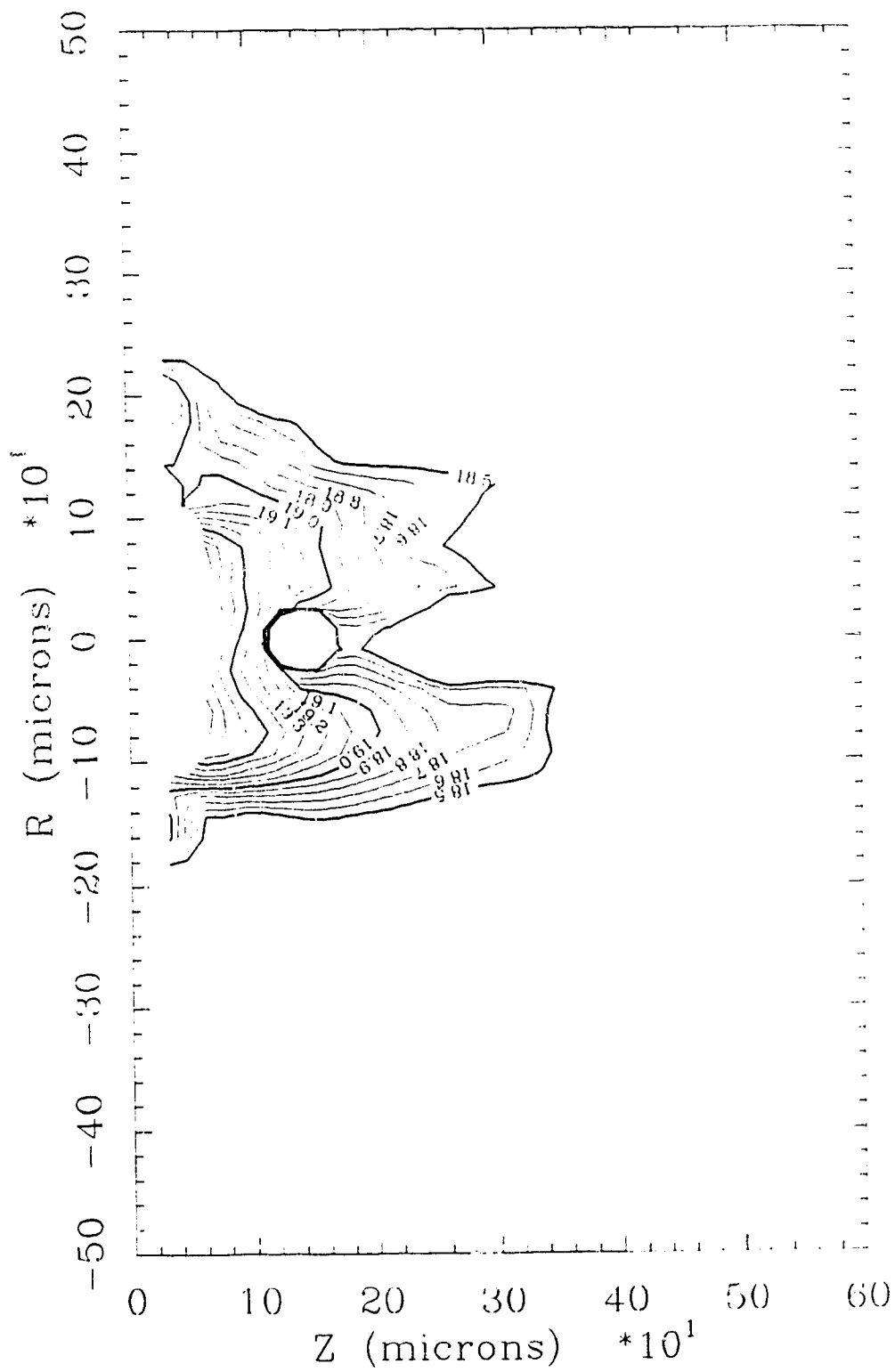
SHOT # 22078824
ENERGY = 271 mJ
FWHM = 2.4 ns
TIME = .7 ns



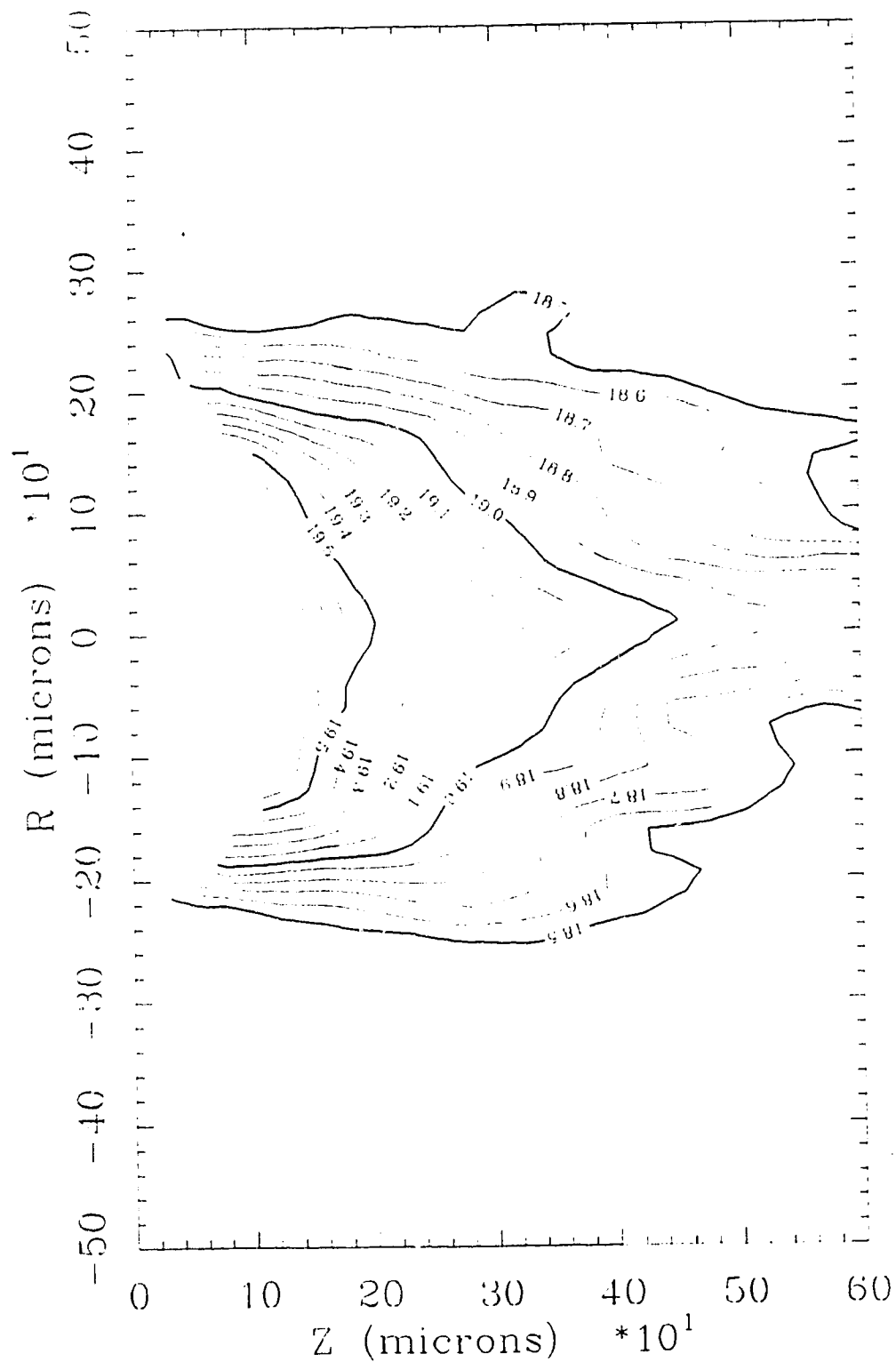
SHOT # 14108803
ENERGY = 1430 mJ
FWHM = 1.5 ns
TIME = 1.3 ns



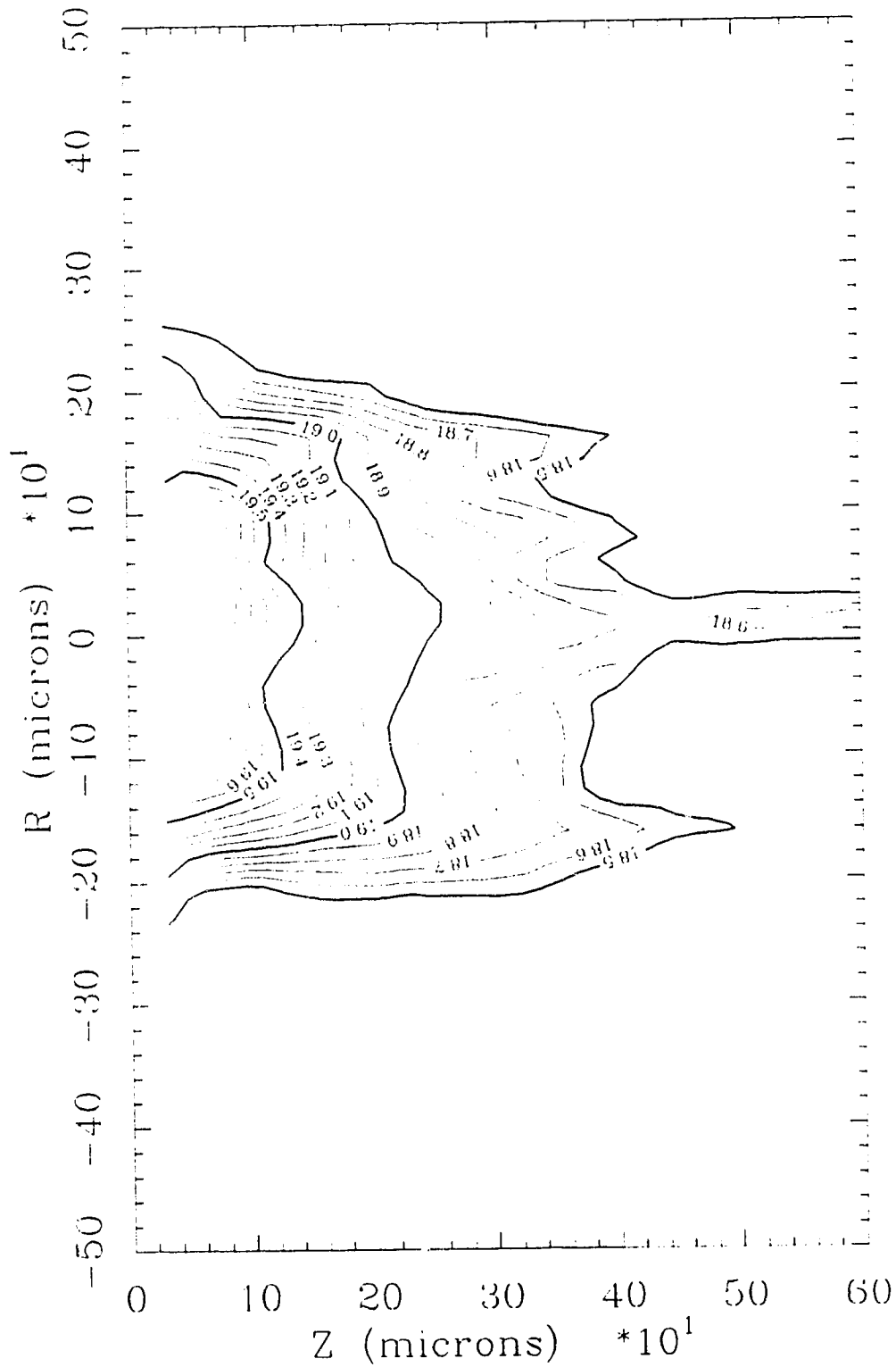
SHOT # 12108807
ENERGY = 187 mJ
FWHM = -99.0 ns
TIME = 1.5 ns



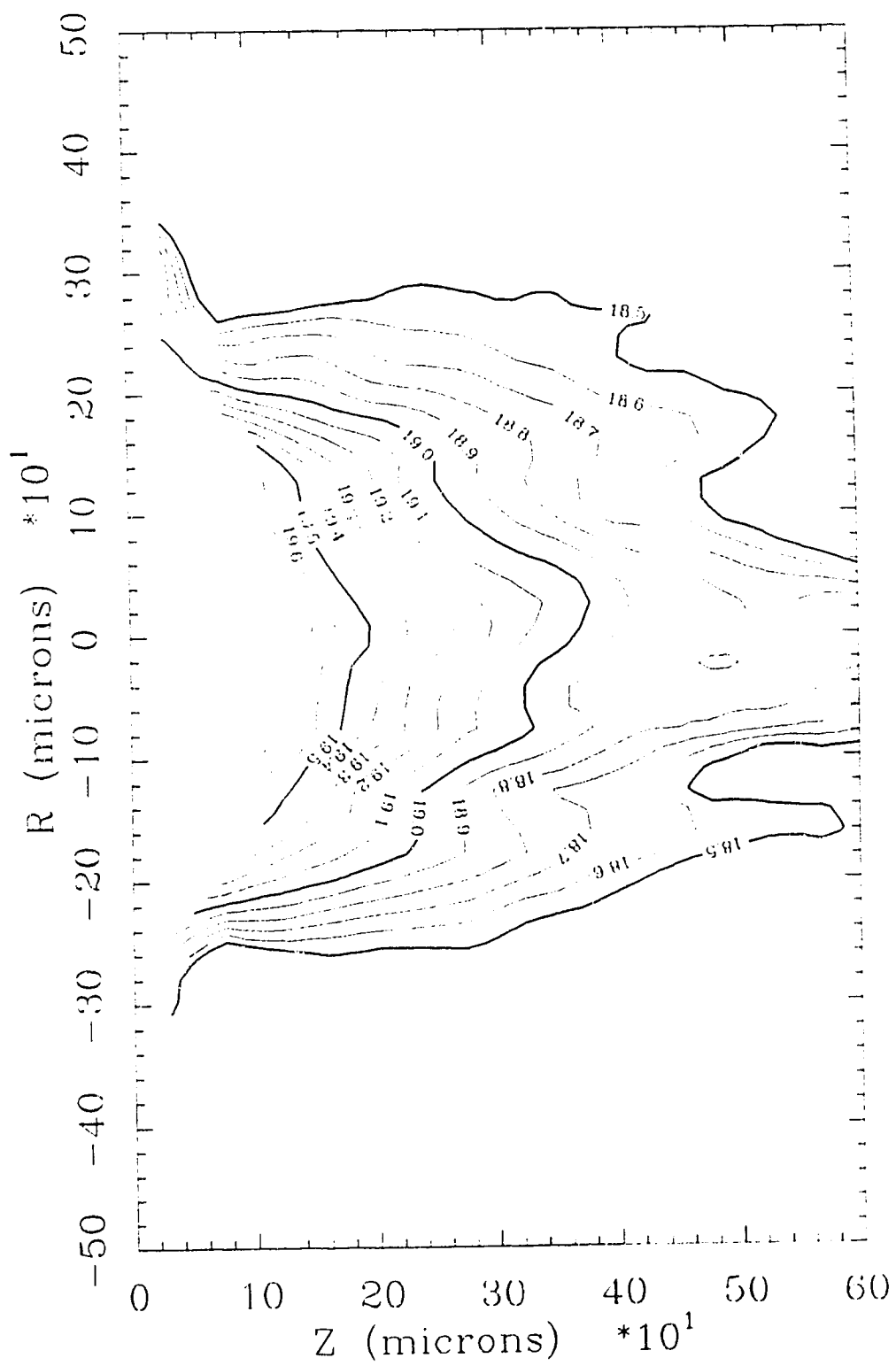
SHOT # 14108808
ENERGY = 1154 mJ
FWHM = 1.7 ns
TIME = 1.5 ns



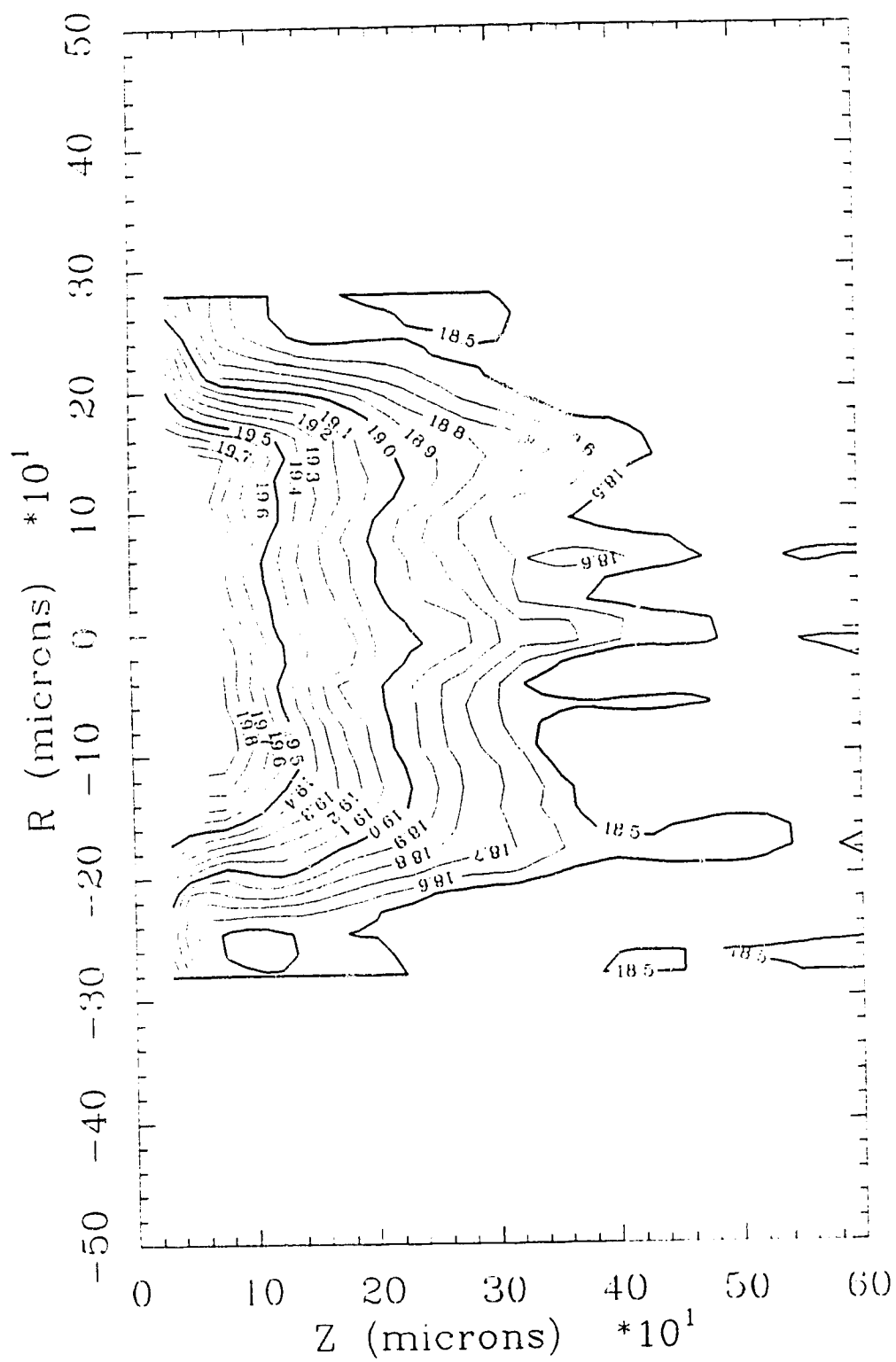
SHOT # 12108808
ENERGY = 722 mJ
FWHM = 2.5 ns
TIME = 1.8 ns



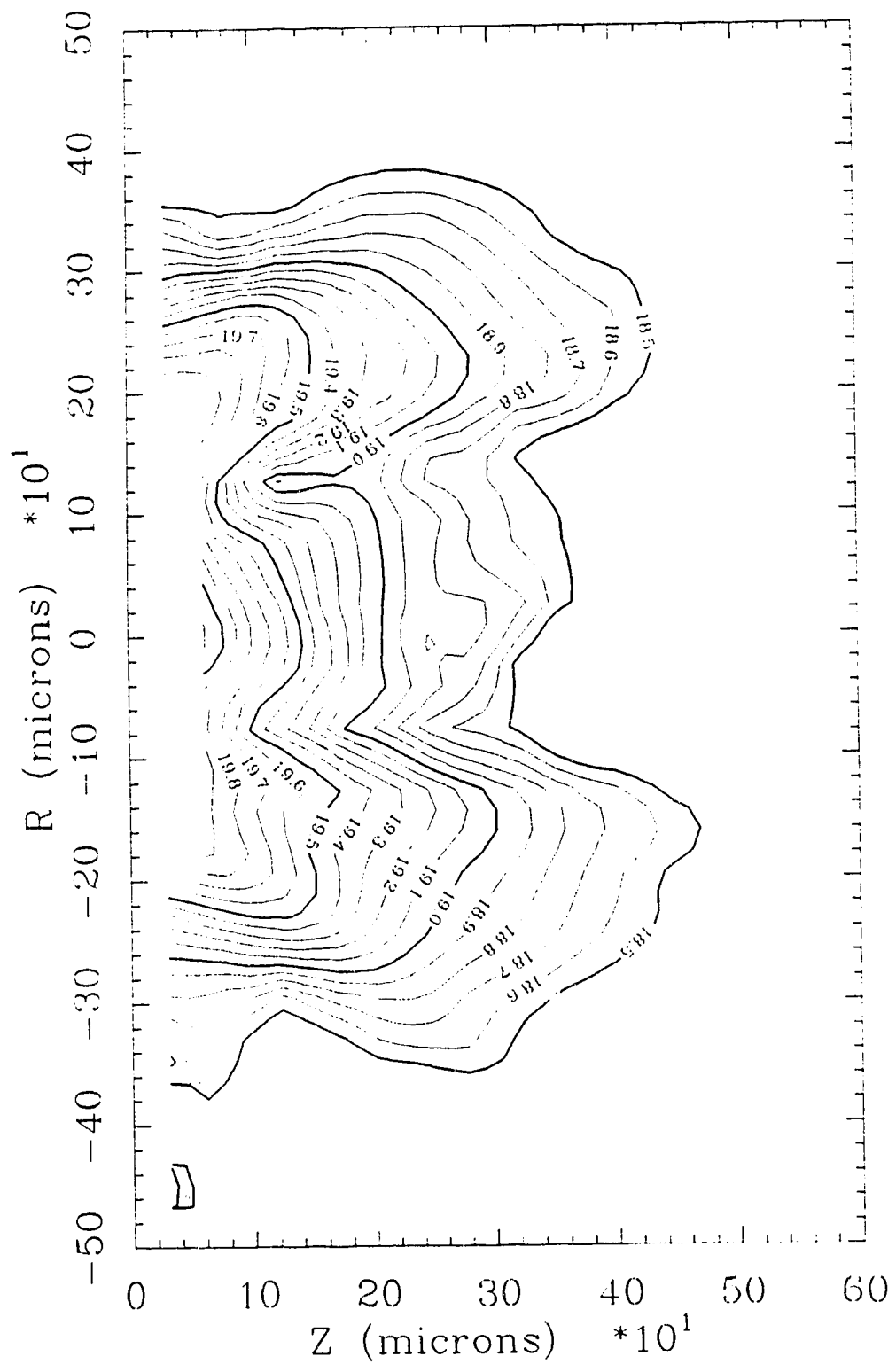
SHOT # 14108802
ENERGY = 1647 mJ
FWHM = -99.0 ns
TIME = 2.2 ns



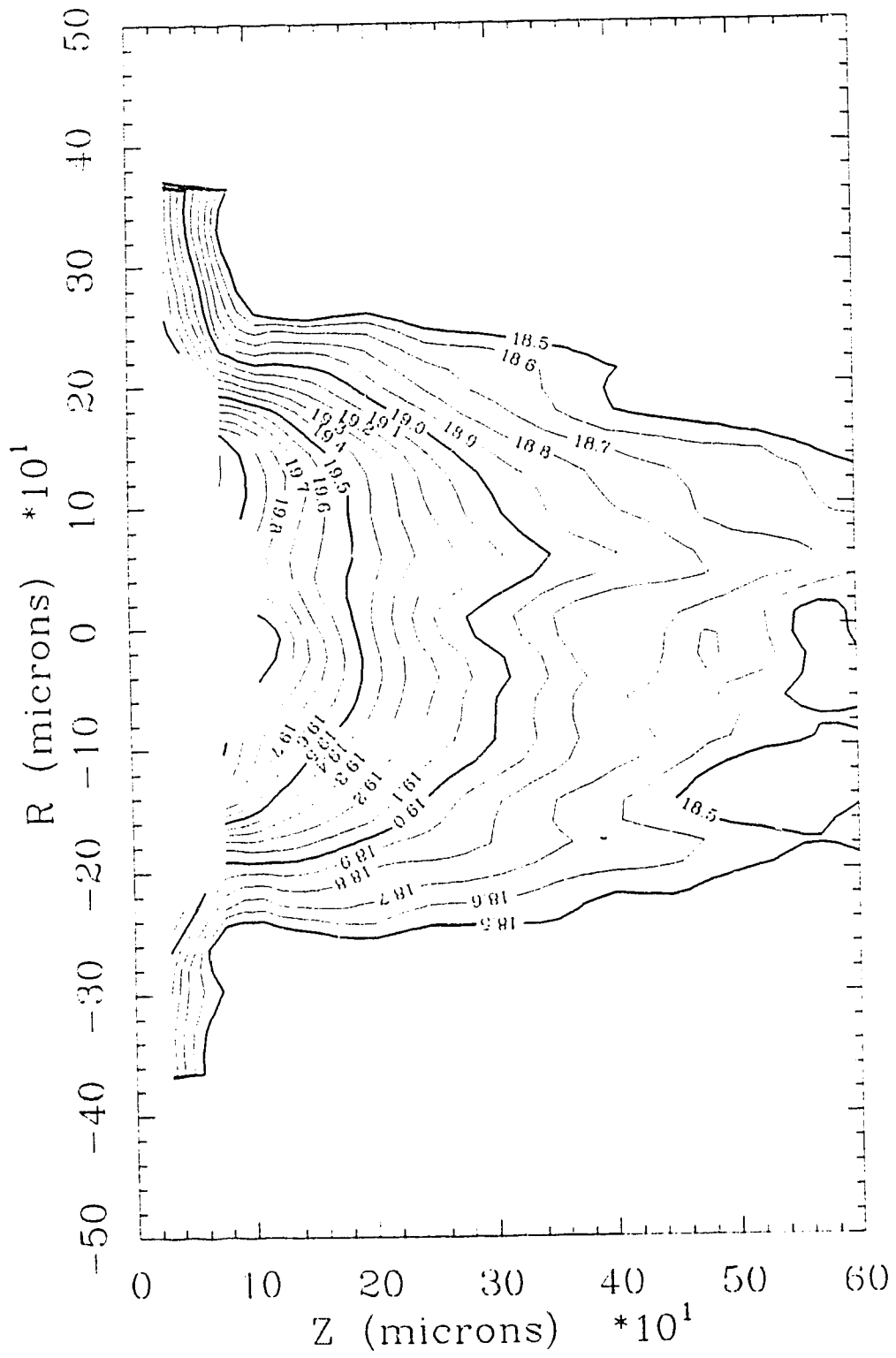
SHOT # 28078801
ENERGY = 280 mJ
FWHM = 2.5 ns
TIME = 2.4 ns



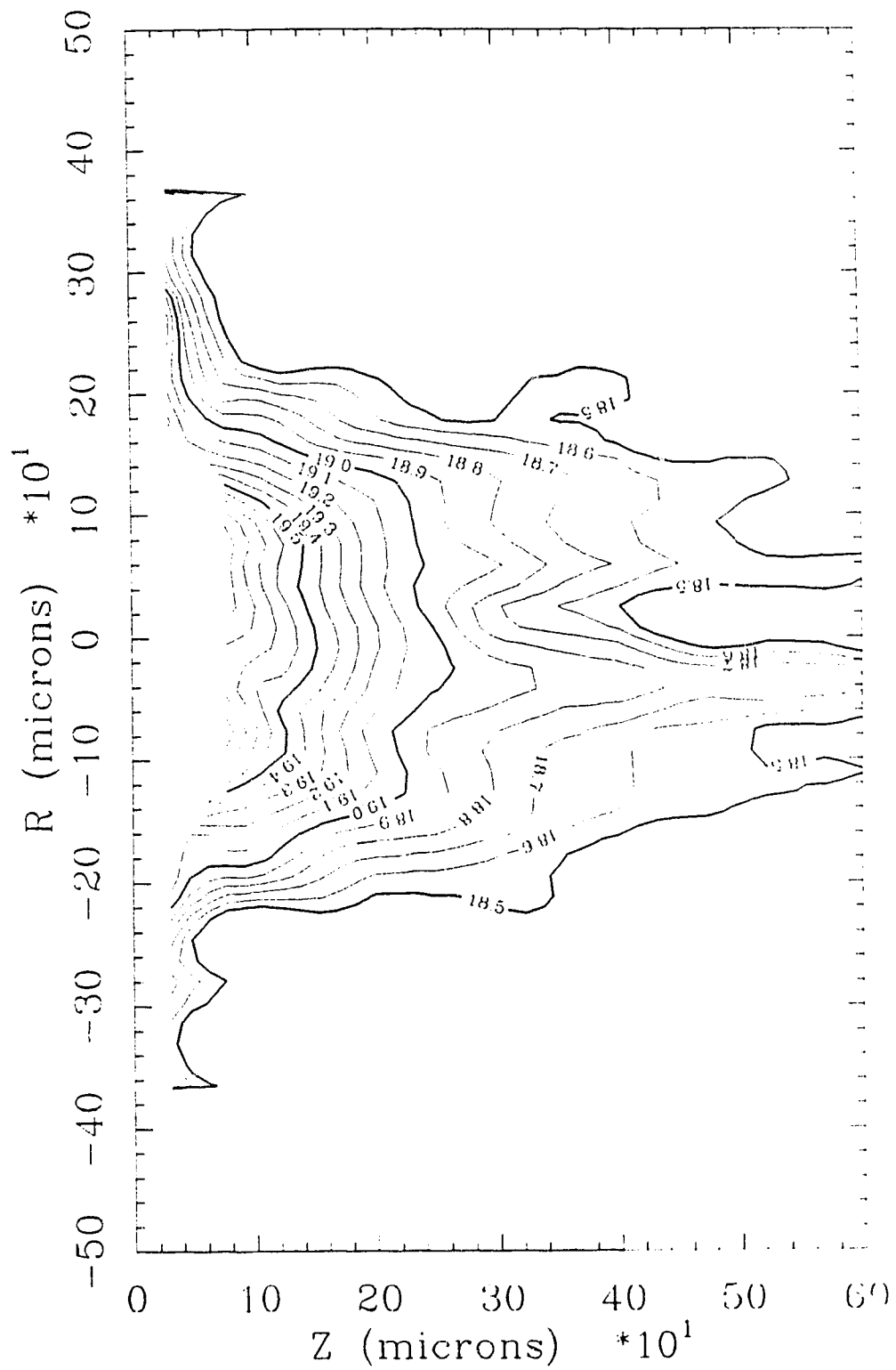
SHOT # 20078812
ENERGY = 256 mJ
FWHM = 1.4 ns
TIME = 2.5 ns



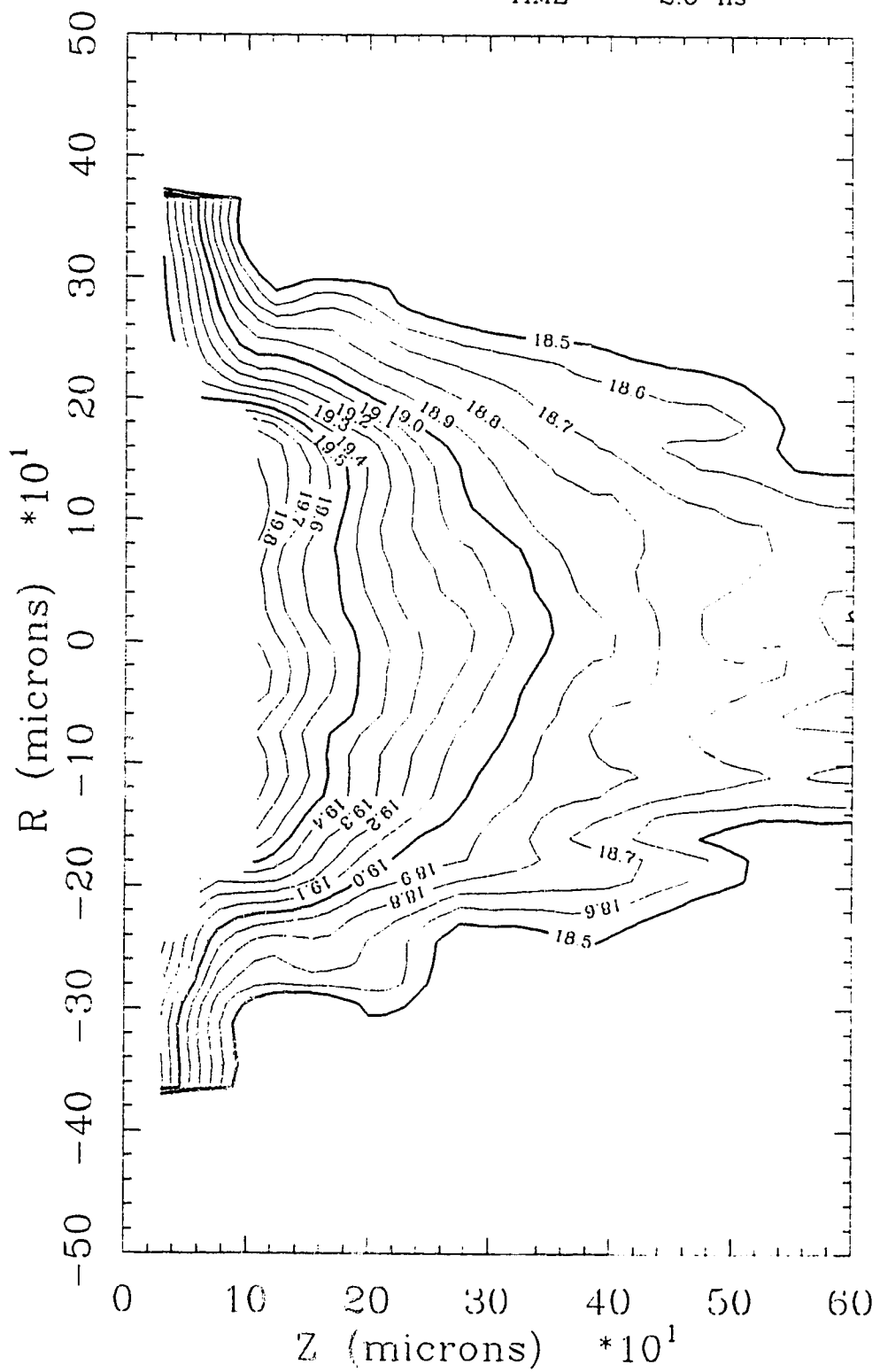
SHOT # 21078819
ENERGY = 521 mJ
FWHM = 1.5 ns
TIME = 2.5 ns



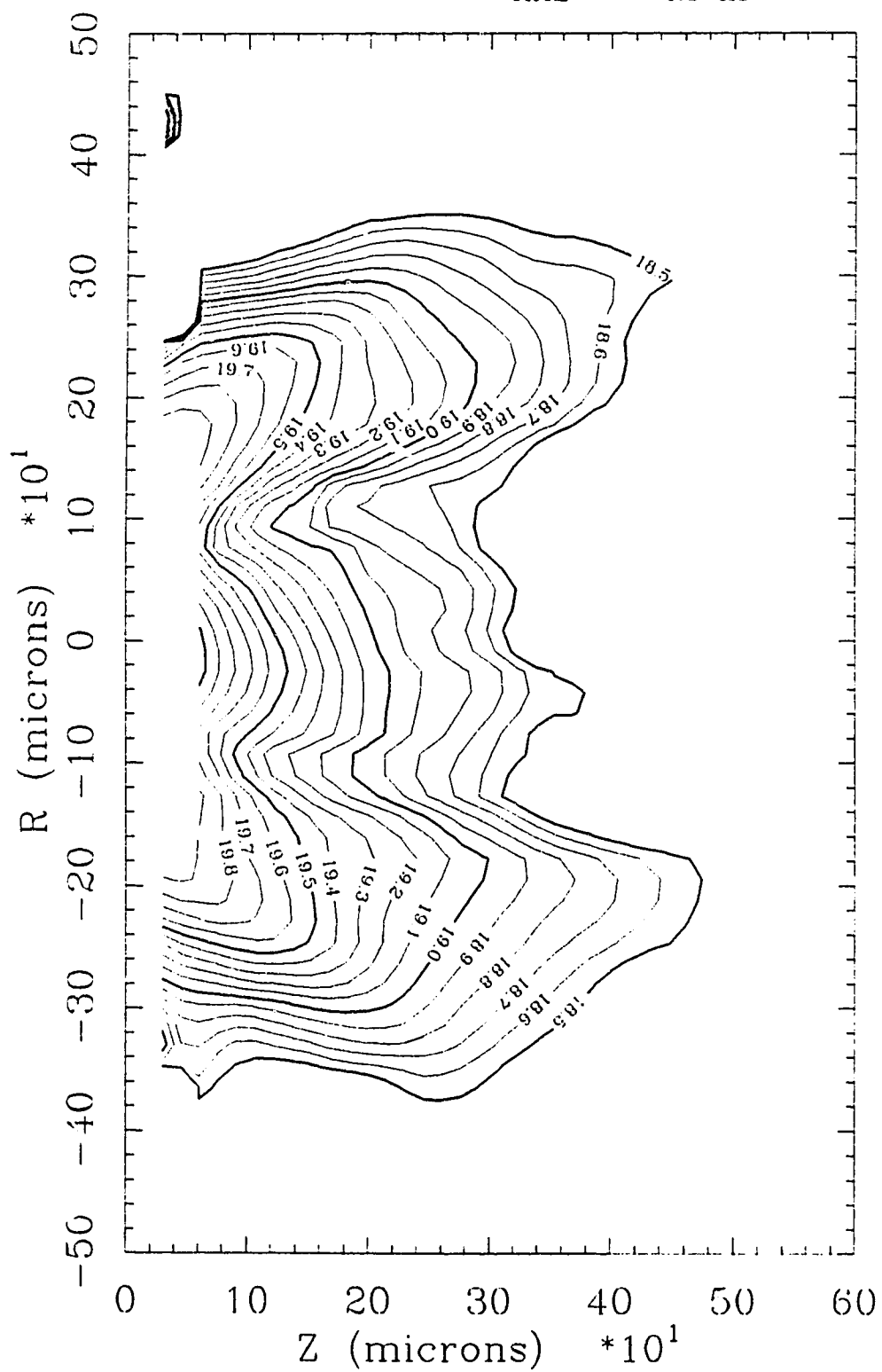
SHOT # 22078804
ENERGY = 233 mJ
FWHM = 2.2 ns
TIME = 2.6 ns



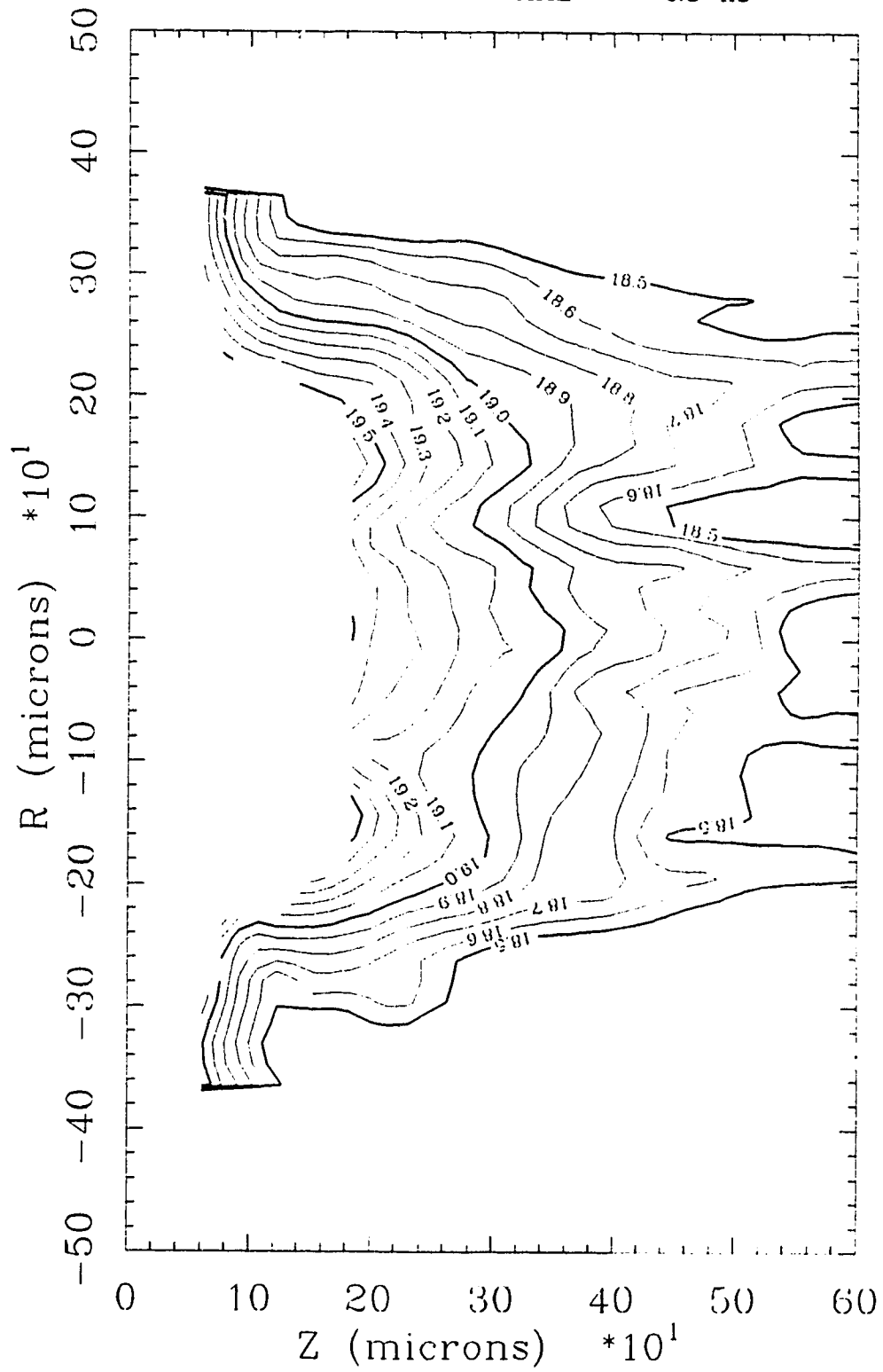
SHOT # 21078816
ENERGY = 552 mJ
FWHM = 1.7 ns
TIME = 2.6 ns



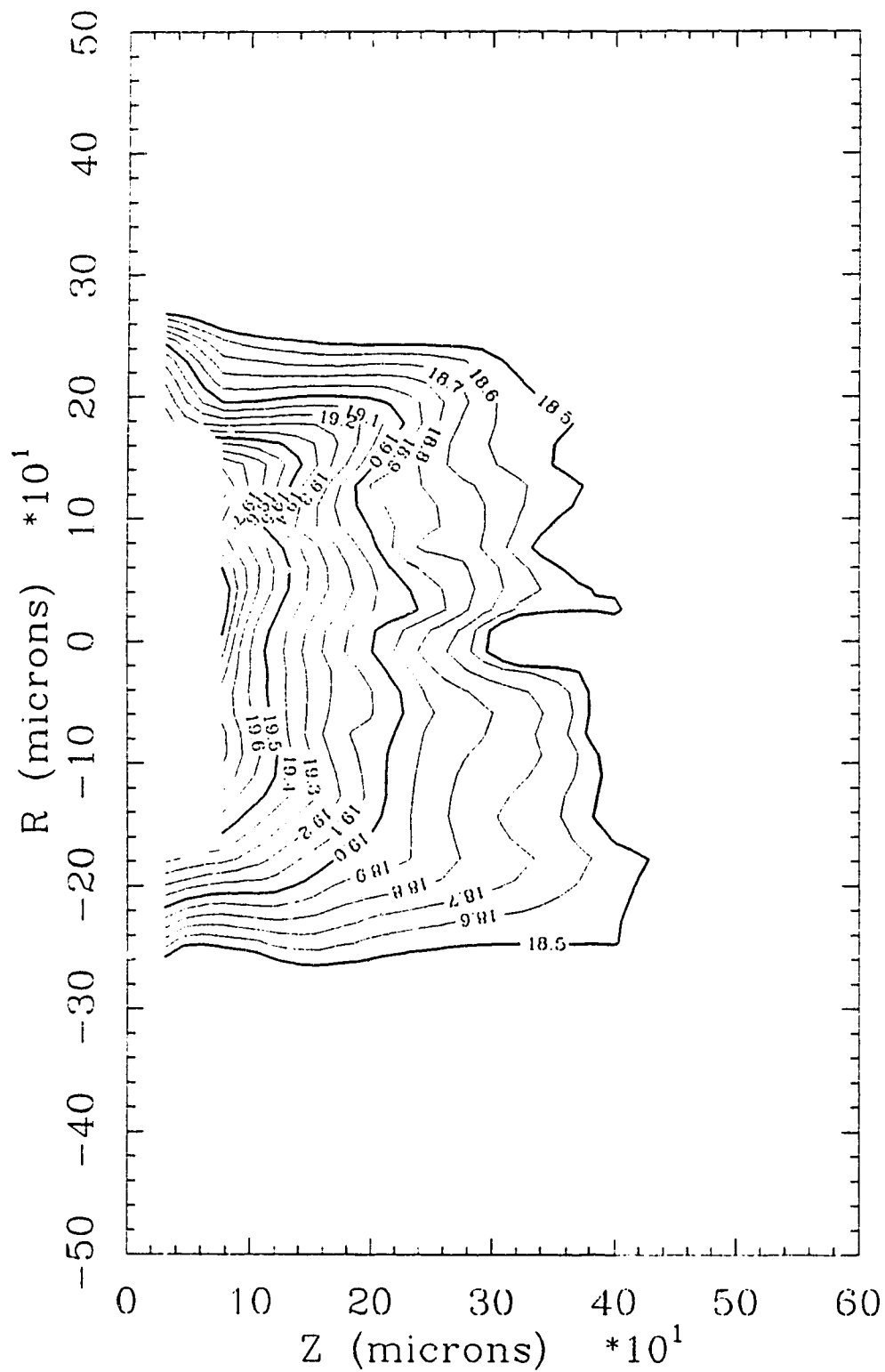
SHOT # 20078815
ENERGY = 264 mJ
FWHM = 1.6 ns
TIME = 2.8 ns



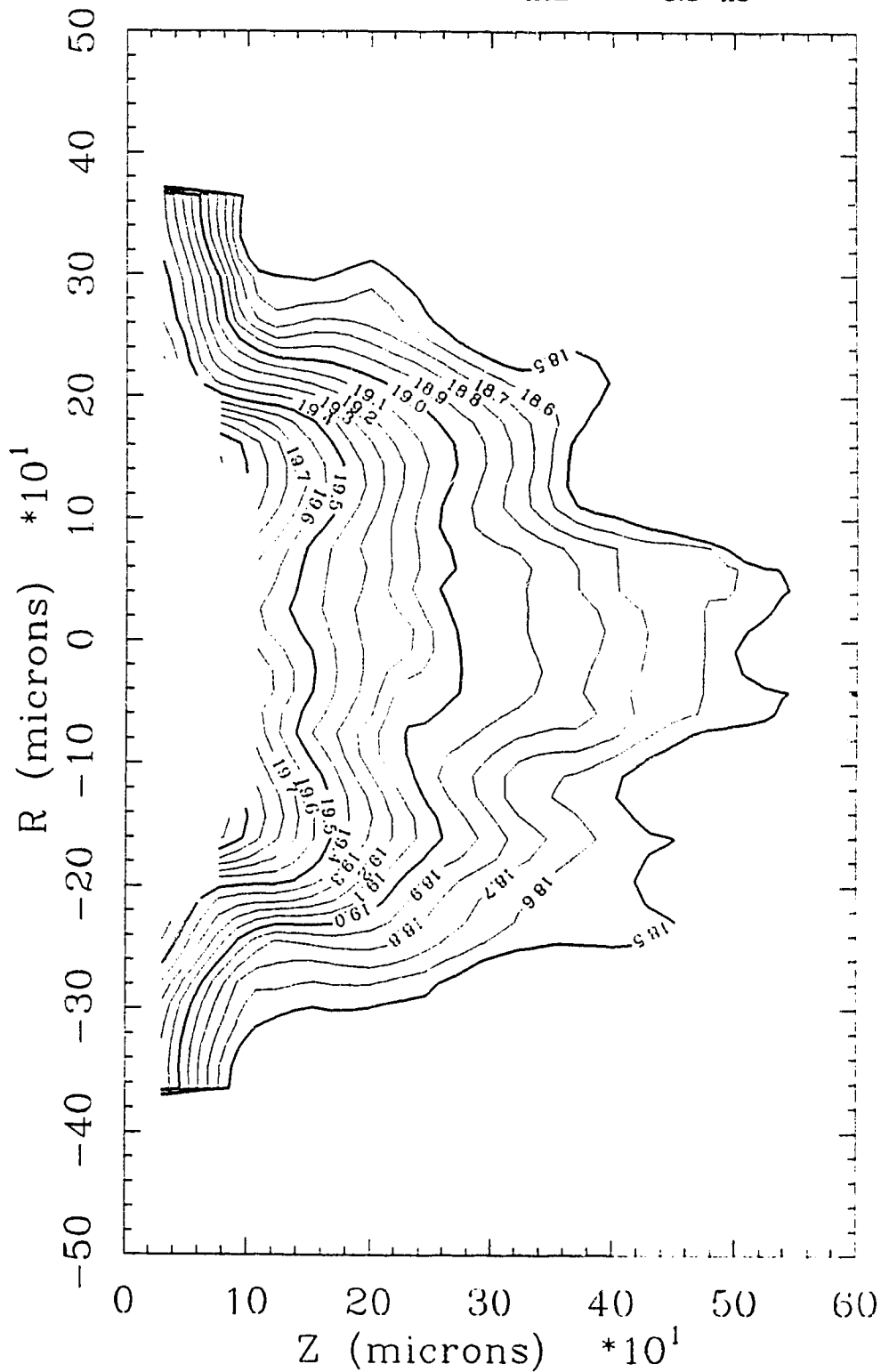
SHOT # 25078803
ENERGY = 956 mJ
FWHM = -99.0 ns
TIME = 2.8 ns



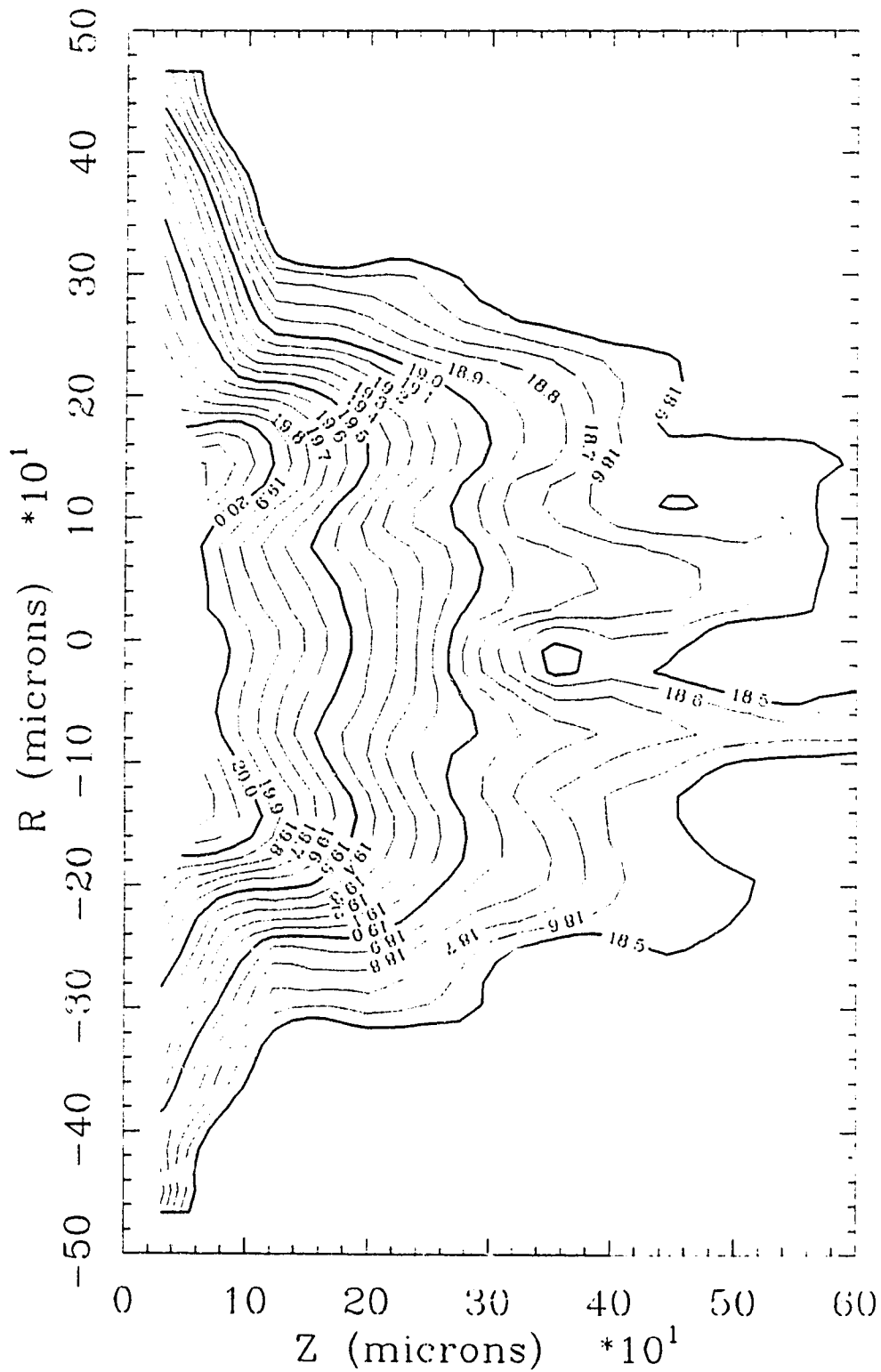
SHOT # 12108811
ENERGY = 653 mJ
FWHM = 2.8 ns
TIME = 3.2 ns



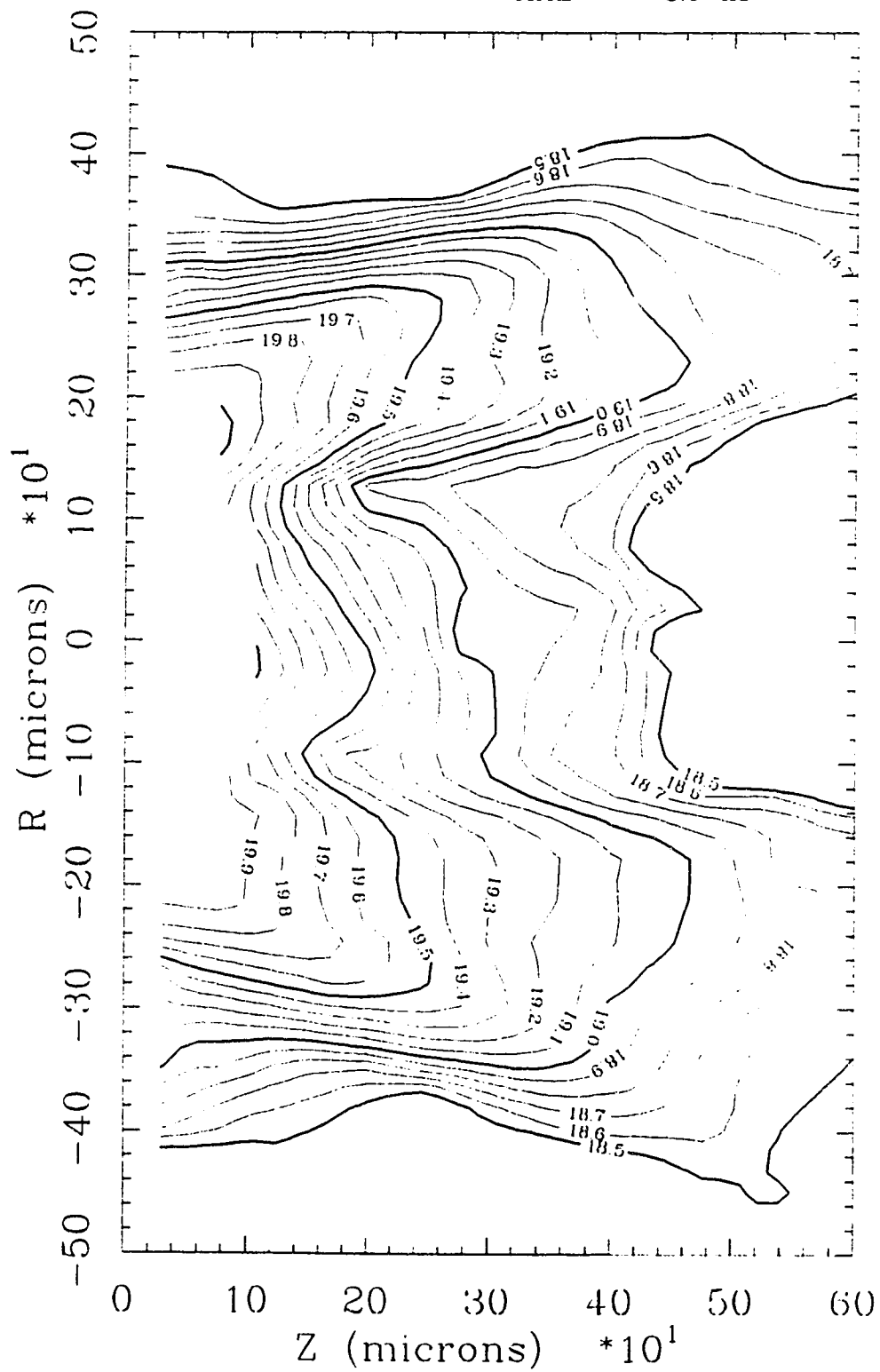
SHOT # 21078809
ENERGY = 466 mJ
FWHM = 1.5 ns
TIME = 3.3 ns



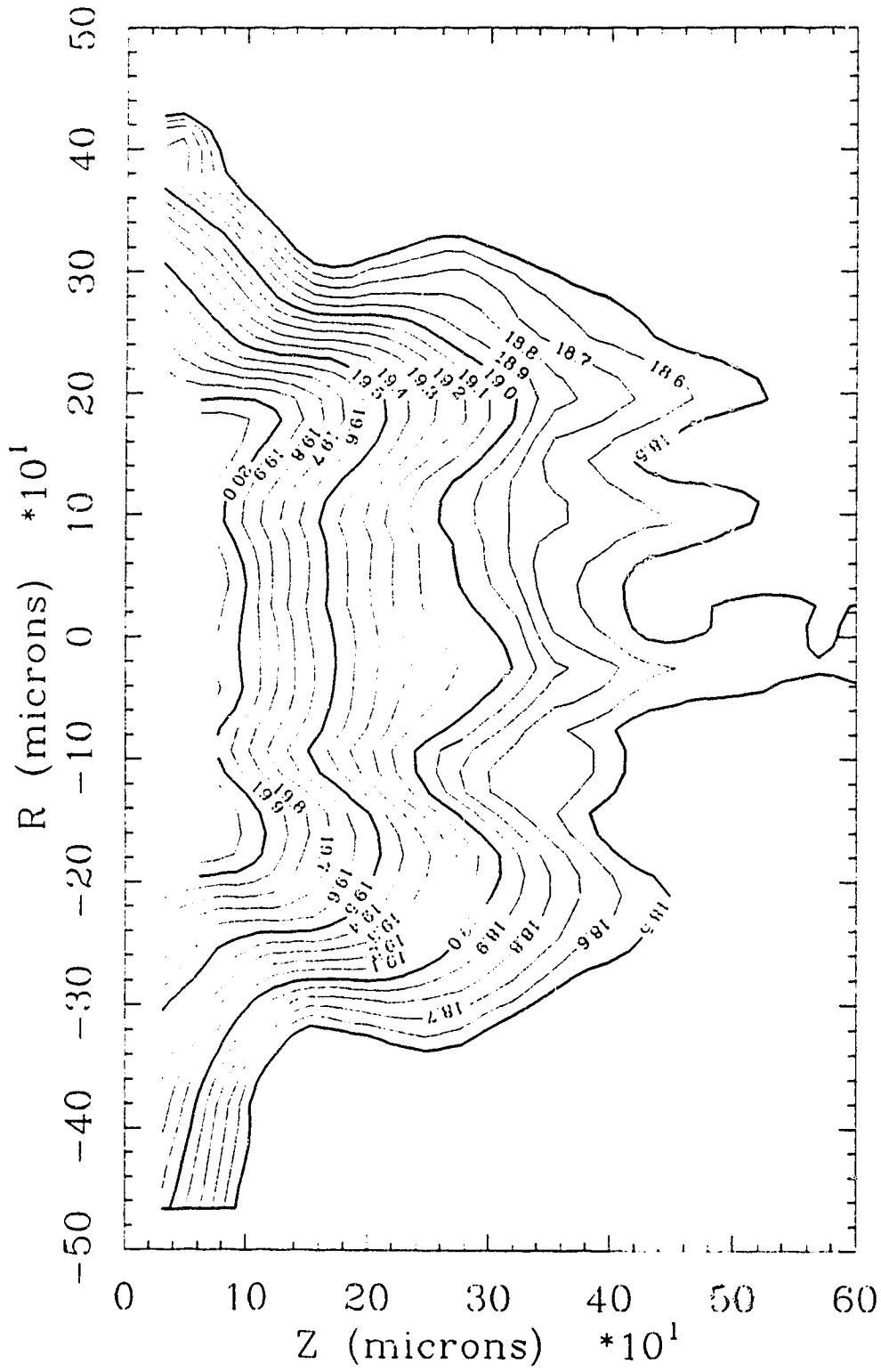
SHOT # 21078814
ENERGY = 653 mJ
FWHM = -99.0 ns
TIME = 3.5 ns



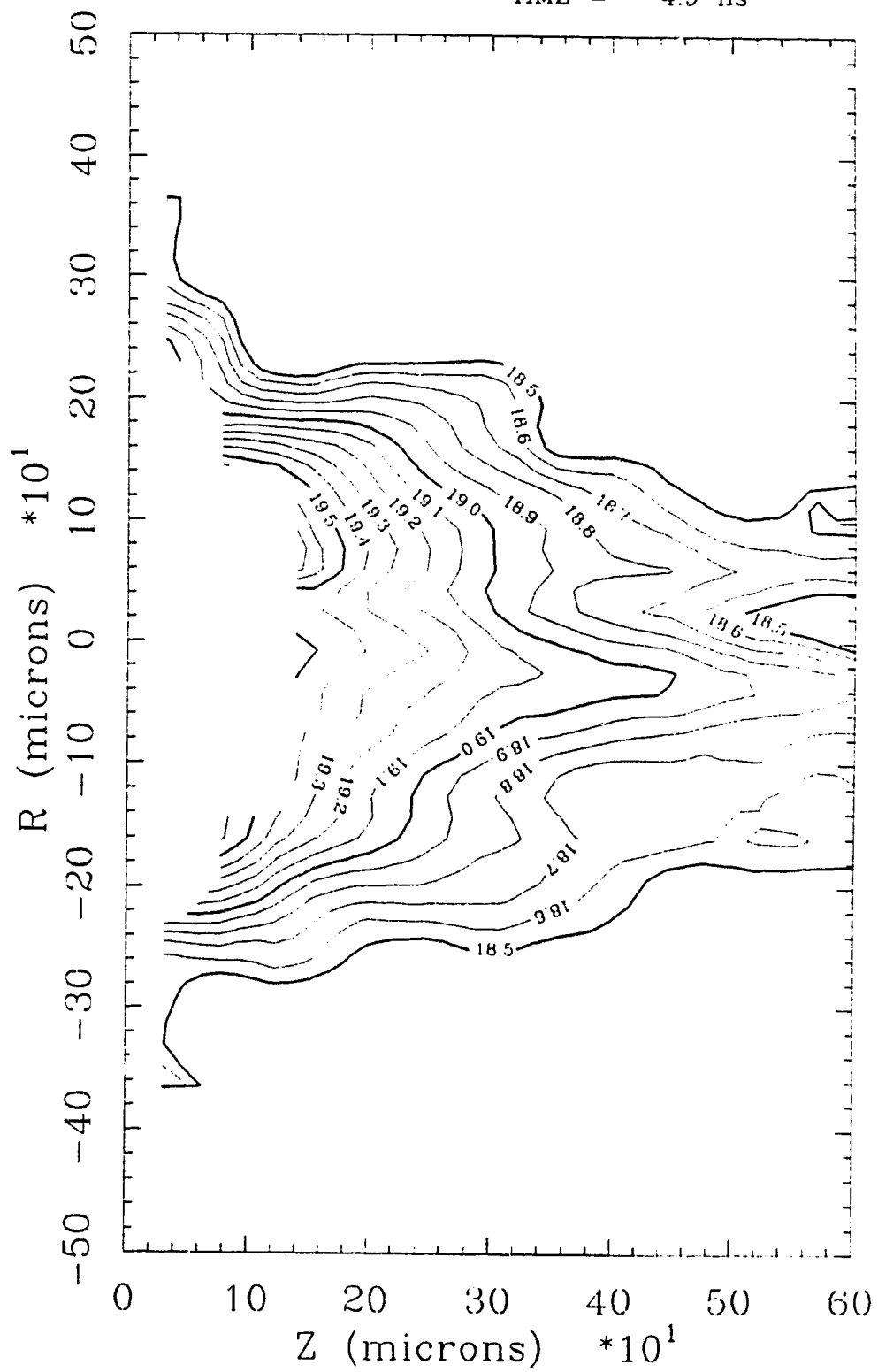
SHOT # 20078817
ENERGY = 404 mJ
FWHM = 1.6 ns
TIME = 3.9 ns



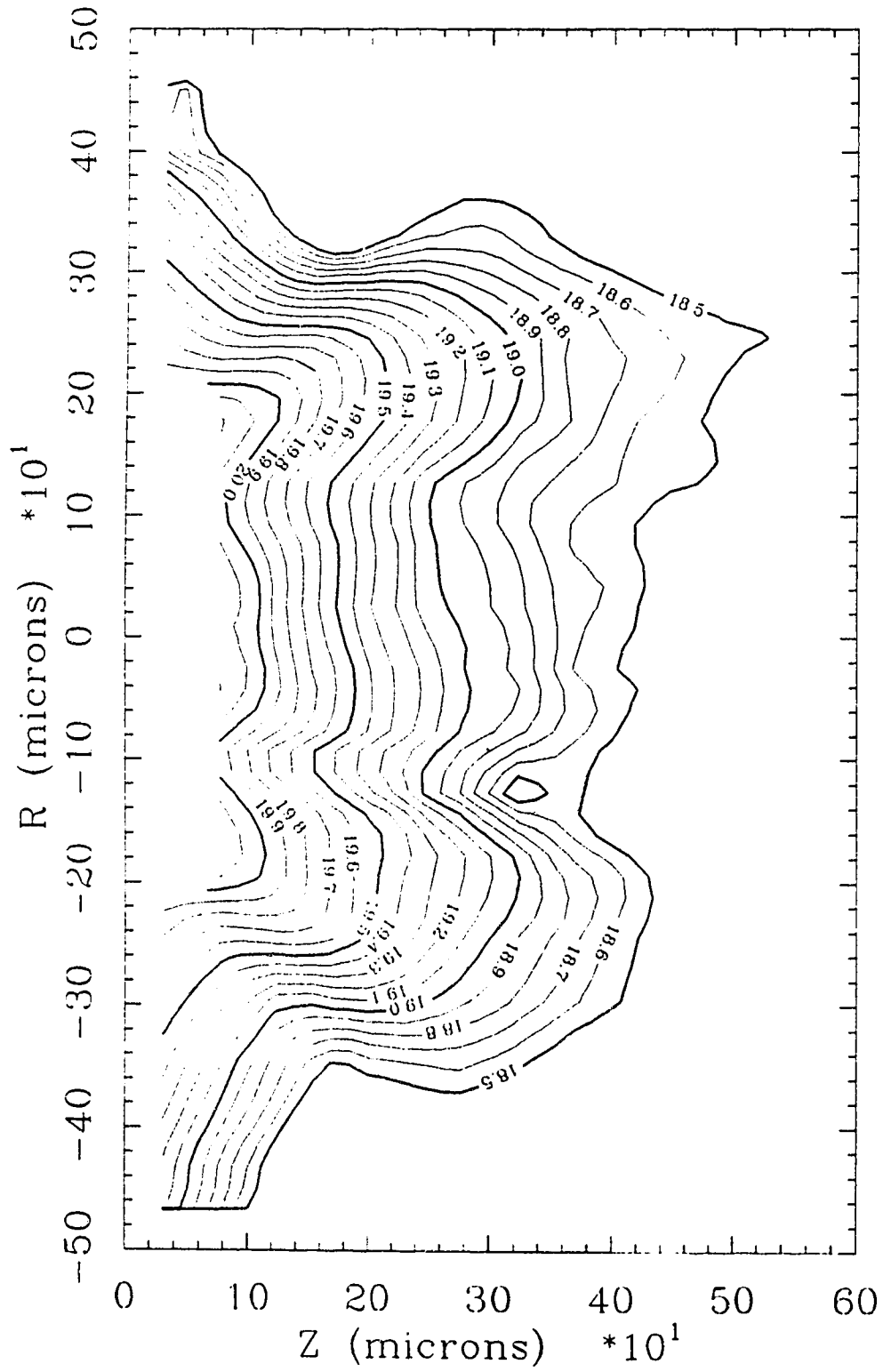
SHOT # 22078826
ENERGY = -99 mJ
FWHM = -99.0 ns
TIME = 4.9 ns



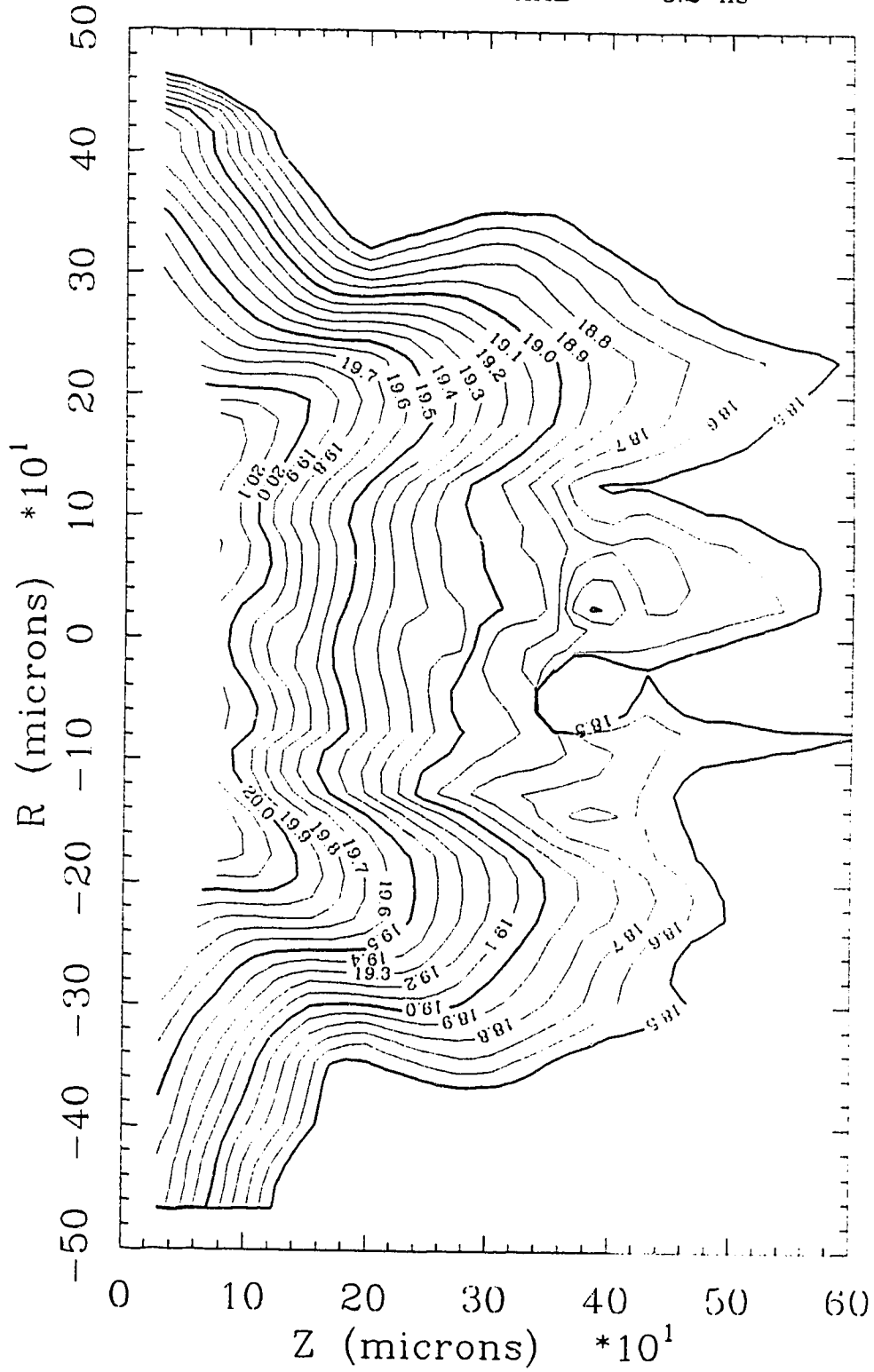
SHOT # 27078801
ENERGY = -99 mJ
FWHM = -99.0 ns
TIME = 4.9 ns



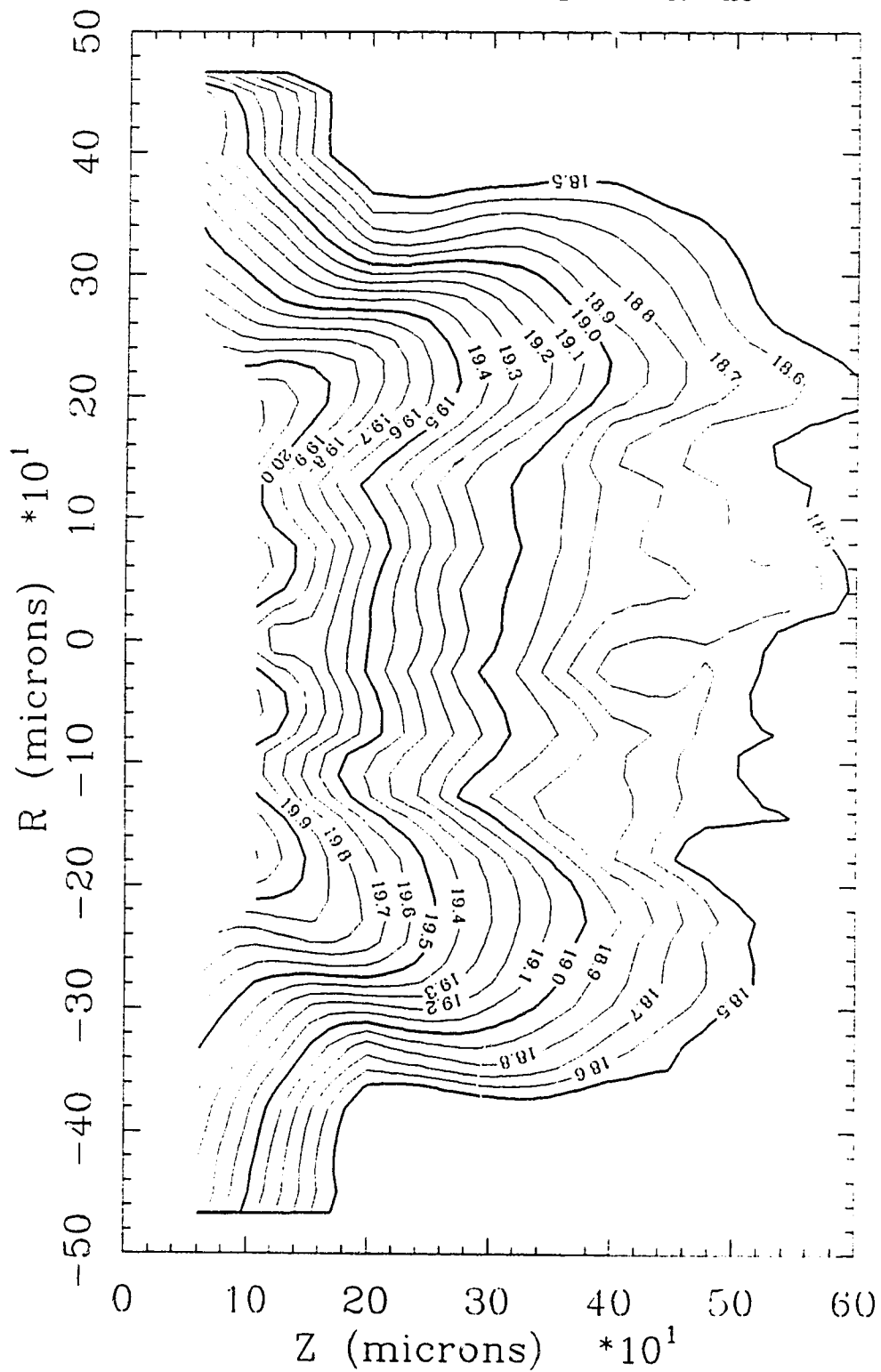
SHOT # 22078821
ENERGY = 840 mJ
FWHM = 2.0 ns
TIME = 5.2 ns



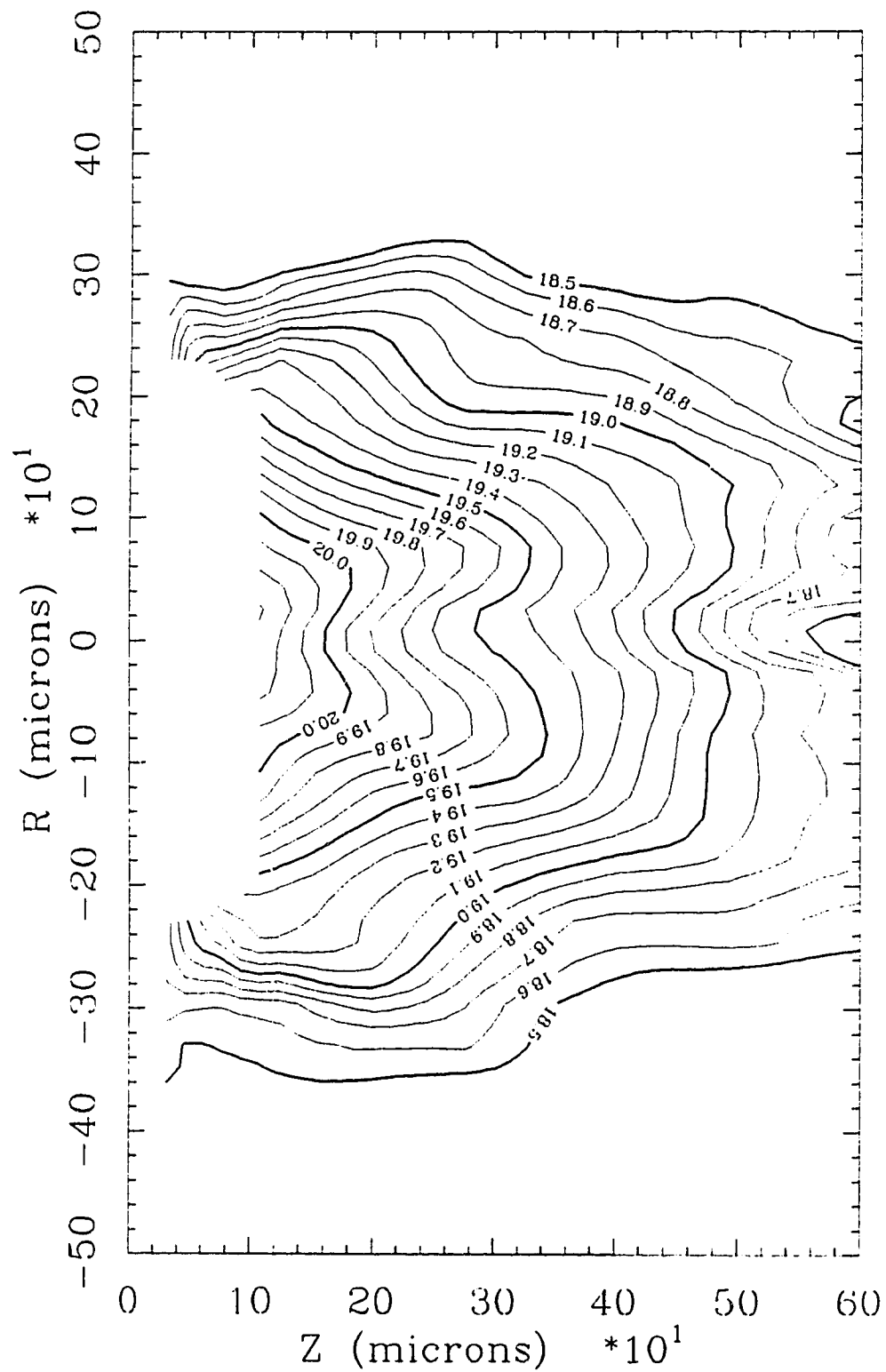
SHOT # 22078808
ENERGY = 940 mJ
FWHM = 1.9 ns
TIME = 5.2 ns



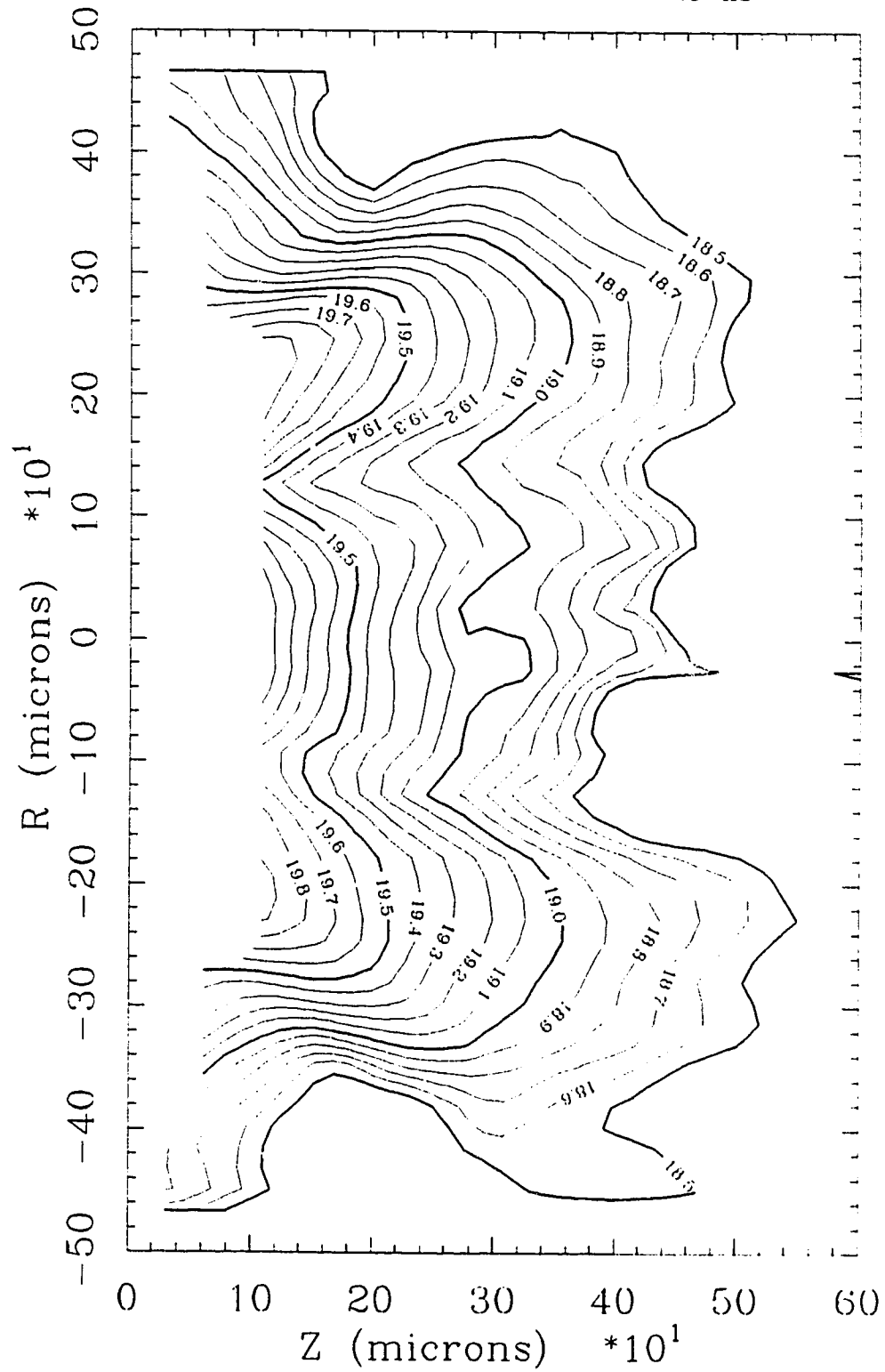
SHOT # 22078806
ENERGY = 1033 mJ
FWHM = 2.1 ns
TIME = 5.7 ns



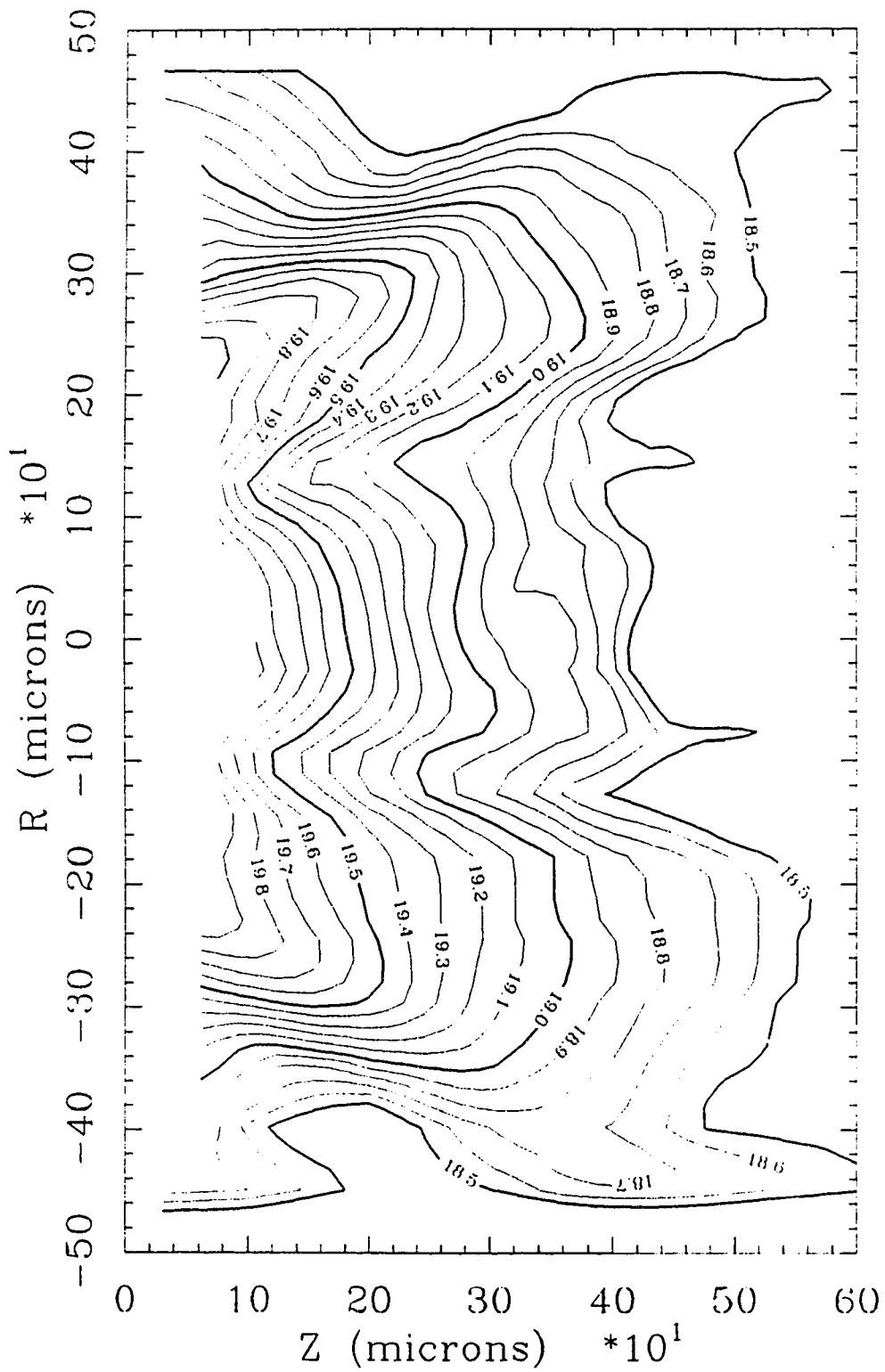
SHOT # 20078813
ENERGY = 233 mJ
FWHM = 1.7 ns
TIME = 7.5 ns



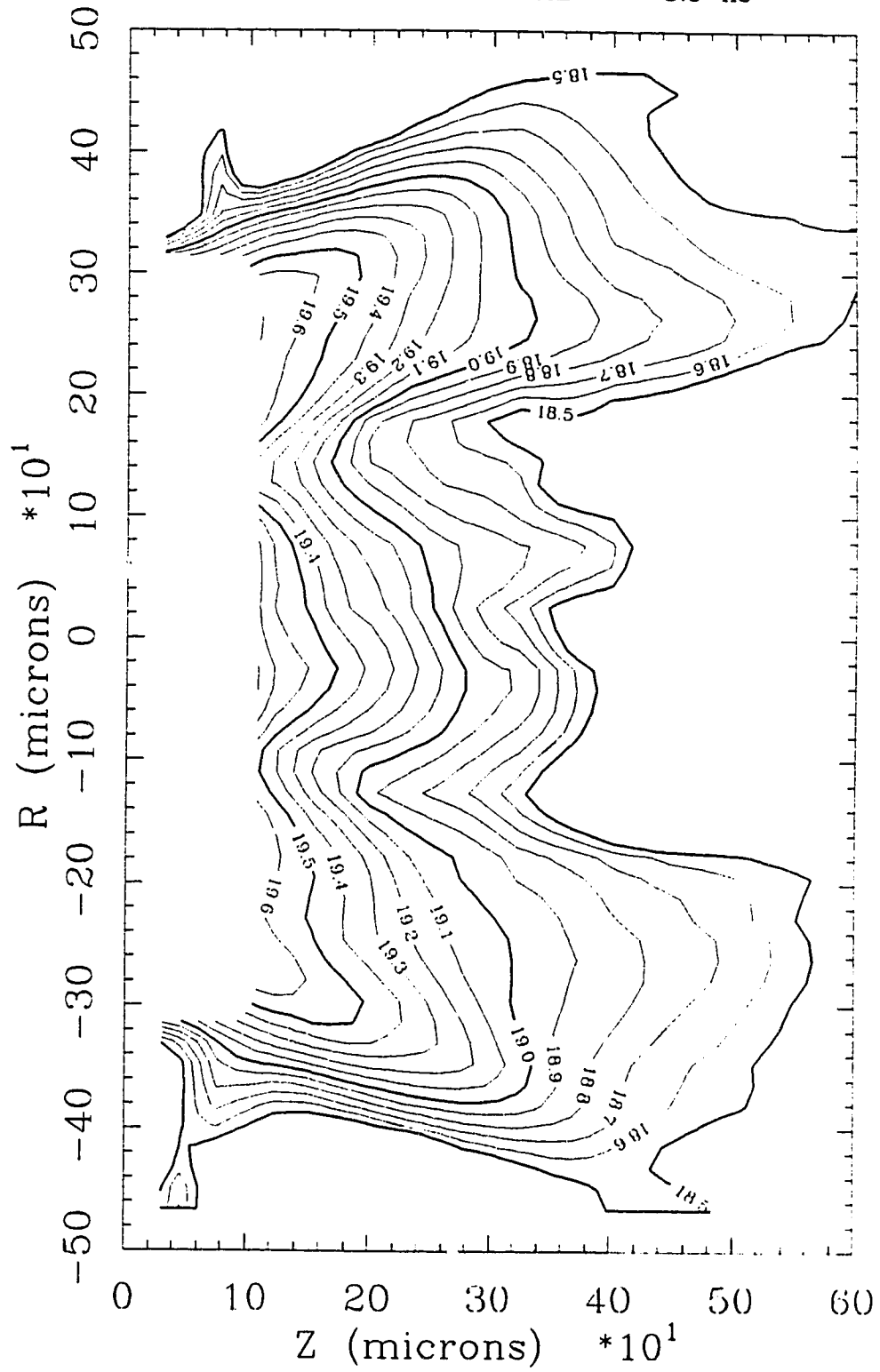
SHOT # 21078807
ENERGY = 746 mJ
FWHM = 1.7 ns
TIME = 7.5 ns



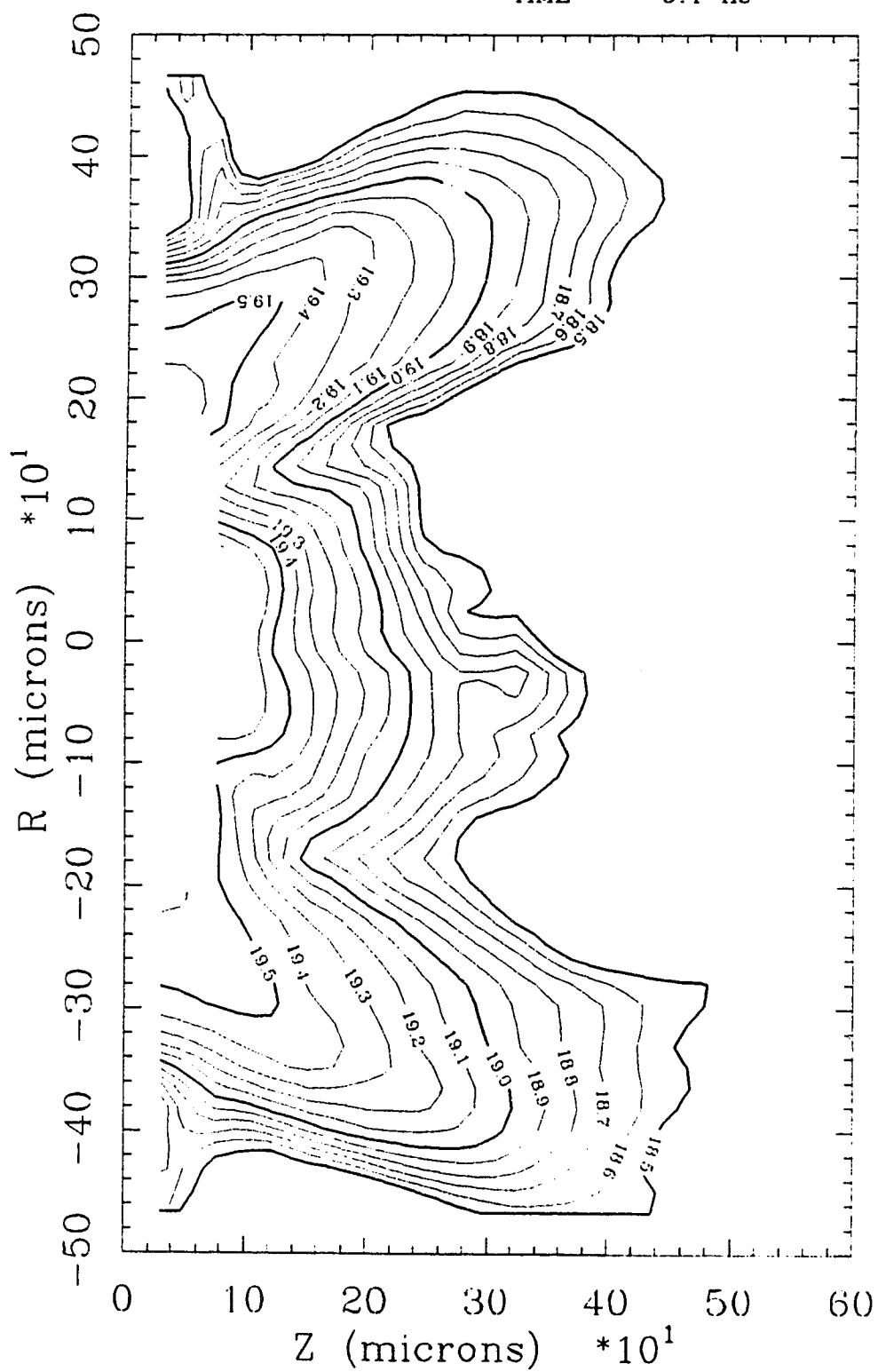
SHOT # 21078808
ENERGY = 715 mJ
FWHM = 1.6 ns
TIME = 6.3 ns



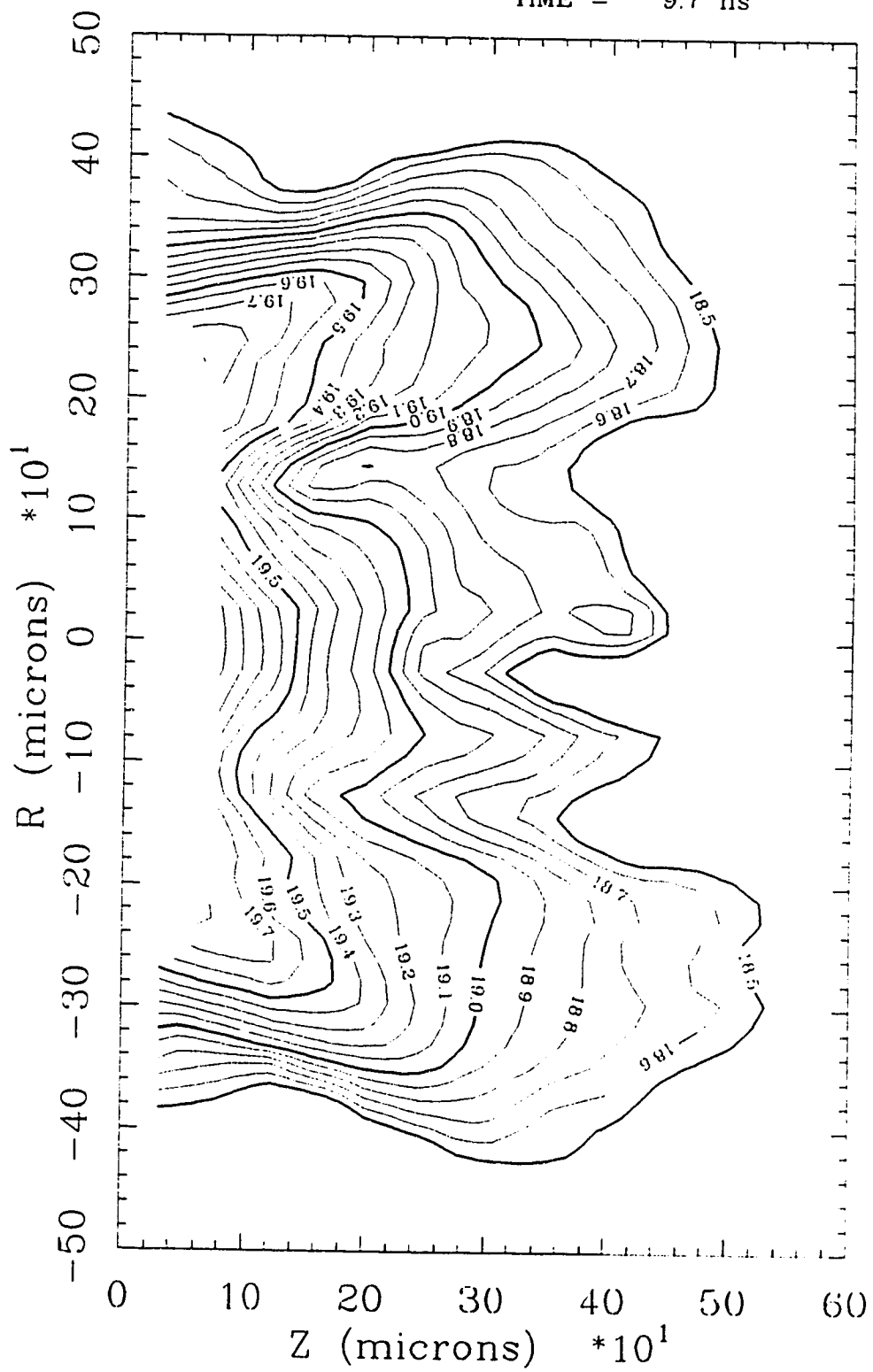
SHOT # 20078809
ENERGY = 521 mJ
FWHM = 1.6 ns
TIME = 8.5 ns



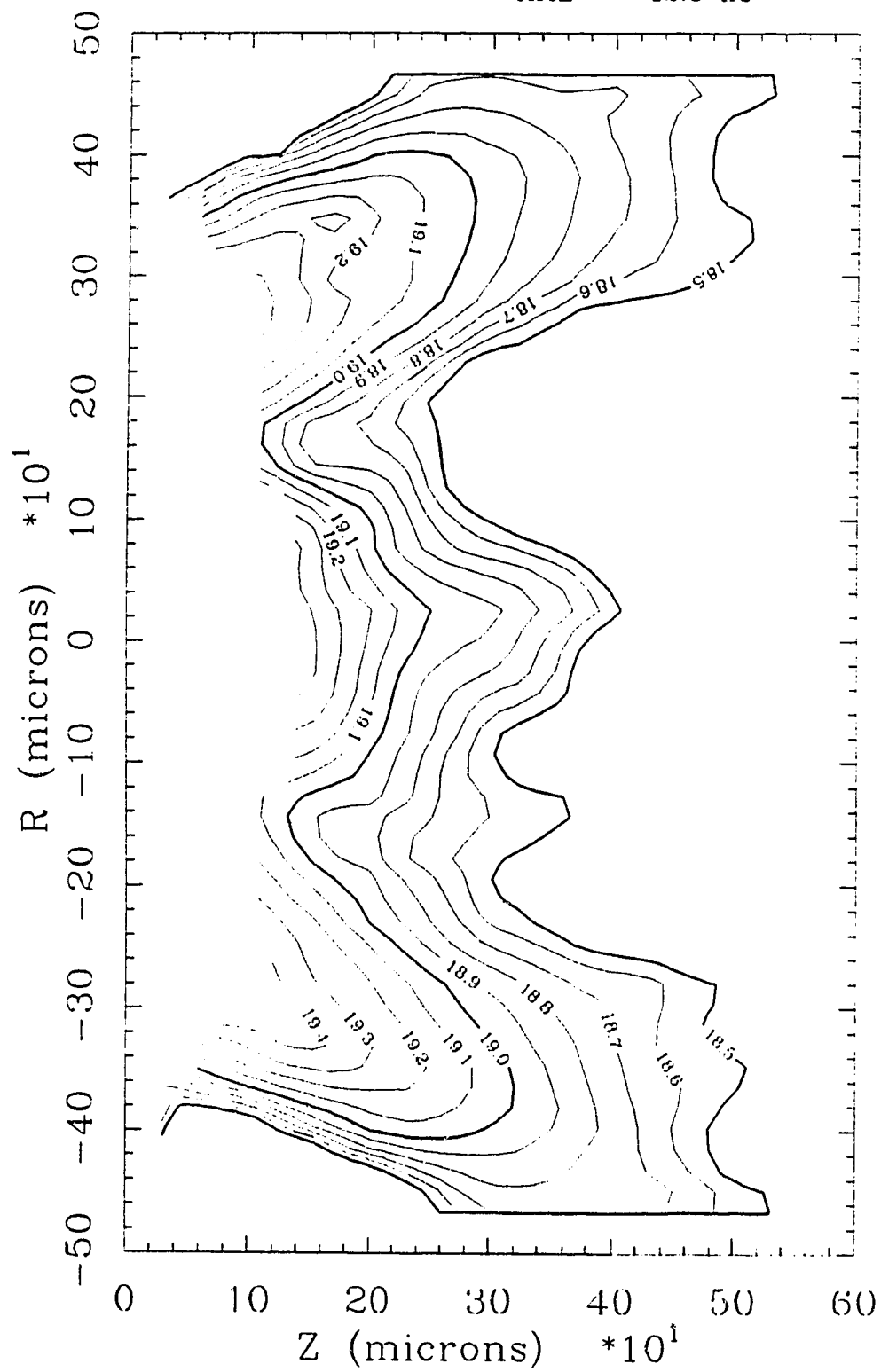
SHOT # 20078808
ENERGY = 404 mJ
FWHM = 1.6 ns
TIME = 9.4 ns



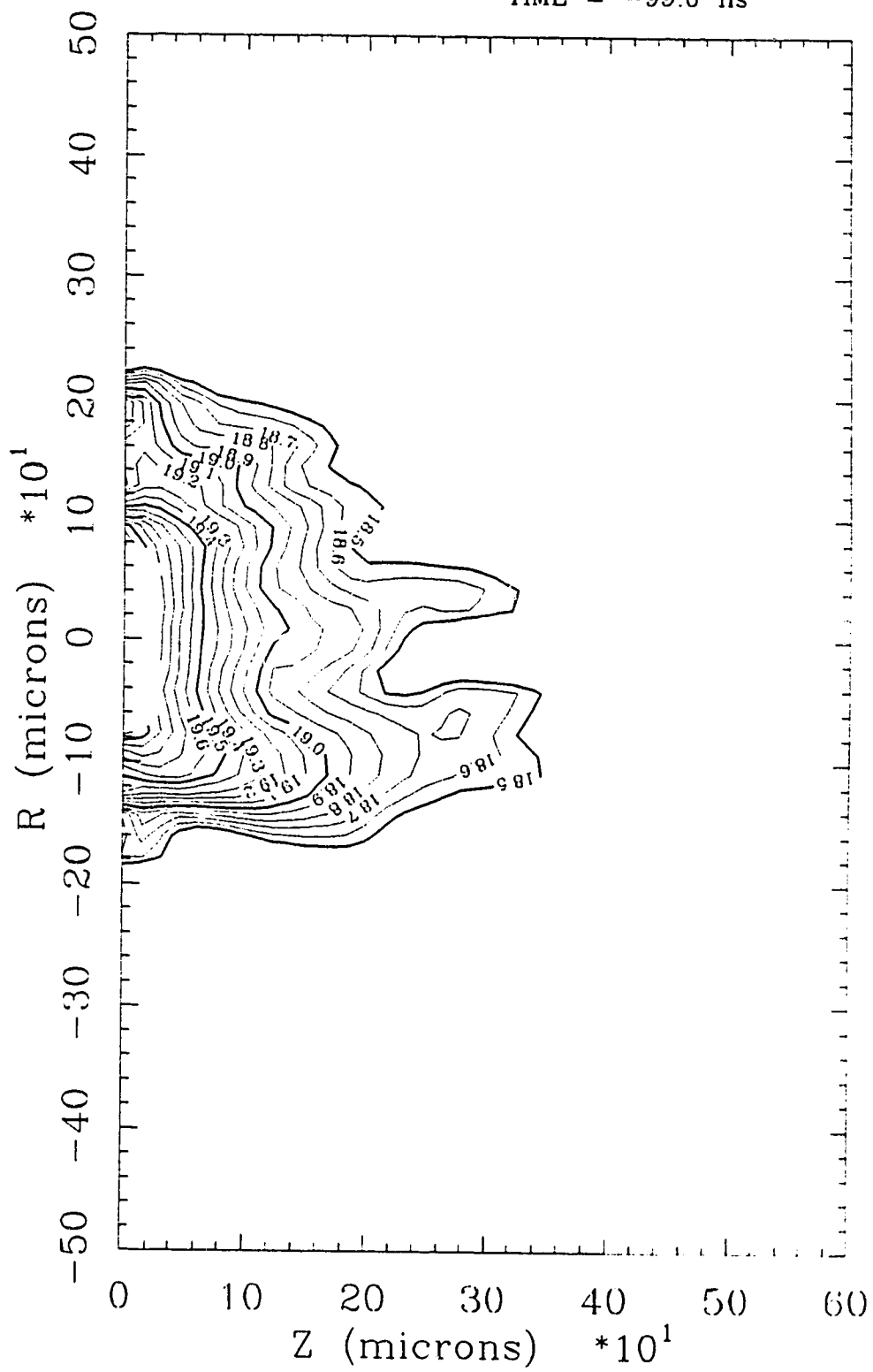
SHOT # 21078805
ENERGY = 505 mJ
FWHM = 1.8 ns
TIME = 9.7 ns



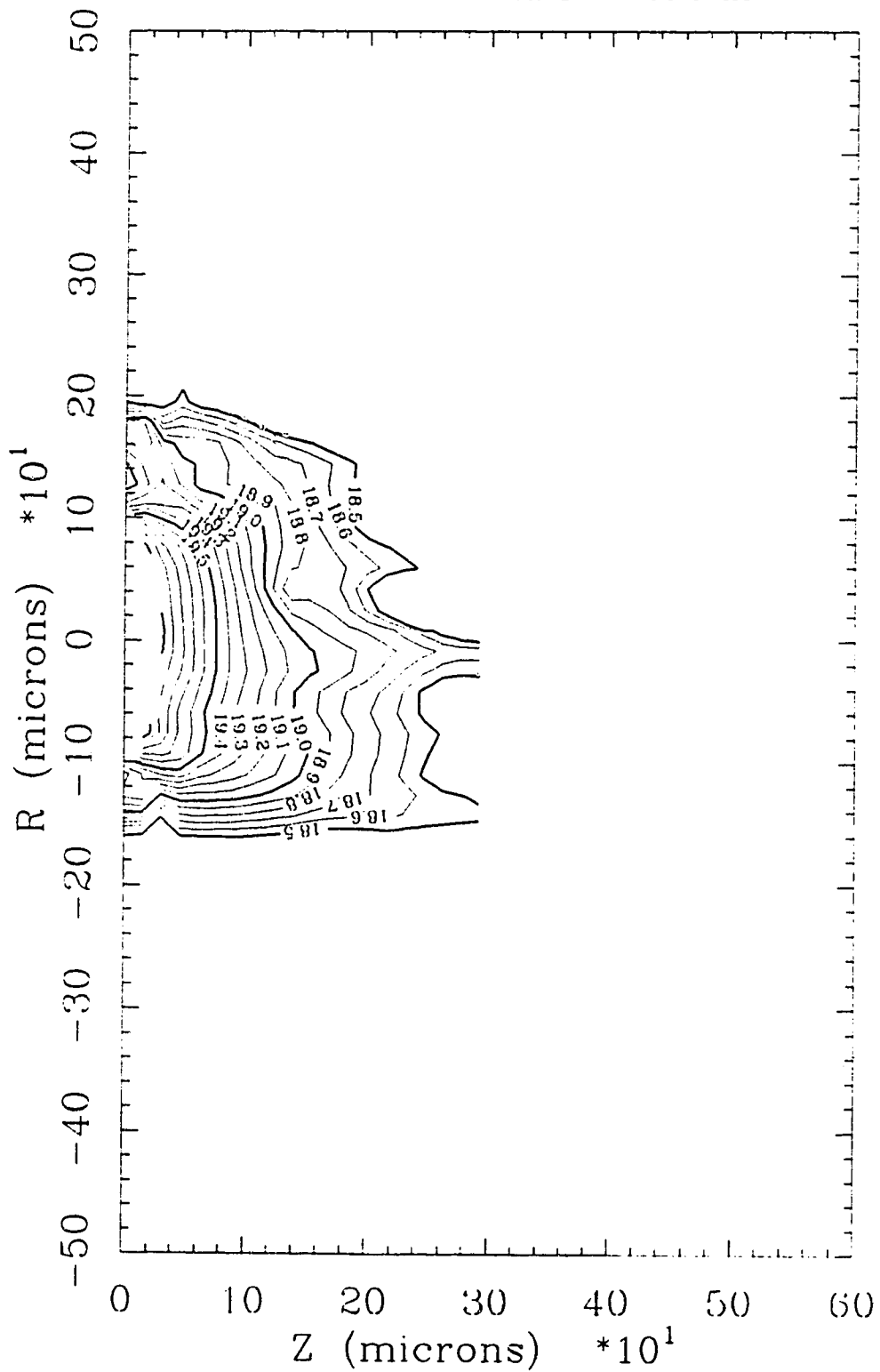
SHOT # 20078804
ENERGY = 427 mJ
FWHM = -99.0 ns
TIME = 12.0 ns



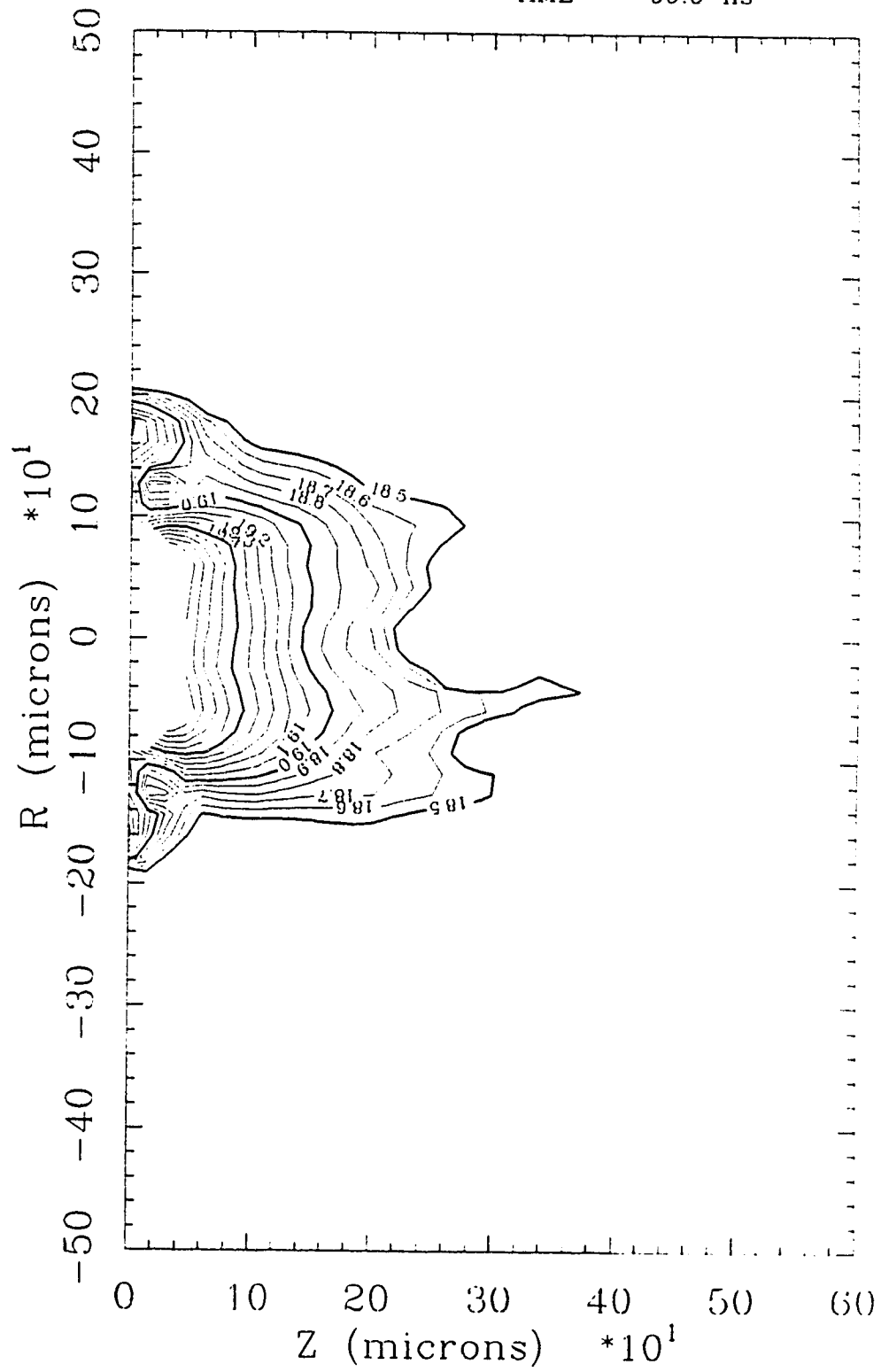
SHOT # 12108806
ENERGY = 66 mJ
FWHM = -99.0 ns
TIME = -99.0 ns



SHOT # 12108813
ENERGY = 100 mJ
FWHM = -99.0 ns
TIME = -99.0 ns



SHOT # 12108815
ENERGY = 231 mJ
FWHM = -99.0 ns
TIME = -99.0 ns



SHOT # 22078805
ENERGY = 528 mJ
FWHM = 1.5 ns
TIME = -99.0 ns

